MECHANISTIC INVESTIGATION INTO POST-TRANSLATIONAL MODIFICATIONS CATALYZED BY RADICAL *S*-ADENOSYLMETHIONINE ENZYMES

by

William Gura Walls III

A dissertation submitted in partial fulfillment
of the requirements for the degree

of

Doctor of Philosophy

in

Biochemistry

MONTANA STATE UNIVERSITY
Bozeman, Montana

May 2025

©COPYRIGHT

by

William Gura Walls III

2025

All Rights Reserved

DEDICATION

To my mom, dad, and sister, who always support me when I need it most. To my wife, Lauren, for always encouraging me to be the best version of myself. And in loving memory of William G. Walls Sr. and Dorothy Airoldi.

ACKNOWLEDGEMENTS

First and foremost, I must extend my deepest gratitude to my advisor Prof. Joan Broderick; her patience and wisdom has helped shaped me into the scientist I am today. I must also thank my committee members: Prof. Brian Bothner, Prof. Valerie Copie, and Prof. Mike Mock for their support. Thank you to Prof. Dr. Jörn Piel and Dr. Anna Vagstad for their collaboration and insights into radical SAM RiPP maturation. Thank you to Prof. Brian Hoffman and Dr. Hao Yang for help with RFQ and ENDOR experiments, and for hosting me at Northwestern University. At MSU, I want to thank Prof. William Broderick for his wonderful insights and discussions over the years. Thank you to Dr. Eric Shepard for his help with EPR troubleshooting, best practices, and scientific discussions. I must also thank Dr. Brigitta Nemeth and Dr. Maike Lundahl for their patience and training when I began my studies. Thank you to Dr. Batu Balci for his helpful discussions over the years and for being a wonderful colleague to maneuver the hardships of graduate school with. I must also thank Dr. Don Smith for his help troubleshooting my mass spec experiments; it has made a huge difference in my work. I want to thank the Gordon Research Conferences and the Enzyme Mechanisms Conference for providing a place for scientific discussions and presentations. I want to thank the Kopriva committee at MSU for financial support and the opportunity for me to share my work with the community. And finally, a sincere thank you to MSU College of Letters and Science and the NIH for funding that made this work possible.

TABLE OF CONTENTS

1. INTRODUCTION 1

Radical SAM Enzymes 1
Background 1
Structure 2
SPASM and twitch domains 3
Proposed Mechanism of Radical Initiation 4
Organometallic intermediate Ω 6
Glycyl Radical Enzymes 7
Activation and Mechanism 7
Amino acyl radical enzymes 8
B_{12}-independent glycerol dehydratase 9
Ribosomally Synthesized and Post Translationally Modified Peptide Natural Products 9
Background 9
Maturation 10
Epimerases 11
Proteusins 13
Epipeptides 15
Splicotides 17
References 18

2. THE B_{12}-INDEPENDENT GLYCEROL DEHYDRATASE ACTIVATING ENZYME FROM *CLOSTRIDIUM BUTYRICUM* CLEAVES SAM TO PRODUCE 5'-DEOXYADENOSINE AND NOT 5'-DEOXY-5'-(METHYLTHIO)ADENOSINE 29

Contribution of Authors and Co-Authors 29
Manuscript Information 31
Abstract 32
Introduction 32
Materials and Methods 35
GD-AE Cloning and Protein Expression 35
GD-AE Protein Purification 36
Glycerol Dehydratase Cloning and Protein Expression 38
Glycerol Dehydratase Protein Purification 39
Cloning and Purification of CsdA 40
Quantification of Protein, Iron, and Sulfide 41
Enzymatic Reconstitution of GD-AE 42
Electron Paramagnetic Resonance Spectroscopy 43
Enzyme Activity Assays with GD Peptide Substrate 44
Mass spectrometry of 5'-dAdoH 45

TABLE OF CONTENTS CONTINUED

Activation of GD by GD-AE 45
Generation of GD-AE Homology Model 46
Results 48
Purification and Characterization of GD-AE 48
Assays of GD-AE for SAM Cleavage 51
Activation of GD by GD-AE 54
Discussion 56
Supplemental Material 60
References 63

3. DIRECT DETECTION OF THE α-CARBON RADICAL INTERMEDIATE FORMED BY OspD: MECHANISTIC INSIGHT INTO RADICAL SAM PEPTIDE EPIMERIZATION 70

Contribution of Authors and Co-Authors 70
Manuscript Information 71
Abstract 72
Introduction 72
Methods and Materials 76
Materials 76
Site-Directed Mutagenesis 76
Protein Expression 77
Expression of Isotopically-labeled OspA 78
Protein Purification 79
Protein Quantification 80
Iron Analysis 81
Iron-Sulfur Cluster Reconstitution 81
UV-visible spectroscopy 82
EPR Sample Preparation 82
EPR spectroscopy 82
Epimerization Assay 84
Protease Digest of OspA and LC-MS Analysis 84
Results 86
Characterization of wild-type and mutant OspD. 86
Trapping a substrate-based radical on OspA. 87
Directionality of sequential epimerizations on OspA. 91
Trapping a Cα radical generated by wild-type OspD. 92
Discussion 93
Conclusion 95
Supplemental Material 95
Supplemental References 106
References 107

TABLE OF CONTENTS CONTINUED

4. MECHANISTIC INSIGHTS INTO POST-TRANSLATIONAL α-KETO-β-AMINO ACID FORMATION BY A RADICAL *S*-ADENOSYL METHIONINE PEPTIDE SPLICEASE....115

Contribution of Authors and Co-Authors....115
Manuscript Information....117
Abstract....118
Introduction....118
Methods and Materials....122
Materials....122
General....122
Cloning of splicease expression plasmids....123
Protein production tests....123
Protein production and purification....124
Anaerobic reconstitution of splicease iron-sulfur clusters....126
In vitro splicease reactions....126
LC-HRMS analyses....127
Quantification of splicease iron and sulfide content....128
UV-Vis Spectroscopy....129
EPR Spectroscopy....129
Characterization of the isomeric shunt product....130
Heterologous coexpression and culture extraction of Type III splicease genes from Thiothrix nivea....130
Attempts to detect small-molecule coproducts....131
Density Functional Theory calculations....132
Protein expression and purification for EPR....132
Enzymatic reconstitution for EPR....134
Protein, iron and sulfide quantification of protein prepared for EPR....134
Results....135
Establishment of in vitro splicease activity....135
Spectroscopic characterization of reconstituted PcpXY....138
Deuterium labeling studies define the site of initial H-abstraction....140
Characterization of shunt metabolites informs the splicease mechanism....143
Thermodynamic analysis of mechanistic proposals for the splicease reaction....146
Discussion....150
Supplemental Material....152
References....175

TABLE OF CONTENTS CONTINUED

5. THE RADICAL SAM ENZYME EpeE EXHIBITS DISTINCT SITE REACTIVITY DURING THE BIOSYNTHESIS OF THE RIPP NATURAL PRODUCT EPIPEPTIDE 182

Contribution of Authors and Co-Authors 182
Manuscript Information 184
Abstract 185
Introduction 185
Methods and Materials 190
Materials 190
Cloning 191
Site-directed Mutagenesis 191
Protein Expression 192
Expression of Isotopically labeled MBP-EpeX$_{18-49}$ 193
Protein Purification 194
Purification of EpeX$_{18-49}$ 195
Amino Acid Analysis and Protein Quantification 196
Iron Analysis 196
Enzyme Reconstitution 196
D_2O Buffer Preparation and Protein Buffer Exchange 197
UV-Visible Spectrophotometry 197
EPR Sample Preparation 198
Rapid Freeze Quench 198
Continuous Wave X-Band EPR Spectroscopy 199
Enzyme Activity Assays 199
Protease Digest of MBP-EpeX$_{18-49}$ and LC-MS Analysis 199
Results 200
Production and Characterization of EpeE WT and C223S Variant 200
Activity of EpeE towards MBP-EpeX$_{18-49}$ substrate 201
EpeE Forms Ω and Anneals to a Substrate Radical 202
EpeE Preferentially Forms a Cα• on Val4 of MBP-EpeX$_{18-49}$ 204
EpeE Forms Cα radicals on Val4 and Ile12 with distinct hyperfine coupling constants 206
Substrate Position Determines Radical Conformation 209
Ile12 Cα• is Quenched Faster than Val4 Cα• 210
Discussion 212
Supplemental Material 215
References 242

6. CONCLUSION 248

GRE Activation 248

TABLE OF CONTENTS CONTINUED

RiPP Maturation 249
References 258

CUMULATIVE REFERENCES CITED 261

LIST OF TABLES

Table Page

1. Table S3.1. Primers used to mutate Cys334 of OspD to Ser. Primers were designed using NEBaseChanger (https://nebasechanger.neb.com/) with *ospD/pCDF-6xH-v* as the template [3]. 106

1. Table S4.1.Type I splicease pathways screened for heterologous production and protein stability. XYG motifs within the core sequences are underlined as potential targets of the splicease reaction. 171

2. Table S4.1 Continued. 172

3. Table S4.2. Sequences of splicease pathway proteins screened for heterologous production in E. coli. The N-terminal affinity and solubility tag fusion sequences are given below. 172

4. Table S4.2 Continued. 173

5. Table S4.3. Primers used to amplify splicease pathway genes from cyanobacterial gDNA 173

6. Table S4.3 Continued. 174

7. Table S4.4. Expression plasmids used in this study. Multigene cassettes were amplified with their native intergenic regions. Forward and reverse primers are provided in Table S3. Plasmids pCDF-6xH-v, pCDF-6xH-MBP-v, and pCDF-6xH-bdSUMO are modified pCDFDuet-1 (Novagen) described in Table S2. Molecular weights were calculated using the Expasy ProtParam web tool.3 Spt, spectinomycin; Amp, ampicillin; Chl, chloramphenicol. 174

8. Table S4.4 Continued. 175

9. Table S4.5. Peptides detected by LC-HRMS in positive ion mode. Monoisotopic mass (M) or mass-to-charge (*m/z*) ratios are shown. The extracted ion chromatogram (EIC) list is for the most abundant charge state and isotope. 175

10. Table 5.1. Simulation parameters of Val4 and Ile12 Cα radicals. 208

LIST OF TABLES CONTINUED

11. Table S5.1. Primers used in this study were designed using NEBasechanger.com. Sequences in lowercase are the introduced mutations. 225

12. Table S5.1 Continued. 226

13. Table S5.2. Spin quantitation's of EPR signals for Figure 5.5. See Methods for spin quantitation details. 226

14. Table S5.3. Spin quantitation's and simulation weights of Val4 Cα• and Ile12 Cα• used for Fig. 5.7. 226

15. Table S5.4. MS/MS fragment ions of peptide VNDLWYFVK from trypsin digestion of no enzyme control reaction with MBP-EpeX$_{18\text{-}49}$ (Fig. S5.3, top). 227

16. Table S5.5. MS/MS fragment ions of peptide WILGSGH from trypsin digestion of no enzyme control reaction with MBP-EpeX$_{18\text{-}49}$ (Fig. S5.3, top). 227

17. Table S5.6. MS/MS fragment ions of peptide VNDLWYF(D-V)K from trypsin digestion following reaction of EpeE WT and MBP-EpeX$_{18\text{-}49}$ (Fig. S5.3, middle). 228

18. Table S5.7. MS/MS fragment ions of peptide W(D-I)LGSGH from trypsin digestion following reaction of EpeE WT and MBP-EpeX$_{18\text{-}49}$ (Fig. S5.3, middle). 228

19. Table S5.8. MS/MS fragment ions of peptide VNDLWYF(D-V)K from trypsin digestion following reaction of EpeE C223S and MBP-EpeX$_{18\text{-}49}$ (Fig. S5.3, bottom). 229

20. Table S5.9. MS/MS fragment ions of peptide W(D-I)LGSGH from trypsin digestion following reaction of EpeE C223S and MBP-EpeX$_{18\text{-}49}$ (Fig. S5.3, bottom). 229

21. Table S5.10. MS/MS fragment ions of peptide VNDLWYFVK from EpeX$_{18\text{-}49}$ following trypsin digestion (Fig. S5.4, left panel). 230

22. Table S5.11. MS/MS fragment ions of peptide WILGSGH from EpeX$_{18\text{-}49}$ following trypsin digestion (Fig. S5.4, top). 230

LIST OF TABLES CONTINUED

23. Table S5.12. MS/MS fragment ions of peptide VNDLWYFVK from trypsin digestion of no enzyme control reaction with MBP-EpeX$_{18-49}$ I12W (Fig. S5.6, top). 231

24. Table S5.13. MS/MS fragment ions of peptide WWLGSGH from trypsin digestion of no enzyme control reaction with MBP-EpeX$_{18-49}$ I12W (Fig. S5.6, right panel). 231

25. Table S5.14. MS/MS fragment ions of peptide VNDLWYF(D-V)K from trypsin digestion following reaction of EpeE WT and MBP-EpeX$_{18-49}$ I12W (Fig. S5.6, middle). 232

26. Table S5.15. MS/MS fragment ions of peptide VNDLWYF(D-V)K from trypsin digestion following reaction of EpeE C223S and MBP-EpeX$_{18-49}$ I12W (Fig. S5.6, bottom). 232

27. Table S5.15 Continued. 233

28. Table S5.16. MS/MS fragment ions of peptide VNDLWYFWK from trypsin digestion following no enzyme control reaction with MBP-EpeX$_{18-49}$ V4W (Fig. S5.7, left panel). 233

29. Table S5.17. MS/MS fragment ions of peptide WILGSGH from trypsin digestion following no enzyme control reaction with MBP-EpeX$_{18-49}$ V4W (Figure S5.7, top). 233

30. Table S5.17 Continued. 234

31. Table S5.18. MS/MS fragment ions of peptide W(D-I)LGSGH from trypsin digestion following reaction of EpeE WT and MBP-EpeX$_{18-49}$ V4W (Figure S5.7, middle). 234

32. Table S5.19. MS/MS fragment ions of peptide W(D-I)LGSGH from trypsin digestion following reaction of EpeE C223S and MBP-EpeX$_{18-49}$ V4W (Figure S5.7, bottom). 234

33. Table S5.19 Continued. 235

34. Table S5.20. MS/MS fragment ions of peptide VNDLWYFWK from trypsin digestion following no enzyme control reaction with MBP-EpeX$_{18-49}$ V4W/ I12V (Figure S5.10, left panel). 235

LIST OF TABLES CONTINUED

35. Table S5.21. MS/MS fragment ions of peptide WVLGSGH from trypsin digestion following no enzyme control reaction with MBP-EpeX$_{18\text{-}49}$ V4W/ I12V (Figure S5.10, top). 235

36. Table S5.21 Continued. 236

37. Table S5.22. MS/MS fragment ions of peptide W(D-V)LGSGH from trypsin digestion following reaction of EpeE WT and MBP-EpeX$_{18\text{-}49}$ V4W/ I12V (Figure S5.10, middle). 236

38. Table S5.23. MS/MS fragment ions of peptide W(D-V)LGSGH from trypsin digestion following reaction of EpeE C223S and MBP-EpeX$_{18\text{-}49}$ V4W/ I12V (Figure S5.10, bottom). 236

39. Table S5.23 Continued. 237

40. Table S5.24. MS/MS fragment ions of peptide VNDLWYFVK from trypsin digested MBP-EpeX$_{18\text{-}49}$ labeled with [3-D$_1$]-L-Val. 237

41. Table S5.25. MS/MS fragment ions of peptide WILGSGH from trypsin digested MBP-EpeX$_{18\text{-}49}$ labeled with [3-D$_1$]-L-Val. 237

42. Table S5.25 Continued. 238

43. Table S5.26. MS/MS fragment ions of peptide VNDLWYFVK from trypsin digested MBP-EpeX$_{18\text{-}49}$ labeled with [U-D$_{10}$]-L-Ile. 238

44. Table S5.27. MS/MS fragment ions of peptide WILGSGH from trypsin digested MBP-EpeX$_{18\text{-}49}$ labeled with [U-D$_{10}$]-L-Ile. 238

45. Table S5.27 Continued. 239

46. Table S5.28. MS/MS fragment ions of peptide VNDLWYFVK from trypsin digested MBP-EpeX$_{18\text{-}49}$ labeled with both [U-D$_{10}$]-L-Ile and [3-D$_1$]-L-Val. 239

47. Table S5.29. MS/MS fragment ions of peptide WILGSGH from trypsin digested MBP-EpeX$_{18\text{-}49}$ labeled with both [U-D$_{10}$]-L-Ile and [3-D$_1$]-L-Val. 239

48. Table S5.29 Continued. 240

49. Table S5.30. MS/MS fragment ions of peptide VNDLWYFVK from trypsin digested MBP-EpeX$_{18\text{-}49}$ V4W labeled with [U-D$_{10}$]-L-Ile. 240

LIST OF TABLES CONTINUED

50. Table S5.31. MS/MS fragment ions of peptide WILGSGH from trypsin digested MBP-EpeX$_{18\text{-}49}$ V4W labeled with [U-D$_{10}$]-L-Ile. 240

51. Table S5.31 Continued. 241

52. Table S5.32. MS/MS fragment ions of peptide VNDLWYFVK from trypsin digested MBP-EpeX$_{18\text{-}49}$ I12W labeled with [3-D$_1$]-L-Val. 241

LIST OF FIGURES

Figure Page

1. Figure 1.1. X-ray crystal structures of PFL-AE and anaerobic sulfatase maturating enzyme (anSME).. 3
2. Figure 1.2. Proposed radical initiation mechanism by the radical SAM enzyme superfamily. 5
3. Figure 1.3. Activation and general mechanism of GRE superfamily.. 8
4. Figure 1.4. Overview of maturation of RiPP natural products from biosynthetic gene cluster (BGC). 10
5. Figure 1.5. Overview of Landornamide A biosynthesis and structure.. 14
6. Figure 1.6. Proposed mechanism of amino acid epimerization by OspD. 15
7. Figure 1.7. Biosynthesis of epipeptide RiPP natural products and structure of radical SAM epimerase EpeE.. 16
8. Figure 1.8. Proposed mechanism of amino acid epimerization by EpeE. 17
9. Figure 2.1. Reductive cleavage pathways in radical SAM enzymes.. 34
10. Figure 2.2. EPR spectroscopy of GD-AE.. 49
11. Figure 2.3. Temperature-dependent EPR of reduced GD-AE. 50
12. Figure 2.4. HPLC based endpoint assays of GD-AE.. 52
13. Figure 2.5. Kinetics of 5'-dAdoH and MTA production by GD-AE.. 53
14. Figure 2.6. EPR spectroscopy of activated GD. 55
15. Figure 2.7. HPLC Chromatogram of GD Activation Reaction. 55
16. Figure 2.8. Homology model of GD-AE.. 57
17. Figure S2.1. Purification of GD-AE using 10x-His-SUMO tag.. 60
18. Figure S2.2. Purification of 6x-His-GD-AE. 61
19. Figure S2.3. Purification of 6x-His-GD.. 62

LIST OF FIGURES CONTINUED

20. Figure S2.4. Plots of signal amplitude vs. temperature for the EPR spectra shown in Figure 3. 62

21. Figure S2.5. EPR power saturation studies of reconstituted, reduced GD-AE with and without SAM. 63

22. Scheme 3.1. Overview of biosynthesis of RiPP natural products. 73

23. Figure 3.1. Biosynthesis of the RiPP natural product landornamide A. 75

24. Figure 3.2. Normalized UV-visible (A) and X-band EPR spectra (B) of reconstituted WT and C334S OspD. 87

25. Figure 3.3. X-band EPR spectra (black) and simulations (red) of 15 s freeze-quenched reactions of OspD C334S, SAM, and OspA carried out in H_2O (top) or D_2O (bottom). 89

26. Scheme 3.2. Structures of [U-D_{10}]-L-isoleucine and [3-D_1]-L-valine. 89

27. Figure 3.4. X-band EPR spectra (black) and simulations (red) of 15 s freeze-quenched reactions of OspD C334S, SAM, and OspA reveal Ile4 as the initial site of H-atom abstraction. 91

28. Figure S3.1. Multiple sequence alignment of characterized proteusin epimerases OspD (D8G6F8_9CYAN), PoyD (J9ZW29_BACS1), AvpD (Q3ME30_TRIV2), and PlpD (WP_019503883). 96

29. Figure S3.2. AlphaFold [1] model of the OspD active site. 97

30. Figure S3.3. Power dependence of NaDT-reduced OspD at 10 K (left, spectra acquired with 1 mW microwave power at 10 K are non-saturating), and the OspA radical at 75 K (right, spectra acquired with 335 μW microwave power are non-saturating). 97

31. Figure S3.4. OspD C334S reacted with OspA and SAM in buffered H_2O or 90% D_2O and quenched at 15 s. 98

32. Figure S3.5. Mass spectra (top) and expected peptide ions (bottom) of GluC and trypsin digested natural-abundance OspA. 99

33. Figure S3.6. Mass spectra (top) and expected peptide ions (bottom) of GluC and trypsin digested OspA labeled with [U-D_{10}]-L-isoleucine. 99

LIST OF FIGURES CONTINUED

34. Figure S3.7. Mass spectra (top) and expected peptide ions (bottom) of GluC and trypsin digested OspA labeled with [3-D_1]-L-valine. 100

35. Figure S3.8. Mass spectra (top) and expected peptide ions (bottom) of GluC and trypsin digested OspA labeled with both [U-D_{10}]-L-isoleucine and [3-D_1]-L-valine. 101

36. Figure S3.9. LC-MS/MS fragmentation of GluC and trypsin digested natural abundance and isotopically labeled OspA core peptide encompassing residues -5 to +8. Y- ions clearly show a 9 Da increase that localizes to Ile4. 102

37. Figure S3.10. LC-MS/MS fragmentation of GluC and trypsin digested natural abundance and isotopically labeled OspA core peptide encompassing residues +9 to +15. Y- ions clearly show a 1 Da increase that localizes to Val13. 103

38. Figure S3.11. Mass spectroscopic evaluation of epimerization of OspA by WT and C334S OspD following a 17 h reaction (see SI methods). 103

39. Figure S3.12. EPR monitored decay of [U-D_{10}]-L-Ile labeled OspA radical over time. 104

40. Figure S3.13. EPR monitored decay of [3-D_1]-L-Val labeled OspA radical over time. 105

41. Figure S3.14. EPR spectra of OspD WT and OspA substrate freeze quenched in buffered H_2O and D_2O. 106

42. Figure 4.1. Post-translational spliceases modify ribosomally translated precursor proteins. 120

43. Figure 4.2. In vitro splicease activity detected by LC-HRMS. 137

44. Figure 4.3. X-band EPR spectra of reconstituted and sodium dithionite–reduced PcpXY in the presence and absence of SAM. 140

45. Figure 4.4. Deuterium-labeling studies of in vitro splicease reactions. 142

46. Figure 4.5. Detection of shunt metabolites and coproducts from splicease reactions. 145

47. Figure 4.6. Mechanistic proposals for the splicease reaction. 148

LIST OF FIGURES CONTINUED

48. Figure S4.1. Protein production screens for five type I splicease pathways from Cyanobacteria. 153

49. Figure S4.2. Ni^{2+}-affinity column chromatography purified proteins used for in vitro reactions with the Pcp splicease. 154

50. Figure S4.3. LC-HRMS analysis of $PcpA_{32–64}$ fragment b gave only minor amounts of spliced Tyr56 product. 154

51. Figure S4.4. LC-HRMS spectra of an efficient Pcp splicease reaction shows time-dependent accumulation of the product with two ketoamides, $PcpA_{-7–64}$ with a Δ-270.12 mass difference β. 155

52. Figure S4.5. Splicease reaction timecourse. 156

53. Figure S4.6 . The reductant system affects the efficiency of in vitro splicease reactions. 157

54. Figure S4.7. Untagged PcpY co-purifies with His_6-PcpX. 158

55. Figure S4.8. Addition of extra PcpY to complete reactions did not improve product yields, suggesting untagged PcpY is copurified in stoichiometric amounts with 6xH-v-PcpX from PcpXY coproductions. 158

56. Figure S4.9. Comparison of as-purified and anaerobically reconstituted PcpXY.. 159

57. Figure S4.10. X-band EPR spectra of as-reconstituted PcpXY. 160

58. Figure S4.11. Temperature dependence of EPR spectra of the dithionite-reduced PcpXY complex in the a) absence and b) presence of SAM. 160

59. Figure S4.12. Power-saturation of the EPR spectra of the dithionite-reduced PcpXY complex in the a) absence and b) presence of SAM. 161

60. Figure S4.13. Stable isotope-labeled PcpA variants used as substrates for in vitro splicease reactions.. 161

61. Figure S4.14. In vitro PcpXY splicease reactions (21 h timepoint) with differentially deuterium-labeled PcpA substrates or with unlabeled PcpA in D_2O. 162

62. Figure S4.15. In vitro PcpXY splicease reaction time course in D_2O.. 163

LIST OF FIGURES CONTINUED

63. Figure S4.16. Enzymatic production of (2-^{2}H)- L-Tyr and its incorporation into PcpA. 164

64. Figure S4.17 . In vitro PcpXY splicease reactions with differentially deuterium labeled PcpA substrates (top)..... 165

65. Figure S4.18. Isomeric shunt product 6 contains D-tyrosine... 166

66. Figure S4.19. 4-Hydroxybenzaldehyde 7 was detected as a co-product of the splicing reaction in extracts of E. coli BL21(DE3) expressing the type III spliceotide system from Thiothrix nivea DSM 5205. 167

67. Figure S4.20. Identification of shunt products from the production of PlpA3-P11A mutant with PlpXY in E. coli BL21(DE3).. 168

68. Figure S4.21. Commercial 4-hydroxymandelonitrile **11** rapidly degrades to 4-hydroxybenzaldehyde **7** under our in vitro splicease reaction conditions in support of our mechanistic proposal.. 169

69. Figure S4.22. Mechanistic proposals for Pathway A of the splicease reaction involving an [4Fe-4S] cubane as catalyst relative to no catalyst. 170

70. Figure S4.23. rSAM enzymes that act on tyrosine/tyrosyl substrates.. 171

71. Figure 5.1. Overview of Epipeptide biosynthesis and structure of EpeE peptide epimerase..... 187

72. Scheme 5.1. Proposed mechanism of peptide epimerization by EpeE. 188

73. Figure 5.2. EPR spectra of EpeE RFQ..... 203

74. Figure 5.3. EPR spectra of EpeE, SAM, and MBP-EpeX$_{18\text{-}49}$ reveals formation of a Cα•.. 204

75. Figure 5.4. EpeX isotopic labeling reveals substrate Cα radical resides primarily on Val4. 205

76. Figure 5.5. EPR spectra of MBP-EpeX$_{18\text{-}49}$ Trp mutations shows Val4 Cα• and Ile12 Cα• form with distinct hyperfine coupling interactions. 207

77. Figure 5.6. EpeE forms Val Cα radicals on MBP-EpeX$_{18\text{-}49}$ at position 4 and 12 with distinct hyperfine coupling constants.. 209

78. Figure 5.7. Ile12 Cα• decays faster than Val4 Cα•.....211

LIST OF FIGURES CONTINUED

79. Figure S5.1. 4-20% SDS-PAGE analysis of purified proteins used in this study.. 215

80. Figure S5.2. Spectroscopic characterization of EpeE WT and C223S variant... 216

81. Figure S5.3. EICs of 18-hour assays of EpeE, SAM, and MBP-EpeX$_{18-49}$ in buffered D_2O. 217

82. Figure S5.4. EICs of 18-hour assays between EpeE and EpeX$_{18-49}$ in buffered D_2O.. 218

83. Figure S5.5. RFQ EPR spectra of EpeE C223S, SAM, and MBP-EpeX$_{18-49}$ at 20 ms, 500 ms, and 1 s.. 219

84. Figure S5.6. EICs of 18-hour assays of EpeE and MBP-EpeX$_{18-49}$ I12W in buffered D_2O.. 220

85. Figure S5.7. EICs of 18-hour assays of EpeE and MBP-EpeX$_{18-49}$ V4W in buffered D_2O.. 221

86. Figure S5.8. Isotopic labeling of MBP-EpeX$_{18-49}$ I12W to determine hyperfine coupling constants. 222

87. Figure S5.9. Isotopic labeling of MBP-EpeX$_{18-49}$ V4W to determine hyperfine coupling constants.. 223

88. Figure S5.10. EICs of 18-hour assays of EpeE and MBP-EpeX$_{18-49}$ V4W/ I12V in buffered D_2O.. 224

89. Figure S5.11. EICs of peptide VNDLWYFVK and peptide WILGSGH following reaction of EpeE C223S, MBP-EpeX$_{18-49}$, and SAM for 1 min or 30 min and trypsin digestion.. 225

ABSTRACT

Radical *S*-adenosyl-L-methionine (SAM) enzymes form one of the largest enzyme superfamilies and are found in all kingdoms of life. They catalyze a wide diversity of reactions but are united by the use of a [4Fe-4S] cluster and SAM to generate a 5′-dAdo radical which initiates catalysis through H-atom abstraction and formation of a substrate radical intermediate. Trapping and characterizing radical intermediates is challenging due to their high reactivity, and therefore many reactions catalyzed by radical SAM enzymes contain proposed intermediates that lack experimental evidence. This work seeks to trap and characterize radical intermediates to test proposed mechanisms of radical SAM enzymes involved in the post-translational modification of glycyl radical enzymes (GRE) and ribosomally synthesized and post-translationally modified peptide (RiPP) natural products. This work primarily made use of electron paramagnetic resonance (EPR) spectroscopy, enzyme activity assays, and site-directed mutagenesis techniques. Mechanistic investigation of the enzyme glycerol dehydratase activating enzyme (GD-AE) showed that it produced the SAM cleavage product 5′-deoxyadenosine and not 5′-deoxy-5′-methylthioadenosine (MTA) when activating glycerol dehydratase (GD) as previously reported. Spectroscopic characterization of the splicease enzyme PcpX supported the hypothesis that it coordinates three [4Fe-4S] clusters. These results helped form mechanistic proposals for α-keto-β-amino acid formation during RiPP maturation. Mechanistic investigations of the radical SAM epimerases from proteusin (OspD) and epipeptide (EpeE) RiPP natural product families identified similarities and differences in their catalytic mechanisms. Both enzymes initiate catalysis by abstraction of Hα from a substrate Val or Ile residue to form a Cα radical intermediate. Trapping of the Cα radicals in both OspD and EpeE was made possible by mutating the quenching cysteine (Cys) to serine (Ser). Cα radicals trapped in the active site of OspD or EpeE exhibited variable hyperfine coupling to Hβ or the amide proton, indicating different conformations. Collectively, these studies provided key insights into radical SAM enzyme mechanism during post-translational modification of GREs and RiPPs that will aid future bioengineering efforts to produce novel peptide therapeutics.

INTRODUCTION

Radical SAM Enzymes

Background

Radical *S*-adenosyl-L-methionine (SAM) enzymes are found in all kingdoms of life and catalyze an astounding diversity of chemical reactions involved in processes such as metallocofactor assembly, nucleotide modification, anaerobic metabolism, and natural product biosynthesis [1-3]. The superfamily was first identified in a seminal bioinformatics study in 2001 [3], which showed that the enzymes lysine 2,3-aminomutase (LAM), biotin synthase (BioB), lipoic acid synthase (LipA), pyruvate formate lyase activating enzyme (PflA, or PFL-AE), and anaerobic ribonucleotide reductase activating enzyme (NrdG, or RNR-AE) were related by their use of SAM to generate a 5′-deoxyadenosyl radical for catalysis (5′-dAdo•) that in turn initiates catalysis by H-atom abstraction from the substrate. While the initial report by Sofia et al. [3] identified approximately 600 proteins in the superfamily, that number has now grown to over 700,000 proteins (Interpro database [4], IPR007197) with more being rapidly predicted due to advances in bioinformatics and DNA sequencing. To handle the large sequence space of the family, radicalSAM.org was introduced [5], which represents the superfamily as a network of sequence similarity networks. The rate at which sequences are bioinformatically predicted largely outpaces the rate at which they are experimentally investigated, thus, only a small fraction of the predicted members of the radical SAM superfamily have been characterized. An even smaller portion of characterized radical SAM enzymes have experimental evidence of proposed radical intermediates due to their high reactivity, making them difficult to trap and characterize.

A large subgroup of the radical SAM superfamily catalyzes post-translational modifications on proteins and peptides; specifically, those involved in the activation of glycyl radical enzymes (GREs) and maturation of ribosomally synthesized and post-translationally modified peptide (RiPP) natural products. The work presented herein seeks to expand upon our knowledge of radical SAM enzymes involved in the post-translational modification of proteins and peptides primarily by trapping and characterizing radical intermediates formed during catalysis. In this chapter, the structure and proposed radical initiation mechanism of the radical SAM enzyme superfamily will be described, as well as background on the GRE superfamily and RiPP natural products where radical SAM enzymes are key players in installing post-translational modifications.

Structure

Radical SAM enzymes have been shown to adopt a triose phosphate isomerase (TIM) barrel fold which is composed of alternating alpha helices and beta strands connected by loop regions (Fig. 1.1A). Radical SAM enzymes may adopt full $(\beta\alpha)_8$ TIM barrel folds or partial ones such as $(\beta\alpha)_6$, however, even smaller barrels or those with unequal number of alpha helices and beta strands have been observed [1]. The openness of the TIM barrel correlates with the size of the substrate, where more closed TIM barrel radical SAM enzymes catalyze reactions on small molecules and more open TIM barrel radical SAM enzymes may act on larger molecules such as macromolecules [1]. Despite the limited sequence similarity of radical SAM enzymes at the primary sequence level, they share some characteristic motifs, the most notable of which is the CX_3CX_2C motif. This motif is responsible for coordinating the [4Fe-4S] cluster and is typically found on a loop between the first alpha helix and beta strand. Other important motifs that are not

strictly conserved include the GGE motif, the "GXIXGXXE" motif, and the β6 motif which provide interactions to various moieties on SAM [6].

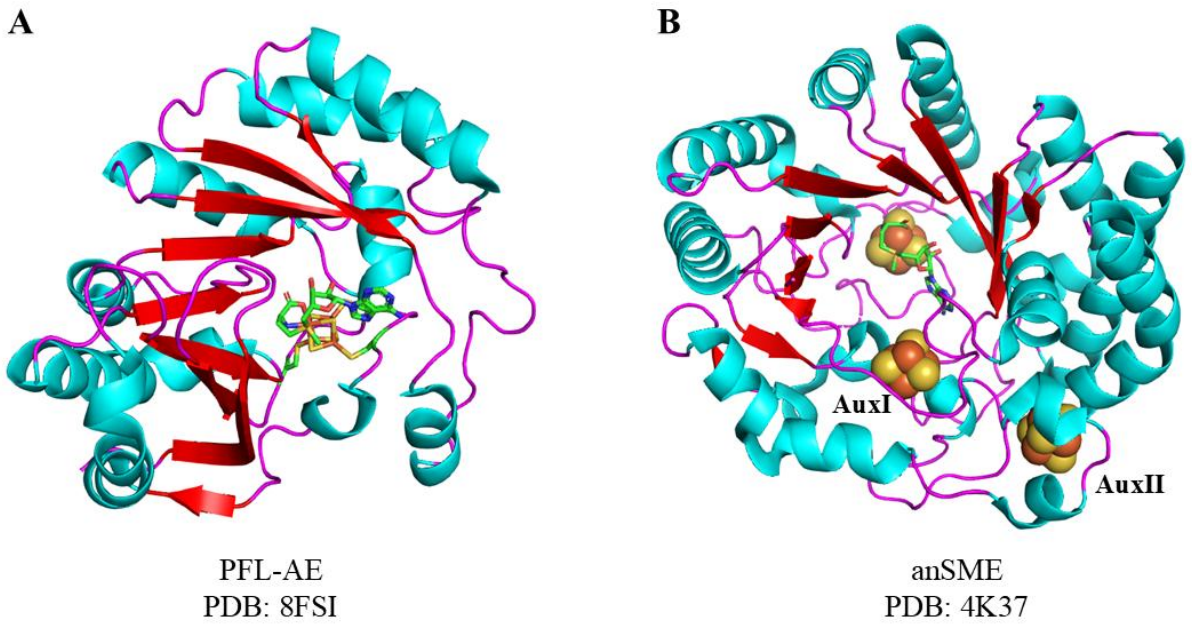


Figure 1.1. X-ray crystal structures of PFL-AE and anaerobic sulfatase maturating enzyme (anSME). A, Structure of PFL-AE with SAM bound and [4Fe-4S] cluster in the radical SAM domain (PDB ID: 8FSI) [7]. B, Structure of anSME with SAM bound, one [4Fe-4S] cluster in radical SAM domain, and two [4Fe-4S] clusters in SPASM domain (PDB ID: 4K37) [8]. Alpha helices are colored in cyan, beta strands in red, and loops in purple. Color code for SAM and the [4Fe-4S] clusters: green, carbon; red, oxygen; blue, nitrogen; yellow, sulfur; orange, iron.

SPASM and twitch domains

A large subset of radical SAM enzymes have been found to contain a C-terminal domain called a SPASM domain, named after the founding members [6]. The SPASM domain contains a seven cysteine motif ($CX_{9-15}GX_4CX_nCX_2CX_5CX_3CX_nC$) that coordinates two auxiliary [Fe-S] clusters, typically referred to as AuxI which is closer to the RS cluster, and AuxII which is distal (Fig. 1.1B). A truncated SPASM domain that only coordinates one auxiliary cluster is a called a twitch domain [6]. The auxiliary clusters are usually [4Fe-4S] clusters, however, a [2Fe-2S]

cluster has been observed in the AuxI position in some proteins [9-12]. The roles of these clusters are protein-dependent, but may include electron transfer, substrate coordination, and structural stabilization [13-19]. Removing one or both clusters by mutation of the coordinating Cys residues usually renders the protein insoluble or inactive, limiting insights into the roles of the clusters. Radical SAM enzymes with SPASM or twitch domains are typically involved in the biosynthesis of RiPP natural products [20-22].

Proposed Mechanism of Radical Initiation

Radical SAM enzymes utilize SAM and a site-differentiated [4Fe-4S] cluster for catalysis [1, 23-26]. Cysteine thiolates from the CX_3CX_2C motif coordinate three iron ions of the cluster. The fourth iron, called the unique iron, is coordinated through the amino and carboxylate moieties of SAM, positioning the sulfonium in orbital overlap with the unique iron [27-29]. Spectroscopic evidence for this binding mode was first discovered through a combination of Mossbauer and electron nuclear double resonance (ENDOR) spectroscopies [30]. Since then, this binding mode has been observed in all X-ray structures of radical SAM enzymes with SAM bound to the cluster [31].

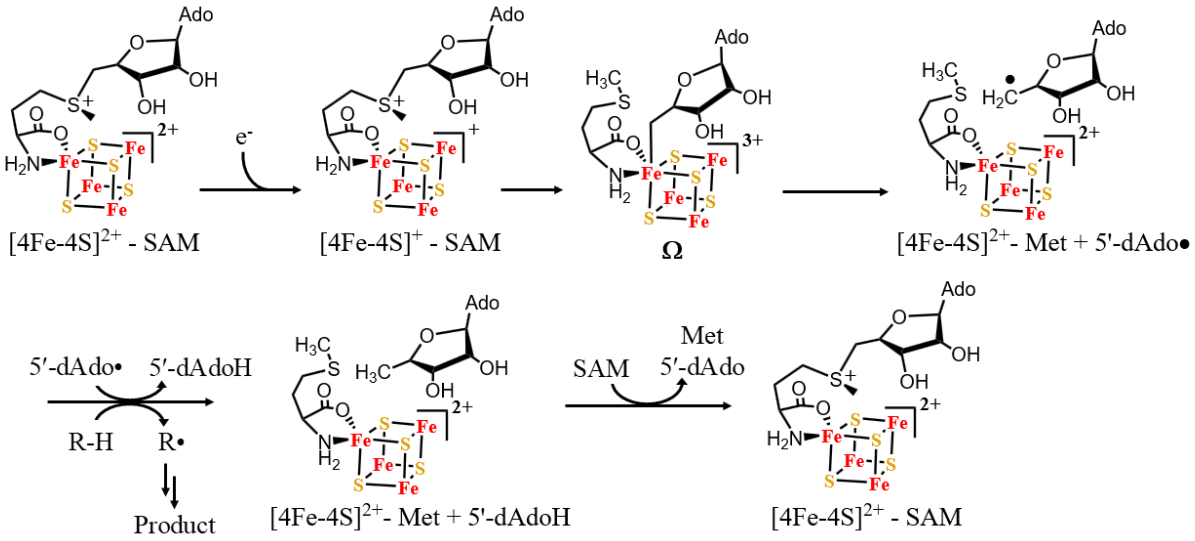


Figure 1.2. Proposed radical initiation mechanism by the radical SAM enzyme superfamily.

The proposed radical generation mechanism begins with the reduction of the [4Fe-4S] cluster from the 2+ to the 1+ oxidation state (Fig. 1.2). This is thought to be achieved *in vivo* through low potential electron transfer proteins such as flavodoxin or ferredoxin [32-35]. Typical reduction potentials of radical SAM [4Fe-4S] clusters typically lie in the range of -450 to -600 mV, necessitating the use of strong reductants [36]. This is typically accomplished *in vitro* by the use of the chemical reductant dithionite (Em = -660 mV, pH 7 [37]), although Ti(III) citrate and photoreduced 5-deazariboflavin [38] have also been used.

Following reduction of the cluster, coordination of SAM and substrate triggers electron transfer to the sulfonium center, causing homolytic reductive cleavage of the S-C(5′) of SAM. The complex rearranges to form the organometallic intermediate **Ω** which features a covalent Fe-C bond between the unique iron of the cluster and the C(5′) of dAdo and with the amino and carboxylate moieties of methionine still coordinated (Fig. 1.2) [39]. Homolysis of the Fe-C(5′) bond of omega then releases the highly oxidizing 5′-dAdo radical which regio- and

stereoselectively abstracts a H-atom from its substrate to form a substrate radical intermediate (Fig. 1.2) [23, 24].

Organometallic intermediate Ω

The organometallic intermediate Ω was originally discovered during rapid freeze quench (RFQ) experiments using the enzyme PFL-AE which installs a stable glycyl radical on the enzyme pyruvate formate lyase (PFL) [39]. RFQ of the reaction at 500 ms and subsequent analysis by electron paramagnetic resonance (EPR) spectroscopy revealed an axial signal with principal *g*-values of $g_{\parallel} = 2.036$ and $g_{\perp} = 2.004$. The $g_{ave} > 2.0$ suggested the species was a $[4Fe\text{-}4S]^{3+}$ cluster. ENDOR spectroscopy with ^{13}C-labeled SAM showed strong coupling between the unpaired spin on the cluster and the 5′-^{13}C which indicated a covalent linkage [39]. Thermal annealing of the 500 ms RFQ sample and analysis by EPR showed conversion of Ω into the product glycyl radical on PFL, providing evidence for Ω as a catalytically competent intermediate [39].

A subsequent study on Ω repeated the 500 ms RFQ experiments but with a range of radical SAM enzymes that catalyze reactions on a variety of substrates or have auxiliary [Fe-S] clusters [40]. In all cases, Ω could be clearly observed at 500 ms, leading to the hypothesis that Ω was a ubiquitous intermediate among the superfamily. However, this proposal raised questions such as what structural movements were required to form the Ω intermediate and what its purpose in the mechanism was. Synthetic models of alkylated [4Fe-4S] clusters showed that reversible formation of carbon radicals was feasible when the unique iron was hexacoordinate, suggesting that Ω may be a way of "storing" the 5′-dAdo radical until proper positioning of the substrate was achieved [41, 42]. Multiple studies have observed Ω during enzyme turnover,

contributing to the hypothesis that this intermediate is catalytically relevant and ubiquitous among the superfamily [15, 43-45].

Glycyl Radical Enzymes

Activation and Mechanism

Glycyl radical enzymes (GREs) utilize a post-translationally installed backbone glycyl radical to initiate a wide range of reactions involved in anaerobic glucose metabolism, anaerobic metabolism of hydrocarbons, and glucose dehydration among others [46-48]. The backbone glycyl radical is installed by radical SAM enzymes which abstract the pro-*S* hydrogen from a conserved glycine residue on the "Gly loop". The radical SAM activating enzymes are referred to as GRE activating enzymes or GRE-AEs. In the presence of PFL-AE, the GRE PFL can sample conformations in which the "Gly loop" is flipped out of the protein to be bound in the active site of the activating enzyme for glycyl radical installation, which may be a common mechanism for activation among the GRE superfamily [49]. While glycyl radicals are stable protein-based radicals, they are extremely sensitive to oxygen and result in cleavage of the protein backbone when exposed [50]. Incredibly, in some organisms, a "spare part protein" that resembles the cleaved region of the GRE can restore activity to the oxygen damaged protein [51-53].

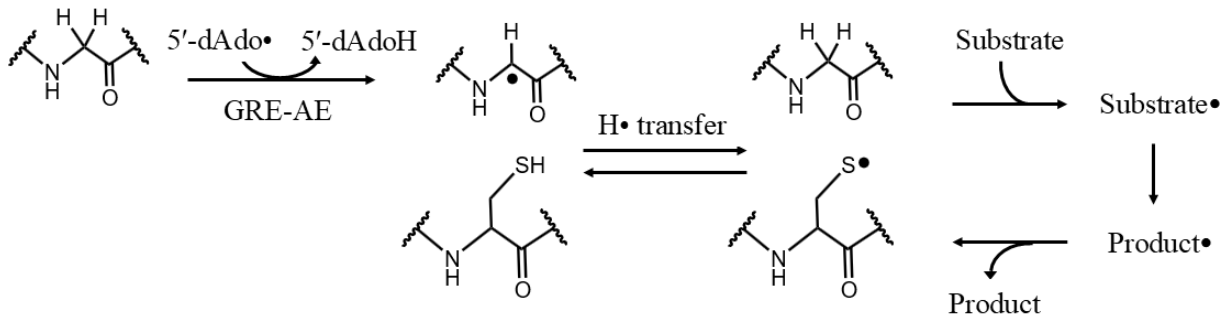


Figure 1.3. Activation and general mechanism of GRE superfamily. Activation of the GRE begins with abstraction of H-atom from conserved glycine to form a stable glycyl radical, catalyzed by a cognate GRE-AE radical SAM enzyme.

To initiate catalysis, the glycyl radical first abstracts a hydrogen from a conserved Cys residue on the nearby "Cys loop" (Fig. 1.3) [46, 47]. This transient Cys thiyl radical abstracts a hydrogen from the substrate to form a substrate based radical. Following conversion of the substrate radical into the product radical, the product radical is reductively quenched by reabstracting a hydrogen atom from the conserved Cys, which in turn abstracts a hydrogen atom from the conserved glycine to reform the stable glycyl radical.

Amino acyl radical enzymes

A recent study by Fu et al. [54] discovered that some members of the GRE superfamily also encode alanine (ARE), serine (SRE), and threonine (TRE) in place of the canonical glycine residue. They demonstrated that by incubating the proteins with their cognate activating enzyme, they could form alanyl, serinyl, and threonyl Cα radicals. With the expansion of the GRE family to include these new Cα radicals, the family has been renamed the amino acyl radical enzyme (AARE) family. While the authors were not able to test whether the activated AAREs were catalytically active, they demonstrated that following radical installation, Hα could exchange

with solvent deuterium when incubated in D_2O, indicating radical exchange with the catalytic Cys residue was possible [54]. It will interesting to see if the non-glycyl radicals are capable of catalysis, what reactions they catalyze, and how they compare to canonical GREs overall.

B_{12}-independent glycerol dehydratase

The B_{12}-independent glycerol dehydratase (GD) from *Clostridium butyricum* is a GRE that catalyzes the dehydration of glycerol to 3-hydroxylpropionaldehyde (3-HPA) [55, 56]. The catalytic glycyl radical on GD is installed by its cognate radical SAM activating enzyme, GD-AE [56]. A study investigating the activation of GD by GD-AE reported that GD-AE produced 5′-deoxy-5′-methylthioadenosine (MTA) along with glycyl radical formation [57]. This suggested that GD-AE reductively cleaved the S-$C_{\gamma,Met}$ bond of SAM to form a 3-amino-3-carboxypropoyl (ACP) radical that would carry out H-atom abstraction on GD. Evidence for this proposal came from HPLC chromatograms looking at SAM reductive cleavage products following reaction of GD and GD-AE after only 15 seconds [57]. Accumulation of MTA was not shown to be time-dependent and is in stark contrast to all other canonical radical SAM enzymes that cleave the S-C(5′) bond of SAM to produce the 5′-dAdo radical [1]. Chapter 2 focuses on investigating what SAM cleavage products are produced by GD-AE from *Clostridium butyricum* during activation of GD.

Ribosomally Synthesized and Post Translationally Modified Peptide Natural Products

Background

Natural products are bioactive compounds produced by living organisms to provide a competitive advantage. Peptide based natural products are produced by two major pathways in

Nature. One is a non-ribosomal pathway called non-ribosomal peptide synthetases (NRPS) that are composed of large, megacomplexes of enzyme modules where each module appends a specific amino acid to the growing polypeptide chain [58]. The other pathway is ribosomally based and are termed ribosomally synthesized and post-translationally modified peptides (RiPPs) [59, 60]. Due to advances in bioinformatics, analytical tools, and DNA sequencing, the field of RiPP natural products has seen rapid growth in recent years [59]. RiPP natural products exhibit an impressive diversity of chemical scaffolds that has led to the discovery of novel bioactivities and enzymology. Some bioactivities of RiPPs include antibacterial, antiviral, and apoptosis-inducing [61-65]. Some RiPP pathways also lead to the production of enzyme cofactors such as pyrroloquinoline quinone (PQQ) [66, 67] and Mycofactocin [68-70].

Maturation

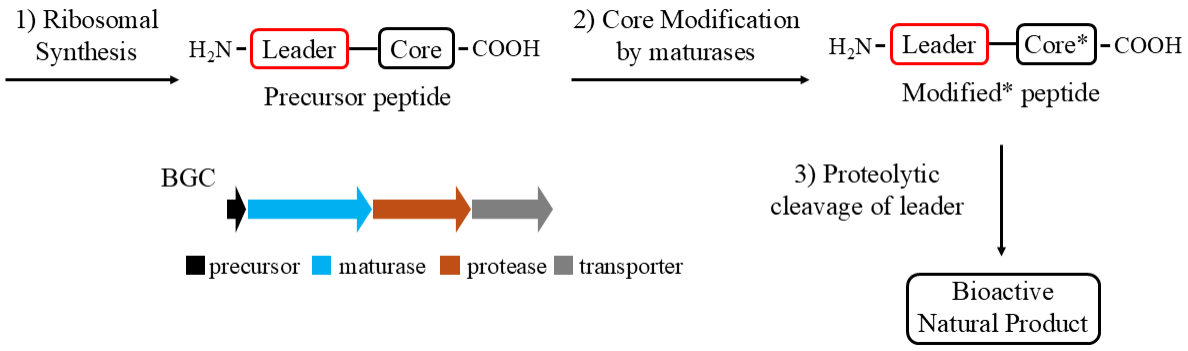


Figure 1.4. Overview of maturation of RiPP natural products from biosynthetic gene cluster (BGC).

Maturation of RiPP natural products begins with the ribosomal production of the precursor peptide (Fig. 1.4). The precursor peptide is typically composed of an N-terminal leader and C-terminal core region, although some have been shown to possess additional C-terminal follower regions. The leader region is responsible for recruiting and binding maturating enzymes

which install PTMs in the core region of the precursor peptide. These primary modifications are class defining for the RiPP natural product. Following primary modification, the leader is cleaved from the core, typically by a dedicated protease. Additional tailoring enzymes may catalyze further reactions on the leader-cleaved and partially modified peptide. The mature peptide natural product is then usually excreted form the producing cell to exert its bioactivity.

Genes encoding for the precursor peptide, maturating enzymes, proteases, transport proteins, and immunity factors are found clustered together in the genomes of organisms forming a biosynthetic gene cluster (BGC) (Fig. 1.4). Many RiPP pathways also contain a RiPP recognition element (RRE) that is found as a small discrete protein or an auxiliary domain of maturating enzymes that is proposed to assist in binding of the maturating enzyme and precursor peptide via interactions with the leader region of the peptide [71]. Because genes involved in RiPP maturation are found clustered together, conserved or prevalent features can be used as bioinformatic “handles” to search for uncharacterized or unannotated members in databases [72]. For example, bioinformatic mining for new RiPP natural products or new enzymology has made use of homology to known RiPP enzymes [73, 74], conservation of the RRE domain [75], or coclustering of genes, such as those involved in quorum sensing [76] or transporter proteins [77].

Epimerases

A prevalent modification in RiPP biosynthesis is Cα epimerization to convert L-amino acids into D-amino acids. D-amino acids are known for their ability to enhance stability by resisting proteolysis, as many proteases are not able to recognize and bind the D-configured amino acid [78]. D-amino acids may also endow or improve specific bioactivities such as

antiviral or antibacterial properties. Epimerization of amino acids in RiPP biosynthesis can be achieved through polar or radical-based mechanisms.

Amino acid epimerization using polar mechanisms has been found in multiple RiPP natural products. In lanthipeptide biosynthesis, serine or threonine residues are first dehydrated to form dehydroalanine or dehydrobuyrine, respectively. The dehydrated residues are then hydrogenated by NAD(P)H-dependent reductases to form D-Ala or D-aminobutyric acid [79]. In bottromycin biosynthesis, the enzyme BotH provides hydrogen bonds to allow a substrate Asp residue side-chain to abstract its own α-proton, followed by reprotonation from an ordered water molecule [80]. The substrate Asp residue is adjacent to a thiazoline ring, which allows stabilization of the resulting enamine intermediate [80]. The lasso peptide epimerase MslH catalyzes epimerization of the substrate C-terminal tryptophan residue facilitated by a Ca^{2+} ion [81, 82]. The proposed mechanism involves deprotonation of the substrate α-proton by an Asp-activated His residue with stabilization of the resulting enolate by coordination to the Ca^{2+} ion [81]. The enolate then tautomerizes to the keto form which abstracts a proton from another His residue, which in turn abstracts a proton from an Asp residue [81]. While epimerization via polar mechanisms is feasible, it has so far been limited to only a few types of amino acids.

Epimerization of amino acids in RiPP biosynthesis may also be achieved through radical-based mechanisms catalyzed by radical SAM enzymes [83]. Radical SAM epimerases have been characterized from both the proteusin and epipeptide RiPP natural product families. These enzymes are promiscuous, accepting a range of amino acid substitutions [84, 85]. A recently discovered radical SAM epimerase was also shown to epimerize the Cβ on a substrate threonine (Thr) residue to yield L-allo-Thr [86]. It is tempting to speculate there may be a natural product

where a radical SAM epimerase is capable of epimerizing the Cβ of an Ile residue to yield L-allo-Ile.

Proteusins

Unlike other RiPP natural products families that share a common PTM, proteusins are united by a unique precursor protein architecture where the leader region resembles nitrile hydratase proteins [87]. The founding member, polytheonamide, is a large, highly cytotoxic peptide that contains 49 PTMs installed by only seven enzymes [88-90]. Polytheonamide contains 18 D-amino acids which alternate with their L- counterparts only skipping glycine and are installed by one radical SAM enzyme, PoyD [88]. A bioinformatic search using PoyD as the query led to the discovery other radical SAM peptide epimerases that acted on a variety of amino acids with different epimerization patterns [91].

One of the PoyD homologs, OspD, is part of a BGC from the cyanobacterial species *Kamptonema sp*. PCC 6506 [91]. The BGC is composed of the precursor peptide OspA, a lanthionine synthetase OspM, a radical SAM peptide epimerase OspD, a peptide arginase OspR, and transporter proteins (Fig. 1.5A) [92-94]. Coexpression of the BGC followed by purification of OspA led to the discovery of the RiPP natural product Landornamide A which was shown to exhibit antiviral activity against lymphocytic choriomeningitis virus (Fig. 1.5C) [93]. The radical SAM epimerase OspD is responsible for the epimerization of Ile4 and Val13 on OspA (Fig. 1.5B).

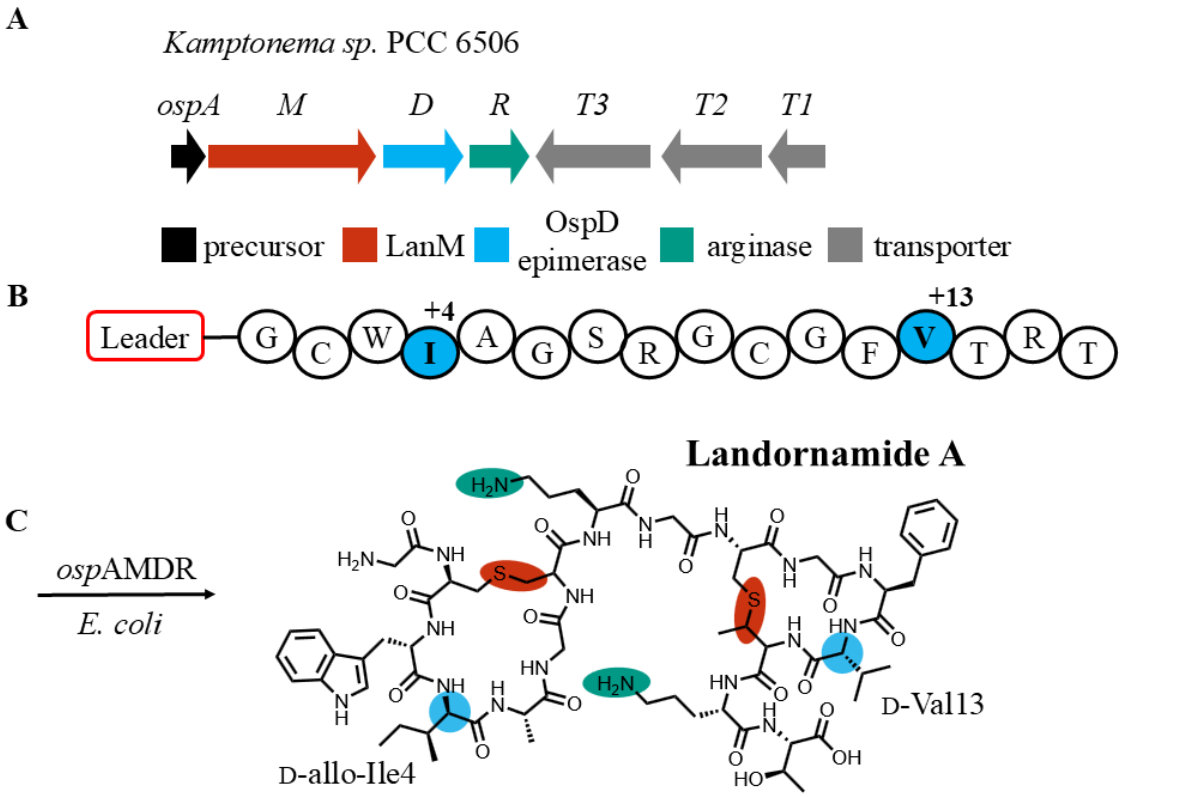


Figure 1.5. Overview of Landornamide A biosynthesis and structure. A, BGC from *Kamptonema sp*. PCC 6506. B, Sequence of OspA core region with target residues Ile4 and Val13 for epimerization by OspD colored blue. C, Coexpression of *ospAMDR* genes in *E. coli* and cleavage of leader region results in production of the antiviral RiPP Landornamide A.

Mechanistic studies with OspD showed that the enzyme would abstract a hydrogen from the Cα of the amino acid to be epimerized [95]. RFQ-EPR experiments with OspD and its substrate OspA showed formation of Ω when quenched at 500 ms [40]. These observations led to the following proposed mechanism (Fig. 1.6): reductive cleavage of SAM forms Ω, which releases the 5′-dAdo radical to abstract a hydrogen atom from the Cα position of the amino acid to be epimerized, resulting in an α-carbon radical intermediate [95]. This Cα radical intermediate is then quenched by H-atom transfer from a conserved Cys residue to yield the D-amino acid and

a thiyl radical [95]. The thiyl radical is thought to be quenched by proton-coupled electron transfer facilitated by redox-active amino acids such as tyrosine or tryptophan [95].

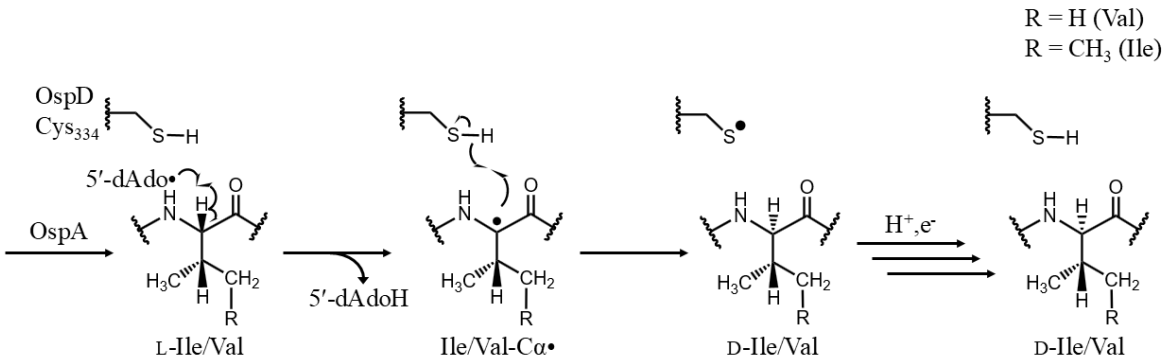


Figure 1.6. Proposed mechanism of amino acid epimerization by OspD.

Epipeptides

Epipeptides are a class of RiPP natural products that are widespread among the Bacillota phylum [85]. Epipeptides exert antibiotic activity against the producing strain and closely related strains by depolarizing the bacterial membrane via membrane permeabilization [98, 99]. To date, there is only one characterized biosynthetic gene cluster from *B. subtilis* str. 168 which is composed of the precursor peptide EpeX, a radical SAM peptide epimerase EpeE, a membrane-associated protease EpeP, and autoimmunity proteins EpeAB (Fig. 1.7A) [99, 100]. The radical SAM enzyme EpeE epimerizes Val4 and Ile12 on EpeX [99]. Epimerization and proteolytic cleavage of the leader region are the only modifications to yield the mature epipeptide natural product, suggesting they could be utilized as minimalistic peptide antibiotics to target opportunistic human pathogens in the Bacillota phylum.

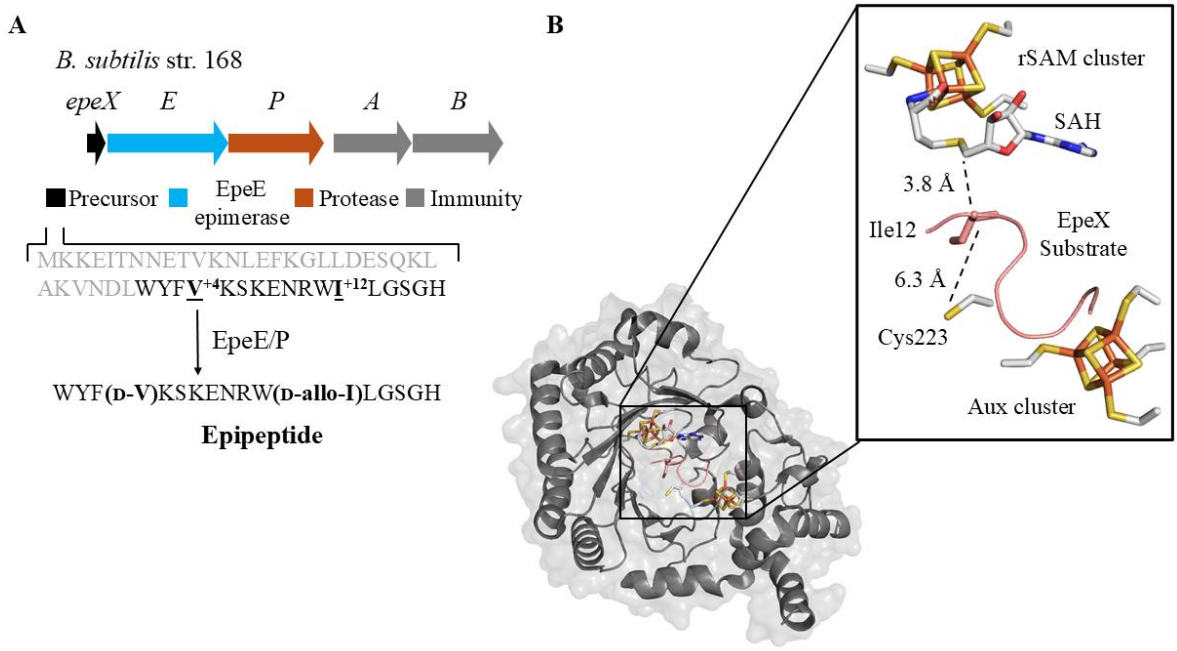


Figure 1.7. Biosynthesis of epipeptide RiPP natural products and structure of radical SAM epimerase EpeE. A, Epipeptide biosynthesis from *B. subtilis* str. 168. B, X-ray crystal structure of EpeE with EpeX peptide substrate bound (PDB ID: 8AI2).

X-ray crystal structures of EpeE revealed the presence of a C-terminal twitch domain harboring an auxiliary (Aux) [4Fe-4S] cluster, in addition to the N-terminal partial TIM barrel fold (β_6/α_5) (Fig. 7B) [101]. Structures of EpeE with a peptide substrate bound in the active site showed Ile12 (of EpeX) perfectly positioned for H-atom abstraction from the Cα position, with Cys223 on the opposite face of the peptide. It is noteworthy that at the time of this writing, these are the only structures of a radical SAM enzyme involved in RiPP biosynthesis with its substrate bound in the active site, albeit a truncated one.

The proposed mechanism of amino acid epimerization by EpeE starts with the reductive cleavage of SAM to form **Ω**, which releases the 5′-dAdo radical to abstract an H-atom from the amino acid to be epimerized (Fig. 1.8). This forms a central Cα radical intermediate which is in turn stereoselectively quenched by H-atom transfer from Cys223 to yield the D-amino acid and a

thiyl radical on Cys223. Reduction of the thiyl radical is thought to be mediated by the Aux [4Fe-4S] cluster, with proton transfer from aspartate 210 to return the enzyme to the resting state. While X-ray structures and mutational studies support aspects of this mechanism, evidence for multiple intermediates is lacking such as the substrate Cα radical intermediate and Ω [99, 101]. Chapter 5 focuses on testing the proposed mechanism, specifically probing the formation of Ω and the substrate Cα radical intermediate.

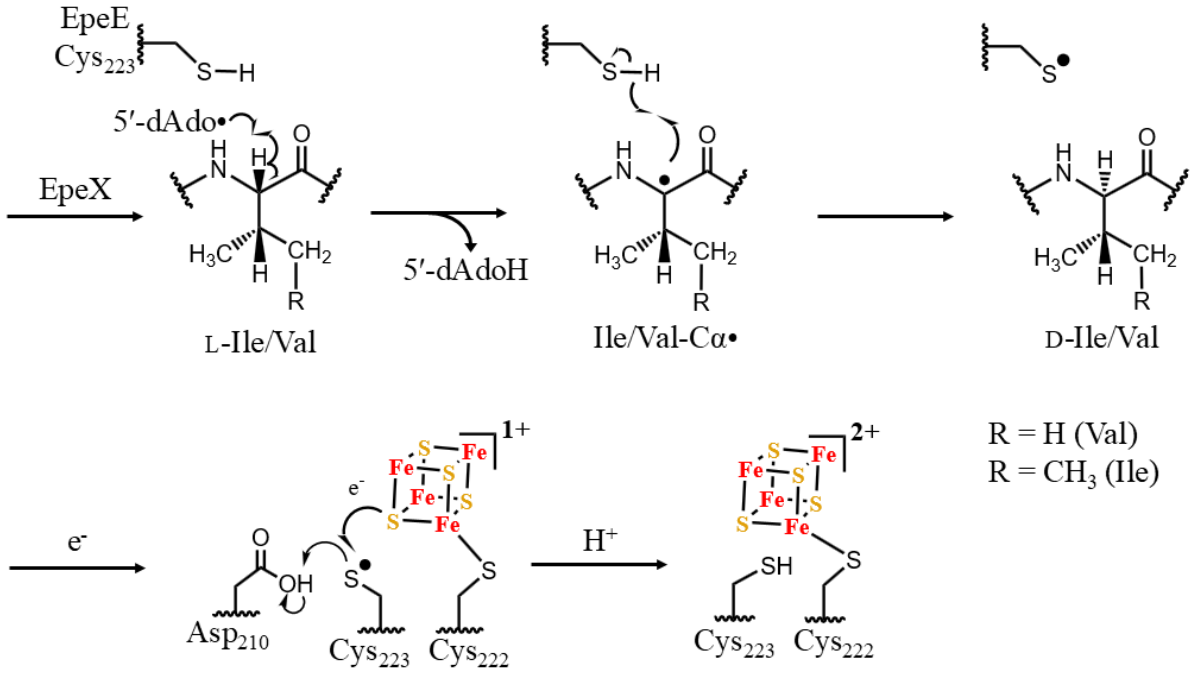


Figure 1.8. Proposed mechanism of amino acid epimerization by EpeE.

Splicotides

Splicotides are RiPP natural products featuring α-keto-β^3-amide (referred to as ketoamides) functional groups that are installed by radical SAM enzymes called spliceases [102]. Splicotides are widespread among the bacterial kingdom and function as potent protease inhibitors [103]. Spliceases catalyze the excision of a "tyramine equivalent" from a conserved

XYG motif in the precursor peptide core, followed by splicing of the peptide fragments to yield the ketoamide product. The splicease enzymes are also predicted to contain a C-terminal SPASM domain which harbors two Aux [4Fe-4S] clusters [102]. The AuxI cluster, which is closer to the radical SAM cluster, is predicted to be ligated by only three cysteine residues, leaving an open coordination site that may play a part in the catalytic mechanism [104]. Chapter 4 focuses on mechanistic investigations of multiple spliceases in order to reach a proposed mechanism for ketoamide formation.

References

1. Broderick, J. B.; Duffus, B. R.; Duschene, K. S.; Shepard, E. M., Radical *S*-adenosylmethionine enzymes. *Chem Rev* **2014**, *114* (8), 4229-317.

2. Nicolet, Y., Structure–function relationships of radical SAM enzymes. *Nature Catalysis* **2020**, *3* (4), 337-350.

3. Sofia, H. J.; Chen, G.; Hetzler, B. G.; Reyes-Spindola, J. F.; Miller, N. E., Radical SAM, a novel protein superfamily linking unresolved steps in familiar biosynthetic pathways with radical mechanisms: functional characterization using new analysis and information visualization methods. *Nucleic Acids Research* **2001**, *29* (5), 1097–1106.

4. Blum, M.; Andreeva, A.; Florentino, Laise C.; Chuguransky, Sara R.; Grego, T.; Hobbs, E.; Pinto, Beatriz L.; Orr, A.; Paysan-Lafosse, T.; Ponamareva, I.; Salazar, Gustavo A.; Bordin, N.; Bork, P.; Bridge, A.; Colwell, L.; Gough, J.; Haft, Daniel H.; Letunic, I.; Llinares-López, F.; Marchler-Bauer, A.; Meng-Papaxanthos, L.; Mi, H.; Natale, Darren A.; Orengo, Christine A.; Pandurangan, Arun P.; Piovesan, D.; Rivoire, C.; Sigrist, Christian J. A.; Thanki, N.; Thibaud-Nissen, F.; Thomas, Paul D.; Tosatto, Silvio C. E.; Wu, Cathy H.; Bateman, A., InterPro: the protein sequence classification resource in 2025. *Nucleic Acids Research* **2024**, *53* (D1), D444-D456.

5. Oberg, N.; Precord, T. W.; Mitchell, D. A.; Gerlt, J. A., RadicalSAM.org: A Resource to Interpret Sequence-Function Space and Discover New Radical SAM Enzyme Chemistry. *ACS Bio & Med Chem Au* **2022,** *2* (1), 22-35.

6. Grell, T. A.; Goldman, P. J.; Drennan, C. L., SPASM and twitch domains in *S*-adenosylmethionine (SAM) radical enzymes. *J Biol Chem* **2015**, *290* (7), 3964-71.

7. Moody, J. D.; Hill, S.; Lundahl, M. N.; Saxton, A. J.; Galambas, A.; Broderick, W. E.; Lawrence, C. M.; Broderick, J. B., Computational engineering of previously crystallized pyruvate formate-lyase activating enzyme reveals insights into SAM binding and reductive cleavage. *J Biol Chem* **2023**, *299* (6), 104791.

8. Goldman, P. J.; Grove, T. L.; Sites, L. A.; McLaughlin, M. I.; Booker, S. J.; Drennan, C. L., X-ray structure of an AdoMet radical activase reveals an anaerobic solution for formylglycine posttranslational modification. *Proc Natl Acad Sci U S A* **2013**, *110* (21), 8519-24.

9. Grell, T. A. J.; Kincannon, W. M.; Bruender, N. A.; Blaesi, E. J.; Krebs, C.; Bandarian, V.; Drennan, C. L., Structural and spectroscopic analyses of the sporulation killing factor biosynthetic enzyme SkfB, a bacterial AdoMet radical sactisynthase. *J Biol Chem* **2018**, *293* (45), 17349-17361.

10. Zhu, W.; Walker, L. M.; Tao, L.; Iavarone, A. T.; Wei, X.; Britt, R. D.; Elliott, S. J.; Klinman, J. P., Structural Properties and Catalytic Implications of the SPASM Domain Iron-Sulfur Clusters in *Methylorubrum extorquens* PqqE. *J Am Chem Soc* **2020**, *142* (29), 12620-12634.

11. Tao, L.; Zhu, W.; Klinman, J. P.; Britt, R. D., Electron Paramagnetic Resonance Spectroscopic Identification of the Fe-S Clusters in the SPASM Domain-Containing Radical SAM Enzyme PqqE. *Biochemistry* **2019**, *58* (51), 5173-5187.

12. Barr, I.; Stich, T. A.; Gizzi, A. S.; Grove, T. L.; Bonanno, J. B.; Latham, J. A.; Chung, T.; Wilmot, C. M.; Britt, R. D.; Almo, S. C.; Klinman, J. P., X-ray and EPR Characterization of the Auxiliary Fe-S Clusters in the Radical SAM Enzyme PqqE. *Biochemistry* **2018**, *57* (8), 1306-1315.

13. Rush, K. W.; Eastman, K. A. S.; Kincannon, W. M.; Blackburn, N. J.; Bandarian, V., Peptide Selenocysteine Substitutions Reveal Direct Substrate-Enzyme Interactions at Auxiliary Clusters in Radical *S*-Adenosyl-L-methionine Maturases. *J Am Chem Soc* **2023,** *145* (18), 10167–10177.

14. Eastman, K. A. S.; Jochimsen, A.; Bandarian, V., Intermolecular electron transfer in radical SAM enzymes as a new paradigm for reductive activation. *J Biol Chem* **2023**, *299* (9), 105058.

15. Balo, A. R.; Caruso, A.; Tao, L.; Tantillo, D. J.; Seyedsayamdost, M. R.; Britt, R. D., Trapping a cross-linked lysine–tryptophan radical in the catalytic cycle of the radical SAM enzyme SuiB. *Proc. Natl. Acad. Sci. U.S.A.* **2021**, *118* (21), e2101571118.

16. Bruender, N. A.; Wilcoxen, J.; Britt, R. D.; Bandarian, V., Biochemical and Spectroscopic Characterization of a Radical *S*-Adenosyl-L-methionine Enzyme Involved in the Formation of a Peptide Thioether Cross-Link. *Biochemistry* **2016**, *55* (14), 2122-34.

17. Lees, N. S.; Ha¨nzelmann, P.; Hernandez, H. L.; Subramanian, S.; Schindelin, H.; Johnson, M. K.; Hoffman, B. M., ENDOR Spectroscopy Shows That Guanine N1 Binds to [4Fe-4S] Cluster II of the *S*-Adenosylmethionine-Dependent Enzyme MoaA: Mechanistic Implications. *J Am Chem Soc* **2009**, *131* (26), 9184–9185.

18. Walker, L. M.; Kincannon, W. M.; Bandarian, V.; Elliott, S. J., Deconvoluting the Reduction Potentials for the Three [4Fe-4S] Clusters in an AdoMet Radical SCIFF Maturase. *Biochemistry* **2018**, *57* (42), 6050-6053.

19. Maiocco, S. J.; Grove, T. L.; Booker, S. J.; Elliott, S. J., Electrochemical Resolution of the [4Fe-4S] Centers of the AdoMet Radical Enzyme BtrN: Evidence of Proton Coupling and an Unusual, Low-Potential Auxiliary Cluster. *J Am Chem Soc* **2015**, *137* (27), 8664-7.

20. Benjdia, A.; Balty, C.; Berteau, O., Radical SAM Enzymes in the Biosynthesis of Ribosomally Synthesized and Post-translationally Modified Peptides (RiPPs). *Front Chem* **2017**, *5*, 87.

21. Mahanta, N.; Hudson, G. A.; Mitchell, D. A., Radical *S*-Adenosylmethionine Enzymes Involved in RiPP Biosynthesis. *Biochemistry* **2017**, *56* (40), 5229-5244.

22. Latham, J. A.; Barr, I.; Klinman, J. P., At the confluence of ribosomally synthesized peptide modification and radical S-adenosylmethionine (SAM) enzymology. *J Biol Chem* **2017**, *292* (40), 16397-16405.

23. Hoffman, B. M.; Broderick, W. E.; Broderick, J. B., Mechanism of Radical Initiation in the Radical SAM Enzyme Superfamily. *Annu Rev Biochem* **2023**, *92*, 333-349.

24. Broderick, J. B.; Broderick, W. E.; Hoffman, B. M., Radical SAM enzymes: Nature's choice for radical reactions. *FEBS Lett* **2023,** *597*, 92-101.

25. Broderick, W. E.; Broderick, J. B., Radical SAM enzymes: surprises along the path to understanding mechanism. *Journal of Biological Inorganic Chemistry* **2019**, *24* (6), 769-776.

26. Broderick, W. E.; Hoffman, B. M.; Broderick, J. B., Mechanism of Radical Initiation in the Radical *S*-Adenosyl-L-methionine Superfamily. *Acc Chem Res* **2018**, *51* (11), 2611-2619.

27. Walsby, C. J.; Ortillo, D.; Broderick, W. E.; Broderick, J. B.; Hoffman, B. M., An Anchoring Role for FeS Clusters: Chelation of the Amino Acid Moiety of *S*-Adenosylmethionine to the Unique Iron Site of the [4Fe-4S] Cluster of Pyruvate Formate-Lyase Activating Enzyme. *J Am Chem Soc* **2002**, *124*, 11270-11271.

28. Walsby, C. J.; Hong, W.; Broderick, W. E.; Cheek, J.; Ortillo, D.; Broderick, J. B.; Hoffman, B. M., Electron-Nuclear Double Resonance Spectroscopic Evidence That *S*-

Adenosylmethionine Binds in Contact with the Catalytically Active [4Fe-4S]$^{+}$ Cluster of Pyruvate Formate-Lyase Activating Enzyme. *J Am Chem Soc* **2002**, *124*, 3143-3151.

29. Krebs, C.; Broderick, W. E.; Henshaw, T. F.; Broderick, J. B.; Huynh, B. H., Coordination of Adenosylmethionine to a Unique Iron Site of the [4Fe-4S] of Pyruvate Formate-Lyase Activating Enzyme: A Mo1ssbauer Spectroscopic Study. *Journal of the American Chemical Society* **2002**, *124*, 912-913.

30. Walsby, C. J.; Ortillo, D.; Yang, J.; Nnyepi, M. R.; Broderick, W. E.; Hoffman, B. M.; Broderick, J. B., Spectroscopic Approaches to Elucidating Novel Iron−Sulfur Chemistry in the "Radical-SAM" Protein Superfamily. *Inorganic Chemistry* **2005**, *44*, 727-741.

31. Lachowicz, J.; Lee, J.; Sagatova, A.; Jew, K.; Grove, T. L., The new epoch of structural insights into radical SAM enzymology. *Current Opinion in Structural Biology* **2023**, *83*, 102720.

32. Bruender, N. A.; Young, A. P.; Bandarian, V., Chemical and Biological Reduction of the Radical SAM Enzyme 7-Carboxy-7-deazaguanine Synthase. *Biochemistry* **2015**, *54* (18), 2903-10.

33. Crain, A. V.; Broderick, J. B., Flavodoxin cofactor binding induces structural changes that are required for protein-protein interactions with NADP(+) oxidoreductase and pyruvate formate-lyase activating enzyme. *Biochim Biophys Acta* **2013**, *1834* (12), 2512-9.

34. Bianchi, V.; Eliasson, R.; Fontecave, M.; Mulliez, E.; Hoover, D. M.; Matthews, R. G.; Reichard, P., Flavodoxin Is Required for the Activation of the Anaerobic Ribonucleotide Reductase. *Biochemical and Biophysical Research Communications* **1993**, *197* (2), 792-797.

35. Arcinas, A. J.; Maiocco, S. J.; Elliott, S. J.; Silakov, A.; Booker, S. J., Ferredoxins as interchangeable redox components in support of MiaB, a radical *S*-adenosylmethionine methylthiotransferase. *Protein Sci* **2019**, *28* (1), 267-282.

36. Maiocco, S. J.; Walker, L. M.; Elliott, S. J., Determining Redox Potentials of the Iron-Sulfur Clusters of the AdoMet Radical Enzyme Superfamily. *Methods Enzymol* **2018**, *606*, 319-339.

37. Mayhew, S. G., The Redox Potential of Dithionite and SO; from Equilibrium Reactions with Flavodoxins, Methyl Viologen and Hydrogen plus Hydrogenase. *Eur. J. Biochem* **1978**, *85*, 535-547.

38. Henshaw, T. F.; Cheek, J.; Broderick, J. B., The [4Fe-4S]$^{1+}$ Cluster of Pyruvate Formate-Lyase Activating Enzyme Generates the Glycyl Radical on Pyruvate Formate-Lyase: EPR-Detected Single Turnover. *J Am Chem Soc* **2000**, *122*, 8331-8332.

39. Horitani, M.; Shisler, K.; Broderick, W. E.; Hutcheson, R. U.; Duschene, K. S.; Marts, A. R.; Hoffman, B. M.; Broderick, J. B., Radical SAM catalysis via an organometallic intermediate with an Fe–[5′-C]-deoxyadenosyl bond. *Science* **2016**, *352* (6287), 822-824.

40. Byer, A. S.; Yang, H.; McDaniel, E. C.; Kathiresan, V.; Impano, S.; Pagnier, A.; Watts, H.; Denler, C.; Vagstad, A. L.; Piel, J.; Duschene, K. S.; Shepard, E. M.; Shields, T. P.; Scott, L. G.; Lilla, E. A.; Yokoyama, K.; Broderick, W. E.; Hoffman, B. M.; Broderick, J. B., Paradigm Shift for Radical *S*-Adenosyl-L-methionine Reactions: The Organometallic Intermediate **Ω** Is Central to Catalysis. *J Am Chem Soc* **2018**, *140* (28), 8634-8638.

41. Ye, M.; Brown, A. C.; Suess, D. L. M., Reversible Alkyl-Group Migration between Iron and Sulfur in [Fe_4S_4] Clusters. *J Am Chem Soc* **2022**, *144* (29), 13184-13195.

42. Brown, A. C.; Suess, D. L. M., Reversible Formation of Alkyl Radicals at [Fe_4S_4] Clusters and Its Implications for Selectivity in Radical SAM Enzymes. *J Am Chem Soc* **2020**, *142* (33), 14240-14248.

43. Lundahl, M. N.; Yang, H.; Broderick, W. E.; Hoffman, B. M.; Broderick, J. B., Pyruvate formate-lyase activating enzyme: The catalytically active 5'-deoxyadenosyl radical caught in the act of H-atom abstraction. *Proc Natl Acad Sci U S A* **2023**, *120* (47), e2314696120.

44. Lundahl, M. N.; Sarksian, R.; Yang, H.; Jodts, R. J.; Pagnier, A.; Smith, D. F.; Mosquera, M. A.; van der Donk, W. A.; Hoffman, B. M.; Broderick, W. E.; Broderick, J. B., Mechanism of Radical *S*-Adenosyl-L-methionine Adenosylation: Radical Intermediates and the Catalytic Competence of the 5'-Deoxyadenosyl Radical. *J Am Chem Soc* **2022**, *144* (11), 5087-5098.

45. Pagnier, A.; Yang, H.; Jodts, R.; James, C.; Shepard, E. M.; Impano, S.; Broderick, W.; Hoffman, B. M.; Broderick, J. B., The Radical SAM enzyme Spore Photoproduct Lyase: Properties of the **Ω** Organometallic Intermediate and Identification of Stable Protein Radicals Formed During Substrate-Free Turnover. *J Am Chem Soc* **2020,** *142* (43), 18652–18660.

46. Backman, L. R. F.; Funk, M. A.; Dawson, C. D.; Drennan, C. L., New tricks for the glycyl radical enzyme family. *Crit Rev Biochem Mol Biol* **2017**, *52* (6), 674-695.

47. Shisler, K. A.; Broderick, J. B., Glycyl radical activating enzymes: structure, mechanism, and substrate interactions. *Arch Biochem Biophys* **2014**, *546*, 64-71.

48. Hioe, J.; Savasci, G.; Brand, H.; Zipse, H., The stability of Cα peptide radicals: why glycyl radical enzymes? *Chemistry* **2011**, *17* (13), 3781-9.

49. Peng, Y.; Veneziano, S. E.; Gillispie, G. D.; Broderick, J. B., Pyruvate formate-lyase, evidence for an open conformation favored in the presence of its activating enzyme. *J Biol Chem* **2010**, *285* (35), 27224-27231.

50. King, D. S.; Reichard, P., Mass Spectrometric Determination of the Radical Scission Site in the Anaerobic Ribonucleotide Reductase of *Escherichia Coli*. *Biochemical and Biophysical Research Communications* **1995**, *206* (January 17), 731-735.

51. Andorfer, M. C.; Backman, L. R. F.; Li, P. L.; Ulrich, E. C.; Drennan, C. L., Rescuing activity of oxygen-damaged pyruvate formate-lyase by a spare part protein. *J Biol Chem* **2021**, *297* (6), 101423.

52. Bowman, S. E. J.; Backman, L. R. F.; Bjork, R. E.; Andorfer, M. C.; Yori, S.; Caruso, A.; Stultz, C. M.; Drennan, C. L., Solution structure and biochemical characterization of a spare part protein that restores activity to an oxygen-damaged glycyl radical enzyme. *J Biol Inorg Chem* **2019**, *24* (6), 817-829.

53. Wagner, A. F.; Schultz, S.; Bomke, J.; Pils, T.; Lehmann, W. D.; Knappe, J., YfiD of Escherichia coli and Y06I of bacteriophage T4 as autonomous glycyl radical cofactors reconstituting the catalytic center of oxygen-fragmented pyruvate formate-lyase. *Biochem Biophys Res Commun* **2001**, *285* (2), 456-62.

54. Fu, B.; Yang, H.; Kountz, D. J.; Lundahl, M. N.; Beller, H. R.; Broderick, W. E.; Broderick, J. B.; Hoffman, B. H.; Balskus, E. P., Discovery of a New Class of Aminoacyl Radical Enzymes Expands Nature's Known Radical Chemistry. *J Am Chem Soc* **2024,** *146* (43), 29645–29655.

55. Raynaud, C. l.; Sarc¸abal, P.; Meynial-Salles, I.; Croux, C.; Soucaille, P., Molecular characterization of the 1,3-propanediol (1,3-PD) operon of Clostridium butyricum. *Proc Natl Acad Sci U S A* **2003**, *100*, 5010-5015.

56. O'Brien, J. R.; Raynaud, C.; Croux, C.; Girbal, L.; Soucaille, P.; Lanzilotta, W. N., Insight into the Mechanism of the B_{12}-Independent Glycerol Dehydratase from *Clostridium butyricum*: Preliminary Biochemical and Structural Characterization. *Biochemistry* **2004**, *43*, 4635-4645.

57. Demick, J. M.; Lanzilotta, W. N., Radical SAM activation of the B_{12}-independent glycerol dehydratase results in formation of 5'-deoxy-5'-(methylthio)adenosine and not 5'-deoxyadenosine. *Biochemistry* **2011**, *50* (4), 440-2.

58. Ruijne, F.; Kuipers, O. P., Combinatorial biosynthesis for the generation of new-to-nature peptide antimicrobials. *Biochem Soc Trans* **2021**, *49* (1), 203-215.

59. Montalban-Lopez, M.; Scott, T. A.; Ramesh, S.; Rahman, I. R.; van Heel, A. J.; Viel, J. H.; Bandarian, V.; Dittmann, E.; Genilloud, O.; Goto, Y.; Grande Burgos, M. J.; Hill, C.; Kim, S.; Koehnke, J.; Latham, J. A.; Link, A. J.; Martinez, B.; Nair, S. K.;

Nicolet, Y.; Rebuffat, S.; Sahl, H. G.; Sareen, D.; Schmidt, E. W.; Schmitt, L.; Severinov, K.; Sussmuth, R. D.; Truman, A. W.; Wang, H.; Weng, J. K.; van Wezel, G. P.; Zhang, Q.; Zhong, J.; Piel, J.; Mitchell, D. A.; Kuipers, O. P.; van der Donk, W. A., New developments in RiPP discovery, enzymology and engineering. *Nat Prod Rep* **2021**, *38* (1), 130-239.

60. Arnison, P. G.; Bibb, M. J.; Bierbaum, G.; Bowers, A. A.; Bugni, T. S.; Bulaj, G.; Camarero, J. A.; Campopiano, D. J.; Challis, G. L.; Clardy, J.; Cotter, P. D.; Craik, D. J.; Dawson, M.; Dittmann, E.; Donadio, S.; Dorrestein, P. C.; Entian, K. D.; Fischbach, M. A.; Garavelli, J. S.; Goransson, U.; Gruber, C. W.; Haft, D. H.; Hemscheidt, T. K.; Hertweck, C.; Hill, C.; Horswill, A. R.; Jaspars, M.; Kelly, W. L.; Klinman, J. P.; Kuipers, O. P.; Link, A. J.; Liu, W.; Marahiel, M. A.; Mitchell, D. A.; Moll, G. N.; Moore, B. S.; Muller, R.; Nair, S. K.; Nes, I. F.; Norris, G. E.; Olivera, B. M.; Onaka, H.; Patchett, M. L.; Piel, J.; Reaney, M. J.; Rebuffat, S.; Ross, R. P.; Sahl, H. G.; Schmidt, E. W.; Selsted, M. E.; Severinov, K.; Shen, B.; Sivonen, K.; Smith, L.; Stein, T.; Sussmuth, R. D.; Tagg, J. R.; Tang, G. L.; Truman, A. W.; Vederas, J. C.; Walsh, C. T.; Walton, J. D.; Wenzel, S. C.; Willey, J. M.; van der Donk, W. A., Ribosomally synthesized and post-translationally modified peptide natural products: overview and recommendations for a universal nomenclature. *Nat Prod Rep* **2013**, *30* (1), 108-60.

61. Pfeiffer, I. P.; Schroder, M. P.; Mordhorst, S., Opportunities and challenges of RiPP-based therapeutics. *Nat Prod Rep* **2024,** *41*, 990-1019.

62. Fu, Y.; Jaarsma, A. H.; Kuipers, O. P., Antiviral activities and applications of ribosomally synthesized and post-translationally modified peptides (RiPPs). *Cell Mol Life Sci* **2021**, *78* (8), 3921-3940.

63. Vagstad, A. L., Engineering ribosomally synthesized and posttranslationally modified peptides as new antibiotics. *Curr Opin Biotechnol* **2023**, *80*, 102891.

64. Xiong, J.; Luo, S.; Qin, C. X.; Cui, J. J.; Ma, Y. X.; Guo, M. X.; Zhang, S. S.; Li, Y.; Gao, K.; Dong, S. H., Biochemical Reconstitution Reveals the Biosynthetic Timing and Substrate Specificity for Thioamitides. *Org Lett* **2022**, *24* (7), 1518-1523.

65. Ayikpoe, R. S.; Shi, C.; Battiste, A. J.; Eslami, S. M.; Ramesh, S.; Simon, M. A.; Bothwell, I. R.; Lee, H.; Rice, A. J.; Ren, H.; Tian, Q.; Harris, L. A.; Sarksian, R.; Zhu, L.; Frerk, A. M.; Precord, T. W.; van der Donk, W. A.; Mitchell, D. A.; Zhao, H., A scalable platform to discover antimicrobials of ribosomal origin. *Nat Commun* **2022**, *13* (1), 6135.

66. Barr, I.; Latham, J. A.; Iavarone, A. T.; Chantarojsiri, T.; Hwang, J. D.; Klinman, J. P., Demonstration That the Radical S-Adenosylmethionine (SAM) Enzyme PqqE Catalyzes de Novo Carbon-Carbon Cross-linking within a Peptide Substrate PqqA in the Presence of the Peptide Chaperone PqqD. *J Biol Chem* **2016**, *291* (17), 8877-84.

67. Wecksler, S. R.; Stoll, S.; Tran, H.; Magnusson, O. T.; Wu, S. P.; King, D.; Britt, R. D.; Klinman, J. P., Pyrroloquinoline quinone biogenesis: demonstration that PqqE from Klebsiella pneumoniae is a radical *S*-adenosyl-L-methionine enzyme. *Biochemistry* **2009**, *48* (42), 10151-61.

68. Ayikpoe, R.; Ngendahimana, T.; Langton, M.; Bonitatibus, S.; Walker, L. M.; Eaton, S. S.; Eaton, G. R.; Pandelia, M. E.; Elliott, S. J.; Latham, J. A., Spectroscopic and Electrochemical Characterization of the Mycofactocin Biosynthetic Protein, MftC, Provides Insight into Its Redox Flipping Mechanism. *Biochemistry* **2019**, *58* (7), 940-950.

69. Ayikpoe, R.; Salazar, J.; Majestic, B.; Latham, J. A., Mycofactocin Biosynthesis Proceeds through 3-Amino-5-[(p-hydroxyphenyl)methyl]-4,4-dimethyl-2-pyrrolidinone (AHDP); Direct Observation of MftE Specificity toward MftA. *Biochemistry* **2018**, *57* (37), 5379-5383.

70. Khaliullin, B.; Ayikpoe, R.; Tuttle, M.; Latham, J. A., Mechanistic elucidation of the mycofactocin-biosynthetic radical *S*-adenosylmethionine protein, MftC. *J Biol Chem* **2017**, *292* (31), 13022-13033.

71. Burkhart, B. J.; Hudson, G. A.; Dunbar, K. L.; Mitchell, D. A., A prevalent peptide-binding domain guides ribosomal natural product biosynthesis. *Nat Chem Biol* **2015**, *11* (8), 564-70.

72. Nguyen, D. T.; Mitchell, D. A.; van der Donk, W. A., Genome Mining for New Enzyme Chemistry. *ACS Catal* **2024**, *14* (7), 4536-4553.

73. Ayikpoe, R. S.; Zhu, L.; Chen, J. Y.; Ting, C. P.; van der Donk, W. A., Macrocyclization and Backbone Rearrangement During RiPP Biosynthesis by a SAM-Dependent Domain-of-Unknown-Function 692. *ACS Cent Sci* **2023**, *9* (5), 1008-1018.

74. Sugiyama, R.; Suarez, A. F. L.; Morishita, Y.; Nguyen, T. Q. N.; Tooh, Y. W.; Roslan, M. N. H. B.; Lo Choy, J.; Su, Q.; Goh, W. Y.; Gunawan, G. A.; Wong, F. T.; Morinaka, B. I., The Biosynthetic Landscape of Triceptides Reveals Radical SAM Enzymes That Catalyze Cyclophane Formation on Tyr- and His-Containing Motifs. *Journal of the American Chemical Society* **2022,** *144* (26), 11580–11593.

75. Nguyen, D. T.; Zhu, L.; Gray, D. L.; Woods, T. J.; Padhi, C.; Flatt, K. M.; Mitchell, D. A.; van der Donk, W. A., Biosynthesis of Macrocyclic Peptides with C-Terminal β-Amino-α-keto Acid Groups by Three Different Metalloenzymes. *ACS Central Science* **2024,** *10* (5), 1022–1032.

76. Bushin, L. B.; Clark, K. A.; Pelczer, I.; Seyedsayamdost, M. R., Charting an Unexplored Streptococcal Biosynthetic Landscape Reveals a Unique Peptide Cyclization Motif. *J Am Chem Soc* **2018**, *140* (50), 17674-17684.

77. Clark, K. A.; Seyedsayamdost, M. R., Bioinformatic Atlas of Radical SAM Enzyme-Modified RiPP Natural Products Reveals an Isoleucine-Tryptophan Crosslink. *J Am Chem Soc* **2022,** *144* (39), 17876–17888.

78. Lu, J.; Xu, H.; Xia, J.; Ma, J.; Xu, J.; Li, Y.; Feng, J., D- and Unnatural Amino Acid Substituted Antimicrobial Peptides With Improved Proteolytic Resistance and Their Proteolytic Degradation Characteristics. *Front Microbiol* **2020**, *11*, 563030.

79. Ayikpoe, R. S.; van der Donk, W. A., Chapter Eighteen - Peptide backbone modifications in lanthipeptides. In *Methods in Enzymology*, Petersson, E. J., Ed. Academic Press: **2021**; Vol. *656*, pp 573-621.

80. Sikandar, A.; Franz, L.; Adam, S.; Santos-Aberturas, J.; Horbal, L.; Luzhetskyy, A.; Truman, A. W.; Kalinina, O. V.; Koehnke, J., The bottromycin epimerase BotH defines a group of atypical alpha/beta-hydrolase-fold enzymes. *Nat Chem Biol* **2020**, *16* (9), 1013-1018.

81. Nakashima, Y.; Kawakami, A.; Ogasawara, Y.; Maeki, M.; Tokeshi, M.; Dairi, T.; Morita, H., Structure of lasso peptide epimerase MslH reveals metal-dependent acid/base catalytic mechanism. *Nat Commun* **2023**, *14* (1), 4752.

82. Feng, Z.; Ogasawara, Y.; Dairi, T., Identification of the peptide epimerase MslH responsible for D-amino acid introduction at the C-terminus of ribosomal peptides. *Chem Sci* **2020**, *12* (7), 2567-2574.

83. Benjdia, A.; Berteau, O., Radical SAM Enzymes and Ribosomally-Synthesized and Post-translationally Modified Peptides: A Growing Importance in the Microbiomes. *Front Chem* **2021**, *9*, 678068.

84. Morinaka, B. I.; Vagstad, A. L.; Piel, J., Radical *S*-Adenosylmethionine Peptide Epimerases: Detection of Activity and Characterization of D-Amino Acid Products. *Methods Enzymol* **2018**, *604*, 237-257.

85. Popp, P. F.; Friebel, L.; Benjdia, A.; Guillot, A.; Berteau, O.; Mascher, T., The Epipeptide Biosynthesis Locus epeXEPAB Is Widely Distributed in Firmicutes and Triggers Intrinsic Cell Envelope Stress. *Microb Physiol* **2021**, *31* (3), 306-318.

86. Johnson, B. A.; Clark, K. A.; Bushin, L. B.; Spolar, C. N.; Seyedsayamdost, M. R., Expanding the Landscape of Noncanonical Amino Acids in RiPP Biosynthesis. *J Am Chem Soc* **2024,** *146* (6), 3805-3815.

87. Hubrich, F.; Lotti, A.; Scott, T. A.; Piel, J., Uncovering Novel Peptide Chemistry from Bacterial Natural Products. *Chimia* (Aarau) **2021**, *75* (6), 543-547.

88. Freeman, M. F.; Gurgui, C.; Helf, M. J.; Morinaka, B. I.; Uria, A. R.; Oldham, N. J.; Sahl, H.-G.; Matsunaga, S.; Piel, J., Metagenome Mining Reveals Polytheonamides as Posttranslationally Modified Ribosomal Peptides. *Science* **2012**, *338* (6105), 387-390.

89. Hamada, T.; Matsunaga, S.; Yano, G.; Fusetani, N., Polytheonamides A and B, Highly Cytotoxic, Linear Polypeptides with Unprecedented Structural Features, from the Marine Sponge, Theonella swinhoei. *J. Am. Chem. Soc*. **2005**, *127* (1), 110-118.

90. Freeman, M. F.; Helf, M. J.; Bhushan, A.; Morinaka, B. I.; Piel, J., Seven enzymes create extraordinary molecular complexity in an uncultivated bacterium. *Nat Chem* **2017**, *9* (4), 387-395.

91. Morinaka, B. I.; Vagstad, A. L.; Helf, M. J.; Gugger, M.; Kegler, C.; Freeman, M. F.; Bode, H. B.; Piel, J., Radical *S*-adenosyl methionine epimerases: regioselective introduction of diverse D-amino acid patterns into peptide natural products. *Angew Chem Int Ed Engl* **2014**, *53* (32), 8503-7.

92. Mordhorst, S.; Badmann, T.; Bosch, N. M.; Morinaka, B. I.; Rauch, H.; Piel, J.; Groll, M.; Vagstad, A. L., Structural and Biochemical Insights into Post-Translational Arginine-to-Ornithine Peptide Modifications by an Atypical Arginase. *ACS Chem Biol* **2023,** *18* (3), 528-536.

93. Bosch, N. M.; Borsa, M.; Greczmiel, U.; Morinaka, B. I.; Gugger, M.; Oxenius, A.; Vagstad, A. L.; Piel, J., Landornamides: Antiviral Ornithine-Containing Ribosomal Peptides Discovered through Genome Mining. *Angew Chem Int Ed Engl* **2020**, *59* (29), 11763-11768.

94. Mordhorst, S.; Morinaka, B. I.; Vagstad, A. L.; Piel, J., Posttranslationally Acting Arginases Provide a Ribosomal Route to Non-proteinogenic Ornithine Residues in Diverse Peptide Sequences. *Angew Chem Int Ed Engl* **2020**, *59* (48), 21442-21447.

95. Vagstad, A. L.; Kuranaga, T.; Puntener, S.; Pattabiraman, V. R.; Bode, J. W.; Piel, J., Introduction of d-Amino Acids in Minimalistic Peptide Substrates by an *S*-Adenosyl-L-Methionine Radical Epimerase. *Angew Chem Int Ed Engl* **2019**, *58* (8), 2246-2250.

96. Korneli, M.; Fuchs, S. W.; Felder, K.; Ernst, C.; Zinsli, L. V.; Piel, J., Promiscuous Installation of D-Amino Acids in Gene-Encoded Peptides. *ACS Synth Biol* **2021**, *10* (2), 236-242.

97. Walls, W. G.; Vagstad, A. L.; Delridge, T.; Piel, J.; Broderick, W. E.; Broderick, J. B., Direct Detection of the α-Carbon Radical Intermediate Formed by OspD: Mechanistic Insights into Radical *S*-Adenosyl-L-methionine Peptide Epimerization. *J Am Chem Soc* **2024**, *146* (8), 5550-5559.

98. Popp, P. F.; Benjdia, A.; Strahl, H.; Berteau, O.; Mascher, T., The Epipeptide YydF Intrinsically Triggers the Cell Envelope Stress Response of Bacillus subtilis and Causes Severe Membrane Perturbations. *Front Microbiol* **2020**, *11*.

99. Benjdia, A.; Guillot, A.; Ruffie, P.; Leprince, J.; Berteau, O., Post-translational modification of ribosomally synthesized peptides by a radical SAM epimerase in Bacillus subtilis. *Nat Chem* **2017**, *9* (7), 698-707.

100. Butcher, B. G.; Lin, Y. P.; Helmann, J. D., The yydFGHIJ operon of Bacillus subtilis encodes a peptide that induces the LiaRS two-component system. *J Bacteriol* **2007**, *189* (23), 8616-25.

101. Kubiak, X.; Polsinelli, I.; Chavas, L. M. G.; Fyfe, C. D.; Guillot, A.; Fradale, L.; Brewee, C.; Grimaldi, S.; Gerbaud, G.; Thureau, A.; Legrand, P.; Berteau, O.; Benjdia, A., Structural and mechanistic basis for RiPP epimerization by a radical SAM enzyme. *Nat Chem Biol* **2023**, *20*, 382-391.

102. Morinaka, B. I.; Lakis, E.; Verest, M.; Helf, M. J.; Scalvenzi, T.; Vagstad, A. L.; Sims, J.; Sunagawa, S.; Gugger, M.; Piel, J., Natural noncanonical protein splicing yields products with diverse β-amino acid residues. *Science* **2018**, *359*, 779-782.

103. Scott, T. A.; Verest, M.; Farnung, J.; Forneris, C. C.; Robinson, S. L.; Ji, X.; Hubrich, F.; Chepkirui, C.; Richter, D. U.; Huber, S.; Rust, P.; Streiff, A. B.; Zhang, Q.; Bode, J. W.; Piel, J., Widespread microbial utilization of ribosomal β-amino acid-containing peptides and proteins. *Chem* **2022**, *8* (10), 2659-2677.

104. Vagstad, A. L.; Lakis, E.; Csizi, K. S.; Walls, W.; Richter, D.; Soo Lee, K.; Stocker, R.; Gugger, M.; Broderick, W. E.; Broderick, J. B.; Reiher, M.; Piel, J., Mechanistic Insights Into Post-Translational α-Keto-β-Amino Acid Formation by a Radical *S*-Adenosyl Methionine Peptide Splicease. *Angew Chem Int Ed Engl* **2025**, *64*, e202418054.

CHAPTER TWO

THE B_{12}-INDEPENDENT GLYCEROL DEHYDRATASE ACTIVATING ENZYME FROM *CLOSTRIDIUM BUTYRICUM* CLEAVES SAM TO PRODUCE 5'-DEOXYADENOSINE AND NOT 5'-DEOXY-5'-(METHYLTHIO)ADENOSINE

Contribution of Authors and Co-Authors

Manuscript in Chapter 2

Author: William G. Walls

Contributions: Conducted most of the experimental work, prepared figures, wrote sections of the manuscript, edited final draft of manuscript.

Co-Author: James D Moody

Contributions: Carried out experimental work, prepared figures, wrote initial draft of manuscript.

Co-Author: Elizabeth C. McDaniel

Contributions: Prepared enzymes and other material for experiments.

Co-Author: Maria Villanueva

Contributions: Prepared enzymes and other materials for experiments.

Co-Author: Eric M. Shepard

Contributions: Provided experimental insight, helped edit manuscript.

Co-Author: William E. Broderick

Contributions: Provided experimental insight, helped edit manuscript.

Co-Author: Joan B. Broderick

Contributions: Provided oversight for the research direction, interpretation of results, wrote sections of the manuscript, helped edited the manuscript, acquired funding for the research.

Manuscript Information

William G. Walls, James D. Moody, Elizabeth C. McDaniel, Maria Villanueva, Eric M. Shepard,

William E. Broderick, and Joan B. Broderick

Journal of Inorganic Biochemistry

Status of Manuscript:
☐ Prepared for submission to a peer-reviewed journal
☐ Officially submitted to a peer-reviewed journal
☐ Accepted by a peer-reviewed journal
☒ Published in a peer-reviewed journal

Elsevier
2022, 227, 111662
10.1016/j.jinorgbio.2021.111662

Abstract

Glycerol dehydratase activating enzyme (GD-AE) is a radical *S*-adenosyl-L-methionine (SAM) enzyme that installs a catalytically essential amino acid backbone radical onto glycerol dehydratase in bacteria under anaerobic conditions. Although GD-AE is closely homologous to other radical SAM activases that have been shown to cleave the S-C(5') bond of SAM to produce 5'-deoxyadenosine (5'-dAdoH) and methionine, GD-AE from *Clostridium butyricum* has been reported to instead cleave the S-C(γ) bond of SAM to yield 5'-deoxy-5'-(methylthio)adenosine (MTA). Here we re-investigate the SAM cleavage reaction catalyzed by GD-AE and show that it produces the widely observed 5'-dAdoH, and not the less conventional product MTA.

Introduction

The radical *S*-adenosyl-L-methionine (SAM) superfamily of enzymes is large and diverse, catalyzing a wide range of reactions throughout all kingdoms of life [1-4]. These reactions are thought to be initiated by a set of common steps that include coordination of SAM to the unique iron of a [4Fe-4S] cluster [5-7], followed by reductive cleavage to generate the 5'-deoxyadenosyl (5'-dAdo•) radical intermediate responsible for abstracting a hydrogen atom from substrate [8, 9]. The 5'-dAdo• is the same central intermediate involved in radical reactions catalyzed by B_{12} radical enzymes; despite its important role in biological radical reactions, however, the 5'-dAdo• eluded direct observation and characterization until recently [10-12]. Interestingly, both radical SAM enzymes and B_{12} radical enzymes harbor this reactive primary carbon radical as an organometallic species: the Co-C bond containing cofactor adenosylcobalamin in B_{12} enzymes and the Fe-C bond containing Ω intermediate in radical SAM enzymes [13, 14]. In each case,

homolytic metal-carbon bond cleavage generates the key 5'-dAdo• radical intermediate [9], which has been shown to be exquisitely controlled in the radical SAM enzymes [15]. Upon liberation from Ω, the 5'-dAdo• radical abstracts H• from native or alternative substrates to generate the initial substrate radical [8, 9, 16].

The radical SAM enzyme glycerol dehydratase activating enzyme (GD-AE) from *Clostridium butyricum* catalyzes the activation of the B_{12}-independent glycerol dehydratase (GD) [17] by hydrogen atom abstraction from a conserved glycine residue (G763) to generate the active enzyme [18]; GD-AE is thus a member of a subclass of radical SAM enzymes that function to activate glycyl radical enzymes [19]. Unlike these other glycyl radical enzyme activating enzymes (GRE-AEs) however, GD-AE has been reported to produce 5'-deoxy-5'-(methylthio)adenosine (MTA), rather than 5'-deoxyadenosine (5'-dAdoH), as the adenosyl-containing product of SAM cleavage [20]. While photoinduced reductive cleavage of SAM can result in enzyme-dependent differences in regioselectivity [12, 21, 22], radical SAM enzyme catalysis typically involves S-C(5') bond cleavage to generate 5'-dAdoH and methionine. In contrast, MTA would be formed if the S-C(γ) bond were reductively cleaved, with the other product of that cleavage being a 3-amino-3-carboxypropyl radical (ACP•) (Figure 2.1) [1]. Thus the reported observation of MTA and not 5'-dAdoH during GD-AE catalysis suggested that an alternate S-C bond is cleaved during catalysis by this enzyme, and that ACP• rather than 5'-dAdo• abstracts the H-atom from GD to generate the active enzyme [20].

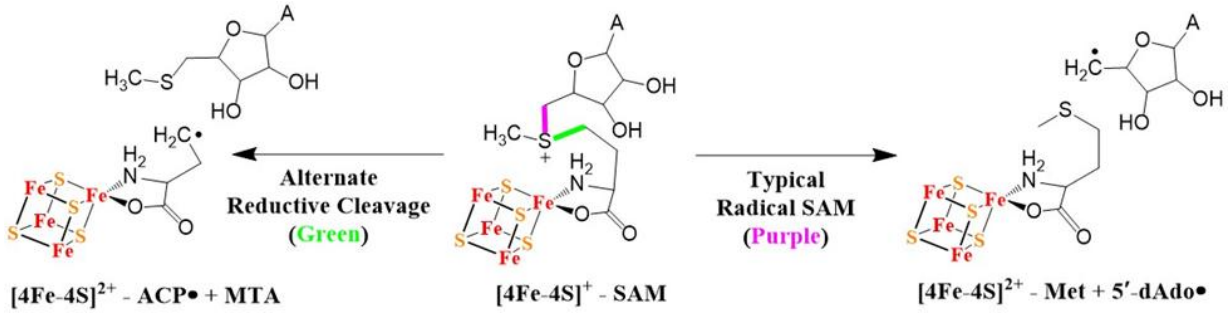


Figure 2.1. Reductive cleavage pathways in radical SAM enzymes. SAM chelates the unique iron of a $[4Fe\text{-}4S]^{+}$ cluster in the active site (center). Reductive cleavage of SAM generally involves homolytic S-C5′ bond cleavage to generate methionine and an intermediate 5′-deoxyadenosyl radical (5′-dAdo•, right). GD-AE has been reported [19] to instead homolytically cleave the S-Cγ bond to generate methylthioadenosine (MTA) and an intermediate aminocarboxypropyl radical (ACP•, left).

A SAM-derived ACP• intermediate is also implicated in the diphthamide biosynthetic enzyme Dph2 from *Pyrococcus horikoshii* [23]. While Dph2 catalyzes radical-based chemistry using SAM and an iron-sulfur cluster, sequence and structural comparisons place it outside of the canonical radical SAM superfamily [1, 24]; further, the ACP• generated does not carry out H-atom abstraction but rather adds to substrate and is subsequently incorporated into the product diphthamide [23]. During the Dph2-catalyzed reaction, the ACP• binds to the cluster at the unique iron to form an organometallic intermediate that is similar to the Ω organometallic intermediate observed for canonical radical SAM enzymes [25-27]. As of this writing, GD-AE remains an anomaly as the only canonical radical SAM enzyme reported to catalyze reductive cleavage of SAM at a location other than the S-C(5') bond.

As part of our efforts to understand the factors that control regioselectivity and mechanism in radical SAM enzymes, we have examined the reaction catalyzed by GD-AE. In the course of these studies, we found that contrary to the prior report [20], GD-AE in fact cleaves SAM at the S-C(5') bond to generate methionine and 5'-dAdoH as products. While small

amounts of MTA were observed in our assays, control experiments showed that the MTA was a contaminant that did not increase in an enzyme-dependent manner. Here we describe these results and their implications in regards to the consensus SAM cleavage mechanism that occurs within all characterized members of the radical SAM superfamily.

Materials and Methods

GD-AE Cloning and Protein Expression

The DNA sequence of *Clostridium butyricum* GD-AE was optimized using the DNAworks application [28], synthesized using a commercial vendor (Integrated DNA Technologies, Coralville, IA, USA), and cloned into a modified pET42 vector (EMD Millipore, Billerica, MA, USA), which appends an N-terminal 10X-histidine-SUMO tag (the SUMO domain corresponds to the yeast Smt3 gene). The DNA sequence encoding the 10X-histidine-SUMO tag was a gracious gift from Dr. Christopher Bahl. The resulting plasmid was used to transform BL21-CodonPlus(DE3)-RIL cells (Agilent Technologies, Santa Clara, CA, USA) along with pDB1282, a modified pAra13 plasmid carrying the genes for 6 ISC operon genes from *Azotobacter vinelandii* (*iscA*, *iscS*, *iscU*, *hscA*, *hscB*, and *fdx*) [29]. The pDB1282 plasmid was a gracious gift from Dr. John Peters. Cells were grown and harvested using a modified version of a previously published method [30]. Six 2.8 L Fernbach flasks, each with 1.5 L of LB medium (with 100 μg/mL ampicillin and 50 μg/mL kanamycin) were each inoculated with 50 mL of saturated overnight culture and grown at 37°C and 230 RPM. At a 600 nm absorbance of 0.3, a sterile filtered solution of 20% arabinose in water was added to a final concentration of 0.2% and the incubation temperature was decreased to 25°C. At a 600 nm absorbance of 0.6, a sterile filtered solution of 1 M IPTG (isopropyl β-D-thiogalactopyranoside) in water was added

to a final concentration of 0.1 mM, and solutions of 300 mM ferrous ammonium sulfate and 300 mM L-cysteine, each dissolved in water, were added to final concentrations of 200 µM each. After an additional 4 hours of shaking at 25°C, ferrous ammonium sulfate and L-cysteine were again added to final concentrations of 200 µM each. At this point, 1 drop of Antifoam-SE was added to each flask, which were then sealed and incubated at 4°C for 16 hours while being actively sparged with nitrogen gas.

Alternatively, the optimized GD-AE coding sequence was inserted into pET-45b expression vector (GenScript) between the Acc651 and BamHI restriction sites, in-frame with a hexahistidine tag. The GD-AE/pET-45b was used to transform chemically competent Rosetta-pLysS(DE3) *E. coli* cells. Following transformation, a single colony was transferred into 50 ml LB (10 g/L Tryptone, 10 g/L KCl, 5 g/L Yeast Extract) liquid culture supplemented with 100 µg/ml Ampicillin and 33 µg/ml Chloramphenicol. The seed culture was used to inoculate 6 L TB media (24 g/L Yeast Extract, 12 g/L Tryptone, 89 mM KPi pH 7.0, 0.5% glycerol). The cultures were incubated at 37ºC with 180 rpm shaking speed until the optical density of the cultures reached OD_{600}=0.6-0.8, then the cultures were transferred to 4ºC for 3 hours. The protein expression was induced by the addition of 0.5 mM IPTG, furthermore the media were supplemented with 600 µM FAS and 600 µM L-cysteine, the cultures were shaken typically for 16-18 hours at 16ºC. The cells were harvested by centrifugation (5000 rpm 10 min 14ºC), the cell paste was frozen in liquid nitrogen and kept at -80ºC until further use.

GD-AE Protein Purification

All steps were completed in an anaerobic chamber (Coy Laboratory Products, Grass Lake, MI, USA) housed in a 4°C room.

For purification of GD-AE expressed with a 10xHis-SUMO tag, cell pellet from 27 L of culture was resuspended in 150 mL of lysis buffer (50 mM Tris, pH 7.5, 300 mM KCl, 1 mM phenylmethylsulfonyl fluoride, 250 μg/ mL lysozyme, 25 μg/mL deoxyribonuclease I, 25 μg/ mL ribonuclease A, 1% Triton X-100, 100 μM dithiothreitol (DTT)) and incubated with stirring for 1 hour. The lysis solution was clarified by centrifugation for 60 minutes at 38,000 g and the supernatant was flowed over a 5 mL nickel-NTA Sepharose column, which was pre-equilibrated with loading buffer (50 mM Tris, pH 7.5, 300 mM KCl). The nickel column was next washed with 50 mL of imidazole wash buffer (50 mM Tris, pH 7.5, 300 mM KCl, 30 mM imidazole), prior to elution with 50 mL of elution buffer (50 mM Tris, pH 7.5, 300 mM KCl, 400 mM imidazole). The brown eluate was immediately added to a 90 mL Sephadex G25 desalting column pre-equilibrated with storage buffer (50 mM Tris, pH 7.5, 300 mM KCl, 10% glycerol). The desalted protein was immediately snap frozen in liquid nitrogen. The next day the protein was thawed and DTT added to a final concentration of 100 μM. Next, a 1/10 molar equivalent of purified SUMO protease was added to the protein solution, which was then incubated for 3 hours at 4°C. The DNA vector encoding the SUMO protease (corresponding to the yeast Ulp1 gene) was a gracious gift from Dr. Christopher Bahl at the University of Washington. Following the 3 hour incubation, the cleavage reaction was flowed over a fresh 5 mL nickel-NTA Sepharose column pre-equilibrated with storage buffer. The brown flow-through was aliquoted and snap frozen. Protein concentration was quantified using a modified version of the method of Bradford [31] and iron content was determined using a SpectrAA 220 Fast Sequential Atomic Absorption Spectrometer (Varian, Palo Alto, CA, USA).

For purification of the 6xHis-tagged protein lacking the SUMO tag, the frozen cell paste was transferred into the Coy chamber where it was resuspended in lysis buffer (75 mM Tris-HCl pH 9.0, 300 mM KCl, 20% glycerol, 25 mg/ ml $MgCl_2$, 0.2 mg/ ml DNAse, 0.2 mg/ ml RNAse, 0.2 mg/ ml lysozyme and 1% Triton X-100. The cells were lysed for 20-30 minutes at room temperature. The chemical-enzymatic lysis was followed with mechanical cell disruption. The partially lysed cell suspension was transferred to a 4ºC Coy chamber were the suspension was sonicated (40% amplitude, 5 sec on, 10 sec off, 5 minutes in total). The sonicated suspension was centrifuged for 45 minutes with 15000 rpm at 14ºC. The resulting supernatant was loaded onto Ni-NTA columns which were equilibrated with 75 mM Tris-HCl pH 9.0, 300 mM KCl, 20% glycerol. The column was washed extensively with equilibration buffer until the UV absorption reached nearly zero, then the column was washed with 75 mM Tris-HCl pH 9.0, 300 mM KCl, 20% glycerol, 100 mM imidazole to eluate the non-specifically binding proteins. The 100 mM imidazole wash was followed by the elution of GD-AE with 75 mM Tris-HCl pH 9.0, 300 mM KCl, 20% glycerol, 500 mM imidazole. The excess imidazole was removed using 10 kDa Amicon filters. The purified protein was aliquoted, flash frozen in liquid nitrogen and stored at -80ºC until further use.

Glycerol Dehydratase Cloning and Protein Expression

The codon optimized Glycerol dehydratase (GD) gene (generated as described above for GD-AE) from *Clostridium butyricum* was inserted into a pET-45b vector (Genscript) between the Acc65I and BamHI restriction sites. The GD/pET-45b was used to transform chemically competent Rosetta-pLysS(DE3) *E. coli* cells. Following transformation, a single colony was transferred into 30 ml LB (10 g/ L Tryptone, 10 g/ L KCl, 5 g/ L Yeast Extract) liquid culture

supplemented with 100 µg/ ml Ampicillin and 33 µg/ml Chloramphenicol and grown overnight (37°C, 180 rpm shaking). The seed culture was used to inoculate 2 L TB media (24 g/ L Yeast Extract, 12 g/L Tryptone, 89 mM KP_i pH 7.0, 0.5% glycerol). The cultures were incubated at 37ºC with 180 rpm shaking speed until the optical density of the cultures reached OD_{600} = 0.5-0.6, then the cultures were placed in an ice-water bath for 1 hour. Protein expression was induced by the addition of 0.5 mM IPTG. Cells were then shaken at 18ºC, 180 rpm for 21 hours. Two hours after induction, 1 mL of Antifoam-SE was added to each flask. The cells were harvested by centrifugation (6000 rpm, 15 min, 4ºC) and the cell paste was frozen in liquid nitrogen and kept at -80ºC until further use.

Glycerol Dehydratase Protein Purification

For purification of the 6xHis-tagged GD, the frozen cell paste was transferred into the Coy chamber where it was resuspended in lysis buffer (50 mM HEPES, pH 7.5, 100 mM KCl, 10% glycerol, 1 mM PMSF, 1.15 mg/ml $MgCl_2$, 0.01 mg/ml DNAse, 0.45 mg/ml lysozyme, and 10 mg/ mL Triton X-100). The cells were lysed for 1 hour at room temperature and then sonicated (40% amplitude, 5 seconds on, 15 seconds off, 5 minutes total time). The sonicated suspension was centrifuged for 45 minutes at 15000 rpm and 4ºC. The resulting supernatant was loaded onto a Ni-NTA column that was equilibrated with 10 column volumes of Buffer A (50 mM HEPES, pH 7.5, 100 mM KCl, 10% glycerol) and 10 mM imidazole. The column was then washed with Buffer A with increasing amounts of imidazole in a step-wise manner starting with 50 mM, then 100 mM, 150 mM, and finally 500 mM to elute any remaining protein. Each fraction was collected separately and subsequently flash frozen in liquid nitrogen and stored at -20°C overnight. Each fraction was then thawed and analyzed by SDS-PAGE for which fractions

contained the GD. Each fraction contained the GD but with decreasing amounts of contaminating proteins (Figure S2.3). Fractions eluted with 150 mM and 500 mM imidazole were pooled and de-salted using a 50 kDa MWCO Amicon spin filter by diluting with Buffer A 10x and centrifuging at 6000 rpm for a total of 3 times. Lastly, the concentrated and de-salted GD was centrifuged in an Eppendorf tube at 13,000 rpm, 10 minutes to remove any precipitated protein. The GD was then aliquoted, flash frozen in liquid nitrogen, and stored at -80°C until further use. GD was quantified by its absorbance at 280 nm using the molar extinction coefficient ε_{280nm} = 76,210 M^{-1} cm^{-1}, calculated using the Protparam tool (https://web.expasy.org/protparam/) assuming all cystines are reduced.

Cloning and Purification of CsdA

The DNA sequence of *Escherichia coli* cysteine desulfurase (*ec*CsdA) was codon optimized and synthesized using a commercial vendor (Genscript) and cloned into a pET-19b vector using the NdeI and BamHI restriction sites. The resulting plasmid was transformed into a BL21(DE3)pLysS cell line. Six 2.8 L Fernbach flasks, each with 1.0 L of LB medium (supplemented with 25 mM KPi, pH = 7.6, 5% glucose, 100 µg/mL ampicillin, and 33 µg/mL chloramphenicol) were each inoculated with 30 mL of saturated overnight culture and grown at 37°C and 180 RPM. Once the OD_{600} reached 0.3, the cells were placed in a 4°C fridge for 1 hour. The cells were then induced with IPTG (0.5 mM final concentration) and allowed to grow for 3 hours at 37°C and 180 RPM shaking. Cells were harvested by centrifugation (6000 RPM, 4°C, 20 minutes) and the cell paste was frozen in liquid nitrogen and stored at -80°C until further use. For purification of *ec*CsdA with a 6xHis Tag, the cell paste was brought into an anaerobic COY chamber and resuspended in lysis buffer (75 mM HEPES, pH = 8.0, 300 mM KCl, 5% glycerol,

0.2 mg/ mL DNAse, RNAse, and lysozyme, 25 mg/ mL $MgCl_2$, and 1% Triton X-100) at a ratio of 2 mL/ g cell paste and incubated at room temperature for 40 minutes. The cell lysate was then moved to a 4°C anaerobic COY chamber for sonication (40% amplitude, 5 sec on, 10 sec off, 5 minutes in total). The lysate was clarified by centrifugation for 45 minutes at 15,000 rpm, 4°C and the supernatant was loaded onto a 5 mL nickel-NTA Sepharose column, which was pre-equilibrated with 5 column volumes of equilibration buffer (75 mM HEPES, pH 8.0, 300 mM KCl, 5% glycerol). The nickel column was washed with 100 mL of imidazole wash buffer (75 mM HEPES, pH 8.0, 300 mM KCl, 5% glycerol, 100 mM imidazole), prior to elution with 50 mL of elution buffer (75 mM HEPES, pH 8.0, 300 mM KCl, 5% glycerol, 400 mM imidazole). The eluate was concentrated to 4 mL using a 30 kDa Amicon spin filter, then de-salted by passing over a NAP25 column equilibrated in equilibration buffer. The de-salted *ec*CsdA was aliquoted, frozen in liquid nitrogen, and stored at -80°C.

Quantification of Protein, Iron, and Sulfide

Purified GD-AE protein was quantified following the procedure by Barr et al [32]. with the minor modification of using 10 kDa MWCO Amicon spin filters to buffer exchange and concentrate the denatured protein. To buffer exchange, the protein was concentrated to 200 µL, diluted to 500 µL with 6 M guanidinium HCl, and concentrated again to 200 µL, repeating for a total of 7 times. The concentrated protein solution was used for downstream analyses. This procedure provided a correction factor of 0.851 ± 0.004.

Iron was quantified following the procedure by Németh et al [33]. with modifications. An iron AA standard (Bicca, 1000 ppm in 3% HCl) was used to generate a calibration curve by first diluting to 0.5 nmol/ µL in water. Following the addition of perchloric acid and water, each

solution was allowed to sit at room temperature for 30 minutes. The solutions were then centrifuged at 13,000 rpm for 15 minutes at room temperature. After the addition of bathophenanthroline disulphonic disodium salt, ammonium acetate, and ascorbic acid, the solutions reacted for 20 minutes. The UV-Visible spectrum of each sample was measured with MQ water as a blank. The absorbance at 535 nm was plotted against nmol of iron to generate a calibration curve that was used to calculate the amount of iron in each protein sample.

Acid-labile sulfide was quantified following the procedure by Broderick et al [34]. with minor modifications. Each sample and standard were brought to a volume of 100 µL using filtered (0.2 µm) deionized water instead of pH 8 water. Also, following the addition of 1% ZnOAc and 12% NaOH, each sample was allowed to sit for at least 15 minutes before the addition of N,N-dimethyl-*p*-phenylenediamine (0.1% in 5 M HCl) and $FeCl_3$ (23 mM in 1.2 M HCl).

Enzymatic Reconstitution of GD-AE

The purified GD-AE was brought into an anaerobic COY chamber to thaw, along with *E. coli* cysteine desulfurase (*ec*CsdA). Ferrous ammonium sulfate hexahydrate (FAS), L-cysteine hydrochloride monohydrate, and dithiothreitol (DTT) were brought into the COY chamber as powders and brought up to 100 mM stock concentrations in Buffer A (80 mM Tris HCl, pH = 9.0, 150 mM KCl, 20% glycerol). The purified GD-AE was diluted to 100 µM with Buffer A in a scintillation vial with a small stir bar. FAS, L-cysteine, and DTT were added to the vial to final concentrations of 1 mM. Then *ec*CsdA was added to the vial to a final concentration of 2 µM to initiate the reconstitution. The reaction mixture was stirred gently for 2.5 hours, after which the contents were centrifuged at 6000 rpm for 10 minutes to remove any precipitates. The

supernatant was then de-salted by passing over a 90 mL column packed with Sephadex G-25 resin equilibrated with 2 column volumes of Buffer A. The eluate was collected and concentrated down to approximately 1 mL with a 30 MWCO Amicon spin filter by centrifuging at 6000 rpm for 3 minutes, 3 times, with gentle agitation after each centrifugation. The reconstituted GD-AE was then aliquoted and frozen in liquid nitrogen, and stored at -80°C.

Electron Paramagnetic Resonance Spectroscopy

Electron paramagnetic resonance (EPR) spectroscopy followed general procedures described previously [35]. Continuous wave EPR X-band EPR spectroscopy was performed using a Bruker EMX EPR spectrometer equipped with a Bruker/ColdEdge (Sumitomo Cyrogenics) 10 K waveguide cryogen free system with an Oxford MercuryiTC controller unit and helium Stinger recirculating unit (Sumitomo Cyrogenics, ColdEdge Technologies). For analysis of iron-sulfur clusters, GD-AE was left non-reduced, reduced with 0.60 mM Na-DT for 10 minutes, or reduced with 0.60 mM Na-DT and incubated with 0.90 mM SAM in the glove box. Each sample was then transferred to EPR tubes, capped, and flash frozen in liquid nitrogen outside the glove box. Each sample was measured at varying temperatures and powers as indicated in the figure captions. Metal-based signals were recorded with a microwave frequency of 9.38 GHz, microwave power of 1 mW, receiver gain of 10000, modulation frequency of 100 kHz, modulation amplitude of 10 G, and time constant of 168.84 ms, with a scanning range from 3000 to 4000 G. The glycyl radical generated on GD by GD-AE was recorded at 75 K using a microwave frequency of 9.38 GHz, microwave power of 212 μW, 2 G modulation amplitude, and 100 kHz modulation frequency. The scan width is 300 G centered at 3350 G. EPR

simulations were performed with Easyspin [36] within the Matlab R2020b software suite (Mathworks inc.). All spectra were cavity subtracted and baseline corrected.

Enzyme Activity Assays with GD Peptide Substrate

All enzyme activity assays were carried out in a Unilab glove box (O_2 ≤ 1 ppm; MBraun, Stratham, NH, USA) or an anaerobic chamber (O_2 ≤ 20 ppm; Coy Laboratory Products, Grass Lake, MI, USA) at 24 - 31°C. SAM was prepared enzymatically as previously described [6]. The GD 7-mer peptide (RVAGYSA) corresponding to amino acid residues 760 – 766 and containing the site of H-atom abstraction by GD-AE (G763) was purchased from GenScript. As-isolated GD-AE (8.0 or 16 μM) was combined with SAM (1.0 - 2.1 mM), DTT (5.0 mM), and the 7-mer target peptide from glycerol dehydratase (3.43 mM) in assay buffer composed of 50 mM Tris-Cl pH 7.5, 300 mM KCl, 10% v/v glycerol. The assay was initiated by the addition of dithionite (2.0 - 2.1 mM). At indicated time points (0.5, 7, 15, 30, and 60 minutes), reaction aliquots were removed and quenched by addition of 1/3 volume of 1 M sodium acetate, pH 4.5 and agitation by vigorously pipetting air into the solution. Quenched aliquots were stored frozen at –20 °C for 16 to 24 hours and were then centrifuged at 20,000 g for 10 minutes. Each supernatant was injected onto a Phenomenex Kinetex 5μ PFP 100Å column equilibrated in 98% solvent A (water with 0.1% acetic acid) and 2% solvent B (acetonitrile with 0.1% acetic acid) on a Series 1100 HPLC (Agilent Technologies, Santa Clara, CA, USA). The column was washed with 2% solvent B at 1 mL/minute for 3.5 minutes, after which a linear gradient was begun, reaching 60% solvent B at 11 minutes. The 60% solvent B was maintained for 3 minutes prior to re-equilibrating the column with 2% solvent B. SAM eluted in the void volume, while 5'-dAdoH eluted with a retention time near 7.8 minutes and MTA eluted near 9.0 minutes. SAM, 5'-dAdoH, and MTA

were detected by their absorbance at 254 nm and dAdo and MTA were identified by comparison of their retention times to those of 5'-dAdoH and MTA standards that were run separately, by standard addition of 5'-dAdoH and MTA to assay samples, and by mass spectrometry. Quantification was carried out by integrating peaks in the ChemStation software, and standard curves were fit using linear regression in Excel. MTA and 5'-dAdoH were quantified by comparison to standard curves of their respective standard solutions. To generate the chromatograms in Figure 5, the raw chromatographic data was processed in Excel as follows: a blank run was subtracted from each data set and the SAM standard was baseline corrected (as it was collected in a different run than the other samples and blank run).

Mass spectrometry of 5'-dAdoH

An HPLC run like that depicted in Figure 5G was fractionated and the fraction corresponding to the 5'-dAdoH peak was dried, resuspended in 0.1% formic acid in water, and run on a Waters Acquity BEH C18 reverse phase (100 x 2.1) mm 1.7 µm column on an Agilent Infinity 1290 UPLC coupled to an Agilent 6538 Q-TOF mass spectrometer. The mobile phases were A: 0.1% formic acid in water, B: 0.1% formic acid in acetonitrile with a flow rate of 0.130 µL/min. The mass spectrometer was run in ESI mode, ion mode positive, scanning from 50-1000 *m/z* with a scan rate of 1 spectra/sec, Vcap of 3500 V, Nebulizer at 55 psig, Fragmentor voltage at 100 V, octapole RF at 500 V. The 5'-dAdoH had an observed mass of 252.1 g/mol, in close agreement with the calculated mass of 251.2 g/mol and with the observed mass of 252.1 g/mol of a pure 5'-dAdoH standard also analyzed by LC-MS.

Activation of GD by GD-AE

In the glove box, 22.3 μM GD and 37.7 μM GD-AE were exchanged into assay buffer (50 mM HEPES, pH = 7.5, 100 mM KCl) using a 10 kDa MWCO Amicon spin filter to remove any glycerol from the storage buffers. They were then transferred to a clean Eppendorf tube where 889 μM Na-DT was added. GD-AE was allowed to reduce for 8 minutes before the addition of 905 μM SAM to initiate the reaction. The reaction mixture was transferred to an EPR tube and quenched by flash freezing in liquid nitrogen after 30 minutes. The sample was then analyzed by CW X-band EPR spectroscopy for glycyl radical detection. Following analysis by EPR spectroscopy, the sample was thawed anaerobically. A 20 μL aliquot of the sample was removed and quenched with ½ volume of 1 M sodium acetate, pH = 4.5 and centrifuged at 14,000 rpm for 15 minutes to remove precipitated protein. The supernatant was transferred to a clean HPLC vial and injected onto a Shimadzu LC-2060C liquid chromatograph equipped with a reversed phase column (Phenomenex Kinetex F5, 2.6 μm, 100 Å, 100 x 4.6 mm). The HPLC method was the same as used for the enzyme activity assay except a washing step was included in which after the 3 minutes at 60% B, the concentration of B was increased to 90%, held for 2 minutes and then decreased to 2% B and re-equilibrated for the next run. Detection was performed at 254 nm. 5′-dAdoH eluted at ~6 minutes and MTA at ~6.8 minutes. Analytes were verified by the method of standard addition and quantified by comparison to standard curves of authentic standards. Each HPLC trace was baseline corrected by subtracting a blank run.

Generation of GD-AE Homology Model

The amino acid sequence of *Clostridium butyricum* glycerol dehydratase activating enzyme (GD-AE) was aligned to the amino acid sequence of *Escherichia coli* pyruvate formate-lyase activating enzyme (PFL-AE) using the Muscle algorithm in Geneious and a BLOSUM

matrix (Geneious version 6.1.7, http://www.geneious.com) [37]. The resulting alignment was then manually edited. A model was generated wherein the structure of *Clostridium acidiurici* 2[4Fe-4S] ferredoxin (PDB ID 2fdn) [38] was inserted between residues 46 and 47 of the structure of PFL-AE bound to the PFL peptide (PDB ID 3cb8) [39]. The orientation of the ferredoxin domain relative to PFL-AE was chosen by aligning the endpoints of the ferredoxin domain to the insertion site on PFL-AE using PyMOL (The PyMOL Molecular Graphics System, Version 1.3 Schrödinger, LLC.). Based on the edited sequence alignment, the PFL-AE-ferredoxin fusion model was modified to the sequence of GD-AE using Foldit [40]. The sequence of the PFL peptide was modified to match the GD peptide sequence and this peptide was present throughout all subsequent modeling steps. The ferredoxin and radical SAM domains of the resulting model were then separated into two distinct chains and the rigid body relationship between the domains, as well as all torsion angles were minimized using the FastRelax application in RosettaScripts [41, 42]. Intra-molecular distance constraints were applied to prevent excessive backbone change within each domain, but no constraints were applied between the domains. The model in which the ferredoxin domain most closely associated with the radical SAM domain was recombined into a single chain and used for further modeling. The connection points between the ferredoxin domain and the radical SAM domain were remodeled using the Rosetta Remodel application [43]. Insertions and deletions in the GD-AE sequence relative to the PFL-AE sequence were also corrected at this point using Rosetta Remodel. The resulting model with the best core packing according to the RosettaHoles algorithm [42] was used in the following steps. All torsion angles within the model were

subjected to a second round of minimization using the FastRelax application in RosettaScripts and the resulting model with the best total score was used in the final step.

To generate the final GD-AE homology model, SAM and [4Fe-4S] cluster molecules were added to the model and the positions of the SAM and nearby protein side chains (Glu 158, Met 179, Arg 218, Leu 251, and Tyr 256) were modified in Coot [44] to alleviate clashes between SAM and the protein. GD-AE sequence covariance constraints from the Gremlin server [45] were used to validate inter-residue contacts throughout the homology model as well as the orientation of the ferredoxin domain relative to the radical SAM domain, although there were few pairs of co-varying residues between the ferredoxin and radical SAM domains.

Results

Purification and Characterization of GD-AE

GD-AE was expressed in *E. coli* as a 10X-His-SUMO fusion for the purposes of purification; following purification, the 10X-His-SUMO tag was removed prior to further experiments (Figure S2.1) [46]. In order to optimize iron-sulfur cluster incorporation during protein expression, this GD-AE/10x-His-SUMO fusion was co-expressed with the ISC operon from *Azotobacter vinelandii* [29]. The resulting purified GD-AE contained ~6 irons per protein monomer, less than the 12 irons per monomer expected given the one CX_3CX_2C radical SAM motif and two $CX_2CX_2CX_NC$ ferredoxin motifs present in the GD-AE sequence. Expression and purification of the GD-AE/6x-His fusion (lacking the SUMO tag, Figure S2.2) also provided protein with less than the expected 12 irons per protein. This protein was enzymatically reconstituted using CsdA, cysteine, and iron to generate protein containing 10.59 ± 0.18 irons

and 12.03 ± 0.53 sulfides per protein. Given that the ratio of iron to sulfide is close to 1:1, it is likely that all of the iron bound to GD-AE is present in iron-sulfur clusters.

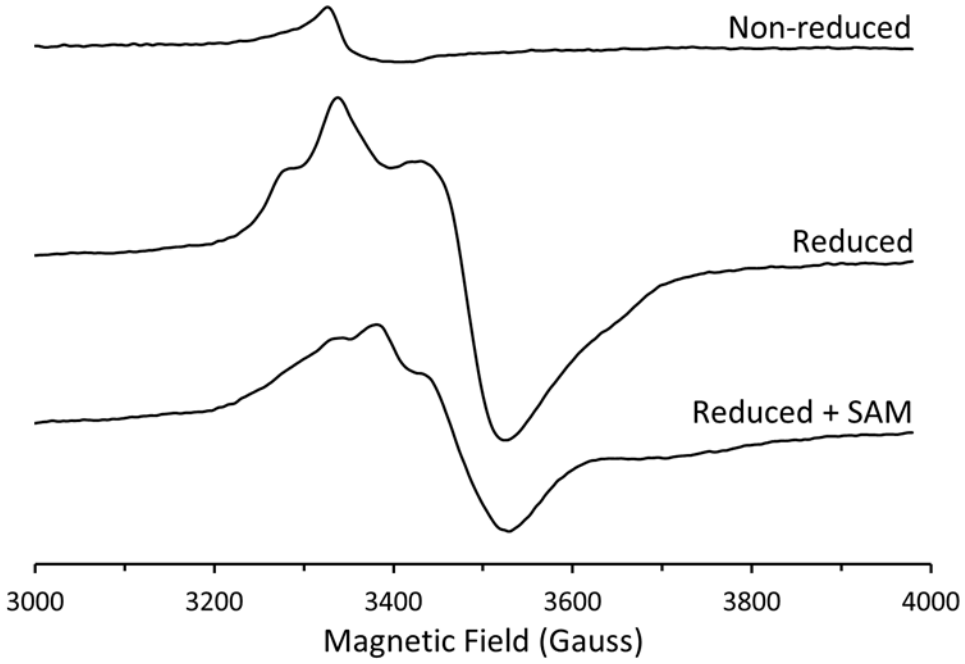


Figure 2.2. EPR spectroscopy of GD-AE. EPR samples were prepared using 6x-His-GD-AE protein (57 μM, 10.59 ± 0.18 iron atoms per protein). Top, GD-AE as-reconstituted. Middle, GD-AE reduced with dithionite. Bottom, GD-AE reduced with dithionite followed by addition of SAM. Sample components, when present, were at the following concentrations: SAM (0.90 mM) and dithionite (0.60 mM). EPR parameters: 12 K, 9.38 GHz, 1 mW, 100 kHz modulation frequency, 10 G modulation amplitude.

Samples of reconstituted GD-AE were examined by EPR spectroscopy. The reconstituted protein shows a small signal characteristic of a $[3Fe\text{-}4S]^{+}$ cluster (Figure 2.2, top). Upon reduction of the reconstituted GD-AE with sodium dithionite (DT), multiple overlapping axial or near-axial EPR signals appear that are consistent with S = ½ $[4Fe\text{-}4S]^{1+}$ clusters (Figure 2.2, middle). These multiple overlapping EPR signals are consistent with the fact that GD-AE has three cysteine motifs, with the radical SAM motif expected to bind a site-differentiated [4Fe-

4S] cluster and the two ferredoxin motifs each expected to bind a ferredoxin-type [4Fe-4S] cluster. Temperature-dependence of the EPR signals (Figures 2.3 and S2.4) shows a rapid loss of signal intensity above 12 K, with essentially no signal observed at 40 K; this behavior is consistent with the fast-relaxing properties typically associated with $[4Fe\text{-}4S]^{+}$ clusters. Examination of the power-dependence of these EPR signals (Figure S2.5) reveals behavior that is also fully consistent with their assignment to $[4Fe\text{-}4S]^{+}$ clusters.

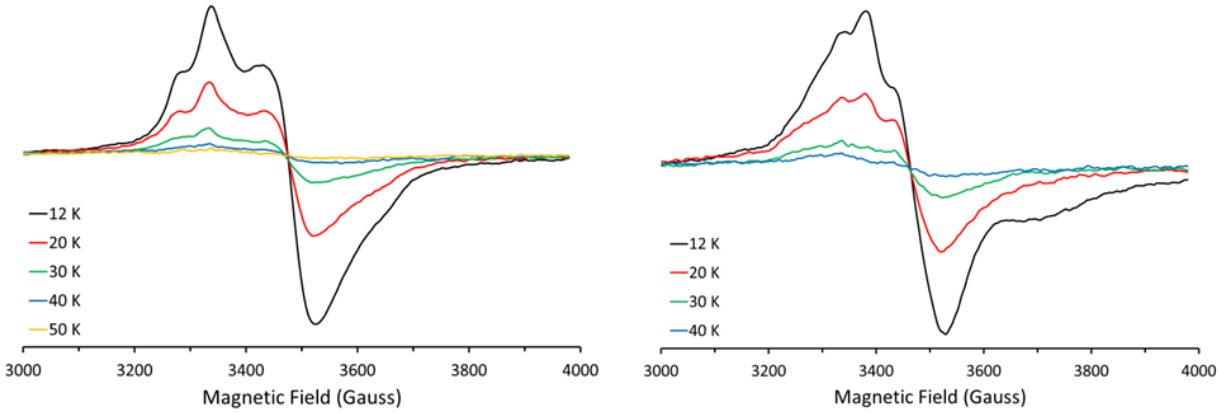


Figure 2.3. Temperature-dependent EPR of reduced GD-AE. EPR spectra of reduced GD-AE (57 μM, 10.59 ± 0.18 Fe/protein) in the absence (left) or presence (right) of SAM were recorded at the temperatures indicated. The loss of signal intensity at temperatures above 12 K is indicative of the presence of rapidly relaxing $[4Fe\text{-}4S]^{+}$ clusters. Sample components, when present, were at the following concentrations: SAM (0.90 mM) and dithionite (0.60 mM). EPR parameters: 12 K, 9.38 GHz, 1 mW, 100 kHz modulation frequency, 10 G modulation amplitude.

Addition of SAM to the DT-reduced enzyme perturbs the EPR signals, while also causing a decrease in the total spin intensity (Figure 2.2, bottom). The loss of some signal intensity upon addition of SAM to the reduced GD-AE is consistent with nonproductive reductive cleavage of SAM at the radical SAM $[4Fe\text{-}4S]^{+}$ cluster, which would cause oxidation to the EPR-silent $[4Fe\text{-}4S]^{2+}$ state. The ferredoxin clusters and any radical SAM cluster that does not get oxidized will continue to contribute to the observed EPR signal for this sample, however the EPR signal of the

radical SAM cluster is expected to be perturbed by the binding of SAM. The observed spectrum therefore remains complex as a result of multiple EPR-active clusters. The temperature relaxation (Figures 2.3 and S2.4) and the power saturation (Figure S2.4) behavior of the reduced GD-AE with SAM added are consistent with the presence of $[4Fe\text{-}4S]^{+}$ clusters.

Assays of GD-AE for SAM Cleavage

GD-AE was assayed for the formation of SAM-derived 5'-dAdoH and MTA using an HPLC-based method. For these assays, a heptamer peptide (RVA**G**YSA) corresponding to the glycine loop of GD [18] and containing the target G763 was used in place of the full GD substrate. A heptamer peptide was previously shown to substitute for the full glycyl radical enzyme substrate when assaying the glycyl radical activating enzyme PFL-AE [47]. Our results in Figure 2.4 demonstrate that the same is true for GD-AE: the corresponding GD heptamer peptide used herein acts as a substrate in stimulating reductive SAM cleavage by GD-AE. The complete reaction (Figure 2.4G) shows the production of a significant amount of 5'-dAdoH when GD-AE, SAM, 7-mer peptide, and dithionite are incubated for 60 minutes. A small peak corresponding to MTA can also be seen for this reaction, however its peak height is similar to the MTA peaks observed for reactions lacking GD peptide (2.4F), lacking GD-AE (2.4E), and lacking both GD-AE and GD peptide (2.4D). We note that the SAM used in the assays (prepared in-house using published protocols) [35] does contain a small amount of MTA contamination, a degradation product of SAM (Figure 2.4C). The presence of a comparably small MTA peak for all these samples (including SAM alone), in contrast to the dramatically increased 5'-dAdoH peak for the complete reaction relative to all others, indicates that the GD-AE catalyzed reaction involves cleavage of the S-C(5') bond of SAM, contrary to a previously published report [20].

This GD-AE catalyzed reductive homolytic cleavage of the S-C(5') bond of SAM is presumably accompanied by 5'-dAdo• mediated abstraction of H• from the target glycyl residue of the peptide substrate to generate 5'-dAdoH and Gly•; the resulting glycyl radical is not observed, likely due to rapid solvent quenching of the exposed peptide backbone radical.

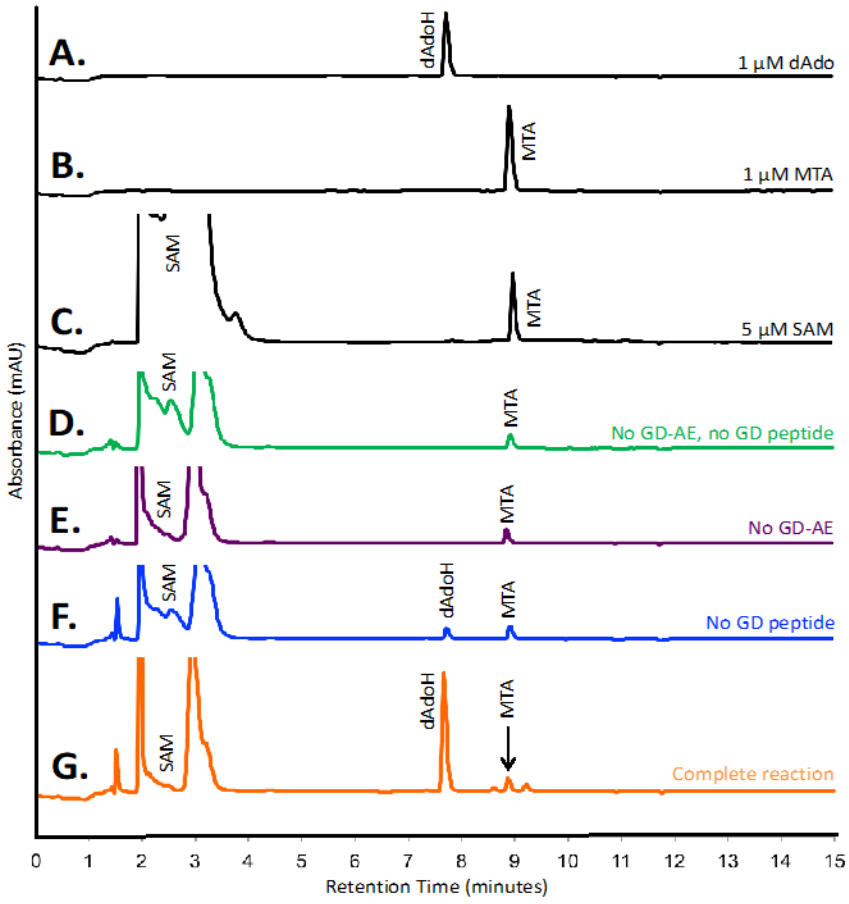


Figure 2.4. HPLC based endpoint assays of GD-AE. Chromatograms A – C are standards, while chromatograms D – G are 120 minute reactions as indicated. A. 1 µM 5'-dAdoH. B. 1 µM MTA. C. 5 mM SAM. D. Control reaction containing SAM (2.0 mM) and dithionite (2.0 mM) but lacking GD-AE and GD peptide. E. Control reaction containing GD peptide (3.4 mM), SAM (2.0 mM), and dithionite (2.0 mM), but lacking GD-AE. F. Reaction of GD-AE (16 µM), SAM (2.0 mM), and dithionite (2.0 mM), in the absence of GD peptide, to probe uncoupled SAM cleavage. G. Complete reaction containing GD-AE (16 µM), GD peptide (3.4 mM), SAM (2.0 mM), and reductant (2.0 mM). The 5'dAdoH peak from HPLC was collected and analyzed by LC-MS, confirming the identity of the 5'-dAdoH.

We also evaluated the rates of change of MTA and 5'-dAdoH concentrations over a 2-hour assay, and these results further support our conclusion that GD-AE catalyzes a conventional SAM reductive cleavage in which the S-C(5') bond is broken (Figure 2.5). We observed that GD-AE in the absence of the GD peptide catalyzes a slow nonproductive cleavage of SAM (0.0098 ± 0.002 moles of dAdo/mole of GD-AE/minute), consistent with the uncoupled SAM cleavage observed for many other radical SAM enzymes [1]. In the presence of the GD peptide, the rate of 5'-dAdoH production by GD-AE increases to 0.16 ± 0.02 moles of 5'-dAdoH/mole of GD-AE/minute, consistent with observations for other radical SAM enzymes [1], where SAM cleavage rates are significantly increased in the presence of substrate (Figure 2.5A). In contrast, although a small increase in MTA is observed over the course of the 2-hour assay, the same increase is observed in all samples, regardless of the presence or absence of GD peptide and GD-AE (Figure 2.5B).

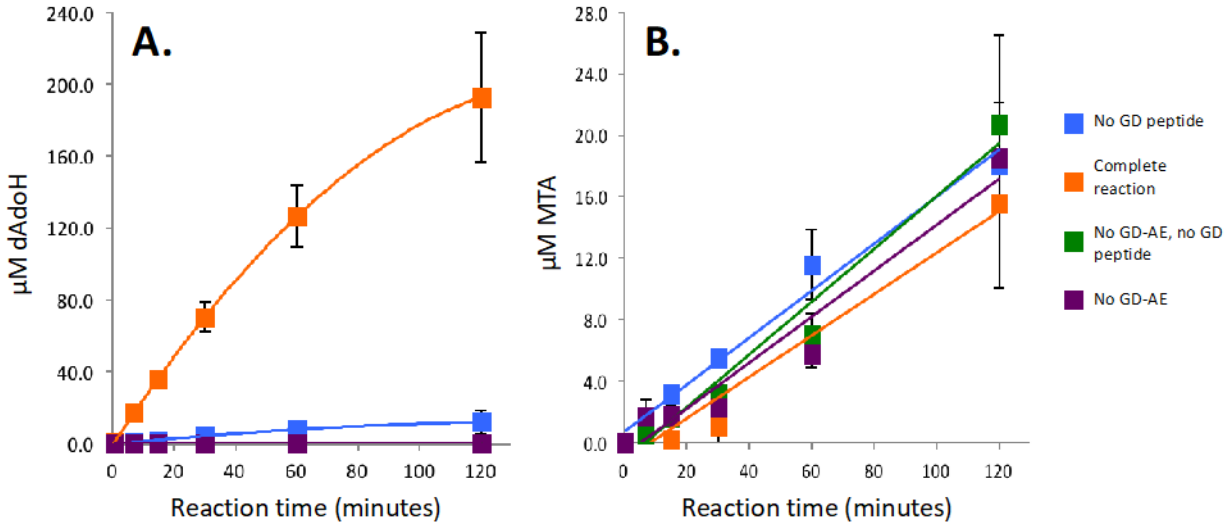


Figure 2.5. Kinetics of 5'-dAdoH and MTA production by GD-AE. A. 5'-dAdoH production as a function of time. B. MTA production as a function of time. Assays are: control containing SAM (2.0 mM) in buffer (green); GD peptide (3.4 mM) and SAM (2.0 mM) in buffer (purple); GD-AE (16 µM) and SAM (2.0 mM) in buffer (blue); complete reaction containing GD-AE (16 µM),

SAM (2.0 mM), and GD peptide (3.4 mM) (orange). All assays contained 2.0 mM dithionite. Data shown are the averages of at least 5 independent assays per condition.

Activation of GD by GD-AE

In order to examine the reactivity of GD-AE with its native substrate GD, the GD-AE sample used for EPR spectroscopic characterization (Figure 2.2) was thawed and mixed with purified GD (final concentrations were 38 μM GD-AE and 22 μM GD). This mixture was exchanged into assay buffer, then SAM and dithionite were added, and the sample was frozen for EPR spectroscopy after 30 min. The EPR spectrum recorded at 75 K (Figure 2.6) shows the presence of a doublet signal as expected for a glycyl radical, demonstrating the activation of the GD by GD-AE. This sample was then analyzed for production of 5'-dAdoH and MTA, to determine whether turnover of the native substrate GD provided the same SAM cleavage products as observed during turnover of the GD peptide. As can be seen in Figure 2.7, HPLC reveals the presence of 5'-dAdoH in the GD/GD-AE/SAM EPR sample; this 5'-dAdoH peak is absent in an identical sample prepared without GD-AE. MTA, a common product of SAM degradation, is also observed in both samples but is unchanged in the sample containing GD-AE. Together, these results substantiate that GD- AE cleaves the S-C5' bond of SAM to form 5'-dAdoH during the activation of GD, as it does when using the 7-mer GD peptide as a model substrate.

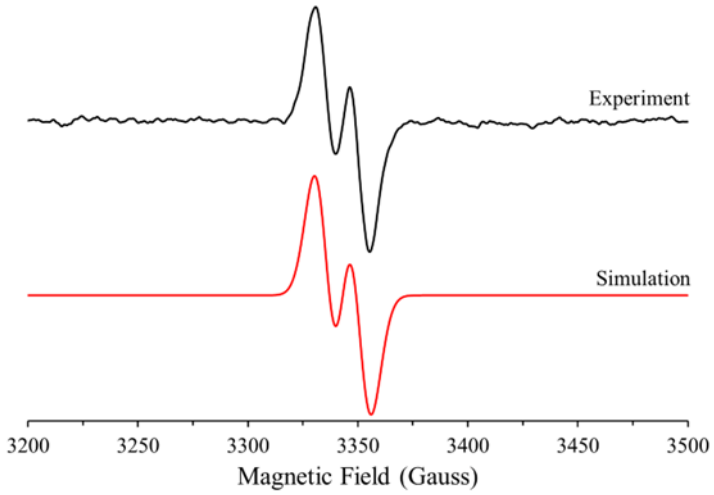


Figure 2.6. EPR spectroscopy of activated GD. EPR sample (black) contained 38 µM 6x-His-GD-AE, 22 µM GD, 0.9 mM SAM, and 0.89 mM DT. The signal was simulated (red) using g = 2.0045, 2.0035, 2.0025 and A = 40 MHz. EPR parameters: 75 K, 9.38 GHz, 0.21 mW, 100 kHz modulation frequency, 2 G modulation amplitude.

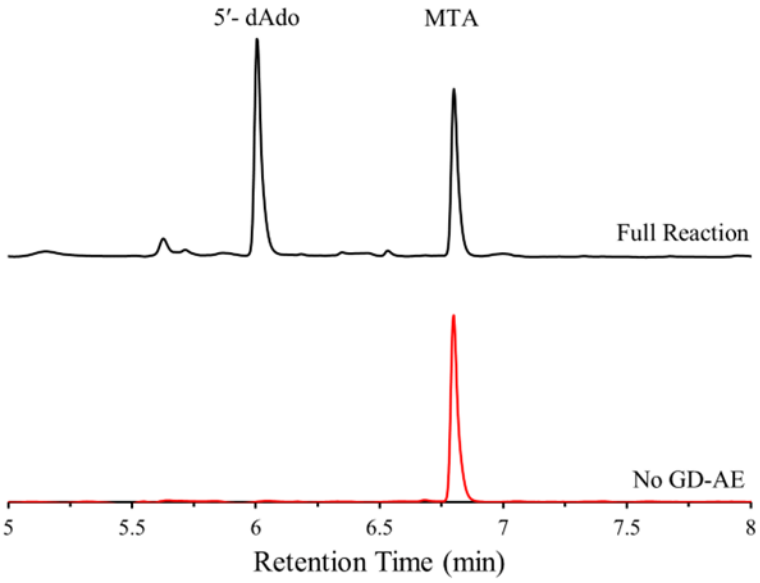


Figure 2.7. HPLC Chromatogram of GD Activation Reaction. The HPLC chromatogram of the full reaction containing GD, GD-AE, SAM, and DT (top) shows a 5'-dAdoH peak that is absent in the sample lacking GD-AE. MTA, a common decomposition product of SAM, is observed with equal intensity in both samples, indicating it is not enzymatically formed by GD-AE.

Discussion

Radical SAM enzymes use a site-differentiated [4Fe-4S] cluster to initiate the regioselective reductive cleavage of SAM to generate an organic radical intermediate. In these enzymes, SAM coordinates the unique iron through its amino and carboxylate moieties [7], with the sulfonium sulfur sitting sufficiently close to the cluster to exhibit orbital overlap [6]. In most of the radical SAM enzymes characterized to date, it is the S-C(5') bond of SAM that is specifically cleaved, giving rise to methionine and a 5'-deoxyadenosyl radical intermediate, the latter of which converts to 5'-dAdoH upon H-atom abstraction from substrate [1]. Recent insights into the origins of regioselectivity in the reductive cleavage of SAM in radical SAM enzymes point to the Jahn-Teller effect associated with the one electron reduced sulfonium center of SAM coupled to active-site forces as the key determinants of S-C bond cleavage regioselectivity [12].

The previous observation of alternate SAM cleavage products for GD-AE was surprising given the significant sequence homology to other well-characterized glycyl radical enzyme activating enzymes [19], notably PFL-AE [48], 4HPD-AE [49] and aRNR-AE [50], which have been shown to produce the standard 5'-dAdoH product of reductive SAM cleavage. Because there is no X-ray crystal structure of GD-AE available, we generated a homology model to provide structural insight. The homology model (Figure 2.8) utilized PFL-AE (PDB ID 3cb8) [39, 51] to model the radical SAM domain of GD-AE, which contains the active site and catalytic iron-sulfur cluster, and a ferredoxin (PDB ID 2fdn) [38] as a template for the ferredoxin domain insertion of GD-AE.

The homology model supports a close structural homology between the radical SAM domain of GD-AE and PFL-AE. The $CX_3CX\phi C$ [4Fe-4S] cluster-binding motif in GD-AE bears

a tryptophan rather than tyrosine at the ϕ position, a substitution occasionally observed in radical SAM enzymes [52, 53]. In addition, GD-AE has tyrosine and histidine residues in place of the two histidine residues in PFL-AE that pack onto the face of the adenine ring. Together, these differences could modestly perturb the position of the adenine ring of SAM in GD-AE relative to that in PFL-AE. However, GD-AE retains other key active site residues, including Asp181 and Lys183 in the same structural positions as the Asp129 and Lys131 in PFL-AE, which interact with the ribose hydroxyl groups and methionine carboxylate of SAM. Overall, the homology model is consistent with an active site architecture and a SAM binding configuration in GD-AE that is similar to that observed in PFL-AE (Figure 2.8).

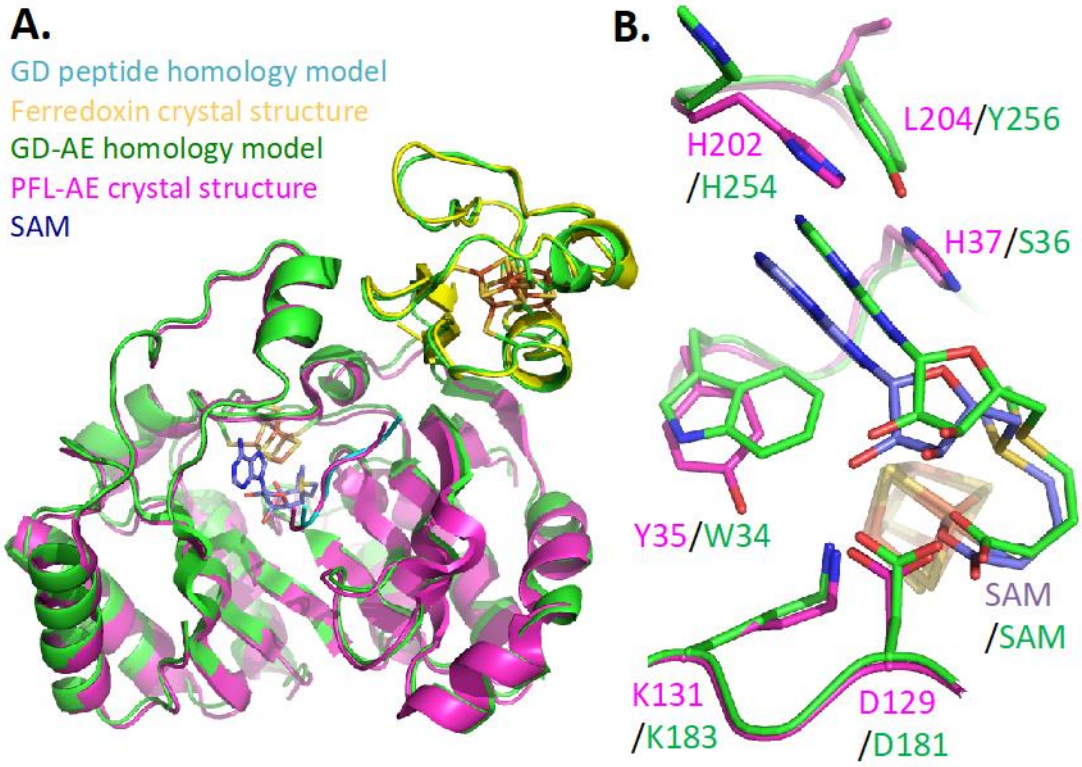


Figure 2.8. Homology model of GD-AE. A. Model of GD-AE (green cartoon) bound to its substrate peptide from GD (cyan cartoon). The crystal structures of the templates used to generate the homology models are superimposed (*E. coli* PFL-AE, PDB ID 3cb8, magenta

cartoon, for the radical SAM domain and *Clostridium acidiurici* 2[4Fe-4S] ferredoxin, PDB ID 2fdn, yellow cartoon, for the N-terminal ferredoxin domain insertion). The [4Fe-4S] clusters, ligating cysteines, and SAM molecule are shown as sticks. B. Close up view of the active site of the GD-AE homology model (green sticks) superimposed onto the structure of PFL-AE (magenta sticks) bound to SAM (purple sticks).

In order to probe the active-site iron-sulfur cluster and catalytic activity of GD-AE, we expressed and purified the protein and carried out EPR spectroscopic studies. The reconstituted protein exhibits a small signal attributed to $[3Fe\text{-}4S]^{+}$ clusters, a common observation for radical SAM enzymes due to the labile unique iron of the [4Fe-4S] cluster [1]. Upon reduction with DT, the $[3Fe\text{-}4S]^{+}$ signal disappears and signals characteristic of $[4Fe\text{-}4S]^{+}$ clusters appear (Figure 2.2). Addition of SAM leads to perturbations of this signal and some loss of signal intensity (Figure 2.2); this is consistent with the binding of SAM to the unique iron of the radical SAM [4Fe-4S] cluster, in addition to some nonproductive SAM cleavage accompanied by cluster oxidation to the EPR-silent $[4Fe\text{-}4S]^{2+}$ state. These spectroscopic observations are all in line with those reported for other radical SAM enzymes.

With the homology model and spectroscopic properties pointing to nothing unusual about the active-site of GD-AE, we decided to re-investigate the reported SAM cleavage activity [20]. As shown in Figures 2.4 and 2.5, we found that GD-AE, like other characterized radical SAM enzymes, catalyzes nonproductive SAM cleavage (SAM cleavage in the absence of substrate) at a low rate to produce 5'-dAdoH. The rate of GD-AE catalyzed SAM cleavage is significantly increased in the presence of the 7-mer peptide substrate corresponding to the glycyl radical loop of GD. MTA was also detected in these assays, however it was present in the SAM stock used in the assay and did not increase in the presence of GD-AE. In fact, as shown in Figure 2.5, the small increase in MTA over time was observed in all samples, regardless of the presence or

absence of GD-AE. In contrast, substantial 5'-dAdoH was formed only in the complete reaction containing both GD-AE and the substrate GD peptide; in this case, the 5'-dAdoH increased over time at a rate consistent with the range of rates observed for other radical SAM enzymes [1].

In order to probe the identity of the SAM cleavage products generated by GD-AE when acting on the native substrate GD, we combined GD-AE, GD, SAM, and reductant and then used EPR spectroscopy to look for generation of the glycyl radical on GD; Figure 2.6 clearly shows a glycyl radical, with its characteristic doublet EPR signal, is generated on GD. This sample was then subjected to HPLC analysis, revealing that 5'-dAdoH, but not MTA, was generated during GD-AE catalyzed activation of GD (Figure 2.7). MTA, a common SAM degradation product, is observed in the control samples lacking GD-AE in Figures 2.4 and 2.7; we have observed that the amount of MTA in a solution of SAM is generally small but can increase with time as the SAM sits at ambient temperature. The prior observation of MTA during the GD-AE catalyzed reaction [20], therefore, may have resulted simply from a small amount of MTA in their SAM stock solution. Note that this prior study provided only a single 15 s time point and did not demonstrate the time-dependent formation of MTA [20], as we do here for the formation of 5'-dAdoH.

Together, our results demonstrate that GD-AE catalyzes a reaction employing the typical S-C(5') bond cleavage observed for other radical SAM enzymes, as opposed to the S-C(γ) bond cleavage previously reported [20]. Thus as of this writing, all characterized canonical radical SAM enzymes initiate radical catalysis via the same initial S-C(5′) bond cleavage to generate the 5'-deoxyadenosyl radical intermediate. While Dph2 performs radical SAM-like chemistry via cleavage of the S-C(γ) bond of SAM [23], it is not a member of the canonical superfamily given

the absence of the key conserved sequence and structural features [23, 52]. Radical SAM superfamily members therefore, though remarkably diverse in the chemistry they catalyze, appear to have in common initial mechanistic steps, including the generation of the 5′-deoxyadenosyl radical intermediate from S-C(5′) bond cleavage of SAM.

Supplemental Material

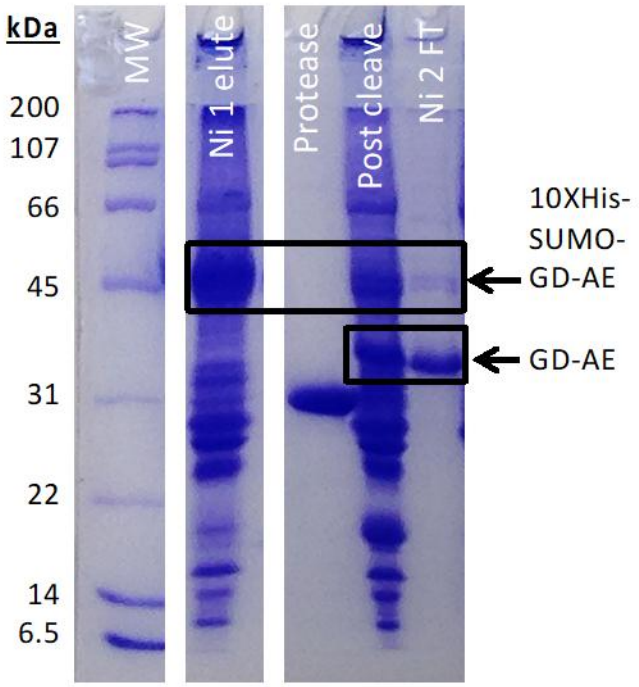


Figure S2.1. Purification of GD-AE using 10x-His-SUMO tag. Lane 1: Molecular weight marker. Lane 2. Elution of 10x-His-SUMO-GD-AE from 1st nickel-NTA column. Lane 3. SUMO protease. Lane 4. GD-AE after treatment with SUMO protease. Lane 5. GD-AE-containing flow through of 2nd nickel NTA column used to capture the His-tagged SUMO protease and 10x-His-SUMO tag.

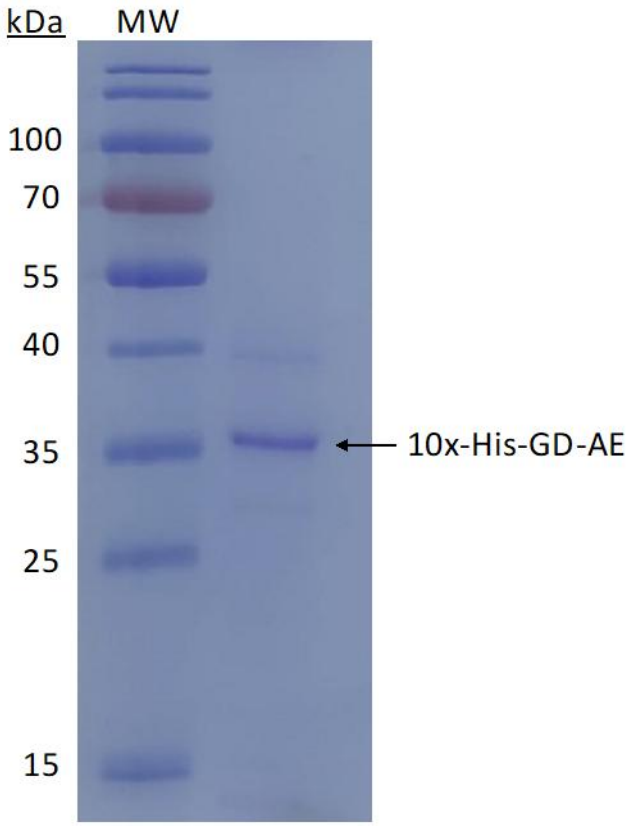


Figure S2.2. Purification of 6x-His-GD-AE. Lane 1: Molecular weight marker. Lane 2. Purified 6x-His-GD-AE.

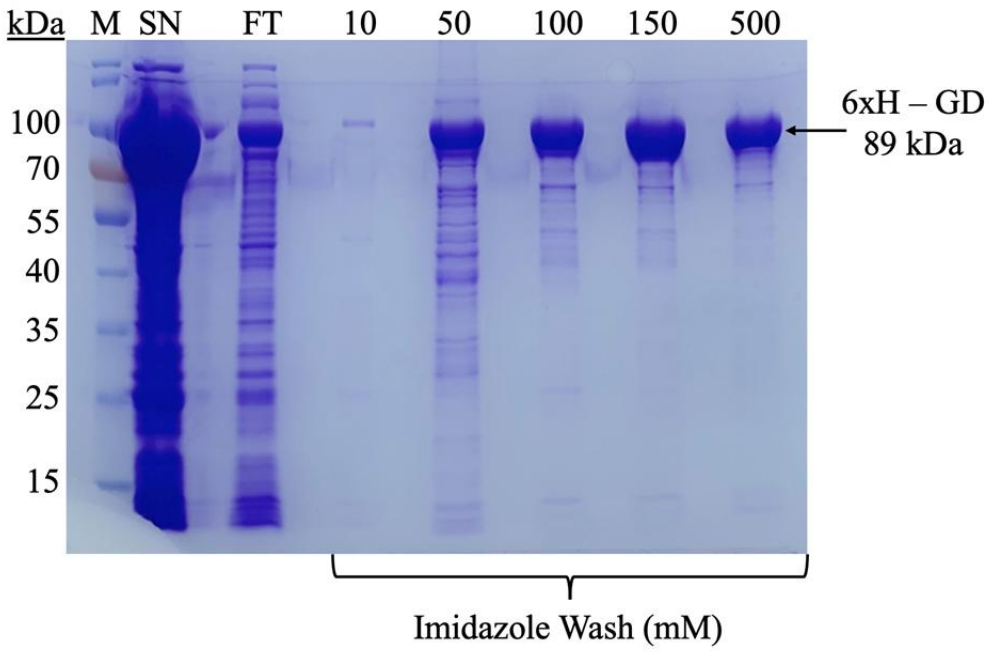


Figure S2.3. Purification of 6x-His-GD. M: Molecular weight marker. SN: Supernatant of cell lysis. FT: Flow-through during loading column. 10, 50, 100, 150, 500: Elution of the 6x-His-GD using a step gradient with the indicated concentrations of imidazole (in mM).

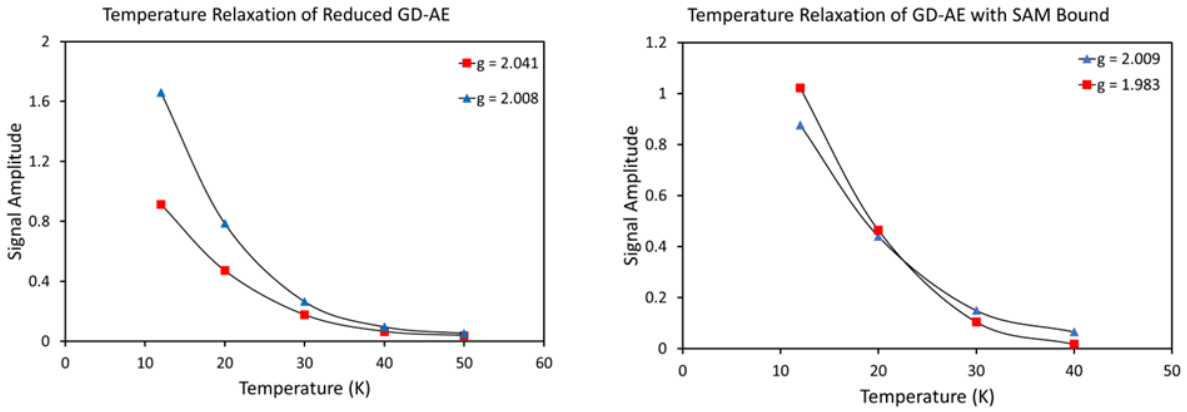


Figure S2.4. Plots of signal amplitude vs. temperature for the EPR spectra shown in Figure 3. EPR spectra were recorded at the temperatures indicated. The signal intensity at two different g-values is plotted for the reduced GD-AE (57 μM) in the absence (left) and presence (right) of SAM. Sample components, when present, were at the following concentrations: SAM (0.90 mM), and dithionite (0.60 mM). EPR parameters: 12 K, 9.38 GHz, 1 mW, 100 kHz modulation frequency, 10 G modulation amplitude.

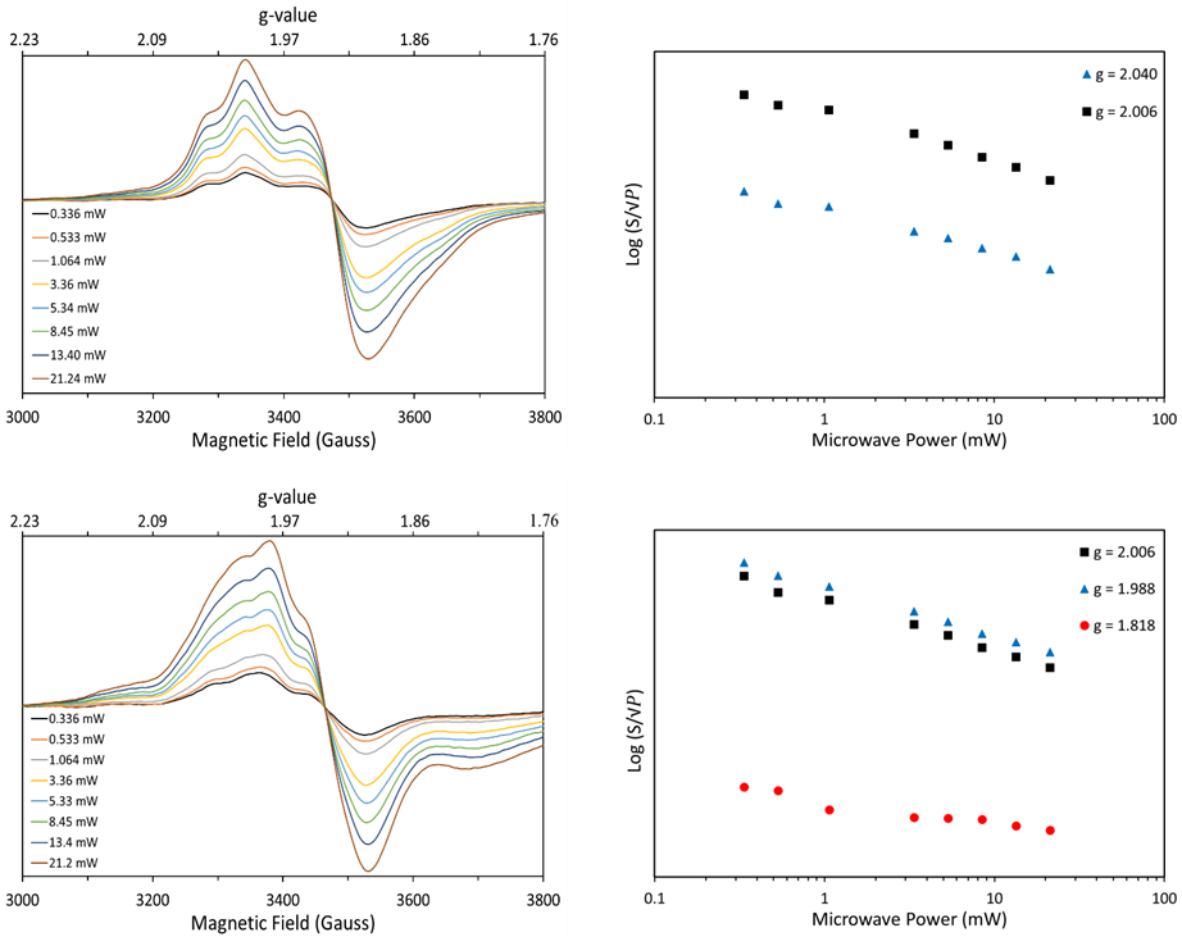


Figure S2.5. EPR power saturation studies of reconstituted, reduced GD-AE with and without SAM. A) Plot of signal intensity against magnetic field (Gauss) at 12 K for dithionite reduced GD-AE. B) Power saturation curves for the two distinct features in A using peak height as signal intensity. C) Plot of signal intensity against magnetic field (Gauss) at 12 K for dithionite reduced GD-AE in the presence of SAM. D) Power saturation curves for three features present in C using peak height as signal intensity. The power saturation curves for GD-AE in the absence or presence of SAM do not saturate readily at powers greater than 10 mW. These data are consistent with the presence of the [4Fe-4S] radical SAM cluster as well as the 2 [4Fe-4S] ferredoxin domain predicted by the conserved binding motif. EPR parameters are: 10 gauss modulation amplitude, 100 kHz modulation frequency, and microwave frequency of 9.38 GHz.

References

1. Broderick, J. B.; Duffus, B. R.; Duschene, K. S.; Shepard, E. M., Radical *S*-Adenosylmethionine Enzymes. *Chem. Rev*. **2014**, *114*, 4229-4317.

2. Frey, P. A.; Hegeman, A. D.; Ruzicka, F. J., The radical SAM superfamily. *Crit. Rev. Biochem. Mol. Biol.* **2008**, *43* (1), 63-88.

3. Landgraf, B. J.; McCarthy, E. L.; Booker, S. J., Radical *S*-adenosylmethionine enzymes in human health and disease. *Annu. Rev. Biochem*. **2016**, *85*, 485-514.

4. Nicolet, Y., Structure-function relationships of radical of radical SAM enzymes. *Nat. Catal.* **2020**, *3*, 337-2020.

5. Krebs, C.; Broderick, W. E.; Henshaw, T. F.; Broderick, J. B.; Huynh, B. H., Coordination of adenosylmethionine to a unique iron site of the [4Fe-4S] of pyruvate formate-lyase activating enzyme: A Mössbauer spectroscopic study. *J. Am. Chem. Soc*. **2002**, *124* (6), 912-913.

6. Walsby, C. J.; Hong, W.; Broderick, W. E.; Cheek, J.; Ortillo, D.; Broderick, J. B.; Hoffman, B. M., Electron-nuclear double resonance spectroscopic evidence that *S*-adenosylmethionine binds in contact with the catalytically active $[4Fe\text{-}4S]^{+}$ cluster of pyruvate formate-lyase activating enzyme. *J. Am. Chem. Soc*. **2002**, *124* (12), 3143-3151.

7. Walsby, C. J.; Ortillo, D.; Broderick, W. E.; Broderick, J. B.; Hoffman, B. M., An anchoring role for FeS Clusters: Chelation of the amino acid moiety of *S*-adenosylmethionine to the unique iron site of the [4Fe-4S] cluster of pyruvate formate-lyase activating enzyme. *J. Am. Chem. Soc*. **2002**, *124* (38), 11270-11271.

8. Broderick, W. E.; Broderick, J. B., Radical SAM enzymes: surprises along the path to understanding mechanism. *J. Biol. Inorg. Chem*. **2019**, *24* (6), 769-776.

9. Broderick, W. E.; Hoffman, B. M.; Broderick, J. B., Mechanism of Radical Initiation in the Radical *S*-Adenosyl-L-methionine Superfamily. *Acc. Chem. Res*. **2018**, *51* (11), 2611-2619.

10. Yang, H.; McDaniel, E. C.; Impano, S.; Byer, A. S.; Jodts, R. J.; Yokoyama, K.; Broderick, W. E.; Broderick, J. B.; Hoffman, B. M., The elusive 5′-deoxyadenosyl radical: Captured and Characterized by Electron Paramagnetic Resonance and Electron Nuclear Double Resonance Spectroscopies. *J. Am. Chem. Soc*. **2019**, *141* (30), 12139-12146.

11. Sayler, R. I.; Stich, T. A.; Joshi, S.; Cooper, N.; Shaw, J. T.; Begley, T. P.; Tantillo, D. J.; Britt, R. D., Trapping and electron paramagnetic resonance characterization of the 5′-dAdo• radical in a radical *S*-adenosylmethionine enzyme reaction with a non-native substrate. *ACS Cent. Sci*. **2019**, *5* (11), 1777-1785.

12. Impano, S.; Yang, H.; Jodts, R. J.; Pagnier, A.; Swimley, R.; McDaniel, E. C.; Shepard, E. M.; Broderick, W. E.; Broderick, J. B.; Hoffman, B. M., Active-Site Controlled, Jahn-Teller Enabled Regioselectivity in Reductive S-C Bond Cleavage of *S*-

Adenosylmethionine (SAM) in Radical-SAM Enzymes. *J. Am .Chem. Soc*. **2021**, *143* (1), 335-348.

13. Horitani, M.; Shisler, K. A.; Broderick, W. E.; Hutcheson, R. U.; Duschene, K. S.; Marts, A. R.; Hoffman, B. M.; Broderick, J. B., Radical SAM catalysis via an organometallic intermediate with an Fe-[5'-C]-deoxyadenosyl bond. *Science* **2016**, *352* (6287), 822-825.

14. Byer, A. S.; Yang, H.; McDaniel, E. C.; Kathiresan, V.; impano, S.; Pagnier, A.; Watts, H.; Denler, C.; Vagstad, A. L.; Piel, J.; Duschene, K. S.; Shepard, E. M.; Shields, T. P.; Scott, L. G.; Lilla, E. A.; Yokoyama, K.; Broderick, W. E.; Hoffman, B. M.; Broderick, J. B., Paradigm shift for radical *S*-adenosyl-L-methionine reactions: The organometallic intermediate Ω is central to catalysis. *J. Am. Chem. Soc*. **2018**, *140* (28), 8634-8638.

15. Horitani, M.; Byer, A. S.; Shisler, K. A.; Chandra, T.; Broderick, J. B.; Hoffman, B. M., Why Nature Uses Radical SAM Enzymes so Widely: Electron Nuclear Double Resonance Studies of Lysine 2,3-Aminomutase Show the 5'-dAdo• "Free Radical" is Never Free. *J. Am. Chem. Soc*. **2015**, *137*, 7111-7121.

16. Pagnier, A.; Yang, H.; Jodts, R. J.; James, C. D.; Shepard, E. M.; Impano, S.; Broderick, W. E.; Hoffman, B. M.; Broderick, J. B., Radical SAM enzyme spore photoproduct lyase: Properties of the Ω organometallic intermediate and identification of stable protein radicals formed during substrate-free turnover. *J. Am .Chem. Soc*. **2020**, *142* (43), 18652-18660.

17. Raynaud, C.; Sarcabal, P.; Meynial-Salles, I.; Croux, C.; Soucaille, P., Molecular characterization of the 1,3-propanediol (1,3-PD) operon of *Clostridium butyricum*. *Proc. Natl. Acad. Sci. U.S.A.* **2003**, *100* (9), 5010-5015.

18. O'Brien, J. R.; Raynaud, C.; Croux, C.; Girbal, L.; Soucaille, P.; Lanzilotta, W. N., Insight into the mechanism of the B_{12}-independent glycerol dehydratase from Clostridium butyricum: Preliminary biochemical and structural characterization. *Biochemistry* **2004**, *43* (16), 4635-4645.

19. Shisler, K. A.; Broderick, J. B., Glycyl Radical Activating Enzymes: Structure, Mechanism, and Substrate Interactions. *Archives of biochemistry and biophysics* **2014**, *546*, 64-71.

20. Demick, J. M.; Lanzilotta, W. N., Radical SAM activation of the B_{12}-independent glycerol dehydratase results in formation of 5'-deoxy-5'-(methylthio)adenosine and not 5'-deoxyadenosine. *Biochemistry* **2011**, *50*, 440-442.

21. Yang, H.; Impano, S.; Shepard, E. M.; James, C. D.; Broderick, W. E.; Broderick, J. B.; Hoffman, B. M., Photoinduced electron transfer in a radical SAM enzyme generates

an *S*-adenosylmethionine derived methyl radical. *J. Am. Chem. Soc*. **2019**, *141* (40), 16117-16124.

22. Impano, S.; Yang, H.; Shepard, E. M.; Swimley, R.; Pagnier, A.; Broderick, W. E.; Hoffman, B. M.; Broderick, J. B., *S*-Adenosyl-L-ethionine is a catalytically competent analog of *S*-adenosyl-L-methionine (SAM) in the radical SAM enzyme HydG. *Angew. Chem. Int. Ed.* **2021**, *60*, 4666-4672.

23. Zhang, Y.; Zhu, X.; Torelli, A. T.; Lee, M.; Dzikovski, B.; Koralewski, R. M.; Wang, E.; Freed, J.; Krebs, C.; Ealick, S. E.; Lin, H., Diphthamide biosynthesis requires an organic radical generated by an iron-sulphur enzyme. *Nature* **2010**, *465*, 891-896.

24. Holliday, G. L.; Akiva, E.; Meng, E. C.; Brown, S. D.; Calhoun, S.; Pieper, U.; Sali, A.; Booker, S. J.; Babbitt, P. C., Atlas of the radical SAM superfamily: Divergent evolution of function using a "Plug and Play" domain. *Methods Enzymol*. **2018**, *606*, 1-71.

25. Dong, M.; Horitani, M.; Dzikovski, B.; Pandelia, M.-E.; Krebs, C.; Freed, J. H.; Hoffman, B. M.; Lin, H., Organometallic complex formed by an unconventional radical S-adenosylmethionine enzyme. *J. Am. Chem. Soc*. **2016**, *138*, 9755-9758.

26. Dong, M.; Horitani, M.; Dzikovski, B.; Freed, J. H.; Ealick, S. E.; Hoffman, B. M.; Lin, H., Substrate-dependent cleavage site selection by unconventional radical *S*-adenosylmethionine enzymes in diphthamide biosynthesis. *J. Am. Chem. Soc*. **2017**, *139*, 5680-5683.

27. Dong, M.; Kathiresan, V.; Fenwick, M. K.; Torelli, A. T.; Zhang, Y.; Caranto, J.; Dzikovski, B.; Sharma, A.; Lancaster, K. M.; Freed, J. H.; Ealick, S. E.; Hoffman, B. M.; Lin, H., Organometallic and radical intermediates reveal mechanism of diphthamide biosynthesis. *Science* **2018**, *359* (6381), 1247-1250.

28. Hoover, D., M.; Lubkowski, J., DNAWorks: an automated method for designing oligonucleotides for PCR-based gene synthesis. *Nucl. Acids Res.* **2002**, *30* (10), e43.

29. Zheng, L.; Cash, V. L.; Flint, D. H.; Dean, D. R., Assembly of Iron-Sulfur Clusters. Identification of an iscSUA-hscBA-fds gene cluster from *Azotobacter vinelandii*. *J. Biol. Chem.* **1998**, *273* (21), 13264-13272.

30. Dong, M.; Su, X.; Dzikovski, B.; Dando, E. E.; Zhu, X.; Du, J.; Freed, J. H.; Lin, H., Dph3 is an electron donor for Dph1-Dph2 in the first step of eukaryotic diphthamide biosynthesis. *J. Am. Chem. Soc*. **2014**, *136* (5), 1754-1757.

31. Bradford, M. M., A rapid and sensitive method for the quantitation of microgram quantities of protein utilizing the principle of protein-dye binding. *Anal. Biochem*. **1976**, *72*, 248-254.

32. Barr, I.; Latham, J. A.; Iavarone, A. T.; Chantarojsiri, T.; Hwang, J. D.; Klinman, J. P., Demonstration that the radical *S*-adenosylmethionine (SAM) enzyme PqqE Catalyzes de Novo carbon-carbon cross-linking within a peptide substrate PqqA in the presence of the peptide chaperone PqqD. *J. Biol. Chem*. **2016**, *291* (17), 8877-8884.

33. Németh, B.; Land, H.; Magnuson, A.; Hofer, A.; Berggren, G., The maturase HydF enables [FeFe] hydrogenase assembly via transient, cofactor-dependent interactions. *J. Biol. Chem*. **2020**, *295* (33), 11891-11901.

34. Broderick, J. B.; Henshaw, T. F.; Cheek, J.; Wojtuszewski, K.; Smith, S. R.; Trojan, M. R.; McGhan, R. M.; Kopf, A.; Kibbey, M.; Broderick, W. E., Pyruvate formate-lyase activating enzyme: strictly anaerobic isolation yields active enzyme containing a [3Fe-4S]$^{+}$ cluster. *Biochem. Biophys. Res. Comm*. **2000**, *269*, 451-456.

35. Byer, A. S.; McDaniel, E. C.; impano, S.; Broderick, W. E.; Broderick, J. B., Mechanistic Studies of Radical SAM Enzymes: Pyruvate Formate-Lyase Activating Enzyme and Lysine 2,3-Aminomutase Case Studies. *Methods Enzymol*. **2018**, *606*, 269-318.

36. Stoll, S.; Schweiger, A., EasySpin, a comprehensive software package for spectral simulation and analysis in EPR. *J. Magn. Res*. **2006**, *178* (1), 42-55.

37. Kearse, M.; Moir, R.; Wilson, A.; Stones-Havas, S.; Cheung, M.; Sturrock, S.; Buxton, S.; Cooper, A.; Markowitz, S.; Duran, C.; Thierer, T.; Ashton, B.; Meintjes, P.; Drummond, A., Geneious Basic: An integrated and extendable desktop software platform for the organization and analysis of sequence data. *Bioinformatics* **2012**, *28* (12), 1647-1649.

38. Dauter, Z.; Wilson, K. S.; Sieker, L. C.; Meyer, J.; Moulis, J.-M., Atomic resolution (0.94Å) structure of *Clostridium acidurici* ferredoxin. Detailed geometry of [4Fe-4S] clusters in a protein. *Biochemistry* **1997**, *36* (51), 16065-16073.

39. Vey, J. L.; Yang, J.; Li, M.; Broderick, W. E.; Broderick, J. B.; Drennan, C. L., Structural basis for glycyl radical formation by pyruvate formate-lyase activating enzyme. *Proc. Natl. Acad. Sci. U.S.A*. **2008**, *105* (42), 16137-16141.

40. Cooper, S.; Khatib, F.; Treuille, A.; Barbero, J.; Lee, J.; Beenen, M.; Leaver-Fay, A.; Baker, D.; Popovic, Z.; Players, F., Predicting protein structures with a multiplayer online game. *Nature* **2010**, *466*, 756-760.

41. Fleishman, S. J.; Leaver-Fay, A.; Corn, J. E.; Strauch, E.-M.; Khare, S. D.; Koga, N.; Ashworth, J.; Murphy, P.; Richter, F.; Lemmon, G.; Meiler, J.; Baker, D., RosettaScripts: A scripting language interface to the Rosetta macromolecular modeling suite. *PLoS ONE* **2011**, *6* (6), e20161.

42. Leaver-Fay, A.; Tyka, M.; Lewis, S. M.; Lange, O. F.; Thompson, J.; Jacak, R.; Kaufman, K.; Renfrew, P. D.; Smith, C. A.; Sheffler, W.; Davis, I. W.; Cooper, S.; Treuille, A.; Mandell, D. J.; Richter, F.; Ban, Y.-E. A.; Fleishman, S. J.; Corn, J. E.; Kim, D. E.; Lyskov, S.; Berrondo, M.; Mentzer, S.; Popovic, Z.; Havranek, J. J.; Karanicolas, J.; Das, R.; Meiler, J.; Kortemme, T.; Gray, J. J.; Kuhlman, B.; Baker, D.; Bradley, P., Rosetta3: An object-oriented software suite for the simulation and design of macromolecules. *Methods Enzymol*. **2011**, *487*, 545-547.

43. Huang, P.-S.; Ban, Y.-E. A.; Richter, F.; Andre, I.; Vernon, R.; Schief, W. R.; Baker, D., RosettaRemodel: A generalized framework for flexible backbone protein design. *PLoS ONE* **2011**, *6* (8), e24109.

44. Emsley, P.; Lohkamp, B.; Scott, W. G.; Cowtan, K., Features and development of Coot. *Acta Cryst D* **2010**, *66*, 486-501.

45. Kamisetty, H.; Ovchinnikov, S.; Baker, D., Assessing the utility of coevolution-based residue-residue contact predictions in a sequence- and structure-rich era. *Proc. Natl. Acad. Sci. U. S. A.* **2013**, *110* (39), 15674-15679.

46. Panavas, T.; Sanders, C.; Butt, T. R., SUMO fusion technology for enhanced protein production in prokaryotic expression systems. *Methods Mol. Biol*. **2009**, *497*, 303-317.

47. Frey, M.; Rothe, M.; Wagner, A. F. V.; Knappe, J., Adenosylmethionine-dependent synthesis of the glycyl radical in pyruvate formate-lyase by abstraction of the glycine C-2 pro-S hydrogen atom. *J. Biol. Chem*. **1994**, *269* (17), 12432-12437.

48. Rödel, W.; Plaga, W.; Frank, R.; Knappe, J., Primary structures of Escherichia coli pyruvate formate-lyase and pyruvate formate-lyase-activating enzyme deduced from the DNA nucleotide sequences. *Eur. J. Biochem*. **1988**, *177*, 153-158.

49. Selvaraj, B.; Pierik, A. J.; Bill, E.; Martins, B. M., 4-Hydroxyphenylacetate decarboxylase activating enzyme catalyses a classical *S*-adenosylmethionine reductive cleavage reaction. *J. Biol. Inorg. Chem*. **2013**, *18*, 633-643.

50. Harder, J.; Eliasson, R.; Pontis, E.; Ballinger, M. D.; Reichard, P., Activation of the Anaerobic Ribonucleotide Reductase from Escherichia coli by *S*-Adenosylmethionine. *J. Biol. Chem*. **1992**, *267*, 25548-25552.

51. Shisler, K. A.; Hutcheson, R. U.; Horitani, M.; Duschene, K. S.; Crain, A. V.; Byer, A. S.; Shepard, E. M.; Rasmussen, A.; Yang, J.; Broderick, W. E.; Vey, J. L.; Drennan, C. L.; Hoffman, B. M.; Broderick, J. B., Monovalent cation activation of the radical SAM enzyme pyruvate formate-lyase activating enzyme. *J. Am. Chem. Soc*. **2017**, *139* (34), 11803-11813.

52. Sofia, H. J.; Chen, G.; Hetzler, B. G.; Reyes-Spindola, J. F.; Miller, N. E., Radical SAM, a novel protein superfamily linking unresolved steps in familiar biosynthetic

pathways with radical mechanisms: functional characterization using new analysis and information visualization methods. *Nucleic Acids Res*. **2001**, *29* (5), 1097-1106.

53. Nicolet, Y.; Drennan, C. L., AdoMet radical proteins--from structure to evolution--alignment of divergent protein sequences reveals strong secondary structure element conservation. *Nucleic Acids Res*. **2004**, *32* (13), 4015-4025.

CHAPTER THREE

DIRECT DETECTION OF THE α-CARBON RADICAL INTERMEDIATE FORMED BY OspD: MECHANISTIC INSIGHT INTO RADICAL SAM PEPTIDE EPIMERIZATION

Contribution of Authors and Co-Authors

Manuscript in Chapter 3

Author: William G. Walls

Contributions: Conducted most of the experimental work, prepared figures, wrote the manuscript, edited drafts of the manuscript.

Co-Author: Anna Vagstad

Contributions: Provided materials, edited manuscript.

Co-Author: Tyler Delridge

Contributions: Helped prepare enzymes, conducted some experiments, edited the manuscript.

Co-Author: Jörn Piel

Contributions: Provided materials, edited manuscript.

Co-Author: William E. Broderick

Contributions: Provided oversight for the research direction, provided experimental insight, helped write and edit manuscript.

Co-Author: Joan B. Broderick

Contributions: Provided oversight for the research direction, interpretation of results, wrote sections of the manuscript, helped edit the manuscript, acquired funding for the research.

Manuscript Information

William G. Walls, Anna Vagstad, Tyler Delridge, Jörn Piel, William E. Broderick, and Joan B. Broderick

Journal of the American Chemical Society

Status of Manuscript:
☐ Prepared for submission to a peer-reviewed journal
☐ Officially submitted to a peer-reviewed journal
☐ Accepted by a peer-reviewed journal
☒ Published in a peer-reviewed journal

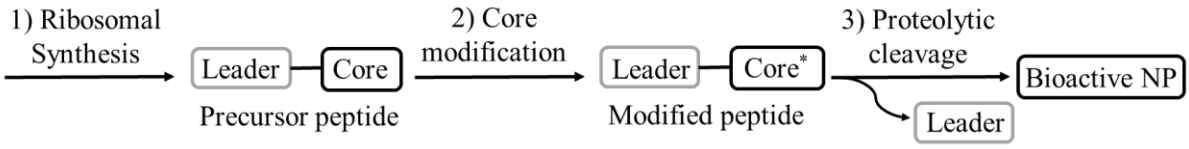
American Chemical Society
2024**,** 146 (8), 5550-5559
10.1021/jacs.3c13829

Abstract

OspD is a radical *S*-adenosyl-L-methionine (SAM) peptide epimerase that converts an isoleucine (Ile) and valine (Val) of the OspA substrate to D-amino acids during biosynthesis of the ribosomally synthesized and post-translationally modified peptide (RiPP) natural product landornamide A. OspD is proposed to carry out this reaction via Cα H-atom abstraction to form a peptidyl Cα radical that is stereospecifically quenched by hydrogen atom transfer (HAT) from a conserved cysteine. Here we use site-directed mutagenesis, freeze-quench trapping, isotopic labeling, and electron paramagnetic resonance (EPR) spectroscopy to provide new insights into the OspD catalytic mechanism, including the direct observation of the substrate peptide Cα radical intermediate. The putative quenching Cys334 was changed to serine to generate an OspD C334S variant impaired in HAT quenching. Reaction of reduced OspD C334S with SAM and OspA freeze-quenched at 15 s exhibits a doublet EPR signal characteristic of a Cα radical coupled to a single β-H. Using OspA isotopologues deuterated at either or both Ile and Val reveals that the initial Cα radical intermediate forms exclusively on Ile of OspA. Time-dependent freeze quench coupled with EPR spectroscopy provided evidence for loss of the Ile Cα radical concomitant with gain of a Val Cα radical, directly demonstrating the N-to-C directionality of epimerization by OspD. These results provide direct evidence for the aforementioned OspD-catalyzed peptide epimerization mechanism via a central Cα radical intermediate during RiPP maturation of OspA, a mechanism that may extend to other proteusin peptide epimerases.

Introduction

Ribosomally synthesized and post-translationally modified peptides (RiPPs) are a structurally diverse class of natural products with a broad range of bioactivities [1, 2]. They have gained attention in recent years due to their engineerability and potential as novel antibiotics and antivirals [3-7]. RiPP biosynthesis begins with a precursor peptide typically composed of an N-terminal leader and a C-terminal core region (Scheme 3.1). Maturation enzymes are recruited by the leader to install post-translational modifications (PTMs) in the core; the leader is then proteolytically cleaved from the core to yield the bioactive natural product, which may be exported from the cell.



Scheme 3.1. Overview of biosynthesis of RiPP natural products.

The large, highly cytotoxic polytheonamides are among the most extensively modified RiPP natural products characterized to date and are the founding members of the proteusin family [8]. Biosynthesis of polytheonamides A and B involves installation of 48 PTMs on the precursor peptide PoyA; of these, 18 are irreversible L- to D- epimerizations at specific amino acids in almost perfect alternation that are installed by the radical *S*-adenosyl-L-methionine (SAM) epimerase PoyD [8, 9]. Epimerization is a frequently observed modification during RiPP maturation, and the resulting D-amino acid residues are known to improve the proteolytic stability of peptides and alter their structure and bioactivity [10-12]. Interest in the PoyD peptide epimerase led to the discovery of homologues in other organisms, including OspD in the *osp* cluster from *Kamptonema* sp. PCC 6506 (Figure 3.1A), which catalyzes epimerization reactions

on the OspA precursor (Figure 3.1B) during biosynthesis of the antiviral RiPP natural product landornamide A (Figure 3.1C) [9, 13]. OspD and other proteusin epimerases were shown to be highly promiscuous, accepting precursor peptides with mutations at the natural site of epimerization, or adjacent to it, and even epimerizing completely unnatural core sequences as long as they are fused to the native leader sequence [14]. Thus, proteusin peptide epimerases may be of interest in synthetic biology approaches to install D-amino acids that can have a stabilizing influence on therapeutic peptides [15].

OspD is a radical SAM (RS) epimerase responsible for the installation of D-*allo*-Ile4 and D-Val13 on OspA (residue numbering referring to the core position) during landornamide A biosynthesis. This epimerization is one example of a vast array of chemical transformations catalyzed by RS enzymes, one of the largest enzyme superfamilies in nature [16-25]. RS enzymes use a SAM-bound [4Fe-4S] cluster to initiate catalysis by electron transfer from the reduced $[4Fe\text{-}4S]^{+}$ cluster to the sulfonium of the [4Fe-4S] coordinated SAM, causing homolytic reductive cleavage to produce a strongly oxidizing 5′-deoxyadenosyl radical (5′-dAdo•, Figure 3.1D) [26-30]. The 5′-dAdo• initially forms an Fe-C(5′) bond with the unique iron of the [4Fe-4S] cluster to yield the organometallic intermediate Ω [31-33] and homolysis of the Fe-C(5′) bond is proposed to release 5′-dAdo• for stereospecific H-atom abstraction from the substrate to form a substrate radical (Figure 3.1D) [34-39]. Due to the high reactivity of radical intermediate species, they are rarely directly observed during enzyme reactions.

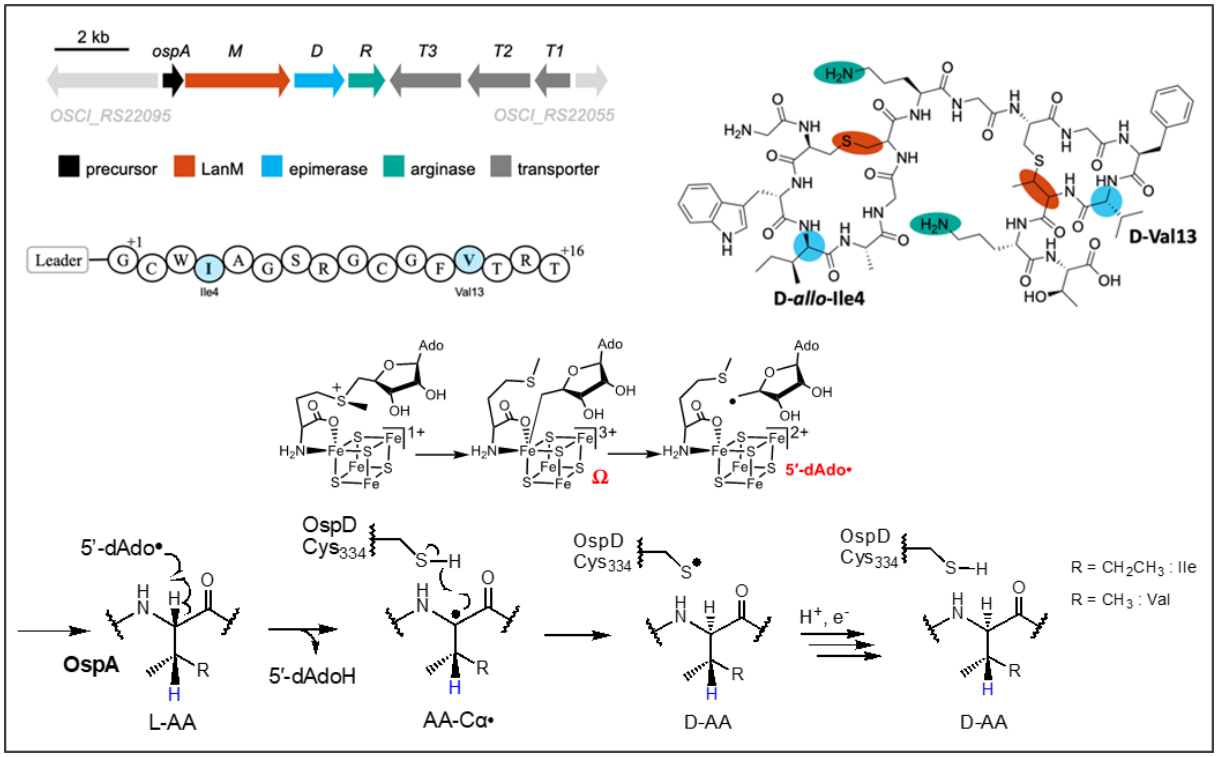


Figure 3.1. Biosynthesis of the RiPP natural product landornamide A. A. The *osp* biosynthetic gene cluster includes genes encoding the substrate OspA and the epimerase OspD, as well as a type 2 lanthionine synthetase (LanM), and an arginase (OspR). B. OspA precursor peptide with core sequence shown. C. Structure of landornamide A, with modifications highlighted in colors corresponding to enzymes shown in (A). D. Proposed mechanism of OspA peptide epimerization by OspD. Top, radical initiation at the RS cluster. Bottom, epimerization of OspA is initiated by Cα H-atom abstraction at an L-amino acid (L-AA) to form a Cα radical; the β-H is highlighted in blue. Stereospecific HAT by Cys334 forms the D-amino acid.

RS-based proteusin peptide epimerization by enzymes such as PoyD and OspD is proposed to proceed via the mechanism illustrated in Figure 3.1D: reductive cleavage of SAM results in formation of Ω, which undergoes homolytic Fe-C(5′) bond cleavage to generate the 5′-dAdo• radical [40-42]. This intermediate subsequently abstracts an H-atom from the α-carbon (Cα) of the core peptide residue to be epimerized, resulting in a peptide Cα radical intermediate. This key Cα radical is proposed to be stereospecifically back-side quenched via H-atom transfer (HAT) from a conserved cysteine (Cys) residue, resulting in inversion of stereochemistry to form

the D-amino acid and a Cys thiyl radical, which in turn is thought to be quenched via proton-coupled electron-transfer [40]. While biochemical evidence from label transfer studies and site-directed mutagenesis supports this mechanism, no direct evidence for the proposed reaction intermediates has been reported [40, 41]. Here we use freeze-quench techniques coupled to electron paramagnetic resonance (EPR) spectroscopy to provide direct evidence for the formation of a peptide substrate Cα radical intermediate by an OspD variant in which the quenching Cys is changed to a serine (Ser). The Cα radical is observed to a lesser extent in wild-type (WT) OspD. Further, use of OspA substrates specifically deuterated at the epimerized amino acid residues reveals that OspD targets Ile4 first, providing direct evidence for N-to-C directionality during sequential epimerizations of OspA by OspD.

Methods and Materials

Materials

Mutagenesis primers were purchased from Integrated DNA Technologies. Dimethyl sulfoxide (DMSO) was obtained from ThermoFisher. Q5 DNA polymerase, KLD Enzyme Mix, dNTPs, and *E. coli* NEB5α competent cells were obtained from New England Biolabs. *E. coli* BL21(DE3) competent cells were obtained from Novagen. Polymerase chain reaction was performed on an Applied Biosystems MiniAmp thermal cycler. [U-D_{10}]-L-Ile and [3-D_1]-L-Val were obtained from Cambridge Isotope Laboratories, Inc. *S*-adenosyl-L-methionine (SAM) was prepared as previously reported [65].

Site-Directed Mutagenesis

Site directed mutagenesis was carried out using Q5 DNA polymerase and following the manufacturer's protocol with 1 ng of template DNA and the addition of 3% (v/v) DMSO. Primers used are listed in Table S3.1. PCR parameters were as follows: 98 °C for 30 s, followed by 25 cycles of 98 °C for 10 s, 62 °C for 25 s, and 72 °C for 2.5 min, after which a final extension at 72 °C for 2 min was used. Following PCR, 5 µL of the reaction mixture was visualized on a 1% agarose gel, stained with thiazole orange. PCR product (1 µL) was then used in a KLD reaction (New England Biolabs) following the manufacturer's protocol. Following incubation at 25 °C for 5 min, 5 µL of the KLD reaction was used to transform chemically competent NEB5α cells. Cells were plated on selective solid LB medium. The following day, single colonies were used to inoculate 5 mL of LB medium (10 g/L tryptone, 10 g/L NaCl, 5 g/L yeast extract) supplemented with 50 µg/mL spectinomycin (Research Products International) and grown overnight at 37 °C with 250 rpm shaking. Plasmid DNA was purified using GeneJet Plasmid Miniprep Kit (ThermoFisher) following the manufacturer's protocol except that the plasmid DNA was eluted from the column using water instead of elution buffer. DNA sequencing was performed at Functional Biosciences (WI, USA) using standard T7 promoter and T7 terminator primers.

Protein Expression

Plasmids *ospD/pCDF-6xH-v* or *ospD_C334S/pCDF-6xH-v* were used to transform chemically competent *E. coli* BL21(DE3) cells. Cells were plated on selective solid LB medium. The following day, a single colony was used to inoculate LB medium supplemented with 50 µg/mL spectinomycin and was subsequently grown at 37 °C with 250 rpm shaking overnight. 2 L of TB medium (12 g/L tryptone, 24 g/L yeast extract, 0.4% (v/v) glycerol, 0.017 M KH_2PO_4,

0.072 M K_2HPO_4) was supplemented with 50 µg/mL spectinomycin and inoculated with overnight culture (1% v/v). The cultures were grown at 37 °C with 220 rpm shaking until an OD_{600nm} = 1.2 was reached. The cultures were then cooled on ice for 15 min and supplemented with 250 µM ferrous ammonium sulfate and 1 mM IPTG. The cultures were grown at 16 °C with 180 rpm shaking overnight for 20 hours. Cells were pelleted by centrifugation (6754 x g, 15 min, 4 °C), flash frozen in liquid nitrogen, and stored at -80 °C. Expression of OspD WT or OspD C334S was visualized on a 4-20% mini-Protean TGX (Bio-Rad) gel stained with Coomassie Brilliant Blue.

Plasmid *ospA/pET28b* [66] was used to transform chemically competent *E. coli* BL21(DE3) cells. Single colonies were used to inoculate LB medium supplemented with 30 µg/mL kanamycin and were subsequently grown at 37 °C with 250 rpm shaking overnight. 2 L of TB medium were supplemented with 30 µg/mL kanamycin and inoculated with overnight culture (1% v/v). The cultures were grown at 37°C with 220 rpm shaking until an OD_{600nm} = 0.7, then supplemented with 1 mM IPTG and grown at 37 °C for 3 hours. Cells were pelleted by centrifugation (6754 x g, 15 min, 4 °C), flash frozen in liquid nitrogen, and stored at -80 °C. Expression of OspA was visualized on a 4-20% mini-Protean TGX gel stained with Coomassie Brilliant Blue.

Expression of Isotopically-labeled OspA

A single colony of *ospA/pET28b* in *E. coli* BL21(DE3) was used to inoculate a seed culture of LB medium supplemented with 30 µg/ mL kanamycin and were subsequently grown at 37 °C with 250 rpm shaking overnight. 0.2 L of LB medium was supplemented with 30 µg/mL kanamycin, inoculated with 1% (v/v) of overnight culture, and grown at 37°C with 250 rpm

shaking until OD_{600nm} = 0.8. The culture was then centrifuged at 4,000 rpm, 4 °C for 10 min. The cells were washed with 25 mL of 1x buffer salts (see below) and centrifuged (4,000 rpm, 4 °C, 10 min). The cell pellet was resuspended in 200 mL LR medium [67] supplemented with amino acid dropout mix (-Ile, -Val), 30 µg/ mL kanamycin, 1 mM IPTG, 0.2% (w/v) glucose, and 8 mg of [U-D_{10}]-l-Ile, [3-D_1]-l-Val, or both. Natural abundance Ile or Val was added to 40 µg/mL concentration depending on the labeled amino acid added so that all 20 amino acids are present in the media. Cultures were then grown at 37 °C for 3 hours with 250 rpm shaking. Cells were pelleted by centrifugation (6754 x g, 10 min, 4 °C) before being flash frozen in liquid nitrogen and stored at -80 °C.

LR medium was prepared from stock solutions of 10x buffer salts (240 g/L K_2HPO_4, 10 g/L NaOH), 100x mineral salts (16.5 g $(NH_4)_2SO_4$, 6.16 mg $MgSO_4$ $7H_2O$, 30 mg $FeSO_4$ $7H_2O$, 0.1 mL conc. H_2SO_4, diluted to 100 mL with DI H_2O), and 20% (w/v) D-glucose. 10x amino acid dropout mix (-Ile, -Val) was prepared from all other 18 amino acids at 400 µg/mL for L-amino acids or 800 µg/mL for DL-amino acids, dissolved in DI H_2O, and filter sterilized. 100x stock solutions of natural abundance L-Ile or L-Val at 4 mg/mL concentration were prepared by dissolving in DI H_2O and filter sterilizing.

Protein Purification

For OspD WT or C334S variant, frozen cell paste was brought into the anerobic chamber (COY laboratories, Inc.) and resuspended in lysis buffer (50 mM HEPES pH 8.0, 150 mM KCl, 10% (v/v) glycerol, 10 mg/mL Triton X-100, 0.5 mg/mL lysozyme, 1.15 mg/mL $MgCl_2$ hexahydrate, 0.01 mg/mL DNAse, and Pierce Protease Inhibitor Tablet(s) EDTA-free) at a ratio of 2 mL per gram cell paste. The cells were incubated for one hour before being sonicated on ice

for 5 min (5 s pulse on, 15 s pulse off, 40% amplitude). The cell lysate was clarified by centrifugation at 26,790 x g for 45 min and 4 °C. The clarified lysate was loaded onto a 5 mL Ni-NTA column (Cytiva) using an AKTA Start FPLC. The column was washed with buffer A (50 mM HEPES pH 8.0, 150 mM KCl, 10% (v/v) glycerol) supplemented with 25 mM imidazole. The protein was eluted from the column with buffer A supplemented with 400 mM imidazole. The purified enzyme was de-salted using a Sephadex G-25 medium (90 mL) column into buffer A and concentrated to about 0.5 mM using a 30 kDa MWCO spin filter (Amicon). The enzyme was aliquoted, flash frozen in liquid nitrogen, and stored at -80°C.

OspA was purified in a similar manner as OspD except that all steps were aerobic and performed at 4 °C. Following elution from the Ni-NTA column, the protein was de-salted into buffer A using a HiPrep 26/10 de-salting column (Cytiva). The de-salted protein was concentrated with a 10 kDa MWCO spin filter (Amicon) to about 1 mM. The purified OspA was then made anaerobic on a Schlenk line with several vacuum/ nitrogen cycles. The anaerobic OspA protein was then aliquoted, flash frozen in liquid nitrogen, and stored at -80 °C. Purified OspA was quantified by its absorbance at 280 nm using an extinction coefficient of 7,115 M^{-1} cm^{-1} calculated using ProtParam (https://web.expasy.org/protparam/).

Protein Quantification

To determine a correction factor for the Bradford assay, an aliquot of purified OspD was buffer exchanged using a PD-10 column into amino acid analysis buffer (50 mM HEPES pH 8.0, 100 mM KCl). The buffer exchanged protein was used for a Bradford assay following the method of Zor and Selinger [68] with Pierce bovine serum albumin as a standard (ThermoFisher). An aliquot of protein was diluted in buffer to 1 mg/mL, in triplicate, and sent to

the Molecular Structure Facility at UC Davis, CA, for amino acid analysis. A correction factor of 0.683 ± 0.005 was then multiplied by the concentration calculated by the Bradford assay.

Iron Analysis

Iron content was determined using an Agilent 240 FS flame atomic absorption spectrometer. A calibration curve was made from 0.4 to 2.0 ppm iron using an iron atomic absorption standard (Ricca, 1000 ppm in 3% HNO_3) diluted in DI water. Protein samples were diluted to 2 μM in buffer A, in triplicate, for analysis. Absorbance from buffer was subtracted from each sample. Iron per protein values were obtained by dividing the moles of iron by the moles of protein in each sample, and represented as the mean ± standard deviation of the triplicate samples.

Iron-Sulfur Cluster Reconstitution

Aliquots of purified OspD WT or C334S mutant were thawed in the anaerobic chamber. The aliquots were diluted to 0.1 mM with buffer A on ice. DTT was added to 5 mM concentration and incubated for 5 min. Stock solutions of $FeCl_3$ and $Na_2S•9H_2O$ were dissolved in buffer A to a final concentration of 10 and 50 mM, respectively. $FeCl_3$ was added slowly over the course of 30 min to a final concentration of 0.6 mM. After incubating for 10 mins, $Na_2S•9H_2O$ was added slowly over the course of 30 min to a final concentration of 0.6 mM. The reaction then stirred on ice for 2 hours before being centrifuged (16,200 xg, 10 min) and de-salted into buffer A using a Sephadex G-25 (90 mL) column. The reconstituted protein was concentrated to approximately the starting volume, flash frozen in liquid nitrogen, and stored at -80 °C. Following reconstitution, the iron content was 4.5 ± 0.2 for the WT enzyme and 3.4 ± 0.2 iron atoms per monomer for the C334S variant.

UV-visible spectroscopy

UV-vis spectra were recorded using an Agilent Cary 60 UV-visible spectrophotometer scanning from 800-200 nm at 600 nm/min. Samples were measured in Spectrosil Quartz cuvettes (Starna Cells, CA, USA) with a 10 mm path length.

EPR Sample Preparation

Samples were prepared in an MBraun glovebox maintained at <1 ppm O_2 and at room temperature. All buffers were degassed on a Schlenk line. A 150 µL solution of 167 µM OspD WT (or C334S variant) was reduced with 1.67 mM sodium dithionite for 10 min before being mixed with a 100 µL solution of 375 µM OspA, 2.5 mM SAM, and 2.5 mM dithionite in an X-band EPR tube (Wilmad Labglass, 4 mm OD). The samples were frozen in liquid nitrogen at the times indicated after mixing. Following mixing, the final concentrations were: 100 µM OspD (WT or C334S), 150 µM OspA, 2 mM sodium dithionite, and 1 mM SAM in buffer A. Buffered D_2O was prepared by evaporating water from buffer A on the Schlenk line, followed by washing the glycerol/ salt solution with 1 mL D_2O and subsequently evaporating, twice. The solution was then diluted with D_2O to the starting volume and the pH_{app} was checked with pH paper (6.0 – 8.0). If necessary, the pH_{app} was adjusted with 6 M KOH. The pH_{app} was not corrected following the recommendation by Rubinson [69].

EPR spectroscopy

Continuous wave EPR X-band EPR spectroscopy was performed using a Bruker EMX EPR spectrometer equipped with a Bruker/ColdEdge (Sumitomo Cyrogenics) 10 K waveguide cryogen free system with an Oxford MercuryiTC controller unit and helium Stinger recirculating unit (Sumitomo Cyrogenics, ColdEdge Technologies). All spectra were recorded at 9.378 GHz

microwave frequency and 100 kHz modulation frequency. Iron-sulfur cluster signals were recorded at 10 K with 10 G modulation amplitude and 1 mW microwave power. Organic radical signals were recorded at 75 K with 3 G modulation amplitude and 0.3 mW (for OspD C334S reactions) or 2 mW (for OspD WT reactions) microwave power. The spectrometer was calibrated with an external standard of 2,2-diphenyl-1-picrylhydrazyl (DPPH) with a *g*-value of 2.0036 (Bruker). Experimental spectra were simulated with Easyspin [44] (5.2.35) within the Matlab R2020b software suite (Mathworks, Inc.).

Spin quantitation was performed by dissolving 4-hydroxy-TEMPO radical (Thermo Scientific) in water in the glove box. The concentration of the stock solution was calculated using an extinction coefficient of 13.4 M^{-1} cm^{-1} at 429 nm [70]. Aliquots were then diluted in water to yield concentrations from 2.5 to 100 µM and transferred to EPR tubes. The standards were analyzed under the same conditions used for the samples and the double integral of the signal was used to construct a linear standard curve.

Simulation details for Figures 3.3, 3.4, S3.10, and S3.11: simulations were generated with Easyspin [44] with g_{iso} = [2.0036], hyperfine tensors $a_{iso}(^1H)$ = 61 MHz and $a_{iso}(N\text{-}^1H)$ = 12 MHz, linewidth = 11 G, and Hstrain = [5] MHz. Singlet species were simulated by substituting the $a_{iso}(^1H)$ = 61 MHz coupling with $a_{iso}(^2H)$ = 9.36 MHz. For Figure 3.4, spectra A and D were simulated with 100% doublet. For the spectrum in Figure 3.4B inclusion of 12% doublet along with 88% singlet was necessary to satisfactorily simulate the spectrum. For the spectrum in Figure 3.4C, inclusion of 15% doublet together with 85% singlet was required for satisfactory simulation. Without inclusion of these doublet signal contributions, unrealistically large linewidths or Hstrain values were needed in order to simulate the width of the spectra. Weights

for Figures S3.10 and S3.11 are provided in the figure captions. Total spin concentrations in Figure 3.4 range from 15-20 μM.

Simulations of EPR spectra allowed us to evaluate the degree of deuteration of radical-harboring OspA substrates; comparison to mass spectroscopic analysis of deuterated OspA substrates provided insights into the sites of the Cα radicals, as described here. Simulation of the EPR signal resulting from the reaction of OspD C334S with SAM and [U-D_{10}]-L-Ile-OspA reveals contributions from 85% singlet and 15% doublet species; the 15% doublet contribution arises due to the presence of ~ 15% unlabeled and partially metabolized [U-D_{10}]-L-Ile which has lost two deuterons, consistent with the mass spectrum of the purified labeled OspA (Figure S3.6). Such partial loss of deuteration during in vivo production of deuterated peptides and proteins has been previously reported, and is attributed to amino transaminase activity present during in vivo production [71, 72]. Simulation of the EPR signal resulting from the reaction of OspD C334S with SAM and [U-D_{10}]-L-Ile/[3-D_1]-L-Val -OspA reveals contributions from 88% singlet and 12% doublet, also consistent with the mass spectrometric analysis of this deuterated OspA (Figure S3.8).

Epimerization Assay

Epimerization of OspA was achieved by combining 10 μM of OspD WT or C334S with 100 μM OspA, 500 μM NaDT, and 500 μM SAM in buffer A. Reactions were carried out in the glove box at 23-25 °C and allowed to proceed overnight (~17 hours). An aliquot (3.9 μL, ~5 μg OspA) of each reaction was digested with GluC and trypsin and desalted with C18 Zip Tips as described below. Each reaction was performed in duplicate.

Protease Digest of OspA and LC-MS Analysis

An aliquot of purified OspA (natural abundance or isotopically labeled) was diluted to 150 µM with DI H_2O and incubated with 10 mM DTT for 10 min. 2.5 µL of DTT-reduced OspA was digested with 100 ng GluC and 50 ng of trypsin in 1x GluC buffer and 20 mM $CaCl_2$, brought to 20 µL with water, and incubated at 37 °C for 3 hours. Trifluoroacetic acid was added to 0.1% (v/v) to quench the digest. The digest was then desalted with C4 Zip Tips (EMD Millipore) following the manufacturers protocol and eluted into 60% acetonitrile, 0.1% formic acid, 39.9% water.

An aliquot (5 µL) was injected onto an Agilent UHPLC 1290 Infinity II equipped with a Zorbax RRHD Eclipse Plus C18 column (2.1 x 50 mm, 1.8 µm, 95 Å) coupled to an Agilent 6538 UHD Accurate-mass Q-TOF mass spectrometer. The sample was eluted using the following method: washing with 2% B for 2 min; linear gradient to 50% B from 2 to 7 min; linear gradient from 7-8 min of 50-98% B; hold at 98% B from 8-9.5 min before equilibrating to 2% B and holding from 9.5 to 10 min. Solvent A is 0.1% formic acid in water and solvent B is acetonitrile with 0.1% formic acid. The separation was carried out with 0.4 mL/ min flow rate and column temperature of 50 °C. Mass spectra was collected with 2 Hz scan rate and a mass range of 103-1700 *m/z*. Expected masses were calculated using the Fiehn laboratory's excel ESI-adduct calculator (https://fiehnlab.ucdavis.edu/staff/kind/metabolomics/ms-adduct-calculator/). Mass spectra were simulated using Prot Pi (https://www.protpi.ch/Calculator/MassSpecSimulator#MassSpecSimulatorResult) then converted into relative abundance and compared with experimental spectra.

For LC-MS/MS fragmentation, OspA (natural abundance or isotopically labeled) substrate was diluted to 0.1 mM with water and reduced with 10 mM DTT for 10 minutes. 10 µg

was then digested with 200 ng GluC and 100 ng trypsin in 20 mM $CaCl_2$ and 1x GluC buffer for 3 hours at 37 °C before being quenched with 0.9 % TFA. The digests were then desalted with C18 Zip Tips and eluted into 20 µL of 60% acetonitrile, 0.1% formic acid, 39.9% water. 2 µL aliquots were then injected onto an Acquity UPLC I-Class PLUS system equipped with an Agilent Eclipse C18 RRHD, 2.1 x 100 mm column coupled to a Waters Synapt XS MS. The peptides were eluted with the following method: 0-1 min, 2% B; 1-8 min, 2-80% B; 8-9 min, 80-98% B; 9-10 min, 2% B. Solvent A is 95:5 water: acetonitrile with 0.1% formic acid; Solvent B is acetonitrile with 0.1% formic acid. Peptides were detected in positive ion mode and sensitive mode, using leucine enkephalin as a lock-mass. Core peptide ions were selected for targeted fragmentation and fragmented with a collision energy profile of 20, 30, and 40. Survey scans were collected at 0.33 s and MS/MS was collected at 0.5 s. Peptide b- and y- ions were calculated using University of Washington data analysis tools (https://proteomicsresource.washington.edu/cgi-bin/fragment.cgi).

Results

Characterization of wild-type and mutant OspD.

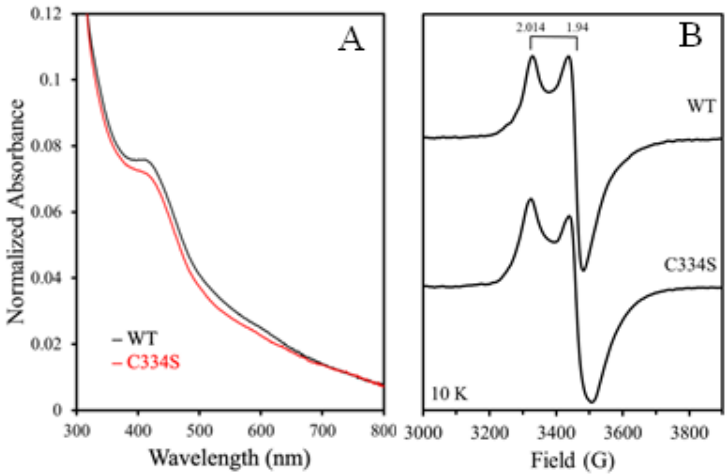


Figure 3.2. Normalized UV-visible (A) and X-band EPR spectra (B) of reconstituted WT and C334S OspD. For EPR, the enzymes are reduced with NaDT. EPR conditions: microwave frequency, 9.38 GHz; modulation, 10 G, T = 10 K.

In order to verify the proposed quenching Cys residue in OspD, a multiple sequence alignment of characterized proteusin epimerases was constructed (Figure S3.1), revealing OspD Cys334 as the most likely candidate. An AlphaFold [43] model of OspD predicts that Cys334 resides in the active site near the conserved CX_3CX_2C motif that coordinates the RS [4Fe-4S] cluster, further supporting a mechanistic role for Cys334 (Figure S3.2). We generated the OspD C334S variant, based on the hypothesis that changing the quenching Cys334 to an isosteric Ser would slow the quenching of the substrate Cα radical intermediate due to the greater O-H bond strength in Ser compared to the S-H in Cys; this change would be predicted to allow an OspA radical intermediate to build up to detectable quantities for EPR spectroscopic characterization. Both the WT OspD and the C334S variant were expressed in *E. coli* BL21(DE3), anaerobically purified, and chemically reconstituted following published procedures with minor changes (SI) [32]. The resulting proteins were brown in color and contained 4.5 ± 0.2 (WT) and 3.4 ± 0.2 (C334S) irons per protein based on atomic absorption. UV-visible spectroscopic analysis of the WT and C334S OspD proteins revealed a broad absorption band centered at 410 nm indicative of [4Fe-4S] clusters (Figure 3.2a) [16]. Reduction of the reconstituted WT and C334S OspD proteins with sodium dithionite (NaDT) provided samples with similar EPR signals (g = 2.014 and 1.94) that are typical of RS enzyme $[4Fe\text{-}4S]^+$ clusters (Figures 3.2b and S3.3) [16]. Together, these results are consistent with both WT and C334S OspD containing one [4Fe-4S] cluster per monomer.

<u>Trapping a substrate-based radical on OspA.</u>

Rapid (500 ms) freeze-quench of the reaction of reduced OspD with OspA and SAM previously revealed formation of the organometallic intermediate **Ω** central to RS catalysis [32]. In order to look for formation of subsequent substrate-based radical intermediates, reduced OspD C334S was mixed with OspA and SAM, freeze-quenched at 15 s, and examined by EPR spectroscopy at 75 K. The resulting sample exhibited an EPR signal with a symmetric doublet, centered at g_{iso} = 2.004. The signal was well-simulated with isotropic ^{1}H hyperfine couplings of 61 and 12 MHz (Figure 3.3). The doublet signal is consistent with the formation of a Cα radical on one or both of the target Ile4 and Val13 residues of OspA, as both have a single β-H (Figure 3.1D) that would split the Cα radical EPR signal into a symmetric doublet. When the reaction was carried out in 90% D_2O, the signal was more intense (Figure 3.3), likely reflecting a slowed quenching of the OspA radical due to H/D exchange at Ser334. In addition, the doublet signal is sharper when generated in D_2O, consistent with the loss of the a_{iso}(H) = 12 MHz coupling (Figures 3.3 and S3.4); we attribute this coupling to the adjacent amide hydrogen, which readily undergoes H/D exchange.

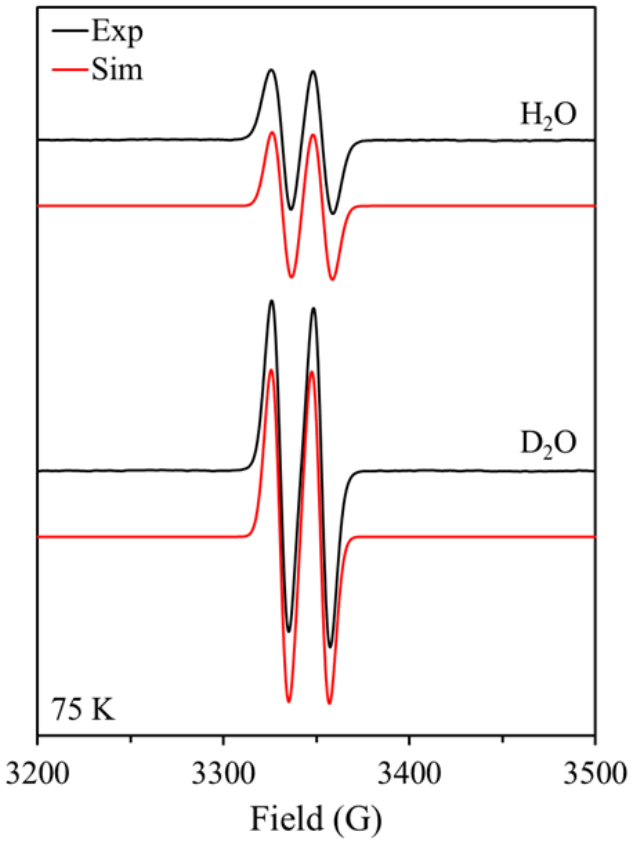
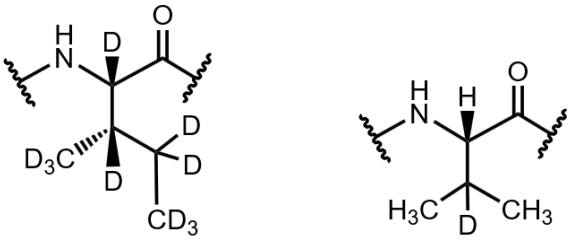


Figure 3.3. X-band EPR spectra (black) and simulations (red) of 15 s freeze-quenched reactions of OspD C334S, SAM, and OspA carried out in H_2O (top) or D_2O (bottom). Simulations were generated with Easyspin with g_{iso} = [2.004], hyperfine tensors $a_{iso}(^1H)$ = 61 MHz, and $a_{iso}(N\text{-}^1H)$ = 12 MHz for the H_2O reaction or $a_{iso}(N\text{-}^2H)$ = 1.84 MHz for the D_2O reaction, linewidth = 11 G, and Hstrain = [5] MHz. EPR conditions: microwave frequency, 9.38 GHz; modulation, 3 G; T = 75 K.



[U-D_{10}]-L-Ile [3-D_1]-L-Val

Scheme 3.2. Structures of [U-D_{10}]-L-isoleucine and [3-D_1]-L-valine.

To test formation of a Cα radical on Ile4 and/or Val13 as proposed for the OspD mechanism (Figure 3.1D), an OspA substrate deuterated at the β-H positions of Ile4 and Val13 was prepared by expression in minimal medium supplemented with both [U-D_{10}]-L-Ile and [3-D_1]-L-Val (Scheme 3.2). The purified labeled OspA was analyzed by LC-MS following GluC and trypsin digestion to verify and quantify incorporation of the labeled amino acids (Figures S3.5-S3.10). Reactions of reduced OspD C334S with SAM and [U-D_{10}]-L-Ile/ [3-D_1]-L-Val-labeled OspA were freeze-quenched at 15 s and examined by EPR spectroscopy. Relative to the doublet observed for unlabeled OspA (Figures 3.3 and 3.4A), the results reveal the EPR signal has collapsed to a singlet with g_{iso} = 2.004 (Figure 3.4B), consistent with the formation of a Cα radical on the deuterated Ile4 and/or Val13 residue(s) on OspA, and supporting the mechanistic proposal shown in Figure 3.1D.

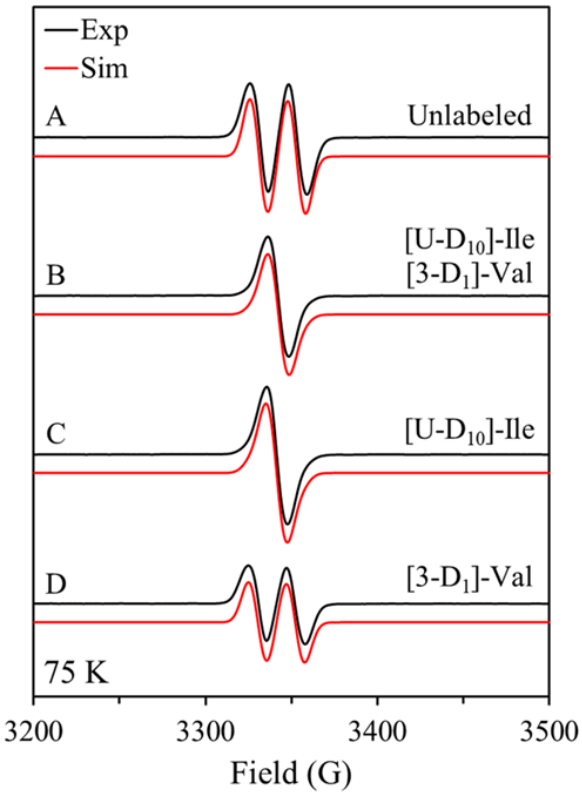


Figure 3.4. X-band EPR spectra (black) and simulations (red) of 15 s freeze-quenched reactions of OspD C334S, SAM, and OspA reveal Ile4 as the initial site of H-atom abstraction. (A) Natural abundance OspA. (B) Both Ile and Val of OspA deuterated. (C) [U-D_{10}]-L-Ile-OspA. (D) [3-D_1]-L-Val-OspA. EPR conditions: microwave frequency, 9.38 GHz; modulation, 3 G; T = 75 K.

In order to determine whether there is specificity for the initial site of epimerization and thus the initial Cα radical formed, reactions were carried out in which only one of Ile4 or Val13 were deuterated. Reaction of OspD C334S with SAM and [U-D_{10}]-L-Ile-OspA for 15 s resulted in a singlet EPR signal (Figure 3.4C), demonstrating that the Cα radical is on the Ile4 and collapsed due to deuteration at the β-C. When OspD C334S was reacted with SAM and [3-D_1]-L-Val-OspA and quenched at 15 s, the result was a doublet EPR signal (Figure 3.4D) essentially identical to that observed for the reaction with the unlabeled OspA (Figure 3.4A), demonstrating that the Cα radical does not reside on Val13. Together, these results provide unequivocal evidence that the initial substrate-based radical observed during reaction of OspD C334S with SAM and OspA is the Cα radical at OspA Ile4.

Directionality of sequential epimerizations on OspA.

Analysis of protease-released OspA core peptides from *in vitro* reactions by LC-MS indicates that OspD C334S can carry out epimerization at Ile4, although to a lesser extent than the WT enzyme (Figure S3.11); this led us to ask whether OspD C334S can proceed from Ile4 to Val13 to initiate a second epimerization. In order to look for procession, the reaction of reduced OspD C334S with SAM and [U-D_{10}]-L-Ile-OspA was freeze-quenched at 5, 30, and 60 min, and analyzed by EPR spectroscopy. Results reveal an initial singlet EPR signal at 5 min due to formation of a Cα radical at deuterated Ile4, and decreasing EPR intensity with increasing time (Figure S3.12). At 30 min and 1 h, the samples show evidence for increasing amounts of a

doublet EPR signal, consistent with progression from the initial deuterated Ile4 Cα radical (singlet EPR) to the non-deuterated Val13 radical (doublet EPR). Similar results were obtained with the [3-D_1]-L-Val-OspA, except in this case the signal starts as a doublet for the unlabeled Ile4 Cα radical but converts to a singlet for the deuterated Val13 Cα radical with increasing time, again indicating progression from Ile4 to the deuterated Val13 (Figure S3.13). In both cases, conversion to the Val13 radical is not quantitative, and overall signal intensity decreases, presumably due to radical quenching during turnover of OspD C334S. Together, the combination of isotopic labeling and time-resolved freeze quench EPR spectroscopy demonstrates that OspD C334S initially targets the Ile4 residue for epimerization, by formation of a peptide Cα radical on Ile4, before back-side quenching to form the D-*allo*-Ile4, and then initiating epimerization at the Val13 residue, providing evidence for N-to-C directionality.

Trapping a Cα radical generated by wild-type OspD.

Next, time-resolved freeze quench of the WT OspD reaction allowed us to trap the key Cα radical formed on OspA directly during catalytic turnover. The reaction of reduced WT OspD with SAM and OspA carried out in H_2O, freeze-quenched at ~ 13 s reveals a low-intensity doublet EPR signal with features similar to those observed for OspD C334S (Figure 3.5). However, substitution of D_2O for H_2O provides the same doublet EPR signal but with markedly increased intensity (Figures 3.5 and S3.14), which we attribute to slowed Cα radical quenching by the H/D exchanged thiol S-D of Cys334. This signal for the WT enzyme can be well simulated with parameters derived from the Ile4 Cα• generated with OspD C334S (Figures 3.4 and 3.5). These results demonstrate that WT OspD initiates epimerization of OspA by the same mechanism involving 5′-dAdo•-mediated H-atom abstraction from Ile4 to form a peptidyl Cα

radical (Figure 3.1D). The lowered signal intensity for the WT enzyme reaction relative to that of C334S OspD is consistent with the proposed role for C334: mediating facile back-side HAT quenching of the substrate Cα radical, thus leading to a shorter-lived Cα radical intermediate in the WT enzyme reaction.

Discussion

Epimerization is a key reaction in both organic synthesis and biosynthesis of natural products, and can proceed through either acid-base or radical mechanisms, with the latter being more broadly applicable to a range of structures including unactivated C(sp3)–H bonds [45]. Radical epimerizations appear to be employed broadly in nature, and RS enzymes catalyzing epimerization reactions have been discovered in several biosynthetic pathways including those for neomycin B, in which NeoN catalyzes the epimerization of a sugar carbon during the final biosynthetic step [46], and hygromycin B, in which HygY catalyzes C2′ epimerization of galacamine [47]. In both HygY and NeoN, the SAM-derived 5′-dAdo• abstracts H• from the sugar carbon undergoing epimerization, and then a conserved Cys residue quenches the intermediate sugar carbon radical. In the case of NeoN, mutation of this conserved Cys to alanine revealed formation of an organic radical, thought to be the substrate carbon radical intermediate, during reaction with SAM and the neomycin C substrate. HygY and NeoN bear similarity to the RS enzymes PolH and NikJ, which catalyze carbon extension in peptidyl nucleoside biosynthesis by forming a substrate radical on the 5′-C of enolpyruvyl UMP, which undergoes cyclization to form a C7′ radical that is then quenched by a conserved cysteine residue. Similar to the case for NeoN, when the conserved cysteine residue of PolH is changed to serine or alanine, a substrate radical intermediate assigned to C7′• is observed by EPR [48]. Adenosylhopane synthase (HpnH)

is another example of a RS enzyme in which the final catalytic step is the stereospecific quenching of a product radical by a conserved cysteine residue [49].

Epimerization of L-amino acid residues is widespread during RiPP maturation, and examples of both radical and non-radical pathways are known [1]. RS peptide epimerases form distinct families that are not closely related: YydG and EpeE from the Epipeptides [50-52], and PoyD, OspD, AvpD, PlpD, AerD, and CcaD from proteusin RiPPs [8, 9, 14, 40, 41, 53-55]. This latter subcategory of RS peptide epimerases, as unequivocally demonstrated here for OspD, may all initiate epimerization by peptide Cα H-atom abstraction to generate a Cα radical intermediate, as previously proposed for PoyD, OspD, and YydG [40, 41, 50]. As with the enzymes discussed above, the carbon radical intermediate formed during peptide epimerization has been proposed to be stereospecifically quenched by a conserved cysteine residue; here we showed that converting this conserved cysteine residue of OspD to a serine slows quenching of the OspA Cα radical intermediate, allowing us to trap and characterize this peptide Cα radical intermediate for the first time and thus provide direct insight into the mechanism. The same Cα radical intermediate was ultimately observed for the WT enzyme as well, although with lower signal intensity due to the presence of the conserved cysteine residue, providing further support for the proposed mechanism.

The directionality of the sequential epimerizations catalyzed by proteusin epimerases is variable: PoyD is proposed to initiate epimerization at the most C-terminal substrate residue target and then proceed towards the N-terminus of the substrate, while OspD is proposed to have the opposite directionality, and others like PlpD seem to display no preferred order [9]. To date, the directionality of epimerization for these peptide epimerases has been inferred from the

distribution of products formed under steady-state reaction conditions, as determined by performing the reactions with labeled substrate or in the presence of D_2O and analyzing products by LC-MS. Here, we have demonstrated a more direct approach can be taken to determine epimerization directionality by using a combination of mutagenesis, isotopic labeling, and time-dependent freeze quench coupled with EPR spectroscopy.

Peptide epimerization has interesting parallels to the reaction catalyzed by glycyl radical enzyme-activating enzymes (GRE-AEs), a large subclass of RS enzymes that catalyze the abstraction of the pro-*S* Cα H-atom from a conserved glycyl residue to generate a stable glycyl radical enzyme [56-60]; Cα radicals have also been implicated in the mechanisms of other RS enzymes [61-64]. In the case of OspD, the Cα radical is a short-lived intermediate rather than a stable cofactor as in GREs; however, the promiscuity of OspD [15, 41], together with the mechanistic insight provided herein, demonstrates that RS chemistry can be used to generate a wide array of catalytically essential peptide and protein Cα radicals.

Conclusion

RS epimerases are proposed to initiate catalysis by H-atom abstraction from the carbon atom to be epimerized, only limited direct mechanistic insight has been provided to date. Here, we have provided direct evidence for the involvement of a central α-carbon radical intermediate during D-amino acid installation in the biosynthesis of landornamide A by the RS enzyme OspD, as well as evidence to support the N-to-C directionality of the successive epimerizations.

Supplemental Material



Figure S3.1. Multiple sequence alignment of characterized proteusin epimerases OspD (D8G6F8_9CYAN), PoyD (J9ZW29_BACS1), AvpD (Q3ME30_TRIV2), and PlpD (WP_019503883). Alignment performed with Clustal Omega using default parameters (https://www.ebi.ac.uk/Tools/msa/clustalo/). The N- and C-terminal sequences have been trimmed for clarity.

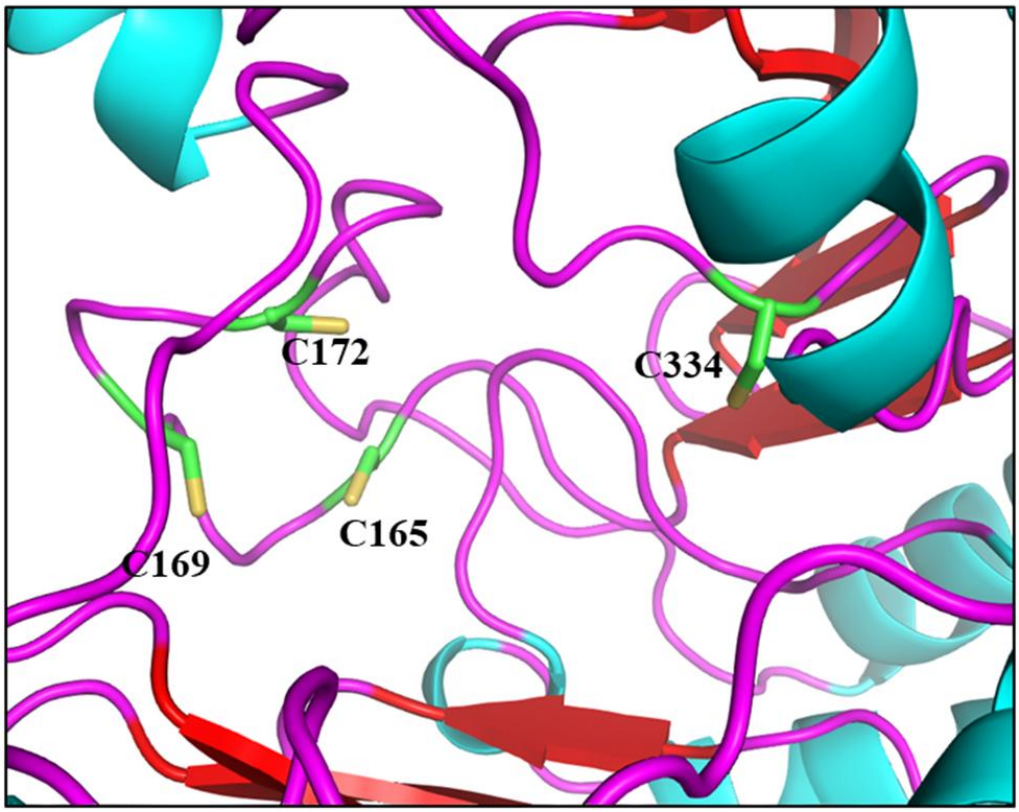


Figure S3.2. AlphaFold [1] model of the OspD active site. C165, C169, and C172 are involved in coordinating the [4Fe-4S] cluster. C334 is responsible for stereoselective quenching of the substrate α-carbon radical intermediate to produce the D-amino acid.

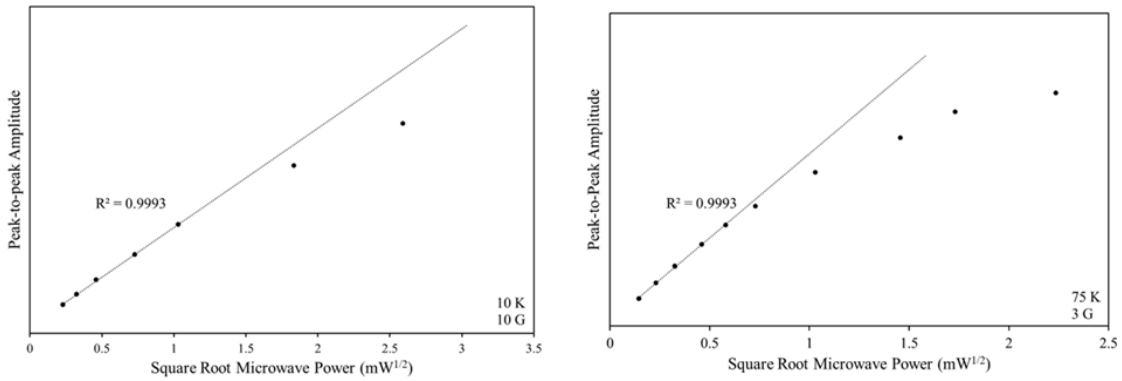


Figure S3.3. Power dependence of NaDT-reduced OspD at 10 K (left, spectra acquired with 1 mW microwave power at 10 K are non-saturating), and the OspA radical at 75 K (right, spectra acquired with 335 μW microwave power are non-saturating).

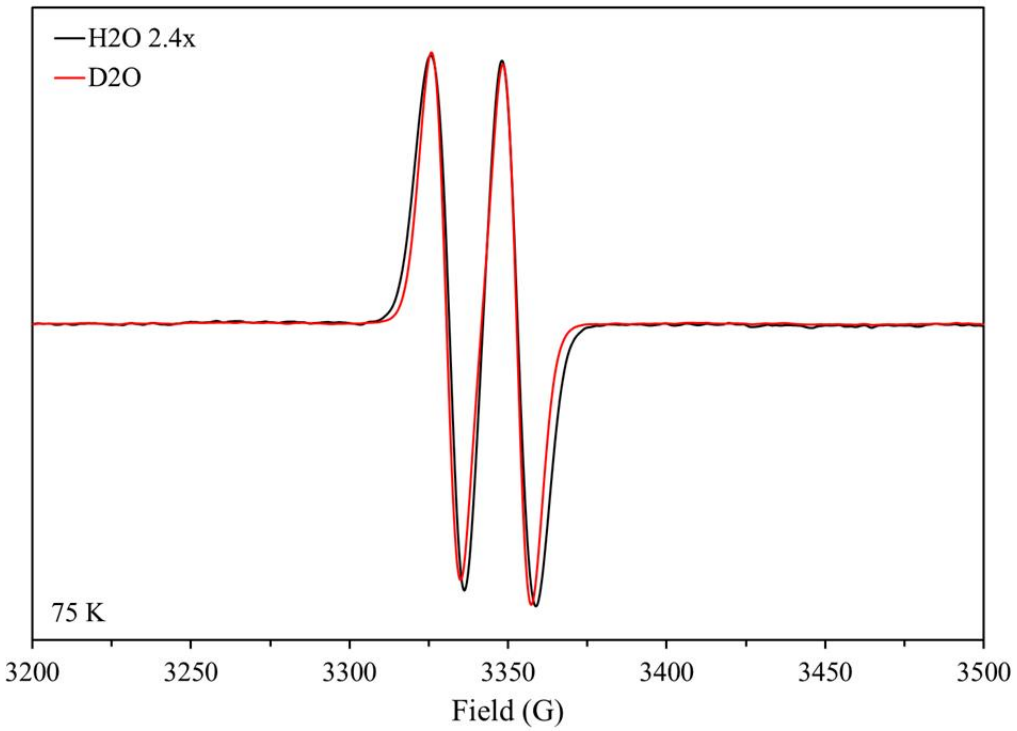
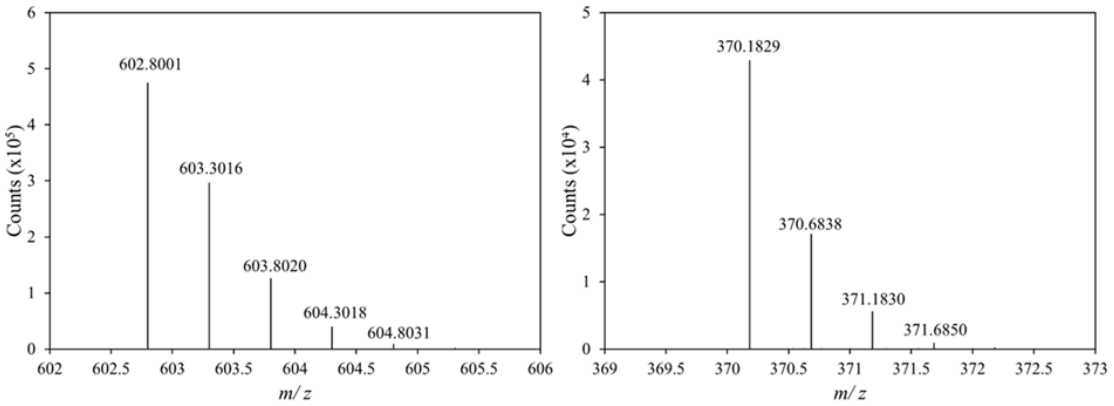
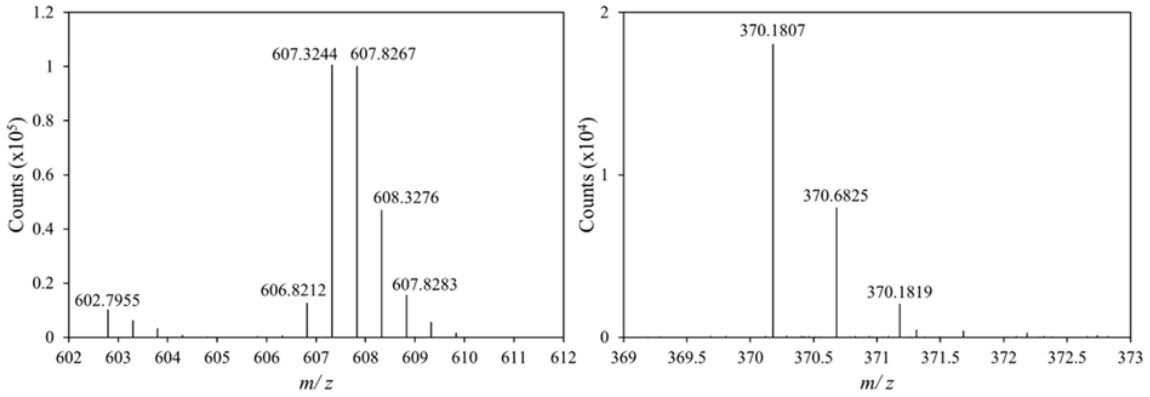


Figure S3.4. OspD C334S reacted with OspA and SAM in buffered H_2O or 90% D_2O and quenched at 15 s. The spectra are overlaid to show that the OspA substrate radical EPR signal is narrower in D_2O, consistent with H/D exchange at the adjacent amide nitrogen. The signal in H_2O is multiplied by 2.4 for easier comparison.



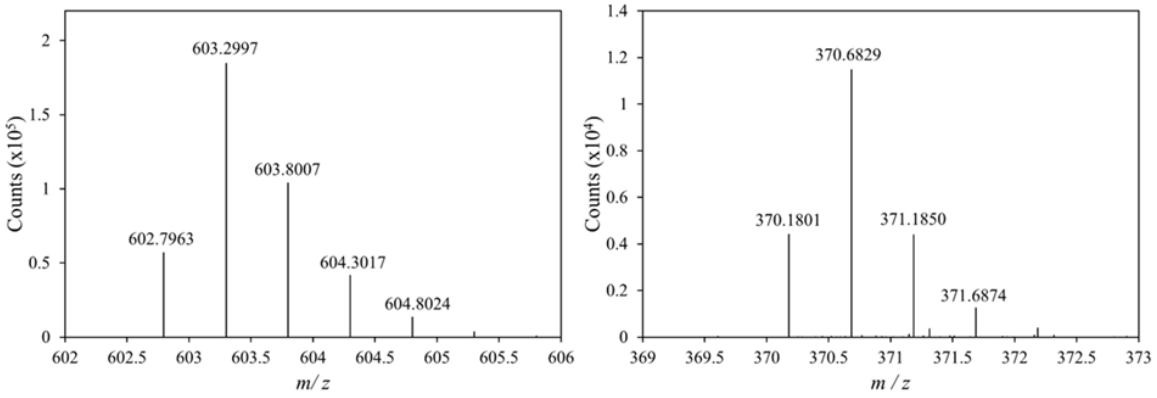
Sequence	Ion	Calc. monoisotopic *m/z*	Obs. *m/z*	Δppm
AVAGGGCW**I**AGSR	$[M+2H]^{2+}$	602.7982	602.8001	3.1
GCGF**V**TR	$[M+2H]^{2+}$	370.1814	370.1829	4.0

Figure S3.5. Mass spectra (top) and expected peptide ions (bottom) of GluC and trypsin digested natural-abundance OspA.



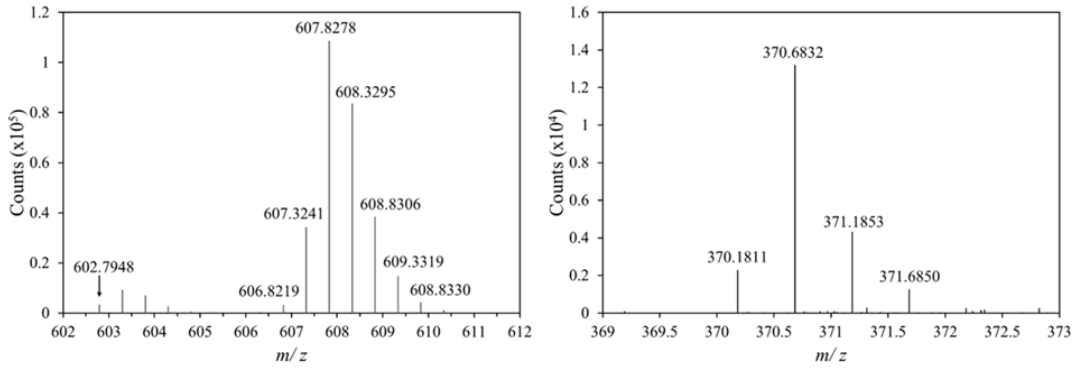
Sequence	Ion	Calc. monoisotopic *m/z*	Obs. *m/z*	Δppm
AVAGGGCW**I**AGSR	$[M+2H]^{2+}$	602.7982	602.7955	-4.4
AVAGGGCW(**D_8-I**)AGSR	$[M+2H]^{2+}$	606.8233	606.8212	-3.4
AVAGGGCW(**D_9-I**)AGSR	$[M+2H]^{2+}$	607.3264	607.3244	-3.3
AVAGGGCW(**D_{10}-I**)AGSR	$[M+2H]^{2+}$	607.8296	607.8267	-4.8
GCGF**V**TR	$[M+2H]^{2+}$	370.1814	370.1807	-1.9

Figure S3.6. Mass spectra (top) and expected peptide ions (bottom) of GluC and trypsin digested OspA labeled with [U-D_{10}]-L-isoleucine. The mass spectrum could be simulated with the following weights: 6.7% unlabeled, 8.3% D_8 labeled, 60.4% D_9 labeled, and 24.6% D_{10} labeled. The total amount of unlabeled and D_8 labeled OspA is 15%, therefore, a weight of 15% doublet was used in the simulation of the [U-D_{10}]-L-isoleucine labeled EPR signal (Figure 3.3c). Loss of deuterium from [U-D_{10}]-L-isoleucine is due to transaminases in *E. coli* [2].



Sequence	Ion	Calc. monoisotopic *m/z*	Obs. *m/z*	Δppm
AVAGGGCW**I**AGSR	$[M+2H]^{2+}$	602.7982	602.7963	-3.1
A(**D_1-V**)AGGGCW**I**AGSR	$[M+2H]^{2+}$	603.3013	603.2997	-2.6
GCGF**V**TR	$[M+2H]^{2+}$	370.1814	370.1801	-3.5
GCGF(**D_1-V**)TR	$[M+2H]^{2+}$	370.6845	370.6829	-4.3

Figure S3.7. Mass spectra (top) and expected peptide ions (bottom) of GluC and trypsin digested OspA labeled with [3-D_1]-L-valine.



Sequence	Ion	Calc. monoisotopic *m/z*	Obs. *m/z*	Δppm
AVAGGGCW**I**AGSR	$[M+2H]^{2+}$	602.7982	602.7948	-5.6
A(**D_1-V**)AGGGCW**I**AGSR	$[M+2H]^{2+}$	603.3013	603.2985	-4.6
AVAGGGCW(**D_8-I**)AGSR	$[M+2H]^{2+}$	606.8233	606.8219	-2.3
A(**D_1-V**)AGGGCW(**D_8-I**)AGSR AVAGGGCW(**D_9-I**)AGSR	$[M+2H]^{2+}$	607.3264	607.3241	-3.8
A(**D_1-V**)AGGGCW(**D_9-I**)AGSR AVAGGGCW(**D_{10}-I**)AGSR	$[M+2H]^{2+}$	607.8296	607.8278	-3.0
A(**D_1-V**)AGGGCW(**D_{10}-I**)AGSR	$[M+2H]^{2+}$	608.3327	608.3295	-5.2
GCGF**V**TR	$[M+2H]^{2+}$	370.1814	370.1811	-0.8
GCGF(**D_1-V**)TR	$[M+2H]^{2+}$	370.6845	370.6832	-3.5

Figure S3.8. Mass spectra (top) and expected peptide ions (bottom) of GluC and trypsin digested OspA labeled with both [U-D_{10}]-L-isoleucine and [3-D_1]-L-valine. The left spectrum could be simulated with the following weights: 2% unlabeled, 4% D_1-labeled, 2% D_8 labeled, 22% D_9 labeled, 60% D_{10} labeled, and 10% D_{11} labeled. The total amount of unlabeled and D_8 labeled OspA is 12%, therefore, a weight of 12% doublet was used in the simulation of the doubly labeled EPR signal (Figure 3.3b).

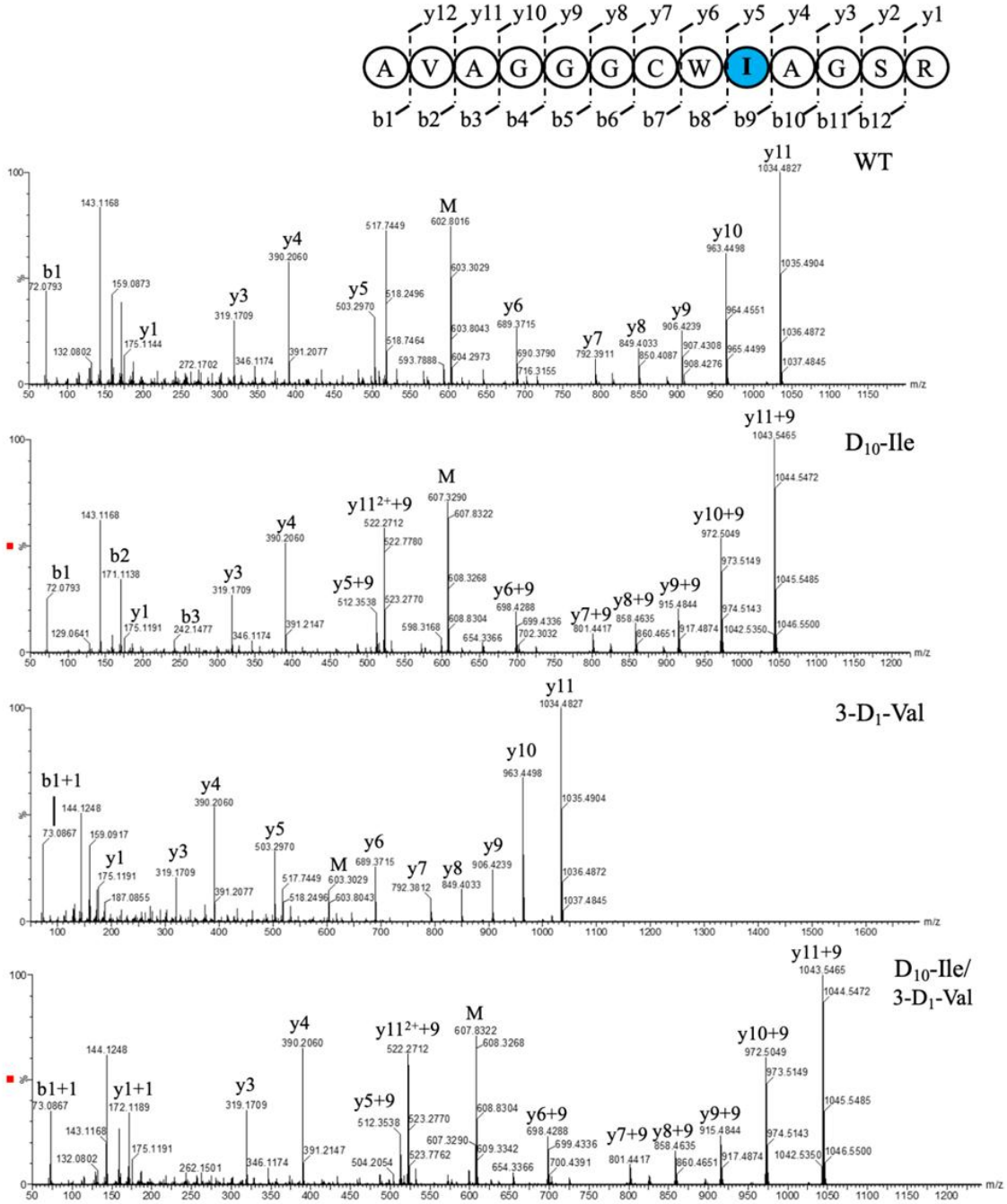


Figure S3.9. LC-MS/MS fragmentation of GluC and trypsin digested natural abundance and isotopically labeled OspA core peptide encompassing residues -5 to +8. Y- ions clearly show a 9 Da increase that localizes to Ile4.

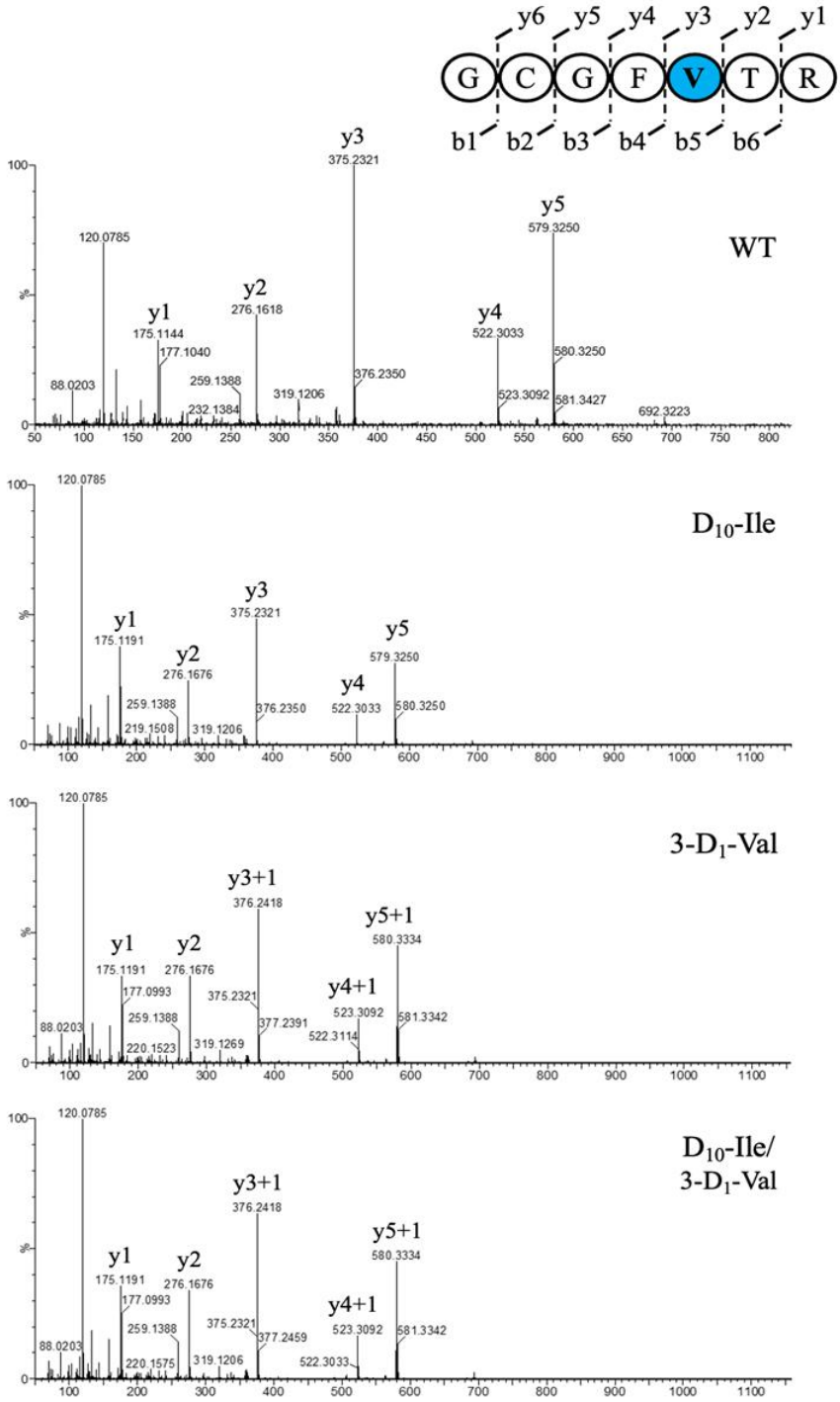


Figure S3.10. LC-MS/MS fragmentation of GluC and trypsin digested natural abundance and isotopically labeled OspA core peptide encompassing residues +9 to +15. Y- ions clearly show a 1 Da increase that localizes to Val13.

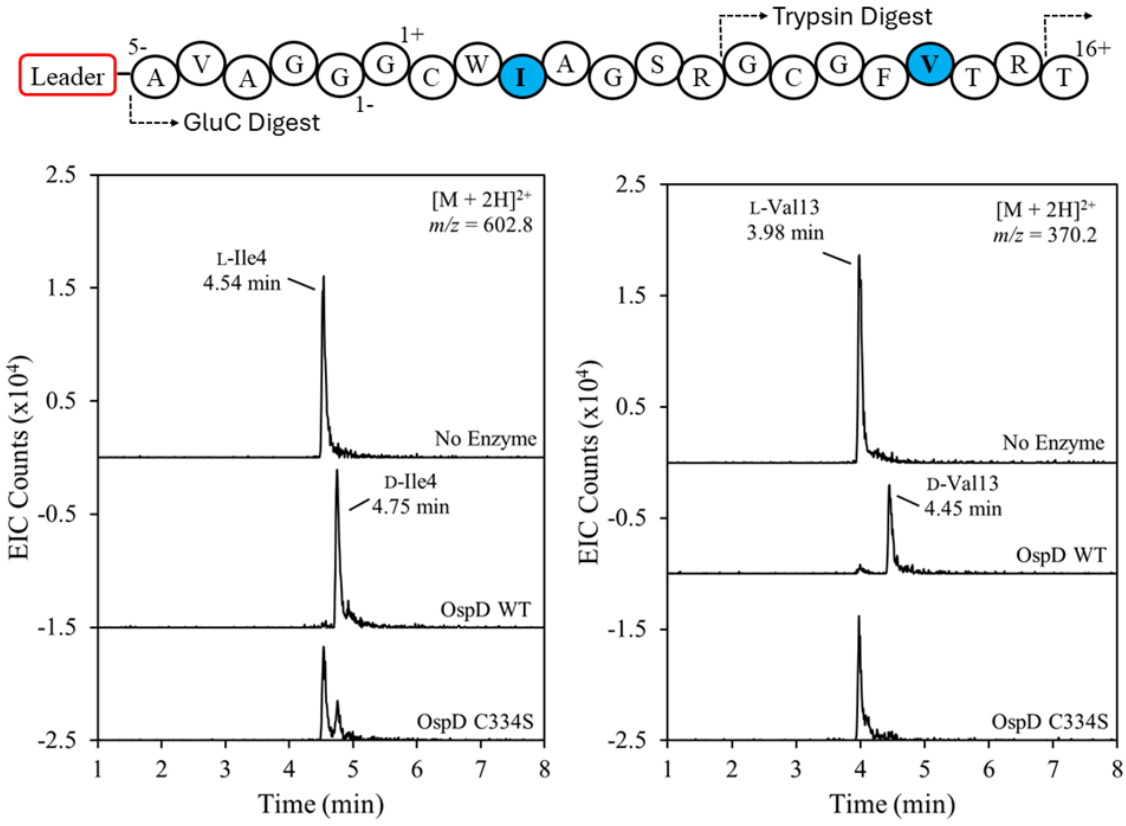


Figure S3.11. Mass spectroscopic evaluation of epimerization of OspA by WT and C334S OspD following a 17 h reaction (see SI methods). The OspA substrate was digested with GluC and trypsin (top) for 3 h prior to analysis by LC-MS (bottom). Left, the Ile4-containing fragment (AVAGGGCWIAGSR) shows full epimerization for WT OspD and partial epimerization using OspD C334S. Right, the Val13-containing fragment (GCGFVTR) shows nearly full epimerization for WT OspD and very little or no epimerization for OspD C334S.

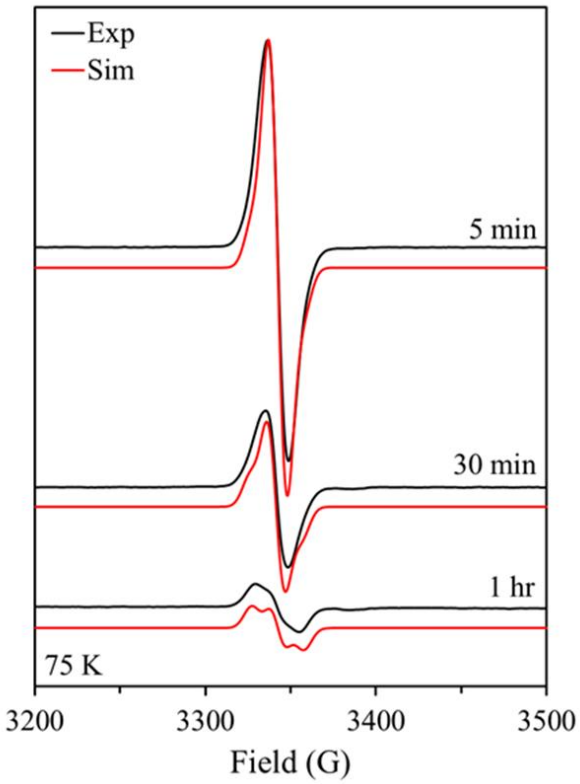


Figure S3.12. EPR monitored decay of [U-D_{10}]-L-Ile labeled OspA radical over time. See Methods for simulation details. Spectra were simulated with weights as follows: 5 min is 80% singlet (21.4 μM) and 20% doublet (5.4 μM), 30 min is 70% singlet (9.4 μM) and 30% doublet (4.0 μM), and 1 hour is 52% singlet (3.3 μM) and 48% doublet (3 μM). EPR conditions: microwave frequency, 9.38 GHz; modulation, 3 G; T = 75 K.

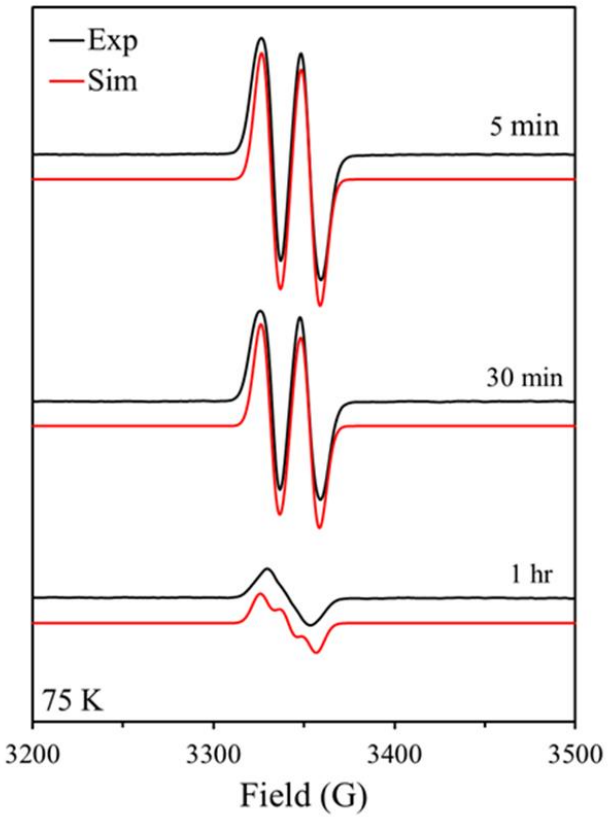


Figure S3.13. EPR monitored decay of [3-D_1]-L-Val labeled OspA radical over time. See Methods for simulation details. Spectra were simulated with weights as follows: 5 min is 5% singlet and 95% doublet, 30 min is 5% singlet and 95% doublet, and 1 h is 45% singlet and 55% doublet. EPR conditions: microwave frequency, 9.38 GHz; modulation, 3 G; T = 75 K.

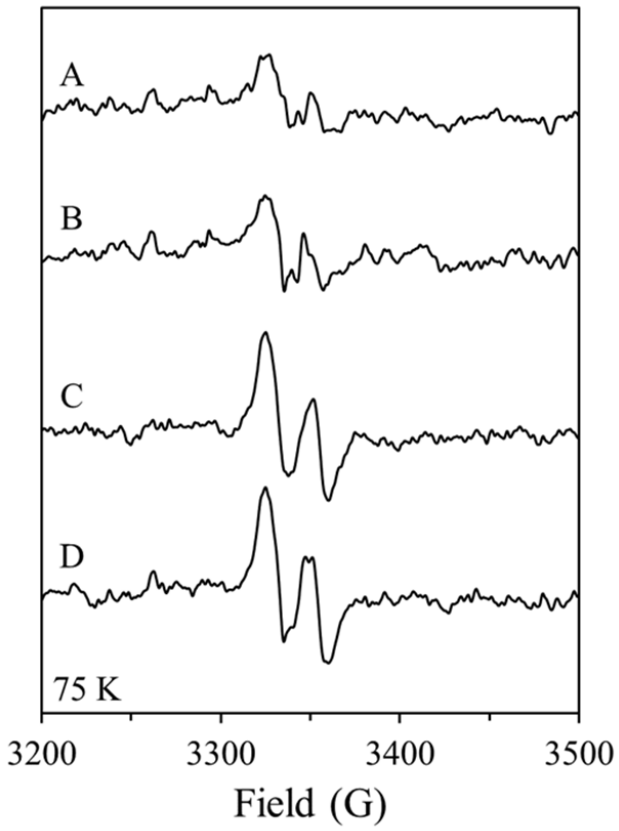


Figure S3.14. EPR spectra of OspD WT and OspA substrate freeze quenched in buffered H_2O and D_2O. Reactions (A) and (B) were performed in buffered H_2O and freeze quenched at ~13 s. Reactions (C) and (D) were performed in buffered D_2O and quenched at ~11 s. Reactions performed in D_2O consistently show higher intensity for the doublet EPR signal. EPR conditions: microwave frequency, 9.38 GHz; modulation, 3 G; T = 75 K.

Table S3.1. Primers used to mutate Cys334 of OspD to Ser. Primers were designed using NEBaseChanger (https://nebasechanger.neb.com/) with *ospD/pCDF-6xH-v* as the template [3].

Primer	Sequence
C334S_Fwd	5′-AACGATTGCTAGCGTAACAGGATTTTTG-3′
C334S_Rev	5′-GATTGGGCTAACTCATCAG-3′

Supplemental References

1. Jumper, J.; Evans, R.; Pritzel, A.; Green, T.; Figurnov, M.; Ronneberger, O.; Tunyasuvunakool, K.; Bates, R.; Zidek, A.; Potapenko, A.; Bridgland, A.; Meyer, C.; Kohl, S. A. A.; Ballard, A. J.; Cowie, A.; Romera-Paredes, B.; Nikolov, S.; Jain, R.; Adler, J.; Back, T.; Petersen, S.; Reiman, D.; Clancy, E.; Zielinski, M.; Steinegger, M.; Pacholska, M.; Berghammer, T.; Bodenstein, S.; Silver, D.; Vinyals, O.; Senior, A. W.; Kavukcuoglu, K.; Kohli, P.; Hassabis, D., Highly accurate protein structure prediction with AlphaFold. *Nature* **2021**, *596* (7873), 583-589.

2. Bode, H. B.; Reimer, D.; Fuchs, S. W.; Kirchner, F.; Dauth, C.; Kegler, C.; Lorenzen, W.; Brachmann, A. O.; Grün, P., Determination of the absolute configuration of peptide natural products by using stable isotope labeling and mass spectrometry. *Chem. Eur. J.* **2012**, *18*, 2342-2348.

3. Kegler, C.; Nollman, F. I.; Ahrendt, T.; Fleischhacker, F.; Bode, E.; Bode, H. B., Rapid determination of the amino acid configuration of xenotetrapeptide. *Chem. Bio. Chem.* **2014**, *15*, 826-828.

4. Vagstad, A. L.; Kuranaga, T.; Puntener, S.; Pattabiraman, V. R.; Bode, J. W.; Piel, J., Introduction of D-Amino Acids in Minimalistic Peptide Substrates by an *S*-Adenosyl-L-Methionine Radical Epimerase. *Angew Chem Int Ed Engl* **2019**, *58* (8), 2246-2250.

References

1. Montalbán-López, M.; Scott, T. A.; Sangeetha, R.; Rahman, I. R.; van Heel, A. J.; Viel, J. H.; Bandarian, V.; Dittman, E.; Genilloud, O.; Goto, Y.; Burgos, M. J. G.; Hill, C.; Kim, S.; Koehnke, J.; Latham, J. A.; Link, A. J.; Martínez, B.; Nair, S. K.; Nicolet, Y.; Rebuffat, S.; Sahl, H.-G.; Sareen, D.; Schmidt, E. W.; Schmitt, L.; Severinov, K.; Süssmuth, R. D.; Truman, A. W.; Wang, H.; Weng, J.-K.; van Wezel, G. P.; Zhang, Q.; Zhong, J.; Piel, J.; Mitchell, D. A.; Kuipers, O. P.; van der Donk, W. A., New developments in RiPP discovery, enzymology, and engineering. *Nat. Prod. Rep*. **2021**, *38*, 130-239.

2. Arnison, P. G.; Bibb, M. J.; Bierbaum, G.; Bowers, A. A.; Bugni, T. S.; Bulaj, G.; Camarero, J. A.; Campopiano, D. J.; Challis, G. L.; Clardy, J.; et al. Ribosomally synthesized and post-translationally modified peptide natural products: overview and recommendations for a universal nomenclature. *Natural Product Reports* **2013**, *30* (1), 108-160.

3. Vagstad, A. L., Engineering ribosomally synthesized and posttranslationally modified peptides as new antibiotics. *Curr. Op. Biotech*. **2023**, *80*, 102891.

4. Ruijne, F.; Kuipers, O. P., Combinatorial biosynthesis for the generation of new-to-nature peptide antimicrobials. *Biochem. Soc. Trans*. **2021**, *49* (1), 203-215.

5. Fu, Y.; Jaarsma, A. H.; Kuipers, O. P., Antiviral activities and applications of ribosomally synthesized and post-translationally modified peptides (RiPPs). *Cell. Molec. Life Sci*. **2021**, *78*, 3921-3940.

6. Wu, C.; van der Donk, W. A., Engineering of new-to-nature ribosomally synthesized and post-translationally modified peptide natural products. *Curr. Op. Biotech*. **2021**, *69*, 221-231.

7. Hudson, G. A.; Mitchell, D. A., RiPP antibiotics: biosynthesis and engineering potential. *Curr. Op. Microbiol*. **2018**, *45*, 61-69.

8. Freeman, M. F.; Gurgui, C.; Helf, M. J.; Morinaka, B. I.; Uria, A. R.; Oldham, N. J.; Sahl, H.-G.; Matsunaga, S.; Piel, J., Metagenome mining reveals polytheonamides as posttranslationally modified ribosomal peptides. *Science* **2012**, *338*, 387-390.

9. Morinaka, B. I.; Vagstad, A. L.; Helf, M. J.; Gugger, M.; Kegler, C.; Freeman, M. F.; Bode, H. B.; Piel, J., Radical *S*-adenosylmethionine epimerases: Regioselective introduction of diverse D-amino acid patterns into peptide natural products. *Angew. Chem. Int. Ed.* **2014**, *53*, 8503-8507.

10. Ogasawara, Y.; Dairi, T., Peptide epimerization machineries found in microorganisms. *Front. Microbiol*. **2018**, *9*, 156.

11. Feng, Z.; Xu, B., Inspiration from the mirror: D-amino acid containing peptides in biomedical approaches. *BioMol. Concepts* **2016**, *7* (3), 179-187.

12. Freeman, M. F.; Helf, M. J.; Bhushan, A.; Morinaka, B. I.; Piel, J., Seven enzymes create extraordinary molecular complexity in an uncultivated bacterium. *Nat. Chem*. **2017**, *9*, 387-395.

13. Bösch, N. M.; Borsa, M.; Greczmiel, U.; Morinaka, B. I.; Gugger, M.; Oxenius, A.; Vagstad, A. L.; Piel, J., Landornamides: Antiviral ornithine-containing ribosomal peptides discovered through genome mining. *Angew. Chem. Int. Ed*. **2020**, *59*, 11763-11768.

14. Morinaka, B. I.; Verest, M.; Freeman, M. F.; Gugger, M.; Piel, J., An orthogonal D_2O-based induction system that provides insights into D-amino acid pattern formation by radical *S*-adenosylmethionine peptide epimerases. *Angew. Chem*. **2017**, *129*, 780-784.

15. Korneli, M.; Fuchs, S. W.; Felder, K.; Ernst, C.; Zinsli, L. V.; Piel, J., Promiscuous installation of D-amino acids in gene-encoded peptides. *ACS Synth. Biol*. **2021**, *10* (2), 236-242.

16. Broderick, J. B.; Duffus, B. R.; Duschene, K. S.; Shepard, E. M., Radical *S*-Adenosylmethionine Enzymes. *Chem. Rev.* **2014**, *114*, 4229-4317.

17. Oberg, N.; Precord, T. W.; Mitchell, D. A.; Gerlt, J. A., RadicalSAM.org: A resource to interpret sequence-function space and discover new radical SAM chemistry. *ACS Bio Med Chem Au* **2022**, *2* (1), 22-35.

18. Sofia, H. J.; Chen, G.; Hetzler, B. G.; Reyes-Spindola, J. F.; Miller, N. E., Radical SAM, a novel protein superfamily linking unresolved steps in familiar biosynthetic pathways with radical mechanisms: functional characterization using new analysis and information visualization methods. *Nucleic Acids Res*. **2001**, *29* (5), 1097-1106.

19. Frey, P. A.; Hegeman, A. D.; Ruzicka, F. J., The radical SAM superfamily. *Crit. Rev. Biochem. Mol. Biol.* **2008**, *43* (1), 63-88.

20. Landgraf, B. J.; McCarthy, E. L.; Booker, S. J., Radical *S*-adenosylmethionine enzymes in human health and disease. *Annu. Rev. Biochem*. **2016**, *85*, 485-514.

21. Nicolet, Y., Structure-function relationships of radical of radical SAM enzymes. *Nat. Catal.* **2020**, *3*, 337-2020.

22. Broderick, J. B.; Broderick, W. E.; Hoffman, B. M., Radical SAM enzymes: Nature's choice for radical reactions. *FEBS Lett*. **2023**, *597* (1), 92-101.

23. Hoffman, B. M.; Broderick, W. E.; Broderick, J. B., Mechanism of radical initiation in the radical SAM enzyme superfamily. *Annu. Rev. Biochem*. **2023**, *92*, 333-349.

24. Yokoyama, K.; Lilla, E. A., C-C bond forming radical SAM enzymes involved in the construction of carbon skeletons of cofactors and natural products. *Nat. Prod. Rep*. **2018**, *35*, 660-694.

25. Bridwell-Rabb, J.; Grell, T. A. J.; Drennan, C. L., A rich man, poor man story of *S*-adenosylmethionine and cobalamin revisited. *Annu. Rev. Biochem*. **2018**, *87*, 555-584.

26. Krebs, C.; Broderick, W. E.; Henshaw, T. F.; Broderick, J. B.; Huynh, B. H., Coordination of adenosylmethionine to a unique iron site of the [4Fe-4S] of pyruvate formate-lyase activating enzyme: A Mössbauer spectroscopic study. *J. Am. Chem. Soc*. **2002**, *124* (6), 912-913.

27. Walsby, C. J.; Hong, W.; Broderick, W. E.; Cheek, J.; Ortillo, D.; Broderick, J. B.; Hoffman, B. M., Electron-nuclear double resonance spectroscopic evidence that *S*-adenosylmethionine binds in contact with the catalytically active $[4Fe\text{-}4S]^{+}$ cluster of pyruvate formate-lyase activating enzyme. *J. Am. Chem. Soc*. **2002**, *124* (12), 3143-3151.

28. Walsby, C. J.; Ortillo, D.; Broderick, W. E.; Broderick, J. B.; Hoffman, B. M., An anchoring role for FeS Clusters: Chelation of the amino acid moiety of *S*-

adenosylmethionine to the unique iron site of the [4Fe-4S] cluster of pyruvate formate-lyase activating enzyme. *J. Am. Chem. Soc*. **2002**, *124* (38), 11270-11271.

29. Walsby, C. J.; Ortillo, D.; Yang, J.; Nnyepi, M.; Broderick, W. E.; Hoffman, B. M.; Broderick, J. B., Spectroscopic approaches to elucidating novel iron-sulfur chemistry in the "Radical SAM" protein superfamily. *Inorg. Chem*. **2005**, *44* (4), 727-741.

30. Henshaw, T. F.; Cheek, J.; Broderick, J. B., The [4Fe-4S]$^{+}$ cluster of pyruvate formate-lyase activating enzyme generates the glycyl radical on pyruvate formate-lyase: EPR-detected single turnover. *J. Am. Chem. Soc*. **2000**, *122*, 8331-8332.

31. Horitani, M.; Shisler, K. A.; Broderick, W. E.; Hutcheson, R. U.; Duschene, K. S.; Marts, A. R.; Hoffman, B. M.; Broderick, J. B., Radical SAM catalysis via an organometallic intermediate with an Fe-[5'-C]-deoxyadenosyl bond. *Science* **2016**, *352* (6287), 822-825.

32. Byer, A. S.; Yang, H.; McDaniel, E. C.; Kathiresan, V.; impano, S.; Pagnier, A.; Watts, H.; Denler, C.; Vagstad, A. L.; Piel, J.; Duschene, K. S.; Shepard, E. M.; Shields, T. P.; Scott, L. G.; Lilla, E. A.; Yokoyama, K.; Broderick, W. E.; Hoffman, B. M.; Broderick, J. B., Paradigm shift for radical *S*-adenosyl-L-methionine reactions: The organometallic intermediate Ω is central to catalysis. *J. Am. Chem. Soc*. **2018**, *140* (28), 8634-8638.

33. Jodts, R. J.; Wittkop, M.; Ho, M. B.; Broderick, W. E.; Broderick, J. B.; Hoffman, B. M.; Mosquera, M. A., Computational description of alkylated iron-sulfur organometallic clusters. *J. Am. Chem. Soc*. **2023**, *145* (25), 13879-13887.

34. Frey, M.; Rothe, M.; Wagner, A. F. V.; Knappe, J., Adenosylmethionine-dependent synthesis of the glycyl radical in pyruvate formate-lyase by abstraction of the glycine C-2 pro-S hydrogen atom. *J. Biol. Chem*. **1994**, *269* (17), 12432-12437.

35. Chandra, T.; Silver, S. C.; Zilinskas, E.; Shepard, E. M.; Broderick, W. E.; Broderick, J. B., Spore Photoproduct Lyase Catalyzes Specific Repair of the 5R but Not the 5S Spore Photoproduct *J. Am. Chem. Soc*. **2009**, *131* (7), 2420-2421.

36. Silver, S. C.; Chandra, T.; Zilinskas, E.; Ghose, S.; Broderick, W. E.; Broderick, J. B., Complete Stereospecific Repair of a Synthetic Dinucleotide Spore Photoproduct by Spore Photoproduct Lyase. *J. Biol. Inorg. Chem*. **2010**, *15* (6), 943-955.

37. Landgraf, B. J.; Booker, S. J., Stereochemical course of the reaction catalyzed by RimO, a radical SAM methylthiotransferase. *J. Am. Chem. Soc*. **2016**, *138* (9), 2889-2892.

38. Landgraf, B. J.; Arcinas, A. J.; Lee, K.-H.; Booker, S. J., Identification of an intermediate methyl carrier in the radical *S*-adenosylmethionine methylthiotransferases RimO and MiaB. *J. Am. Chem. Soc*. **2013**, *135*, 15404-15416.

39. Fan, P.-H.; Geng, Y.; Romo, A. J.; Zhong, A.; Zhang, J.; Yeh, Y.-C.; Lee, Y.-H.; Liu, H.-w., Two radical SAM enzymes are necessary and sufficient for the in vitro production of the oxetane nucleoside antiviral agent albucidin. *Angew. Chem. Int. Ed*. **2022**, *61* (42), e202210362.

40. Parent, A.; Benjdia, A.; Guillot, A.; Kubiak, X.; Balty, C.; Lefranc, B.; Leprince, J.; Berteau, O., Mechanistic investigations of PoyD, a radical *S*-adenosyl-L-methionine enzyme catalyzing iterative and directional epimerizations in polytheonamide A biosynthesis. *J. Am .Chem. Soc*. **2018**, *140*, 2469-2477.

41. Vagstad, A. L.; Kuranaga, T.; Püntener, S.; Pattabiraman, V. R.; Bode, J. W.; Piel, J., Introduction of D-amino acids in minimalistic peptide substrates by an *S*-adenosyl-L-methionine radical epimerase. *Angew. Chem. Int. Ed*. **2019**, *58*, 2246-2250.

42. Benjdia, A.; Berteau, O., Radical SAM enzymes and ribosomally-synthesized and post-translationally modified peptides: A growing importance in the microbiomes. *Front. Chem.* **2021**, *9*, 678068.

43. Varadi, M.; Anyango, S.; Deshpande, M.; Nair, S.; Natassia, C.; Yordanova, G.; Yuan, D.; Stroe, O.; Wood, G.; Laydon, A.; Žídek, A.; Green, T.; Tunyasuvunakool, K.; Petersen, S.; Jumper, J.; Clancy, E.; Green, R.; Vora, A.; Lutfi, M.; Figurnov, M.; Cowie, A.; Hobbs, N.; Kohli, P.; Kleywegt, G.; Birney, E.; Hassabis, D.; Velankar, S., AlphaFold Protein Structure Database: massively expanding the structural coverage of protein-sequence space with high-accuracy models. *Nucl. Acids Res*. **2022**, *50* (D1), D439-D444.

44. Stoll, S.; Schweiger, A., EasySpin, a comprehensive software package for spectral simulation and analysis in EPR. *J. Magn. Res*. **2006**, *178* (1), 42-55.

45. Wang, Y.; Hu, X.; Morales-Rivera, C. A.; Li, G.-X.; Huang, X.; He, G.; Liu, P.; Chen, G., Epimerization of tertiary carbon centers via reversible radical cleavage of unactivated C(sp^3)–H bonds. *J. Am. Chem. Soc*. **2018**, *140*, 9678-9684.

46. Kudo, F.; Hoshi, S.; Kawashima, T.; Kamachi, T.; Eguchi, T., Characterization of a radical *S*-adenosyl-L-methionine epimerase, NeoN, in the last step of neomycin B biosynthesis. *J. Am. Chem. Soc*. **2014**, *136* (39), 13909-13915.

47. Besandre, R. A.; Chen, Z.; Davis, I.; Zhang, J.; Ruszczycky, M. W.; Liu, A.; Liu, H.-w., HygY is a twitch radical SAM epimerase with latent dehydrogenase activity revealed upon mutation of a single cysteine residue. *J. Am. Chem. Soc*. **2021**, *143* (37), 15152-15158.

48. Lilla, E. A.; Yokoyama, K., Carbon extension in peptidylnucleoside biosynthesis by radical SAM enzymes. *Nat. Chem. Biol*. **2016**, *12*, 905-907.

49. Sato, S.; Kudo, F.; Rohmer, M.; Eguchi, T., Biochemical and mutational analysis of radical *S*-adenosyl-L-methionine adenosylhopane synthase HpnH *Zymomonas mobilis* reveals that conserved residue cysteine-106 reduces a radical intermediate and determines the stereochemistry. *J. Am. Chem. Soc*. **2021**, *60* (38), 2865-2874.

50. Benjdia, A.; Guillot, A.; Ruffié, P.; Leprince, J.; Berteau, O., Post-translational modification of ribosomally synthesized peptides by a radical SAM epimerase in Bacillus subtilis. *Nat. Chem*. **2017**, *9*, 698-707.

51. Popp, P. F.; Friebel, L.; Benjdia, A.; Guillot, A.; Berteau, O.; Mascher, T., The epipetide biosynthesis locus epeXEPAB is widely distributed in firmicutes and triggers intrinsic cell envelope stress. *Microb. Physiol*. **2021**, *31* (3), 306-318.

52. Kubiak, X.; Polsinelli, I.; Chavas, L. M. G.; Fyfe, C. D.; Guillot, A.; Fradale, L.; Brewee, C.; Grimaldi, S.; Gerbaud, G.; Thureau, A.; Legrand, P.; Berteau, O.; Benjdia, A., Structural and mechanistic basis for RiPP epimerization by a radical SAM enzyme. *Nat. Chem. Biol*. **2023**, *20*, 382-391.

53. Morinaka, B. I.; Vagstad, A. L.; Piel, J., Radical S-adenosylmethionine peptide epimerases: Detection of activity and characterization of D-amino acid products. *Methods Enzymol*. **2018**, *604*, 237-257.

54. Cogan, D. P.; Bhushan, A.; Reyes, R.; Zhu, L.; Piel, J.; Nair, S. K., Structure and mechanism for iterative amid N-methylation in the biosynthesis of channel-forming peptide cytotoxins. *Proc. Natl. Acad. Sci. U. S. A*. **2022**, *119* (13), e2116578119.

55. Pei, Z.-F.; Zhu, L.; Nair, S. K., Core-dependent post-translational modifications guide the biosynthesis of a new class of hypermodified peptides. *Nat. Commun*. **2023**, *14*, 7734.

56. Shisler, K. A.; Broderick, J. B., Glycyl Radical Activating Enzymes: Structure, Mechanism, and Substrate Interactions. *Archives of biochemistry and biophysics* **2014**, *546*, 64-71.

57. Selmer, T.; Pierik, A. J.; Heider, J., New glycyl radical enzymes catalysing key metabolic steps in anaerobic bacteria. *Biol. Chem*. **2005**, *386*, 981-988.

58. Backman, L. R. F.; Funk, M. A.; Dawson, C. D.; Drennan, C. L., New tricks for the glycyl radical enzyme family. *Crit. Rev. Biochem. Mol. Biol.* **2017**, *52* (6), 674-695.

59. Lundahl, M. N.; Sarksian, R.; Yang, H.; Jodts, R. J.; Pagnier, A.; Smith, D. F.; Mosquera, M. A.; van der Donk, W. A.; Hoffman, B. M.; Broderick, W. E.; Broderick, J. B., Mechanism of radical *S*-adenosyl-L-methionine adenosylation: Radical intermediates and the catalytic competence of the 5′-deoxyadenosyl radical. *J. Am. Chem. Soc.* **2022**, *144* (11), 5087-5098.

60. Lundahl, M. N.; Yang, H.; Broderick, W. E.; Hoffman, B. M.; Broderick, J. B., Pyruvate formate-lyase activating enzyme: The 5′-deoxyadenosyl radical reactive intermediate caught in the act of H-atom abstraction. *Proc. Natl. Acad. Sci. U. S. A*. **2023**, *120* (47), e2314696120.

61. Bruender, N. A.; Bandarian, V., SkfB abstracts a hydrogen atom from Ca on SkfA to initiate thioether cross-link formation. *Biochemistry* **2016**, *55* (30), 4131-4134.

62. Benjdia, A.; Guillot, A.; Lefranc, B.; Vaudry, H.; Leprince, J.; Berteau, O., Thioether bond formation by SPASM domain radical SAM enzymes: Cα H-atom abstraction in subtilosin A biosynthesis. *Chem. Commun*. **2016**, *52*, 6249-6252.

63. Balty, C.; Guillot, A.; Fradale, L.; Brewee, C.; Lefranc, B.; Herrero, C.; Sandström, C.; Leprince, J.; Berteau, O., Biosynthesis of the sactipeptide Ruminococcin C by the human microbiome: Mechanistic insights into thioether bond formation by radical SAM enzymes. *J. Biol. Chem*. **2020**, *295* (49), 16665-16677.

64. Bushin, L. B.; Covington, B. C.; Rued, B. E.; Federle, M. J.; Seyedsayamdost, M. R., Discovery and biosynthesis of streptosactin, a sactipeptide with an alternative topology encoded by commensal bacteria in the human microbiome. *J. Am. Chem. Soc*. **2020**, *142* (38), 16265-16275.

65. Byer, A. S.; McDaniel, E. C.; Impano, S.; Broderick, W. E.; Broderick, J. B., Mechanistic Studies of Radical SAM Enzymes: Pyruvate Formate-Lyase Activating Enzyme and Lysine 2,3-Aminomutase Case Studies. *Methods in Enzymology* **2018**, *606*, 269-318.

66. Morinaka, B. I.; Vagstad, A. L.; Helf, M. J.; Gugger, M.; Kegler, C.; Freeman, M. F.; Bode, H. B.; Piel, J., Radical S-adenosyl methionine epimerases: regioselective introduction of diverse D-amino acid patterns into peptide natural products. *Angew Chem Int Ed Engl* **2014**, *53* (32), 8503-7.

67. LeMaster, D. M.; Richards, F. M., Preparative-Scale Isolation of Isotopically Labeled Amino Acids. *Anal Biochem* **1982**, *122*, 238-247.

68. Zor, T.; Selinger, Z., Linearization of the Bradford Protein Assay Increases Its Sensitivity: Theoretical and Experimental Studies. *Analytic Biochemistry* **1996**, *236*, 302-308.

69. Rubinson, K. A., Practical corrections for p(H,D) measurements in mixed H_2O/D_2O biological buffers. *Analytical Methods* **2017**, *9* (18), 2744-2750.

70. Kooser, R. G.; Kirchmann, E.; Matkov, T., Measurements of Spin Electron Paramagnetic Concentration in Resonance Spectroscopy. *Concepts in Magnetic Resonance* **1992**, *4*, 145-152.

71. Bode, H. B.; Reimer, D.; Fuchs, S. W.; Kirchner, F.; Dauth, C.; Kegler, C.; Lorenzen, W.; Brachmann, A. O.; Grün, P., Determination of the absolute configuration of peptide natural products by using stable isotope labeling and mass spectrometry. *Chem. Eur. J.* **2012**, *18*, 2342-2348.

72. Kegler, C.; Nollman, F. I.; Ahrendt, T.; Fleischhacker, F.; Bode, E.; Bode, H. B., Rapid determination of the amino acid configuration of xenotetrapeptide. *Chem. Bio. Chem*. **2014**, *15*, 826-828.

CHAPTER FOUR

MECHANISTIC INSIGHTS INTO POST-TRANSLATIONAL α-KETO-β-AMINO ACID FORMATION BY A RADICAL *S*-ADENOSYL METHIONINE PEPTIDE SPLICEASE

Contribution of Authors and Co-Authors

Manuscript in Chapter 4

Author: Anna L. Vagstad

Contributions: Conducted majority of experiments, wrote and edited the manuscript, interpreted results.

Co-Author: Edgars Lakis

Contributions: Conducted experiments, edited manuscript, interpreted results.

Co-Author: Katja-Sophia Csizi

Contributions: Provided DFT calculations (Figure 6), edited manuscript.

Co-Author: William Walls

Contributions: Provided EPR spectroscopic data, prepared figures 4.3, S4.9b, S4.10, S4.11, and S4.12, wrote EPR analysis section of the manuscript, and edited manuscript.

Co-Author: Daniel Richter

Contributions: Conducted experiments, edited manuscript, interpreted results.

Co-Author: Kang Soo Lee

Contributions: Conducted Raman spectroscopy measurements and provided associated methods section, edited manuscript.

Co-Author: Roman Stocker

Contributions: Conducted Raman spectroscopy measurements and provided associated methods section, edited manuscript.

Co-Author: Muriel Gugger

Contributions: provided gDNA for the splicease clusters, edited manuscript.

Co-Author: William E. Broderick

Contributions: Wrote EPR analysis section of the manuscript and edited manuscript.

Co-Author: Joan B. Broderick

Contributions: Wrote EPR analysis section of the manuscript and edited manuscript.

Co-Author: Markus Reiher

Contributions: Provided DFT calculations (Figure 6), edited manuscript.

Co-Author: Jörn Piel

Contributions: Provided oversight for the research direction, interpretation of results, wrote sections of the manuscript, helped edited the manuscript, acquired funding for the research.

Manuscript Information

Anna L. Vagstad, Edgars Lakis, Katja-Sophia Csizi, William Walls, Daniel Richter, Kang Soo Lee, Roman Stocker , Muriel Gugger, William E. Broderick, Joan B. Broderick, Markus Reiher, Jörn Piel

Angewandte Chemie International Edition

Status of Manuscript:
☐ Prepared for submission to a peer-reviewed journal
☐ Officially submitted to a peer-reviewed journal
☐ Accepted by a peer-reviewed journal
☒ Published in a peer-reviewed journal

Wiley
2025, e202418054
10.1002/anie.202418054

Abstract

Radical *S*-adenosylmethionine enzymes catalyze a diverse repertoire of post-translational modifications in protein and peptide substrates. Among these, an exceptional and mechanistically obscure example is the installation of α-keto-β-amino acid residues by formal excision of a tyrosine-derived tyramine unit. The responsible spliceases are key maturases in a widespread family of natural products termed spliceotides that comprise potent protease inhibitors, with the installed β-residues being crucial for bioactivity. Here, we established the in vitro activity of the model splicease PcpXY to interrogate the mechanism of non-canonical protein splicing. Identification of shunt and coproducts, deuterium labeling studies, and density functional theory energy calculations of hypothesized intermediates suggest a mechanism involving hydrogen abstraction at tyrosine Cα as the initial site of peptide radical formation and release of 4-hydroxybenzaldehyde as the tyrosine-derived coproduct. The data illuminate key features of this unprecedented radical-mediated biotransformation yielding ketoamide pharmacophores that are also present in peptidomimetic therapeutics.

Introduction

α-Keto-β^3-amides (from here referred to as ketoamides) are pharmacophores of various peptidomimetic drugs and drug candidates that inhibit serine and cysteine proteases (Figure 4.1a) [1]. Examples are the clinically used narlaprevir **1** that blocks hepatitis C virus protease [2], as well as potent inhibitors of coronaviral proteases [3]. In addition to these synthetic compounds, some non-ribosomally synthesized natural peptides contain ketoamides, such as the trypsin inhibitor cyclotheonamide A **2** [4–7]. Through genome mining and heterologous expression, we

previously discovered a family of post-translational modification enzymes that introduce ketoamide moieties into the α-amino acid backbones of ribosomal peptides and proteins [8]. These enzymes belong to the radical *S*-adenosyl methionine (rSAM) superfamily [9] and act on XYG motifs (X being a variable residue) to catalyze a remarkable splicing reaction involving net tyramine excision (Figure 4.1b). Reconnection of the peptide backbone forms a new C–C bond to elongate residue X with the remaining tyrosine-derived C1 carbonyl unit. The resulting ketoamide residues with variable side chains are the defining feature of a large microbial family of ribosomally synthesized and post-translationally modified peptide (RiPP) natural products termed spliceotides [10]. Bioassays with three select spliceotides revealed all of them as potent protease inhibitors. The CyiA spliceotide **3**, for example, exhibited low nanomolar inhibition of neutrophil elastase, a drug target for inflammatory diseases [10,11]. Furthermore, the splicing reaction has been utilized for protein engineering, with the installed chemically unique α-keto functionality serving as a target site for bioorthogonal labeling [12,13].

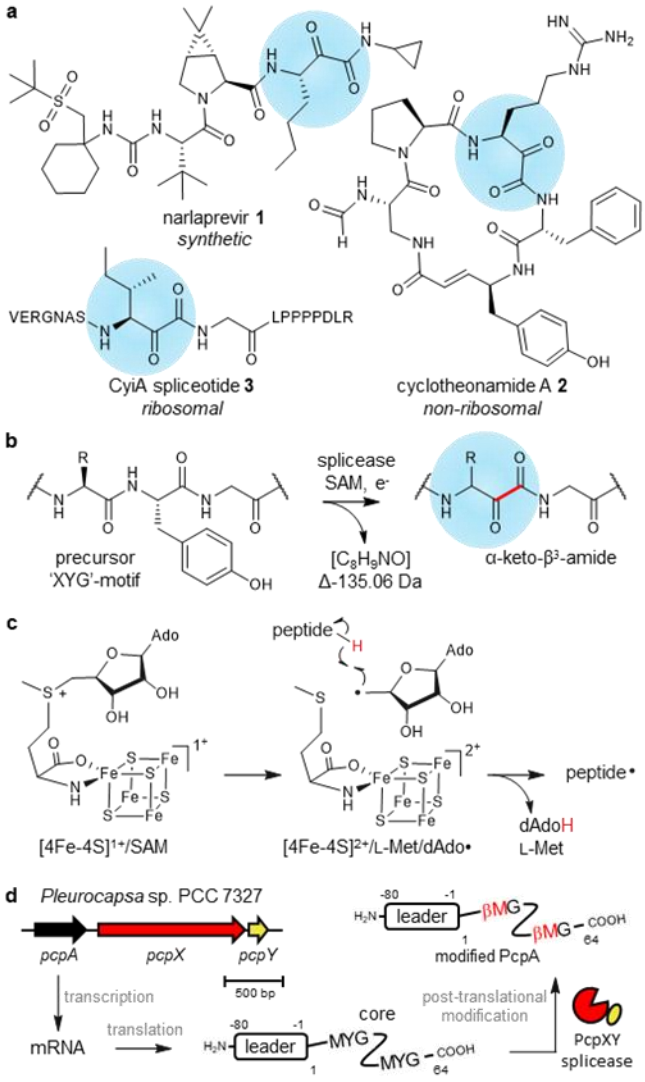


Figure 4.1. Post-translational spliceases modify ribosomally translated precursor proteins. a) A synthetic drug and representative peptide natural products containing the protease-inhibiting ketoamide pharmacophore, highlighted in blue. b) Spliceases catalyze the net excision of tyramine at XYG splice sites. The new bond formed between the C1 of residue X and C1 of the former tyrosine is shown in red. The stereochemistry of the β-amino acid was not determined in this study but was detected as a mixture of the D- and L-isomers from previous coexpression experiments [8]. This position is prone to racemization due to the electrophilicity of the neighboring carbonyl [1]. c) Canonical radical initiation mechanism of peptide-modifying rSAM enzymes. d) The type I splicease biosynthetic gene cluster pcp encoding a Nif11-type precursor (PcpA) containing two MYG splice sites, the splicease (PcpX), and an accessory protein (PcpY) essential for splicing. SAM; *S*-adenosylmethionine. βM; the β-amino acid residue product of Met. dAdo•; 5′-deoxyadenosyl radical. dAdoH; 5′-deoxyadenosine.

RiPPs are matured by post-translational modification of the core region of a gene-encoded precursor [14]. Proteolytic cleavage then releases the mature core from its N-terminal leader (or other recognition elements) to yield the peptide natural product, often concomitant with export outside the cell. In addition to spliceases, rSAM maturases from RiPPs catalyze a myriad of post-translational modifications—including installation of C–C or C–heteroatom cross-links, D-amino acids, and methyl groups—resulting in a large structural and functional diversity [14]. In canonical rSAM catalysis, SAM is reductively cleaved by a coordinating [4Fe-4S] cluster to yield a reactive primary 5′-deoxyadenosyl radical (dAdo•), which abstracts a substrate hydrogen to initiate the reaction (Figure 4.1c) [9, 15]. This [4Fe-4S] cluster is bound by the cysteine thiols of a conserved CX_3CX_2C motif within the rSAM domain (Pfam entry PF04055). Many peptide-modifying rSAM enzymes, including the spliceases, additionally contain a C-terminal SPASM domain (PF13186) that harbors two auxiliary [4Fe-4S] clusters bound by 7–8 cysteine residues [16, 17]. In the case of only seven cysteines, the open iron-coordination site is thought to be important for substrate binding and catalysis.

No precedent exists in nature or synthetic chemistry for the elaborate and as-yet uncharacterized backbone bond breaking and making reactions of spliceases, presenting an intriguing target for mechanistic studies. Here, we established the in vitro activity of the representative type I splicease PcpXY from a cyanobacterium (Figure 4.1d). Characterization of shunt metabolites and coproducts, deuterium-labeling studies, and energy calculations of projected intermediates allowed us to propose a mechanistic hypothesis for splicease catalysis. Insights garnered from these studies expand the knowledge of the diverse reaction paths accessible to rSAM enzymes and might also inspire new methodology in organic synthesis.

Methods and Materials

Materials

Chemicals were purchased from Acros Organics, AppliChem, Fluka, Merck, Rieder, Roth, Sigma-Aldrich, or Tokyo Chemical Industry as eneumerated in Table S4.6. SAM was HPLC-purified, lyophilized, resuspended in 20 mM HCl, adjusted to 100 mM by the UV-Vis absorbance (ε_M = 15,400 M^{-1} cm^{-1} at 260 nm, NanoDrop 2000c spectrophotometer, Witec AG), and stored in aliquots at 80 °C. NucleoSpin™ Plasmid and NucleoSpin™ Gel and PCR Clean-up kits came from Macherey-Nagel. PCR primers were ordered from Microsynth (Balgach, Switzerland). *E. coli* DH5α grown in Lysogeny Broth medium (LB; 5 g/ L yeast extract, 10 g/ L tryptone, 10 g/ L NaCl) was used for cloning and plasmid maintenance. *E. coli* BL21(DE3) was used for expression tests in LB medium and scaled-up production of proteins in Terrific Broth medium (TB; 12 g/ L yeast extract, 20 g/ L tryptone, 0.4% glycerol, 0.017 M KH_2PO_4, 0.072 M K_2HPO_4). Yeast extract and tryptone were Oxoid brand (Thermo Fisher). Solid medium was supplemented with 1.5% agar (Serva). LeMaster and Richard [52] or M9 minimal media were additionally used for expressions with amino acid feeding. Selective antibiotics were used at the following concentrations, unless otherwise stated: 25 µg/mL kanamycin sulfate (Kan), 100 µg/mL ampicillin sodium salt (Amp), 25 µg/mL chloramphenicol (Chl), and 25 µg/mL spectinomycin dihydrochloride pentahydrate (Spt). Endoprotease sources were New England Biolabs for GluC, Promega for Trypsin Gold (MS Grade), and Fugifilm Wako Chemicals for LycC (MS grade).

General

Anaerobic experiments were performed in either a Coy or MBraun (UNIlab pro) glovebox maintained with an 8/92 H_2/N_2 mol% gas mix or 100% N_2 (PanGas), respectively. Protein concentrations were determined by Bradford-type assay using ROTI Nanoquant (Carl Roth) with Bovine Serum Albumin Standard Pre-Diluted Set (Pierce) as the standards. Reagents and kits were used according to the manufacturer's instructions. Protein purification buffers (50 mM Na/PO_4 pH 8.0, 300 mM NaCl, 10% glycerol, with variable imidazole) are named 'Ni-B-X' where X is the concentration of imidazole in mM.

Cloning of splicease expression plasmids

Splicease pathway genes were amplified by polymerase chain reaction (PCR) with Phusion High-Fidelity DNA Polymerase (Thermo) from genomic DNA templates (Pleurocapsa sp. PCC 7319, Pleurocapsa sp. PCC 7327, Nostoc sp. PCC 7120, Nostoc punctiforme PCC 73102, and Pseudanabaena sp. PCC 6802) provided by the collection Pasteur Cultures of Cyanobacteria (Paris, France). Primer sequences and PCR conditions are provided in Table S4.3–S4.4 and the Supporting Methods. PCR products were digested with NdeI and XhoI restriction enzymes and ligated into customized pCDFDuet-1 (Novagen) plasmids containing N-terminal His_6-tags with optional MBP or bdSUMO21 solubility-tag fusions using T4 DNA ligase (NEB). Ligation reactions were transformed into E. coli DH5α and plated on LB agar supplemented with 50 μg/mL Spt. Plasmids were purified from cultures inoculated with a single colony (NucleoSpin™ Plasmid kit), and inserts were sequence verified (Sanger sequencing, Microsynth).

Protein production tests

Expression plasmids were transformed into *E. coli* BL21(DE3) and plated on LB agar. Protein was produced in LB medium (100 mL) inoculated with 1:100 (v/v) saturated overnight culture and grown at 37 °C and 200 rpm to an optical density 600 nm (OD_{600}) of ~0.7–1.0, cooled 5 min on ice, induced with 1 mM IPTG, and expressed for 20–24 h at 18 °C with 150/200 rpm shaking for spliceases/precursors and Y-proteins in 500 mL baffled Erlenmeyer flasks. Cells were harvested by centrifugation (5,000 × g, 10 min) and stored at -80 °C until use. Purification steps were performed on ice or with chilled buffers. Cell pellets were resuspended in 4 mL Ni-B-0, lysed by sonication (40% amplitude, 10 × 10 s on/10 s off, 1 mm probe, Q700 Sonica), and clarified by centrifugation (18,500 × g, 30 min). The supernatant was purified by bench-top, gravity flow Ni^{2+}-affinity column chromatography over 250 µL cOmplete™ His-Tag Purification Resin (Roche) in Poly-Prep™ Chromatography Columns (BioRad). Resin was washed with 30 column volumes (CV) Ni-B-0 and 4 CV Ni-B-20, then eluted with 2x 1 CV Ni-B-250. Samples were analyzed by SDS-PAGE (Laemmli method [53]) and a subset by anti-His Western Blot to assess yield, solubility, and stability (see Figure S4.1).

Protein production and purification

Large-scale production of proteins was performed in *E. coli* BL21(DE3) grown in TB medium (1 L) in ULTRA Yield flasks (Thompson) and purified by Ni^{2+}-affinity column chromatography, similar to above for the test expressions and as previously described (induced with 1 mM IPTG at ~OD_{600} 1.5–2.0 after cooling on ice, expressed at 18 °C for 18–24 h) [41]. Cultures expressing pcpX or pcpXY were supplemented with $FeCl_3$ (25 µM) upon inoculation. Extra $FeCl_3$ (25 µM) and L-cysteine (300 µM) were additionally supplemented prior to induction. Harvested cells were resuspended in Ni-B-5 (4 mL/1 g wet cell paste) supplemented

with 1x cOmplete™ Protease Inhibitor Cocktail (Roche), lysed by sonication (70% amplitude, 10 × 10 s on/10 s off, 12 mm probe, Q700 Sonica), and following centrifugation (27,000 × g, 30 min), the decanted supernatant was bound to cOmplete™ His-Tag Purification Resin (Roche) for 1 h with rocking. Resin was washed 2x 10 CV Ni-B-0, collected by centrifugation (800 × g, 10 min), and transferred to Kimble™ Kontes™ FlexColumns. Protein was purified using a bench-top step gradient (2× 10 CV Ni-B-0, 2× 1 CV Ni-B-20, and eluted with 3× 0.5 CV Ni-B-250). For PcpX and PcpXY, 5 mM DTT was supplemented in the standard purification buffers. Proteins were concentrated by Amicon Ultra Centrifugal Filters (Merck Millipore), introduced to the anaerobic chamber, and buffer exchanged over PD-10 desalting columns (Cytiva) into Buffer A (50 mM HEPES pH 8.0, 150 mM KCl, 10% glycerol).

E. coli MTA nucleosidease (MTAN), cysteine desulfurase (IscS), flavodoxin (FldA), flavodoxin reductase (Fpr), and tryptophanase (TnaA) were produced from the ASKA clone(-) collection strains [54] as N-terminal His_6-tag fusion proteins in E. coli K-12 strain AG1 and purified by standard Ni^{2+}-affinity column chromatography as previously described for MTAN [41].

For production of stable isotope-labeled PcpA variants, L-tyrosine ($^{13}C_9$, 97-99%), L-tyrosine (d_7, 98%), and L-tyrosine (3,3-d_2, 98%) were purchased from Cambridge Isotope Laboratories, and glycine (2,2-d_2, 98%) from Sigma Aldrich. L-Tyrosine (2-d, ~97%), was biosynthesized from L-tyrosine using tryptophanase TnaA in deuterium oxide buffer by the previously reported method [25]. For retention of the Cα-deuterium labels, ($^2H_7$)-Tyr, (2-^{2}H)-Tyr, and (2,2-$^2H_2$)-Gly were incorporated into PcpA by feeding in LeMaster and Richards (LR) minimal medium expression cultures for E. coli Δpenta transaminase deletion mutant strain [26]

harboring pBad-6xH-v-PcpA and induced with 0.2% (+)-arabinose as previously described for our work with rSAM epimerases [41]. ($^{2}H_{7}$)-Tyr was similarly fed to *E. coli* BL21(DE3) harboring pCDF-6xH-v-PcpA in LR minimal medium induced with 1 mM IPTG to give predominantly (3,3,2′,3′,5′,6′-$^{2}H_{6}$)-Tyr labelled protein with H–D mostly exchanged at the Tyr-Cα. ($^{13}C_{9}$)-Tyr and (3,3-$^{2}H_{2}$)-Tyr were fed to expression cultures of BL21(DE3) harboring plasmid pCDF-6xH-v-PcpA in M9 minimal medium induced with 1 mM IPTG. His_{6}-tagged PcpA variants were purified by standard Ni^{2+}-affinity column chromatography and exchanged to anaerobic Buffer A in the glove box.

Anaerobic reconstitution of splicease iron-sulfur clusters

The optimized reactions for reconstitution of the iron-sulfur clusters was 200 μM PcpX(Y), 4 mM DTT, 2.6 mM Iron(II) ethylenediammonium sulfate tetrahydrate, 2.4 mM L-cysteine, 1 μM IscS, 5 μM pyridoxal 5′-phosphate (PLP) in Buffer A incubated at room temperature in 0.5 or 2.5 mL volume with a typical incubation time of 4 h, but up to overnight. Reconstituted PcpX(Y) was buffer exchanged by PD-10 Mini (0.5 mL volume) or MidiTrap (2.5 mL volume) desalting columns into Buffer A. Protein was optionally concentrated by 10 kDa MWCO Amicon Ultra concentration devices. Unused protein was stored anaerobically at 35 °C and could be thawed for use with minimal loss of activity.

In vitro splicease reactions

Unless otherwise stated, reactions contained 50 μM reconstituted PcpXY, 100 μM PcpA, 1 mM SAM, 10 mM DTT with biological reductant (20 μM FldA, 5 μM Fpr, 2 mM NADPH) in Buffer A. Chemical reductants (1 mM sodium dithionite, 1 mM methyl viologen) were optionally used instead of biological reductants. Reaction aliquots were quenched with an equal

volume of 0.5 M formic acid to detect small molecule products. As the acid quench gave variable results for detection of the splicease peptide products (after neutralization and protease digest), reaction aliquots (2.5 μL) were instead directly quenched by dilution into protease cleavage mix (7.5 μL): GluC cleavage mix (1.3×) contained 0.02 μg/μL GluC, 0.32 mM Glu-Glu, 1.3 mM DTT, 67 mM Tris pH 8; GluC + trypsin cleavage mix was the same with 0.01 μg/μL trypsin and 0.33 mM $CaCl_2$ added.

For reactions in deuterium oxide (D_2O), PcpXY and PcpA were buffer exchanged into Buffer A lacking glycerol prepared with D_2O (99.9%, Aldrich) as previously described [41], which also served as the reaction buffer. PcpA was stored in the D_2O buffer lacking glycerol; however, PcpX(Y) was prone to slow precipitation under these conditions. Thus, reconstituted PcpX(Y) was buffer exchanged immediately prior to use. Other reagents were in H_2O solutions to give ~90% (v/v) enrichment of D_2O in the final reactions.

For the reaction set with deuterium labelled PcpA variants (Figure S4.14), standard reaction conditions were used with the '6xH-MBP-v'-tagged version of PcpXY and aliquots were quenched at 21 h. For the follow-up reaction set (Figure 4.4, Figure S4.17), 20 μM reconstituted PcpXY ('6xH-bdSUMO' tagged), 40 μM PcpA, 1 mM SAM, and 10 mM dithiothreitol (DTT) in Buffer A with biological reductants: 5 μM FldA, 1.25 μM Fpr, and 1 mM NADPH was used and aliquots were quenched at 15 min, 60 min, and 16 h.
For detection of 4-hydroxybenzaldehyde 7 (Figure 4.5b), ($^{13}C_9$)-Tyr-PcpA (Figure S4.13) was used as the substrate.

LC-HRMS analyses

LC-HRMS analyses were performed on a Dionex Ultimate 3000 UHPLC coupled to a Thermo Scientific Q Exactive Hybrid Quadrupole-Orbitrap Mass Spectrometer using heated electrospray ionization. LC-HRMS solvents were Optima™ LC-MS grade from Fisher Scientific and the formic acid additive was from Carl Roth. Double-distilled water was obtained from a PURELAB Chorus system (ELGA Veolia). Expected masses were calculated using the ChemCalc online tool [55] and data was analyzed using Thermo Xcaliber Qual Browser (v.4.1.31.9) with peak areas determined by the ICIS peak detection algorithm using the EICs with 10 ppm error and default settings. The most abundant charge state and isotopes were used to generate the EICs (Table S4.5).

Specific details of individual LC-HRMS methods are provided in the Supporting Information. Briefly, peptides were separated over Phenomenex Kinetex® 2.6 µm XB-C18 100 Å columns using gradient methods with water + 0.1% formic acid as solvent A and acetonitrile + 0.1% formic acid as solvent B in positive ion mode. Small-molecule products associated with the lost tyramine equivalent in splicease reactions (e.g., 4-hydroxybenzaldehyde 7 and derivatized cyanide or formaldehyde) were detected in negative ion mode using a gradient method with water as solvent A and methanol as solvent B over a Phenomenex 5 µm C18 Luna (150 × 4.6 mm) column.

dAdoH and L-Met were detected as previously described [41]. Advanced Marfey's analysis with L-FDVA derivatized peptide hydrolysates and tyrosine standards were detected as previously described [56, 57].

Quantification of splicease iron and sulfide content

Bound iron was quantified using the method of W.W. Fish with $FeCl_3$ as the standard [58]. Labile sulfide was quantified using the method of H. Beinert with LiS_2 as the standard [59]. Samples of as-purified and anaerobically reconstititued PcpXY were measured in triplicate in disposable polystyrene semi-micro cuvettes in a NanoDrop 2000c spectrophotometer.

UV-Vis Spectroscopy

UV−Vis spectra were recorded using an Agilent Cary 60 spectrophotometer scanning from 800 to 200 nm at 600 nm/min. Samples were measured in Spectrosil Quartz cuvettes (Starna Cells, CA, USA) with a 10 mm path length. Reconstituted PcpXY was diluted to 4 μM with buffer (50 mM HEPES pH 7.5, 150 mM KCl, 1 mM DTT, 5% (v/v) glycerol) for analysis.

EPR Spectroscopy

Continuous wave X-band EPR spectroscopy was performed using a Bruker EMX EPR spectrometer equipped with a Bruker/ColdEdge (Sumitomo Cyrogenics) 10 K waveguide cryogen free system with an Oxford MercuryiTC controller unit and helium Stinger recirculating unit (Sumitomo Cyrogenics, ColdEdge Technologies). Samples were prepared in an MBraun glove box. PcpXY (0.1 mM) was reduced by incubating with 1 mM DTT and 3 mM sodium dithionite for 10 min. The sample was briefly centrifuged (16,200 × g, 30 s) then transferred to an EPR tube containing buffer (50 mM HEPES pH 8.0, 150 mM KCl, 5% (v/v) glycerol) and mixed thoroughly before being capped, passed out of the glove box, and flash frozen in liquid nitrogen. For samples containing SAM, following reduction of PcpXY, the sample was mixed in an EPR tube with buffer and 1 mM SAM before being capped, passed out the glove box, and flash frozen. For as-reconstituted PcpXY, 0.2 mM was diluted in buffer (75 mM Tris-HCl, pH 9, 300 mM KCl, 10% (v/v) glycerol), transferred to an EPR tube, and flash frozen in liquid

nitrogen. EPR parameters: microwave frequency 9.38 GHz, modulation amplitude 10 Gauss, modulation frequency 100 kHz, Sweep width: 1000 Gauss, Center field: 3480 Gauss, time constant: 164.84 ms, average of 2 scans, 20 dB gain. EPR spectra was plotted using Easyspin [60] within the Matlab R2020b software suite (MathWorks). All spectra are cavity subtracted and baseline corrected.

Characterization of the isomeric shunt product

PcpA core peptides from standard three-day in vitro reactions (1 mL each: '-SAM control' and 'complete') were released by digestion with LahT150 protease [61] and purified by reverse Ni^{2+}-affinity column chromatography followed by solid phase extraction (Strata X-33-100 mg, Phenomenex) using a methanol step gradient in water (20% steps). The 100% methanol fractions were dried (EZ-2 Elite GeneVac evaporator), resuspended in 100 µL water, and the concentration was approximated by UV-Vis spectroscopy (Nanodrop 2000c) using an ε_{280nm} of 20,970 M^{-1} cm^{-1} for the PcpA core predicted by the Expasy, ProtParam tool [62]. The control and complete reaction samples contained approximately 84 µg and 115 µg peptide, respectively. To the samples, 100 µL 12 N HCl was added and incubated at 100 °C for 6.5 h in sealed glass vials. Hydrolysates (27 µL) were treated with 1 M $NaHCO_3$ (3 µL) and mixed with 1% L-FDVA in acetone (30 µL), then incubated at 50 °C for 1 h. Samples were neutralized with 2 N HCl (1.5 µL) and an aliquot was diluted 2-fold with 1:1 (v/v) acetonitrile:water. Samples (10 µL injections) were analyzed by LC-HRMS as described in Morinaka et al. 2014 [56] and compared to authentic samples of L-FDVA-derivatized L- and D-tyrosine.

Heterologous coexpression and culture extraction
of Type III splicease genes from Thiothrix nivea

BL21(DE3) strain was transformed with codon optimized precursor plasmid (pACYC_His6-SUMO-ThnA, WP_002708734) and splicease plasmid (pRSF_ThnX, WP_002708735) selected on LB agar supplemented with Chl and Kan.10 Fresh overnight (37 °C) bacteria culture (300 µL) was inoculated in 30 mL M9 minimal medium in a 100 mL smooth Erlenmeyer flask. At OD_{600} > 1.5 (~8 h) the flask was cooled in an ice bath for 30 min and protein production was induced with 1 mM IPTG. ($^{13}C_9$)- L-Tyrosine solution (10 mL, 2 mg/mL) was added at the same time as IPTG. The cultures were incubated at 24 °C with 180 rpm shaking for 48 h. Cells were pelleted (9,500 × g, 10 min). The separated supernatant was directly used for small molecule detection (see cyanide and formaldehyde detection sections below). Fresh supernatant (30 mL) was transferred to a 50 mL conical plastic tube and mixed with ethyl acetate (20 mL), vortexed and centrifuged (10,000 × g, 5 min). The two-phase solution was left to separate for an additional 2 h at room temperature. The upper ethyl acetate layer was removed by Pasteur pipette. The lower aqueous part was extracted again with fresh ethyl acetate (20 mL). Pooled ethyl acetate was dried on a rotary evaporator, dissolved in 50% methanol in water (50 µL) and centrifuged (13,000 × g, 1 min). The supernatant extract was analyzed by LC-HRMS as described above.

The ThnA precursor was purified from the cell pellet by Ni^{2+}-affinity column chromatography, cleaved with endoprotease LysC, and analyzed by LC-HRMS as previously described [10].

Attempts to detect small-molecule coproducts

4-Hydroxybenzaldehyde (7) was detected by LC-HRMS. Samples were ethyl acetate extracts of the T. nivea splicease expressed in E. coli (see above) and Pcp in vitro reactions either

filtered through a VivaSpin 500 Ultrafiltration device (3 kDa) or quenched with 10% trifluoroacetic acid. The Supporting Information holds detailed information regarding failed attempts to detect cyanide or fromaldehyde. Detection methods were verified by spiking reactions with the relevant standard. Cyanide detection was attempted by Spectroquant® Kit Cyanide Test (Merck), derivatization with 2,3-naphthalenedialdehyde [29], and gold-nanoparticle-based surface-enhanced Raman microspectroscopy [31]. Formaldehyde production was assessed by derivatization with 2,4-dinitrophenylhydrazine (DNPH) and analysis by LC-HRMS [30].

Density Functional Theory calculations

Density Functional Theory (DFT) calculations were carried out with the TURBOMOLE (version 7.2.0) [63] and ORCA [64, 65] (version 4.2.0) suites of programs. DFT structure optimizations applied the PBE [66, 67] density functional and a Ahlrichs def2-TZVP basis set [68]. For all structural motifs containing the [Fe4-S4] cubane, the broken-symmetry DFT approach was applied by converging to the high-spin solution and then re-assigning electrons to the other spin symmetry at selected local sites sites followed by reoptimization of the orbitals. Grimme's D3 [69] dispersion correction was invoked in all calculations. We report electronic energy differences at zero Kelvin as an approximation to reaction enthalpies. A guess structure for the [4Fe-4S] cluster and AdoMet were extracted from X-ray crystallography data of a related rSAM protein (PDB-ID: 3IIX) and subsequently reoptimized. Local spin expectation values were obtained by employing Löwdin's projection operators [70].

Protein expression and purification for EPR

The pCDF-6xH-v-pcpXY plasmid containing the 6xHis-tagged PcpX and PcpY genes was used to transform chemically competent Rosetta(DE3) pLysS cells. A single colony was used to inoculate 50 mL of LB media (10 g/L tryptone, 10 g/L NaCl, 5 g/L yeast extract) containing 50 µg/mL Spt and 33 µg/mL Chl then grown at 37 °C with 180 rpm shaking overnight. The seed culture (7 mL/L) was used to inoculate 6 L of TB media (12 g/L tryptone, 24 g/L yeast extract, 0.5% glycerol, 89 mM KP_i, pH 7.2) then grown at 37 °C with 180 rpm shaking until an OD_{600nm} of 0.8 was reached. The cultures were then cooled at 4 °C for 3 h before receiving 0.3 mM ferrous ammonium citrate, 0.3 M L-cysteine, and 1 mM IPTG. The cultures were then grown at 20 °C with 180 rpm shaking for 18 h. Cells were harvested by centrifugation (4750 × g, 15 min, 8 °C) before being flash frozen in liquid nitrogen. Cells were then stored at -80 °C.

Cells containing PcpXY were introduced to the anaerobic chamber (COY). Cells were combined with lysis buffer (75 mM Tris-HCl pH 9.0, 300 mM KCl, 10% glycerol, 1% triton X-100, 0.2 mg/ mL DNAse, 0.2 mg/ mL RNAse, 0.2 mg/ mL lysozyme, 25 mg/ mL $MgCl_2$) at a ratio of 2 mL/g cell paste and allowed to incubate for 2 h. The cell lysate was then sonicated at 4 °C, for 5 min (5 s on, 10 s off, 40% amplitude). The lysate was then clarified by centrifuging at 26,790 x g for 60 min at 14 °C. The clarified lysate was brought into the COY chamber and loaded onto 2, 5 mL Ni-NTA columns (Cytiva) equilibrated in buffer (75 mM Tris-HCl, pH 9.0, 300 mM KCl, 10% glycerol). The column was then washed with 4 CV of buffer containing 40 mM imidazole. The protein was then eluted from the column with 3 CV of buffer containing 150 mM imidazole. The eluted protein was concentrated to about 2.5 mL using 30 kDa MWCO spin

filters (Amicon). The protein was de-salted over a NAP25 column (Cytiva) equilibrated in buffer before being concentrated, flash frozen in liquid nitrogen, and stored at -80 °C.

Enzymatic reconstitution for EPR

Purified PcpXY and E. coli CsdA were brought into the COY chamber to thaw. CsdA was expressed and purified as previously described [71]. Ferrous ammonium sulfate (FAS), L-cysteine, and DTT were brought in as powders, then brought up to 100 mM stock solutions with buffer (50 mM HEPES pH 8.0, 150 mM KCl, 5% glycerol). In a scintillation vial, PcpXY was diluted to 0.1 mM in buffer with gentle stirring. DTT, FAS, and cysteine were added to final concentrations of 2, 1, and 3 mM, respectively. CsdA was added to 2 μM final concentration to initiate the reaction. After 3 h, the reaction was centrifuged at 16,200 × g for 10 minutes, then de-salted over 90 mL of Sephadex G-25 (Cytiva) into buffer (50 mM HEPES pH 8.0, 150 mM KCl, 5% glycerol, 1 mM DTT). The eluted protein was concentrated to about 1.5 mL, then aliquoted, flash frozen, and stored at -80 °C.

Protein, iron and sulfide quantification
of protein prepared for EPR

Protein was quantified by the method of Zor and Selinger [72], except that concentrated Bradford dye reagent (Bio-Rad) was diluted to 1x concentration for use. To determine a correction factor for the Bradford assay, an aliquot of purified PcpX was buffer exchanged into amino acid analysis buffer (50 mM HEPES pH 7.5, 100 mM KCl) using a Sephadex G-25 column (90 mL). The eluate was collected and concentrated using 30 kDa MWCO centrifugal spin filters (Amicon). Three independent Bradford assays were performed and the average concentration was calculated. An aliquot of PcpX was then diluted to 1 mg/mL based on this

value and sent to the Protein Chemistry Lab at Texas A&M University to be analyzed by amino acid analysis in triplicate. The average protein concentration determined by amino acid analysis was divided by the Bradford determined protein concentration to yield a correction factor of 0.756 ± 0.066. This value is then multiplied by the concentration determined by the Bradford assay to yield the corrected protein concentration.

For iron quantification, PcpXY was diluted to 1 μM in buffer in triplicate. Buffer and samples were then analyzed by atomic absorption spectroscopy (Agilent 240 FS) and compared to a standard curve generated using an iron standard (Ricca, 1000 ppm in 3% HNO_3). Acid-labile sulfide was quantified as previously described [71]. Following reconstitution, PcpXY contained 13.2 ± 0.2 Fe and 11.1 ± 0.4 sulfide per monomer.

Results

Establishment of in vitro splicease activity

rSAM enzymes are inherently challenging to work with in vitro due to their oxygen-sensitive iron-sulfur clusters. For this study, we selected five pathways for protein production and solubility screens (Table S4.1–4.4). The pathways belong to the initially discovered type I spliceotide family from Cyanobacteria [8] and comprise one or several Nif11 type precursors (designated protein A), the splicease (protein X), and an essential accessory protein (protein Y). Eleven types of spliceotide biosynthetic gene clusters from diverse bacteria and some archaea have been identified to date [10]. Types are differentiated by the phylogeny of the splicease and the class of precursor protein substrate. The Nif11 precursor leaders derive their name from similarity to a nitrogen fixation-associated protein and are also found in other RiPP families [18]. The accessory Y proteins are uniquely found in the type I spliceotide pathways and are hypothesized

to serve as RiPP recognition elements (RREs) [19] that mediate protein–protein interactions between the precursor leader and the splicease. Expression tests in *E. coli* indicated that the *pcp* pathway from *Pleurocapsa* sp. PCC 7327 [20] yielded N-terminally His-tagged proteins with the best overall yields and good aerobic stabilities (Figure S4.1). The PcpA precursor contains a 64-amino-acid core with two MYG motifs at Tyr15 and Tyr56 (Figure 4.2a), which were previously shown to be the targets of the PcpXY splicease in *E. coli* heterologous expression experiments [8].

To conduct in vitro assays, PcpX (alone or together with PcpY) and PcpA were heterologously produced in *E. coli* BL21(DE3) and aerobically purified by Ni^{2+}-affinity column chromatography (Figure S4.2). Fusion of PcpX to a SUMO solubility tag [21] improved protein yields and was used in later experiments. The [4Fe-4S] clusters of PcpX were reconstituted anaerobically and the *holo* enzyme used for in vitro reactions. PcpA core peptide fragments were detected by liquid chromatography–high-resolution mass spectrometry (LC-HRMS) following protease digest (Table S4.5). Small molecule products were directly detected from acid-quenched reactions by LC-HRMS.

Overnight reactions were digested with glutamyl endopeptidase (GluC) to release the peptide fragment corresponding to PcpA residues -7 to 64 ($PcpA_{-7–64}$), where position 1 refers to the start of the core. In addition to a peptide fragment derived from the unmodified substrate **4**, we detected another Δ-135.06 Da peptide product **5**, consistent with ketoamide formation at one of the two possible splice sites (Figure 4.2b). The ketoamide peptide is detected as a mixture with its α-ketone hydrate **5'** resulting from water addition. Separation of the PcpA splice sites by additional cleavage with trypsin to release $PcpA_{-7–26}$ and $PcpA_{32–64}$ confirmed Tyr15 as the

preferred splice site with only trace amounts of modified Tyr56 evident (Figure 4.2c, Figure S4.3). In some efficient reactions, a doubly modified PcpA$_{-7–64}$ Δ-270.12 Da species was detected (Figure S4.4). In addition to the spliced products, we also detected a new peptide **6** that was equivalent in mass to the substrate, suggesting it is an isomerized shunt product. Whereas the ketoamide **5** was already abundant after 15 min and maximally produced after approximately 2 h, the isomer **6** predominantly accumulated at later timepoints (Figure S4.5).

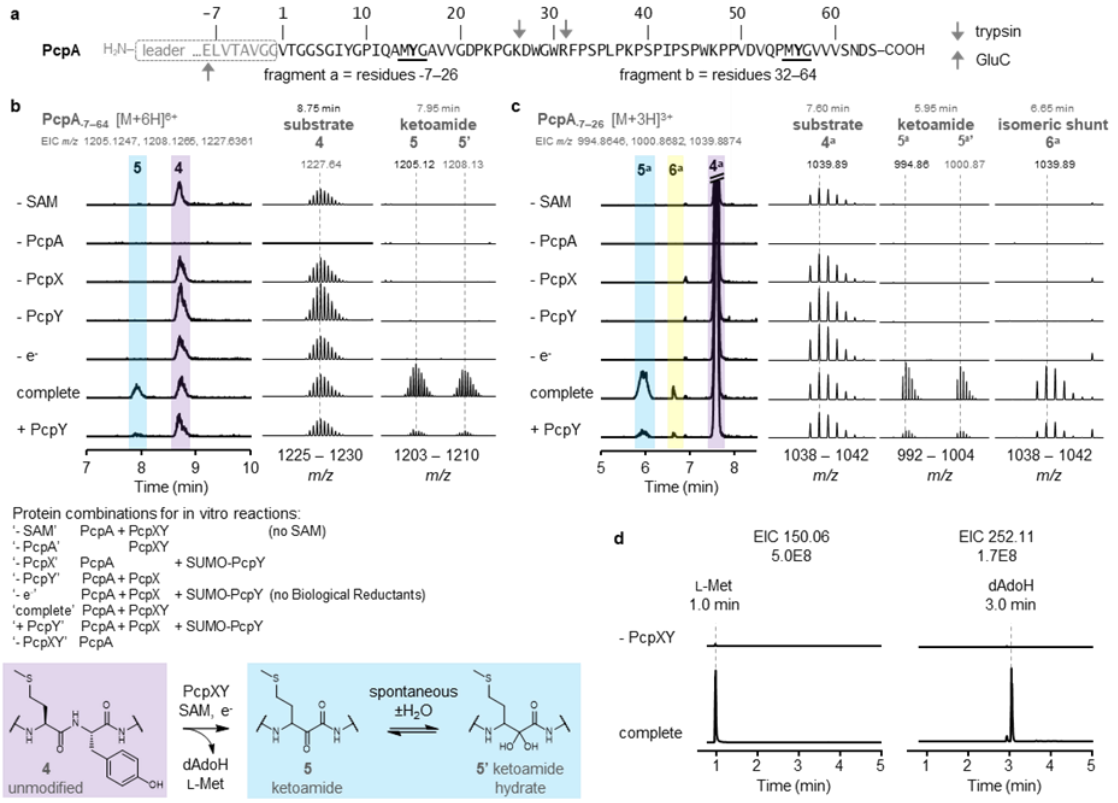


Figure 4.2. In vitro splicease activity detected by LC-HRMS. a) Partial sequence of the PcpA precursor containing the relevant C-terminal core fragments. Splice sites at Tyr15 and Tyr56 are underlined. LC-HRMS extracted ion chromatograms (EICs) for the substrate and product peptide fragments for b) GluC-released PcpA$_{-7–64}$ and c) GluC and trypsin-released PcpA$_{-7–26}$. Only trace amounts of ketoamide product were detected for the PcpA$_{32–64}$ peptide fragment (see Figure S4.3). Ion counts are normalized within each panel. Protein combinations for each reaction are-as described using the biological reductant system (FldA, Fpr, and NADPH) as the electron source and SAM as the cosubstrate. Reactions additionally contain DTT. d) Detection of L-Met and dAdoH splicease coproducts for the complete reaction relative to the negative control lacking

PcpXY. Structures of the peptide substrate and ketoamide products are shown for the net splicease reaction (lower left).

As expected, controls demonstrated that PcpA, PcpX, PcpY, SAM, and reductant were essential reaction components. Inclusion of dithiothreitol (DTT) improved yields, and the biological reductant system [i.e., flavodoxin (FldA), flavodoxin reductase (Fpr), and nicotinamide adenine dinucleotide phosphate (NADPH)] was more effective than chemical reductants (i.e., sodium dithionite and methyl viologen) to generate spliced products (Figure S4.6). Reactions with PcpX expressed alone were complemented by addition of SUMO-tagged PcpY ('+ PcpY' sample, Figure 4.2b–c, Figure S4.3). Furthermore, untagged PcpY co-elutes with His_6-tagged PcpX purified by Ni^{2+}-affinity column chromatography (Figure S4.7) and provision of extra PcpY to complete reactions did not improve conversion (Figure S4.8), indicating PcpX and PcpY form a stable protein complex.

The reductive cleavage products of SAM, 5′-deoxyadenosine (dAdoH) and L-methionine, accumulated in reactions as coproducts (Figure 4.2d). Thus, SAM appears to act as a substrate rather than a regenerated cofactor, in line with other studies on peptide-modifying rSAMs [22]. Initially, no small-molecule products associated with the lost tyramine unit could be identified.

Spectroscopic characterization of reconstituted PcpXY

Next, we assessed the spectroscopic properties of the splicease and its iron-sulfur clusters. PcpXY was purified aerobically and buffer-exchanged to deoxygenated buffer in an anaerobic chamber. A sample of this as-purified PcpXY was retained and compared to the reconstituted enzyme regarding in-vitro activity and iron and sulfide content (Figure S4.9). As-purified PcpXY contained 5.15 ± 0.02 Fe and 6.08 ± 0.19 S^{2-}, consistent with one intact [4Fe-4S]

cluster being present on average. Upon reconstitution, iron and sulfide content increased to 13.6 ± 1.5 and 11.7 ± 0.4, respectively, and the protein developed a prominant UV-Vis absorption band at 410 nm, suggesting three intact [4Fe-4S] clusters are present, as expected for rSAM-SPASM enzymes. Only a trace amount of the ketoamide product was observed for the as-purified splicease, while the reconstituted enzyme produced the ketoamide peptide as described in the previous section.

Reconstituted PcpXY was further characterized by electron paramagnetic resonance (EPR) spectroscopy. The as-reconstituted protein is primarily EPR silent, exhibiting only a small signal with g-values indicative of a $[3Fe\text{-}4S]^{+}$ cluster (Figure S4.10) [23]. Reduction of PcpXY with dithionite yields a composite spectrum composed of multiple overlapping signals (Figure 4.3). All component signals exhibit temperature-relaxation (Figure S4.11) and power saturation (Figure S4.12) behavior consistent with their assignment to $[4Fe\text{-}4S]^{+}$ clusters [24]. Addition of SAM to reduced PcpXY significantly perturbed one of the component signals, as evidenced most clearly by the reduced intensity of the g = 2.018 feature and the appearance of a new feature at g = 1.868. The perturbation of primarily one signal is consistent with SAM coordination to the unique iron of the rSAM [4Fe-4S] cluster, as occurs in a wide range of rSAM enzymes [9]. Addition of SAM also leads to an overall sharpening of signals and the resulting observation of previously unresolved features. While SAM is not expected to directly interact with the iron-sulfur clusters of the SPASM domain, sharpening of the EPR spectrum suggests that SAM binding has structural implications beyond the rSAM cluster.

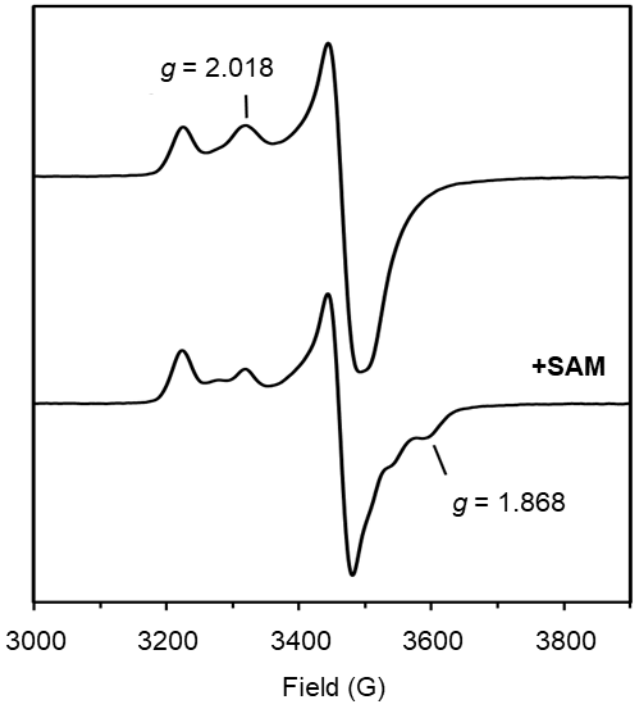


Figure 4.3. X-band EPR spectra of reconstituted and sodium dithionite–reduced PcpXY in the presence and absence of SAM. EPR conditions: microwave frequency, 9.38 GHz; microwave power, 0.1 mW; modulation, 10 G; and T = 10 K.

Deuterium labeling studies define
the site of initial H-abstraction

We then considered which hydrogen is abstracted by dAdo• to initiate catalysis. PcpA variants were differentially labeled with deuterium at the conserved YG of splice sites, and transfer of the label to dAdoH was assessed by LC-HRMS analysis of in vitro reactions. The PcpA variants were obtained by individually feeding the commercially available amino acids ($^{2}H_{7}$)-Tyr, (3,3-$^{2}H_{2}$)-Tyr, and (2,2-$^{2}H_{2}$)-Gly in minimal medium expressions and purifying the resulting precursors (Figure S4.13). Reactions in deuterium oxide were additionally conducted to test whether an exchangeable hydrogen—for example, at the phenol oxygen of tyrosine or of the amide nitrogens—was involved in H-abstraction. The *m/z* 253.12 ion corresponding to

$[M+H]^+$ of dAdoD was only enriched for overnight reactions with ($^2H_7$)-Tyr-labeled PcpA and in deuterium oxide (Figure S4.14). Monitoring of reaction timepoints in deuterium oxide showed only a delayed accumulation of the dAdoD product that did not correspond to the early formation of the ketoamide, demonstrating it arises from a shunt process (Figure S4.15). Thus, the results support the Cα of tyrosine as the probable site of initial H-abstraction.

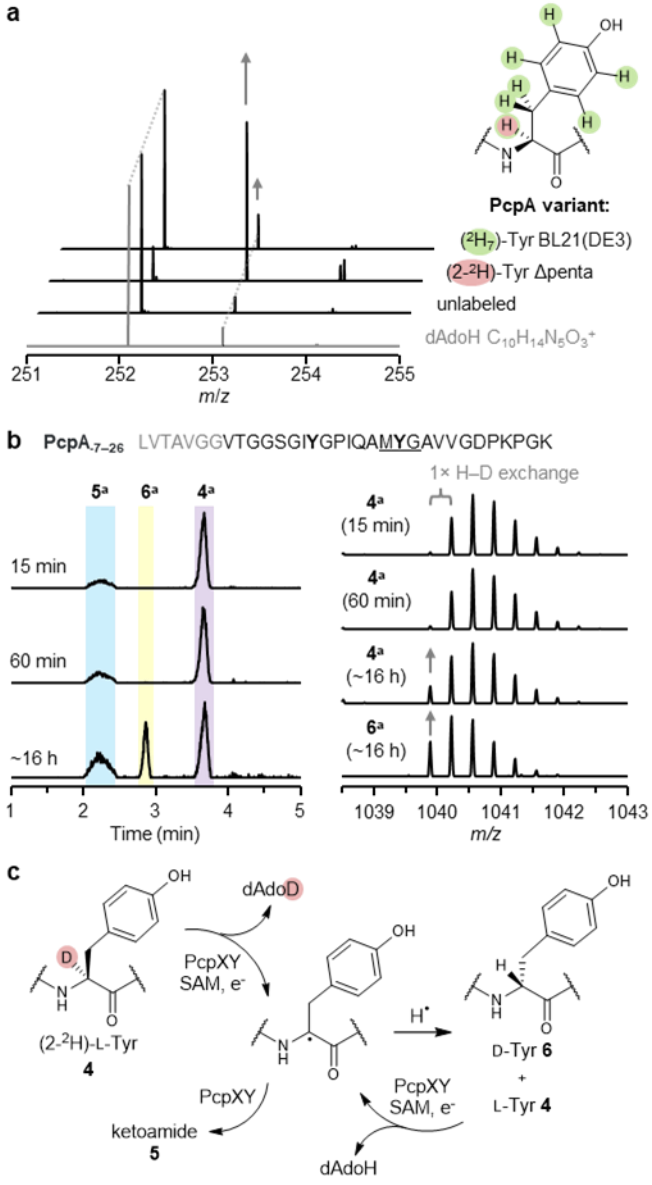


Figure 4.4. Deuterium-labeling studies of in vitro splicease reactions. a) Mass spectra of dAdoH/D products detected from reactions with deuterium-labeled PcpA substrate variants relative to the unlabled control (60 min). The dAdoD product at *m/z* 253.12 accumulates in the (2-^{2}H)-Tyr PcpA substrate produced in the transaminase deletion strain *E. coli* Δpenta. Note that the Cα deuterium of the fed ($^2H_7$)-Tyr is depleted by reversible transamination in BL21(DE3) to yield predominantly ($^2H_6$)-Tyr-labeled PcpA. The simulated mass spectrum of dAdoH with natural isotope abundance is shown for comparison. b) LC-HRMS analysis of the (2-^{2}H)-Tyr PcpA substrate reaction. EICs for the substrate and product peptide fragments for PcpA$_{-7–26}$ released by GluC and trypsin digest are shown (left). Only the spliced ketoamide **5** was detected in the early 15 and 60 min timepoints. Mass spectra (right) show the depletion of the deuterium label from substrate **4** in the 16 h timepoint concomitant with formation of the H–D exchanged isomeric shunt 6. c) Rationale for accumulation of unlabeled dAdoH and H–D exchanged **4** at later timepoints of the (2-^{2}H)-Tyr PcpA reaction.

To further probe the importance of this site, (2-^{2}H)-L-Tyr was enzymatically synthesized from L-Tyr in deuterium oxide by the tryptophanase TnaA [25] and incorporated by feeding into PcpA (Figure S4.16). To avoid depletion of the Cα-deuterium label by reversible transamination, the quintuple transaminase mutant strain *E. coli* Δpenta [26] was used as expression host. In vitro reactions cleanly showed Cα-deuterium abstraction from this substrate to produce dAdoD concomitant with formation of the ketoamide **5** in early timepoints (Figure 4.4a–b, Figure S4.17). The orthogonally labeled substrate was predominantly produced by feeding ($^2H_7$)-Tyr in a BL21(DE3) host where the Cα-deuterium was depleted through transaminase-mediated exchange with hydrogen. As expected, this orthogonally labeled substrate gave minimal enrichment of dAdoD. Thus, we infer that a single equivalent of SAM is utilized in the reaction to the spliced product and that nonproductive turnover of SAM (i.e., accumulation of dAdoH through spontaneous quenching of dAdo•) is minimal at early timepoints.

Analysis of the peptide products from the (2-^{2}H)-Tyr labeled PcpA reaction timecourse revealed that both the starting material **4** and its isomeric shunt product **6** lost a Cα deuterium label in the extended 16 h timepoint (Figure 4.4b). We hypothesize that the Tyr-Cα• intermediate

may be spontaneously quenched in a shunt reaction to give an epimeric mixture of the L- and D-Tyr. In H_2O, these species would incorporate a hydrogen from the protein or another reaction component. The newly labeled L-Tyr substrate **4** would then be subject to hydrogen abstraction to give dAdoH (Figure 4.4c). The dAdoH may additionally arise from uncoupled turnover of SAM, which may occur more frequently in later reaction timepoints as the L-Tyr substrate is depleted.

Characterization of shunt metabolites informs the splicease mechanism

To test the hypothesis that the isomeric product **6** is the D-Tyr shunt, the core peptide from a scaled-up in vitro reaction using conditions that favored accumulation of **6** was subjected to advanced Marfey's analysis (Figure S4.18) [27]. The hydrolyzed and derivatized amino acid monomers were separated by LC-HRMS and compared to similarly derivatized L- and D-Tyr standards and hydrolysates of the unmodified PcpA core peptide isolated from a negative-control reaction lacking SAM. A clear signal for D-Tyr not present in the negative control confirmed the identity of **6** as the D-Tyr epimer (Figure 4.5a).

During early struggles with inconsistent in-vitro splicease activity, no small-molecule products related to the excised tyramine could be detected. We therefore performed a broader LC-HRMS-based metabolomics analysis of culture extracts from *E. coli* expressions of several splicease systems to search for cryptic coproducts. Several reaction products were identified that contributed to our understanding of splicease catalysis. Samples from the Thiothrix nivea DSM 5205 type III spliceotide containing four splice sites [10] revealed 4-hydroxybenzaldehyde **7** (*m/z* 121.03) as a putative tyrosine side-chain product (Figure S4.19). In follow-up experiments, in vitro reactions with ($^{13}C_9$)-Tyr-labeled PcpA demonstrated PcpXY-dependent formation of **7**

enriched with seven ^{13}C labels (*m/z* 128.05, Figure 4.5b), which accounts for the entire tyrosine side chain and leaves only the backbone-derived C2 and N1 unaccounted for. Thus, the excised part is likely not expelled as intact tyramine but rather broken apart.

Consequently, we predicted several other small molecules as possible coproducts that might account for the remaining backbone-derived atoms, such as cyanide or formaldehyde. The presence of these small molecules was probed by derivatizations with selectively reactive agents and detection by LC-HRMS or Surface-enhanced Raman spectroscopy (SERS) [28]. These methods were validated by spiking control reactions with small-molecule standards. Derivatization of splicease reactions with 2,3-napthalenedicarboxaldehyde [29] or 2,4-dinitrophenylhydrazine [30] gave no detectable cyanide or formaldehyde product ions, respectively, by LC-HRMS. Furthermore, a cyanide signal [31] was not found from the SERS measurement. Thus, the fate of the remaining C2 and N1 from the substrate tyrosine is still under investigation after extensive trials.

Other shunt metabolites were identified in various coexpressions of the type I plp splicease (Figure 4.5c, Figure S4.20). His_6-tagged precursor PlpA3-P11A mutant coproduced with PlpXY gave two peptide species corresponding to the loss of two hydrogens, with the 2.016 Da mass change localized to the substrate tyrosine residue by MS^2 fragmentation for the more abundant species eluting at 13.1 min (Figure 4.5d). These minor side products might be the E and Z forms of 2,3-dehydrotyrosine **9**, resulting from an oxidation of the tyrosine side chain directly or via a p-quinone methide **8** intermediate, which is expected to rapidly tautomerize to **9**. As a parallel example of oxidized species resulting from radical-mediated catalysis, aromatic 2,3-dehydroamino acid residues were proposed as shunt products of the $C(sp^2)$–$C\beta(sp^3)$

crosslinking rSAM-SPASM enzymes from triceptide and daropeptide RiPP biosynthesis [32, 33]. We also observed a truncated species corresponding to cleavage between the N1 and C2 of tyrosine to give a terminal amide **10** (Figure 4.5e). The truncated amide was noted in our previous plp study [8] and could arise from hydrolysis of **9** [34] or be a decomposition product of the Cα radical intermediate [35] (Figure S4.20). Peptide Cα radicals are known to react with oxygen to give a hydroxylated Cα species that rapidly degrades to the favored N-terminal amide and C-terminal carbonyl fragments. Neither the amide cleavage product nor the putative dehydrotyrosine species were detected from in vitro reactions with the Pcp system.

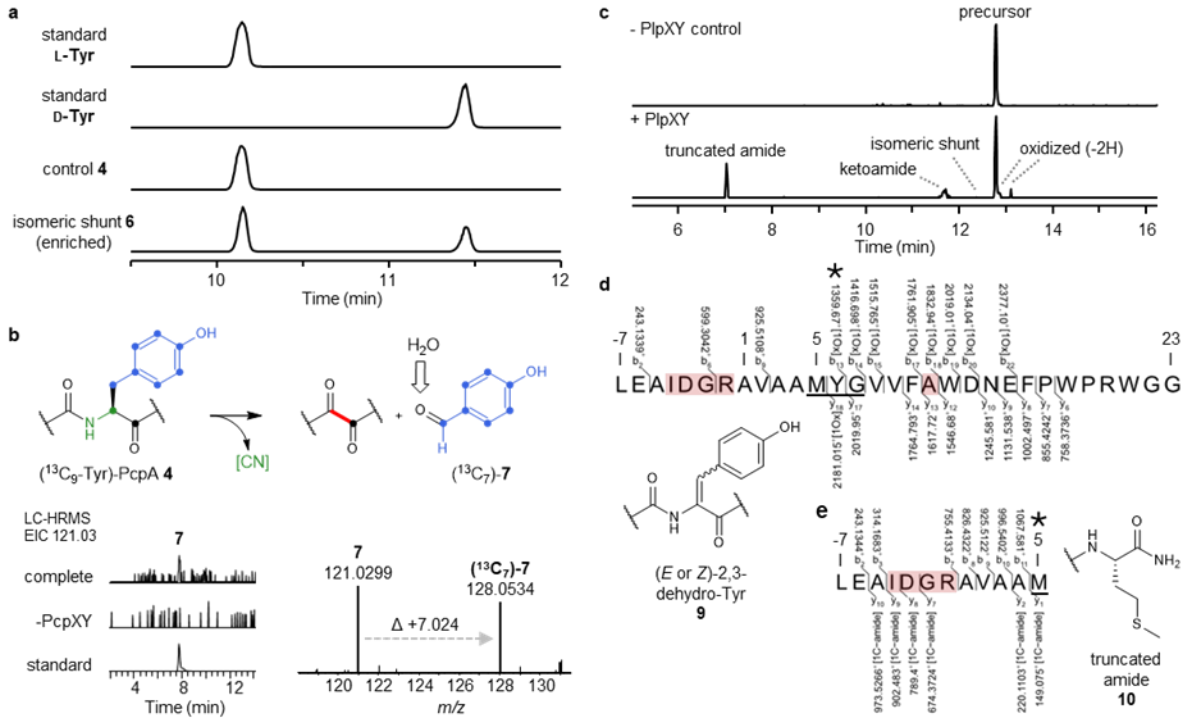


Figure 4.5. Detection of shunt metabolites and coproducts from splicease reactions. a) Marfey's analysis of partially purified $PcpA_{1–64}$ core peptide hydrolysates from an in vitro reaction favoring production of the isomeric shunt **6** compared to a ' SAM' control reaction and L- and D-Tyr standards. EICs for the bis-N-α-(2,4-dinitro-5-fluorophenyl)-L-valinamide (L-FDVA) derivatized Tyr are shown, $[M-H]^-$ = 740.23. b) LC-HRMS analysis of the 4-hydroxybenzaldehyde **7** side chain coproduct of the PcpA ketoamide-forming in vitro reaction. Mass spectra of in vitro reactions with ($^{13}C_9$)-Tyr-label-enriched PcpA produced a mixture of

unlabeled, $[M-H]^-$ = 121.03, and $^{13}C_7$-labeled, $[M-H]^-$ = 128.05, 7. c) Identification of shunt products from a Plp spliceotide mutant produced in *E. coli*. Coproduction of the His_6-tagged PlpA3 mutant with its cognate splicease ('+PlpXY') compared to the precursor only control ('-PlpXY'). LC-HRMS analysis of Ni^{2+}-affinity column chromatography purified precursor cleaved with GluC to give the peptide fragment 'LEAIDGRAVAAMYGVVFAWDNEFPWPRWGG'. Non-native residues are highlighted in red where 'IDGR' is a factor Xa (fx) recognition site substitution and P11A is a proline-to-alanine point mutant at core residue 11. EICs for the precursor/isomeric shunt $[M+3H]^{3+}$ = 1127.55, ketoamide $[M+3H]^{3+}$ = 1082.53, oxidized $[M+3H]^{3+}$ = 1126.88, and truncated amide $[M+2H]^{2+}$ = 608.33 are shown. d) MS^2 analysis of the *m/z* 608.33 feature at 13.1 min localized the -2 Da mass shift ('10x'-labeled fragment ions) to the Tyr residue. Oxidized peptide species are predicted to correspond to the E and Z isomers of **9**. e) MS^2 analysis of the *m/z* 608.33 feature at 7.1 min localized the amide to Met5 ('1C-amide'-labeled fragment ions) of the truncated peptide and is proposed to correspond to structure **10**. Asterisks indicate the modified residue.

Thermodynamic analysis of mechanistic
proposals for the splicease reaction

Collectively, the results support the following mechanistic aspects: (i) Cα of tyrosine in the XYG motif is the site of initial H-abstraction to form the radical intermediate $\mathbf{R1_{red}}$, (ii) quenching of this intermediate with hydrogen regenerates the substrate or forms the D-Tyr **6** shunt product, (iii) 4-hydroxybenzaldehyde **7** from the tyrosine side chain is one of the splice products, and (iv) tyrosine side-chain oxidation occurs either as a side reaction or during splicing. Since the splicing reaction occurs anaerobically, the oxygen atom of **7** is most likely derived from water. A mechanistic rationale that would account for the aldehyde oxygen, the dehydrotyrosine byproduct **9**, and the undetected N1 and C2 atoms of tyrosine is shown in Figure 4.6a. The dehydrotyrosine radical moiety $\mathbf{R1_{ox}}$ would be the precursor of an extruded 7-cyano *p*-quinone methide $\mathbf{P_{ox}}$. Spontaneous addition of water then results in the cyanohydrine **11** that decomposes to the verified aldehyde **7** and a cyanide anion. This spontaneous chemistry has precedence in the degradation of plant cyanogenic glycosides such as dhurrin [36]. Furthermore, we found that commercially acquired **11** rapidly degrades to **7** under our reaction conditions

(Figure S4.21). Although extensive analytical efforts did not detect cyanide, it may be consumed by reacting with other assay components, such as sulfur centers in the splicease or flavodoxin, or splicease iron centers [37].

We considered various hypotheses for the early reaction steps stemming from the experimentally verified Tyr-Cα• **R1$_{red}$**. A possible route involved side-chain oxidation to the quinone methide radical **R1$_{ox}$**, perhaps mediated by the auxiliary [4Fe-4S] clusters. From here, two alternative mechanisms are proposed: In Pathway A, intermediate **A-I$_{ox}$** undergoes fragmentation and 1,3 migration of an acyl radical to yield intermediate **R2$_{ox}$** with the formative backbone C–C bond in place. Fragmentation of **R2$_{ox}$** would then generate the ketoamide **5** and the cyano quinone methide **P$_{ox}$** upon oxidation. In Pathway B, an alternative rearrangement involving a cyclic transition state is considered. In the first differential step, **R1$_{ox}$** undergoes cyclization to the azetine transition state **B-I$_{ox}$**. The azetine decomposes via **R2$_{ox}$** into the cyano quinone methide **P$_{ox}$** and the peptide radical, which is oxidized to the ketoamide **5** as in Pathway A. In both pathways, we hypothesized that intermediates might be held in a favorable conformation by iron chelation at the open coordination site of the auxiliary I cluster.

To examine the feasibility of these mechanistic proposals, we evaluated thermodynamic reaction energies for all steps of the alternative pathways applying density functional theory (Figure 4.6b–c). We employed a simplified structural model of the XYG motif where X is glycine, a confirmed substrate of the Plp splicease [13]. All reactions were analyzed for both the unmodified (‘red’ subscript) and the oxidized quinone-methide (‘ox’ subscript) tyrosine side-chain variants, since the explicit oxidation state could not be accurately described.

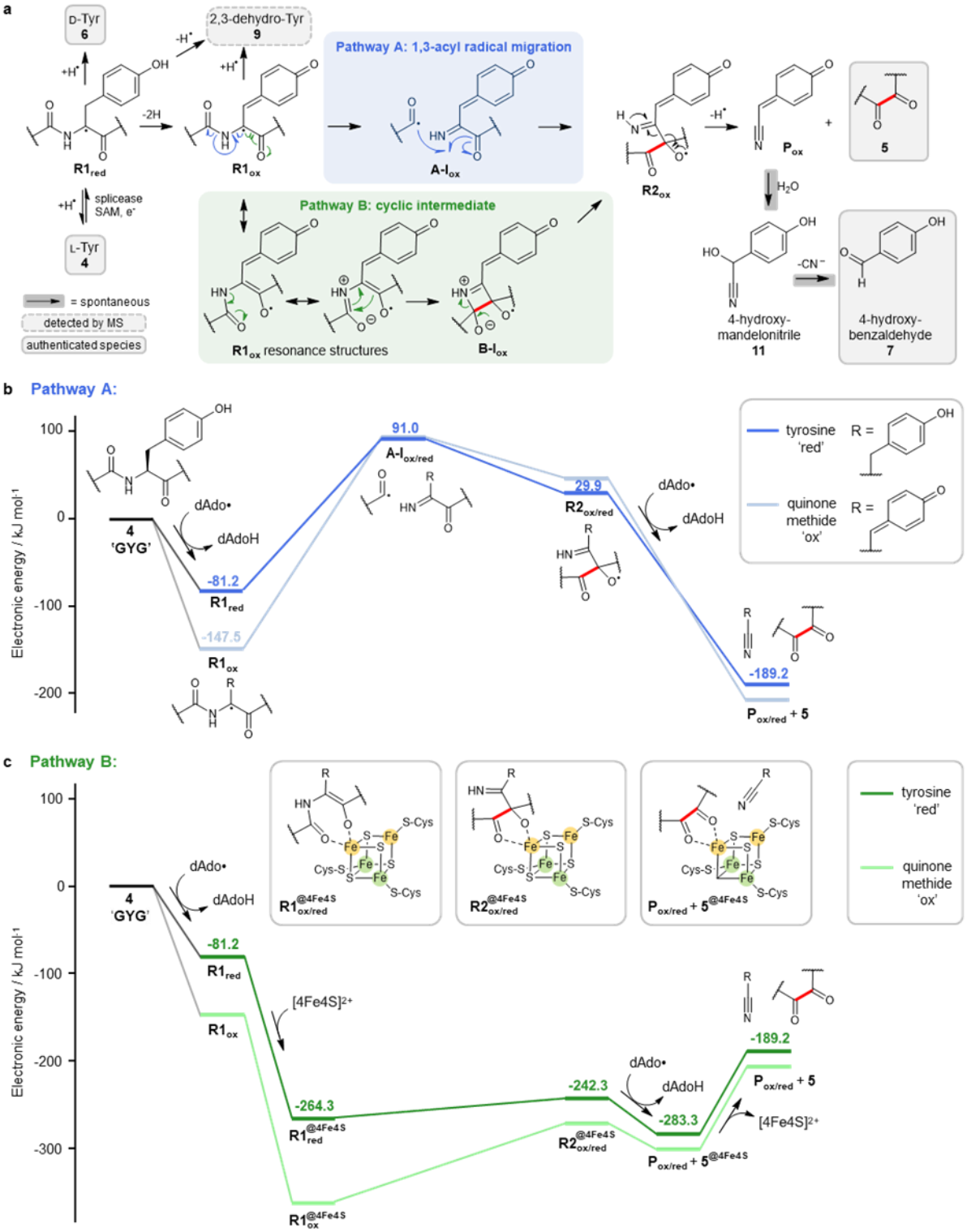


Figure 4.6. Mechanistic proposals for the splicease reaction. a) Alternative proposals to the ketoamide are shown with the critical new C–C bond in red with side-chain oxidation to the

quinone methide. $\mathbf{P_{ox}}$ spontaneously degrades to the verified side-chain coproduct **7**. Thermodynamic reaction profiles are shown for both the tyrosine ('red' subscript) and oxidized quinone methide ('ox' subscript) side chains in the modeled 'GYG' motif for b) the 1,3-acyl radical migration of Pathway A and c) the cyclic transition state of Pathway B. Reaction steps involving the proposed auxiliary I open Fe coordination site as catalyst are labeled with the superscript '@4Fe4S'. Electronic energies of reactions involving the reduced tyrosine side chain are given in kJ/mol relative to the substrate **4**. We label iron sites with excess alpha spin density in orange and with excess beta spin density in green. SAM-derived dAdo• was used as the H-acceptor for the **4** to **R1** and **R2** to **P** + 5 oxidation steps. Empirical evidence now implicates only one SAM cosubstrate in the spliceing reaction, i.e., for the initial H-abstraction (see Figure 4.4a); however, the use of other H-acceptors is not expected to alter the overall electronic energy trends.

We found that initial H-abstraction at the Tyr-Cα of **4** by dAdo• is thermodynamically favored by at least -81 kJ/mol to form $\mathbf{R1_{red}}$ (Figure 4.6b–c). Subsequent formation of intermediate A-I (Pathway A, Figure 4.6b) via C–N bond cleavage, however, is thermodynamically constrained. This is likely due to poor resonance stabilization of the unpaired electron in the acyl radical. We therefore probed the role of the auxiliary I [4Fe-4S] cluster as a catalyst [38]. For the [4Fe-4S] cubane, we find consistent antiferromagnetic coupling of two pairs of iron atoms for all steps evaluated in this work, which is in agreement with previous studies on related clusters [39]. We assessed conversion of $\mathbf{R1_{red}}$ to $\mathbf{A\text{-}I_{red}}$ involving a [4Fe-4S] cubane proceeding either through formation of the acyl radical and subsequent coordination to the vacant metal site, or vice versa. Both variants involve an endothermic step, disfavoring Pathway A as a possible splicease mechanism (Figure S4.22). Species involving iron coordination are indicated by '@4Fe4S' superscript.

In Pathway B, coordination of **R1** to the vacant iron site provides a thermodynamic sink, where bidentate O–O coordination is found (Figure 4.6c). This sink is more exothermic for the quinone methide variant. The subsequent C–C bond formation to yield the iron-coordinated species $\mathbf{R2^{@Fe4S4}}$ is almost thermoneutral for the tyrosine side chain and only slightly

endothermic for the quinone methide variant but could occur spontaneously under standard conditions. This step is likely to proceed via the azetine 4-ring transition state **B-I**$^{@Fe4S4}$. Subsequent dissociation of the side chain and abstraction of a hydrogen equivalent would form [4Fe-4S]-bound **5**$^{@Fe4S4}$ and P in an exothermic reaction step. Ultimately, dissociation of the ketoamide product to recover the iron-catalyst is again only slightly endothermic. Note that we consider dissociation of the product in a dispersion-free environment (i.e., in vacuo). The accurate description of dispersion effects inside the protein cavity might further stabilize the dissociation.

For the overall pathway, we find analogous thermodynamic trends for both side-chain variants (i.e., tyrosine and quinone methide); however, the spontaneous addition of water to give 4-hydroxymandelonitrile **11**, which degrades to the authenticated 4-hydroxybenzaldehyde **7** and a proposed cyanide anion would only occur with the oxidized quinone methide side chain $\mathbf{P_{ox}}$, as shown in Figure 4.6a. In summary, our quantum chemical analysis supports that ketoamide formation proceeds by Pathway B without thermodynamic constraints under standard conditions in the presence of a [4Fe-4S] catalyst.

Discussion

Here we established the Pcp spliceotide pathway as a model system for detailed in vitro studies to reveal a mechanistic proposal for the extraordinary conversion of standard α-amino acids to α-keto-β^3-amino acids in peptide substrates by rSAM spliceases. Our former mechanistic hypothesis [8] had paralleled catalysis by the rSAM enzyme HydG, which acts on a tyrosine substrate to produce the CN^- ligand of the [FeFe]-hydrogenase organometallic H-cluster [40]. We reasoned that ketoamide formation by spliceases would likewise involve dissociation at Cα–

Cβ to give *p*-cresol and a dehydroglycine intermediate, which would undergo CN^- extrusion to yield the spliced ketoamide—possibly initiated by H-abstraction at the analogous amino group of tyrosine (Figure S4.23). Unexpectedly, deuterium labeling experiments and identification of D-Tyr as the isomeric shunt **6** in this study showed that initial H-abstraction occurs predominantly at the Cα of Tyr15 in PcpA, thus necessitating a new mechanistic hypothesis.

Some other RiPP-modifying rSAM enyzmes are also known to initiate H-abstraction at the Cα of peptide residues. These include proteusin [41, 42] and epipeptide [43] epimerases that convert L-amino acids to D-amino acids, sactipeptide maturases that form S–Cα thioether cross-links [44], as well as diverse glycyl radical enzyme activases [45]; however, none of these rSAM enzymes catalyze complex peptide backbone rearrangements. PcpXY appears to use one equivalent of SAM to catalyze ketoamide formation based on the (2-^{2}H)-Tyr-PcpA reactions (Figure 4.4a–b, Figure S4.17), which exclusively formed dAdoD as the coproduct with the ketoamide at early timepoints. If a second equivalent of SAM was utilized, we would have expected coproduction of unlabeled dAdoH. Although the ketoamide has the same oxidation state as the peptide substrate, the favored mechanism based on the dehydrotyrosine radical intermediate $\mathbf{R1_{ox}}$ undergoes a net four-electron oxidation, implicating both the auxiliary [4Fe-4S] clusters and external reagents in accepting the released electrons since SAM acts only as a formal two-electron oxidant. Oxidative rSAM enzymes involved in four-electron processes (for example, HemN and BioB) use two equivalents of SAM during catalysis, whereas the majority of rSAMs that catalyze two-electron oxidations (e.g., C–C and C–S crosslinks) or even neutral reactions (e.g., epimerases) utilize one molecule of SAM [22].

Structures of several rSAM-SPASM enzymes reveal that their peptide substrates are in proximity to the auxiliary clusters [46–48], which could function as an electron sink during oxidative reaction steps. Multiple sequence alignments of rSAM-SPASM enzymes suggest that spliceases have an open auxiliary I iron-coordination site [8], as has also been observed for CteB [48] and MftC [49] from sactipeptide and mycofactocin biosynthesis, respectively. Our thermodynamic energy calculations support that this open site binds precursor protein radical intermediates, which undergo C–C bond formation and side-chain extrusion while coordinated to the catalyst (Figure 4.6c). However, we cannot rule out the use of other non-cysteine iron-ligation partners, as has been identified for some rSAM-SPASM enzymes [50, 51]. Although the fate of the unpaired electrons in splicing reactions is unknown at this time, it likely involves the auxiliary [4Fe-4S] clusters as well as external redox cofactors as part of a larger catalytic system. Future experiments will focus on resolving the role of the auxiliary [4Fe-4S] clusters and the fate of the N1 and C2 of the substrate tyrosine residue proposed to be lost as CN^- to refine our mechanistic hypothesis. The unique qualities of splicease catalysis relative to described rSAM family members and the utility of their ketoamide products as orthogonal handles for protein labeling and protease-inhibiting pharmocophores reveal these enzymes as important targets for continued study.

Supplemental Material

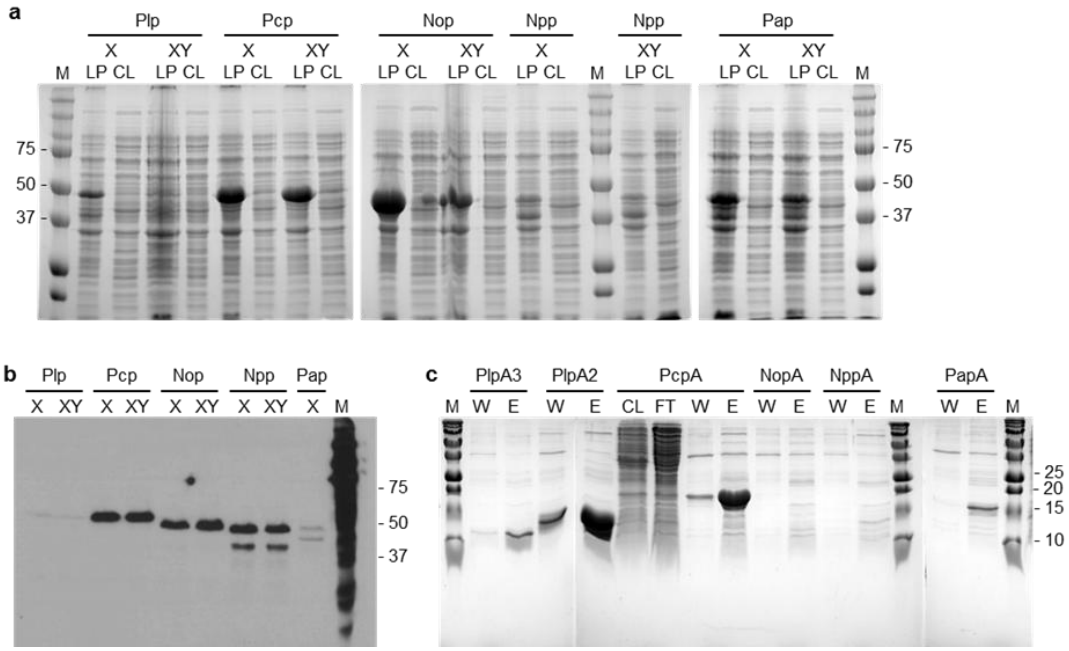


Figure S4.1. Protein production screens for five type I splicease pathways from Cyanobacteria. E. coli BL21(DE3) harboring pCDFDuet-1-based expression vectors (Table S4.4)) were cultured in LB medium, induced with 1 mM IPTG, and expressed overnight at 18 °C. Protein was purified by Ni^{2+}-affinity column chromatography. Images of SDS-PAGE analyses of select purification fractions are shown. a) Lysed pellet (LP) and cleared lysate (CL) samples for X and XY expressions showing insoluble and soluble fractions, respectively, following cell lysis by sonication. b) Anti-His_6 Western Blot of the CL samples. PcpX and NopX showed the best apparent yields and stability. PlpX suffered from low soluble yields. NppX and PapX were prone to degradation with two-bands visible. c) SDS-PAGE of wash (W) and elution (E) fractions from precursor protein test expression purifications. The NopA precursor was not detected. M is Precision Plus Dual Color Standards (Bio-Rad) with molecular weights in kDa.

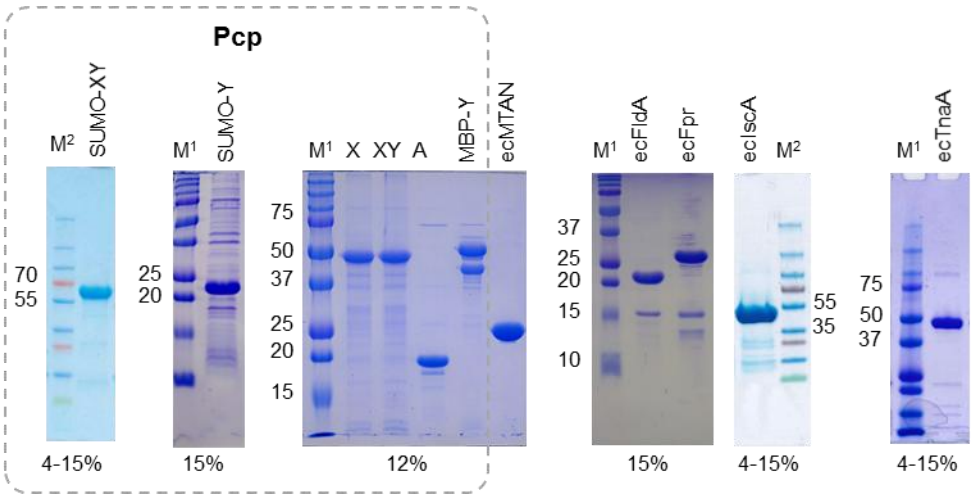


Figure S4.2. Ni^{2+}-affinity column chromatography purified proteins used for in vitro reactions with the Pcp splicease. Pcp proteins were produced in E. coli BL21(DE3). ASKA- collection clones were produced directly from the library in E. coli AG1. Coomassie-stained SDS-PAGE gel images are shown. Expected molecular weights are given in Table S4.4. All proteins contain N terminal His_6-tags; bdSUMO and MBP solubility tags are additionally indicated. Note that the PcpY (6 kDa) is not visible on the gel, but was shown to be present by LC-HRMS, see Figure S4.7. M1 indicates Precision Plus Dual Color Standards (Bio-Rad) and M2 is PageRuler Plus Prestained Protein Ladder (Thermo). Molecular weights are given in kDa. The percent acrylamide is shown below each gel image; the '4–15%' gradient gels are Mini-PROTEAN® TGX™ Precast Protein Gels (BioRad). Much of the expressed 6xH-v-PcpX and 6xH-v-PcpXY samples remained in the insoluble, lysed pellet (LP) fraction (see Figure S1a) and the 6xH-MBP-v-PcpY was prone to degradation (see 'MBP-Y'), leading us to test bdSUMO as a solubility tag. 6xH-bdSUMO gave higher soluble yields of PcpX, PcpXY, and PcpY with good stabilities. Note that solutions of purified 6xH-bdSUMO-PcpY become reversibly cloudy at cold temperatures and required gentle warming to return to a clear solution.

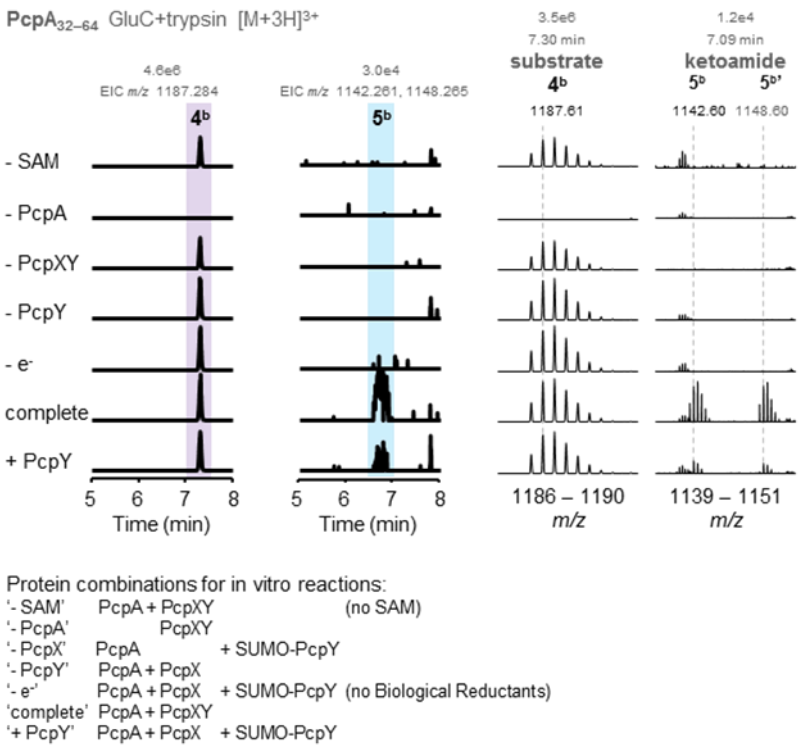


Figure S4.3. LC-HRMS analysis of $PcpA_{32–64}$ fragment b gave only minor amounts of spliced Tyr56 product. Extracted ion chromatograms and the relevant mass spectra for the unmodified substrate 4 and the spliced ketoamide 5 and ketoamide hydrate 5' are indicated. Isomeric shunt 6 was either not detected or co-elutes with 4b. This figure is related to main text Figure 4.2. Peptides were separated by LC Method 1.

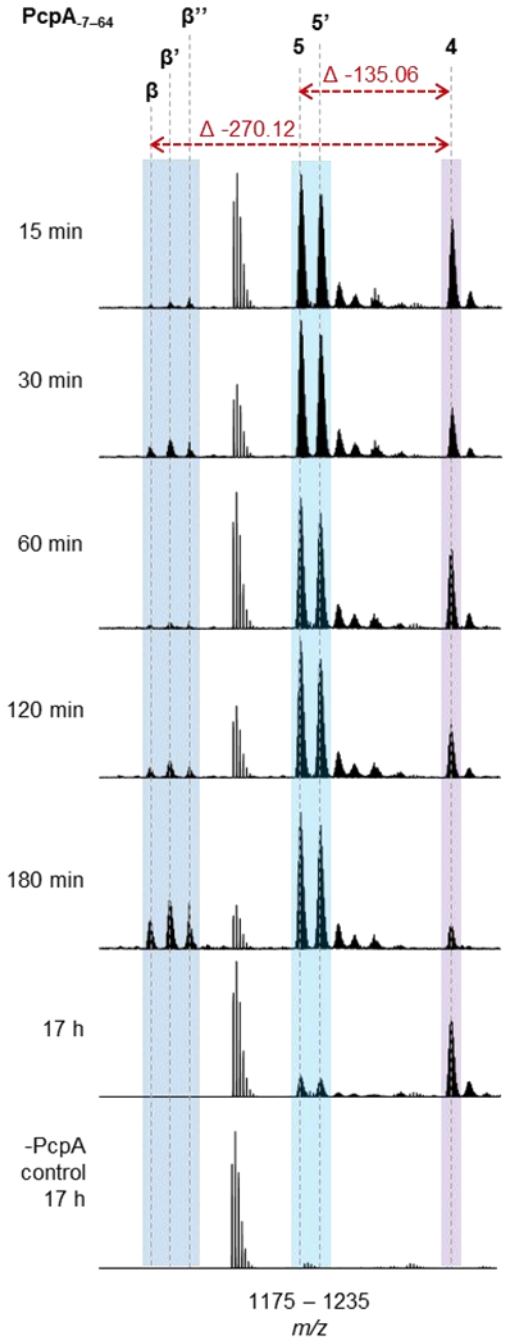


Figure S4.4. LC-HRMS spectra of an efficient Pcp splicease reaction shows time-dependent accumulation of the product with two ketoamides, PcpA$_{-7–64}$ with a Δ-270.12 mass difference β. The β' and β'' species correspond to the α-ketone hydrate at one (Δ+H_2O) or both (Δ+2H_2O) splice sites, respectively. The mass spectra *m/z* 1175–1235 for the t_R = 7–10 min for each LC-HRMS chromatogram are shown (LC Method 1). The reaction contained 100 μM PcpA, 100 μM reconstituted PcpXY ('6xH-SUMO' tagged), 1 mM SAM, and 10 mM DTT in Buffer A with biological reductants: 20 μM ecFldA, 5 μM ecFpr, and 2 mM NADPH. A control reaction

lacking PcpA is shown for comparison (bottom). Note that the spliced products are greatly reduced at 17 h relative to the 180 min timepoint, which suggests the ketoamides are unstable during longer incubations. MS spectra are shown at 100% intensity for each chromatogram.

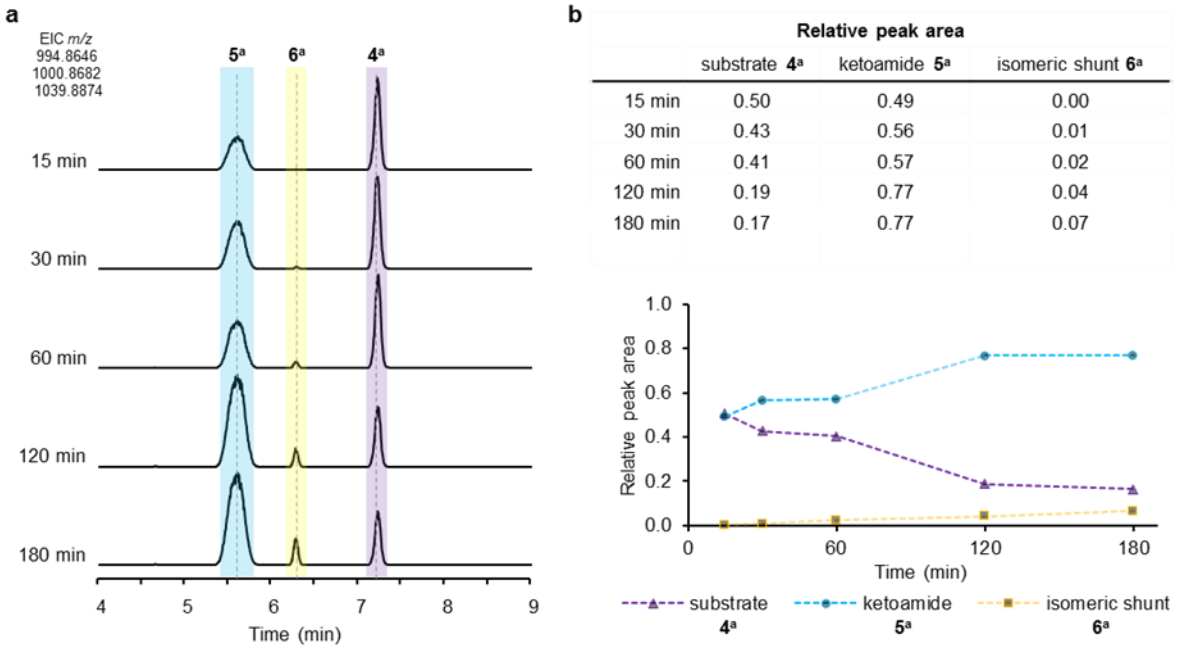


Figure S4.5. Splicease reaction timecourse. a) LC-HRMS analysis of GluC and trypsin-released PcpA$_{-7–26}$ core fragments from in vitro reaction timepoints separated by LC method 1. EICs for the relevant core peptides are shown at 100% intensity for each chromatogram. The reaction contained 100 µM PcpA, 100 µM reconstituted PcpXY ('6xH-SUMO' version), 1 mM SAM, and 10 mM DTT in Buffer A with biological reductants: 20 µM ecFldA, 5 µM ecFpr, and 2 mM NADPH. b) Relative peak areas for 4, 5, and 6 were determined from the EICs and plotted for each timepoint. The spliced product 5 is rapidly produced in early time points and maximally produced after 2 h, whereas the accumulation of isomeric shunt 6 is delayed.

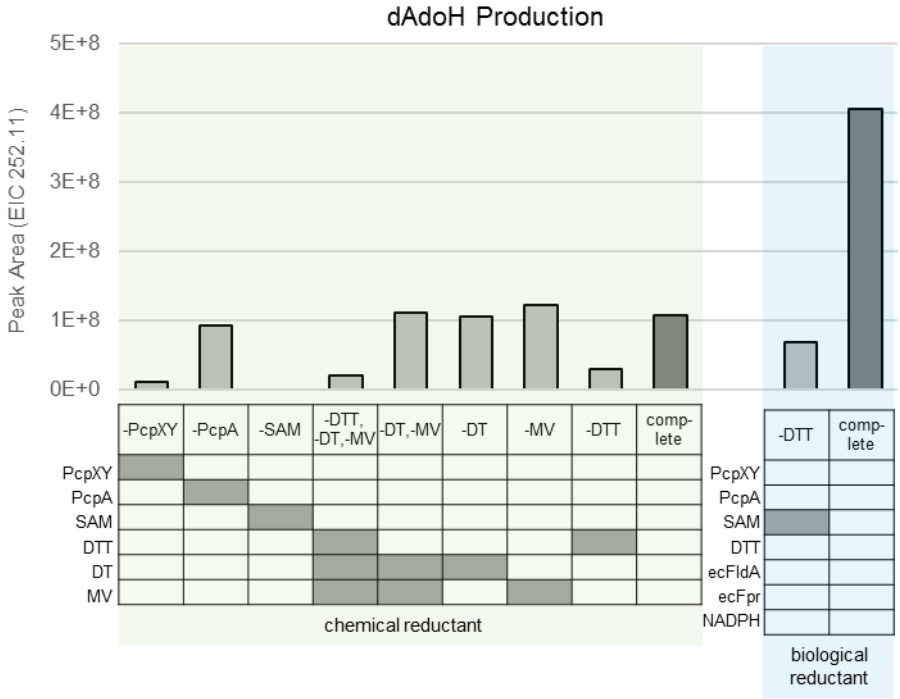


Figure S4.6 . The reductant system affects the efficiency of in vitro splicease reactions. LC-HRMS detection of the dAdoH coproduct resulting from reductive cleavage of SAM. The peak areas for the $[M+H]^+$ = 252.11 EIC are plotted for the different reaction conditions. 'Complete' reactions contained 100 µM PcpA, 25 µM reconstituted PcpXY ('6xH-v' version), 1 mM SAM, and 10 mM DTT in buffer containing 50 mM HEPES pH 8.0 and 10% glycerol. Chemical reductants include 1 mM DT and 1 mM MV. Biological reductants include 20 µM ecFldA, 5 µM ecFpr, and 2 mM NADPH. The greyed boxes indicate the missing reaction component(s). Addition of DTT improved the efficiency of the reaction with biological reductants ~6-fold. Production of small amounts of dAdoH for the reactions lacking PcpXY ('-PcpXY) and the reactions lacking all reductants (' DTT, DT, MV') suggests possible contamination with native *E. coli* rSAM enzyme(s) for this batch of protein.

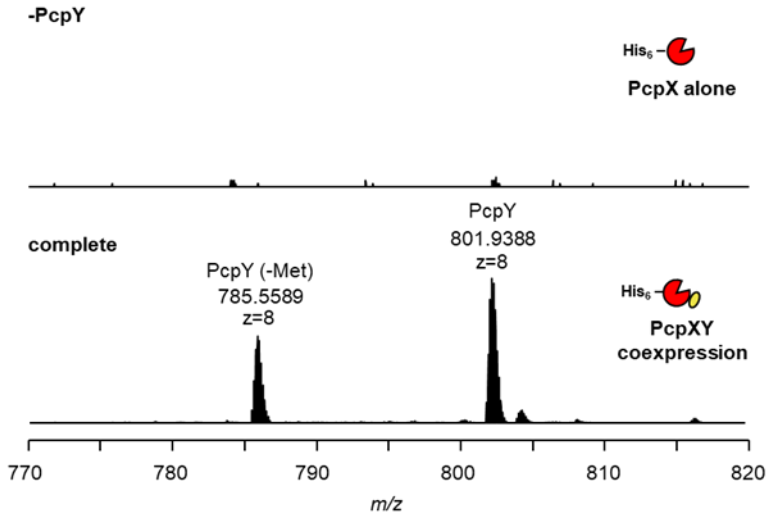


Figure S4.7. Untagged PcpY co-purifies with His_6-PcpX. The PcpXY complex is purified by Ni^{2+}-affinity column chromatography as detected by LC-HRMS analysis of in vitro reactions. The mass spectra of the +8 charge state for the full-length PcpY protein, $[M+8H]^{8+}$ = 801.9390, and PcpY lacking the N-terminal Met, $[M+8H]^{8+}$ = 785.5590 (monoisotopic), are present (t_R = 7.74 min, LC method 1) in a complete reaction (bottom) relative to the reaction lacking PcpY (top).

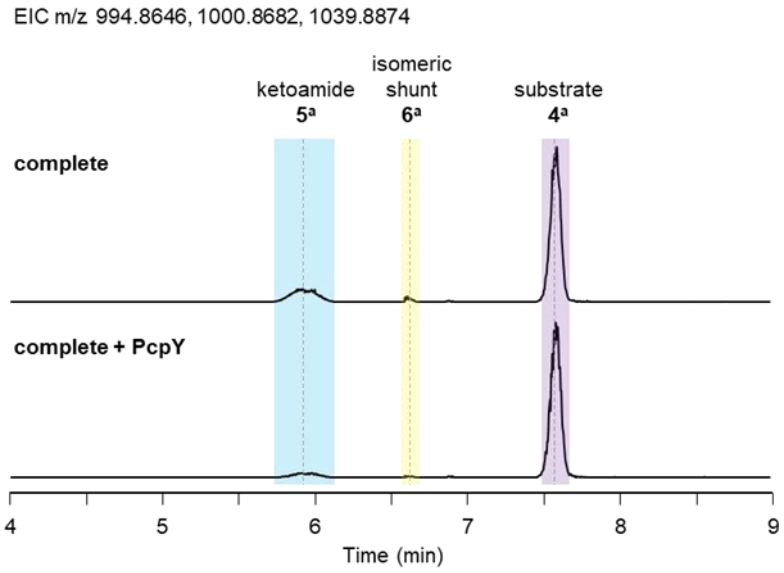


Figure S4.8. Addition of extra PcpY to complete reactions did not improve product yields, suggesting untagged PcpY is copurified in stoichiometric amounts with 6xH-v-PcpX from PcpXY coproductions. LC-HRMS analysis (LC Method 1) of GluC and trypsin released $PcpA_{-7-26}$ core fragment from overnight in vitro reactions are shown. The 'complete' reaction is identical

to the data shown in Figure 4.2c. The reactions contain 100 µM PcpA, 50 µM reconstituted PcpXY ('6xH-v' tagged), 1 mM SAM, and 10 mM DTT in Buffer A with biological reductants: 20 µM ecFldA, 5 µM ecFpr, and 2 mM NADPH. The 'complete + PcpY' reaction was additionally supplemented with 25 µM PcpY ('6xH-SUMO' version).

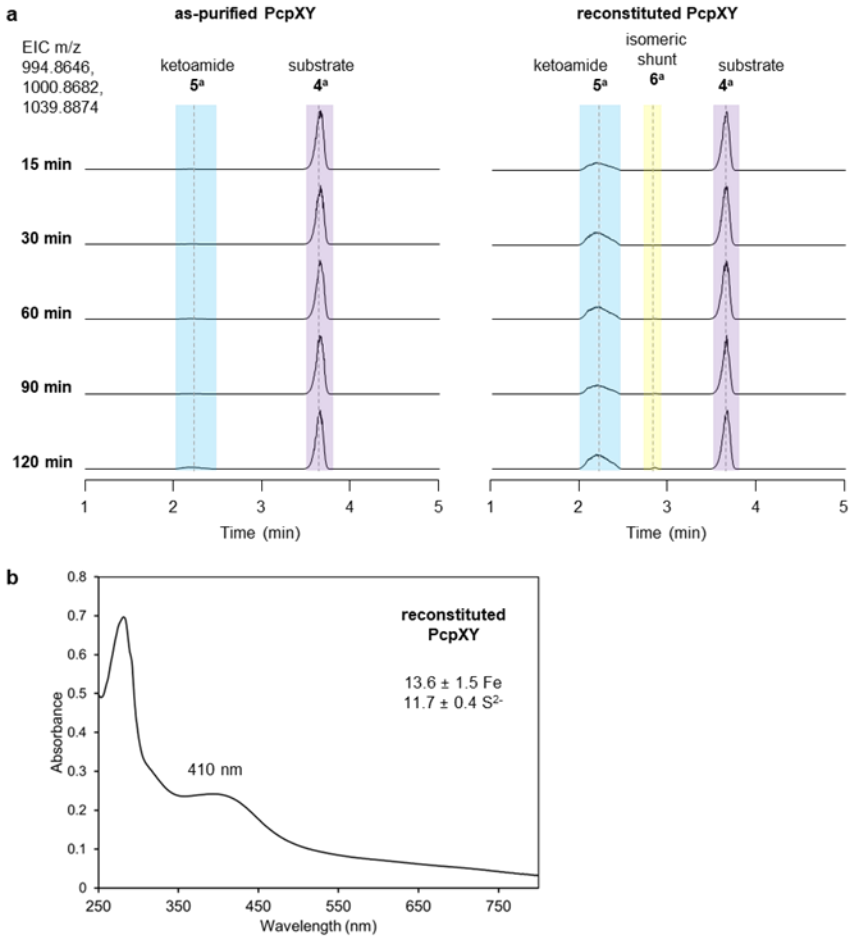


Figure S4.9. Comparison of as-purified and anaerobically reconstituted PcpXY. a) In vitro activity assessed by LC-HRMS analysis of PcpA products (LC Method 2). Only minor amounts of the ketoamide product 5a accumulate in the as-purified splicease reaction. b) UV-Vis spectroscopy shows a prominent 410 nm peak associated with intact [4Fe-4S] clusters. Complexed iron and sulfide were quantified using the methods of W.W. Fish [58] and H.Beinert [59], respectively, with technical replicates in triplicate of PcpXY protein samples. Results indicate three [4Fe-4S] clusters are present in the reconstituted PcpXY enzyme complex. Independent determination of iron content by atomic absorption spectroscopy and sulfide for a unique batch of reconstituted PcpXY used for EPR measurements gave similar results at 13.2 ± 0.2 Fe and 11.1 ± 0.4 sulfide per monomer.

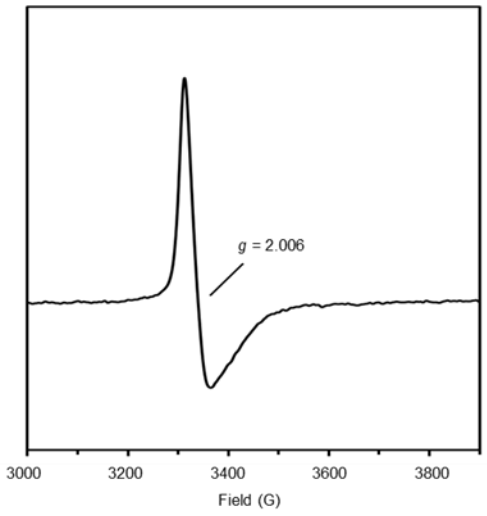


Figure S4.10. X-band EPR spectra of as-reconstituted PcpXY. EPR conditions: microwave frequency, 9.38 GHz; microwave power, 1 mW; modulation, 10 G; and T = 8 K.

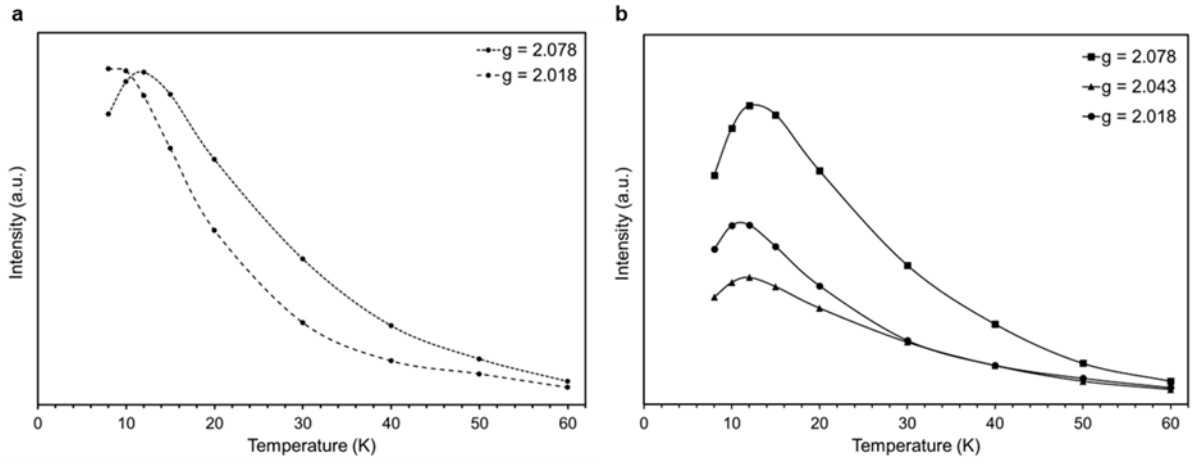


Figure S4.11. Temperature dependence of EPR spectra of the dithionite-reduced PcpXY complex in the a) absence and b) presence of SAM.

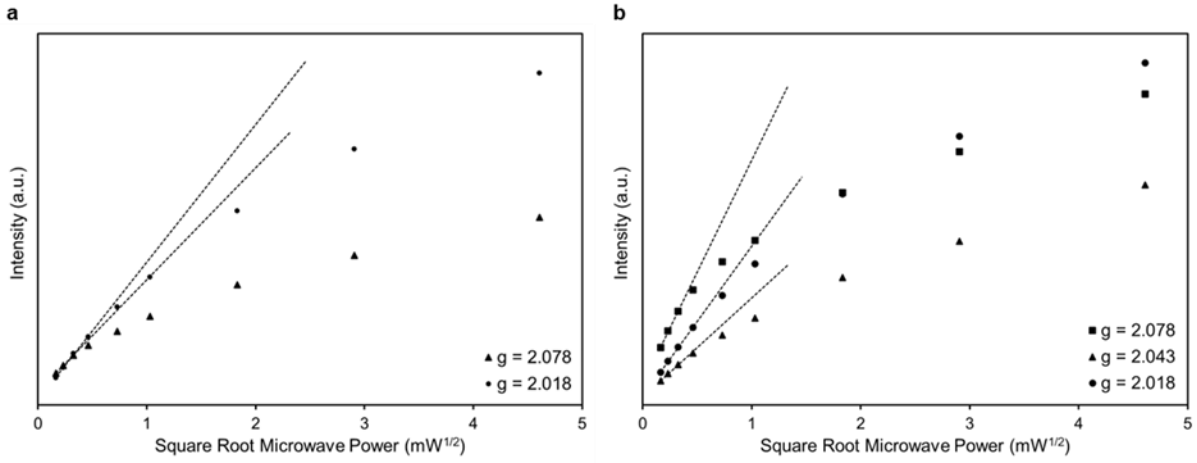


Figure S4.12. Power-saturation of the EPR spectra of the dithionite-reduced PcpXY complex in the a) absence and b) presence of SAM. Extrapolations are shown for the linear region of each plot. In all cases, 0.1 mW is non saturating.

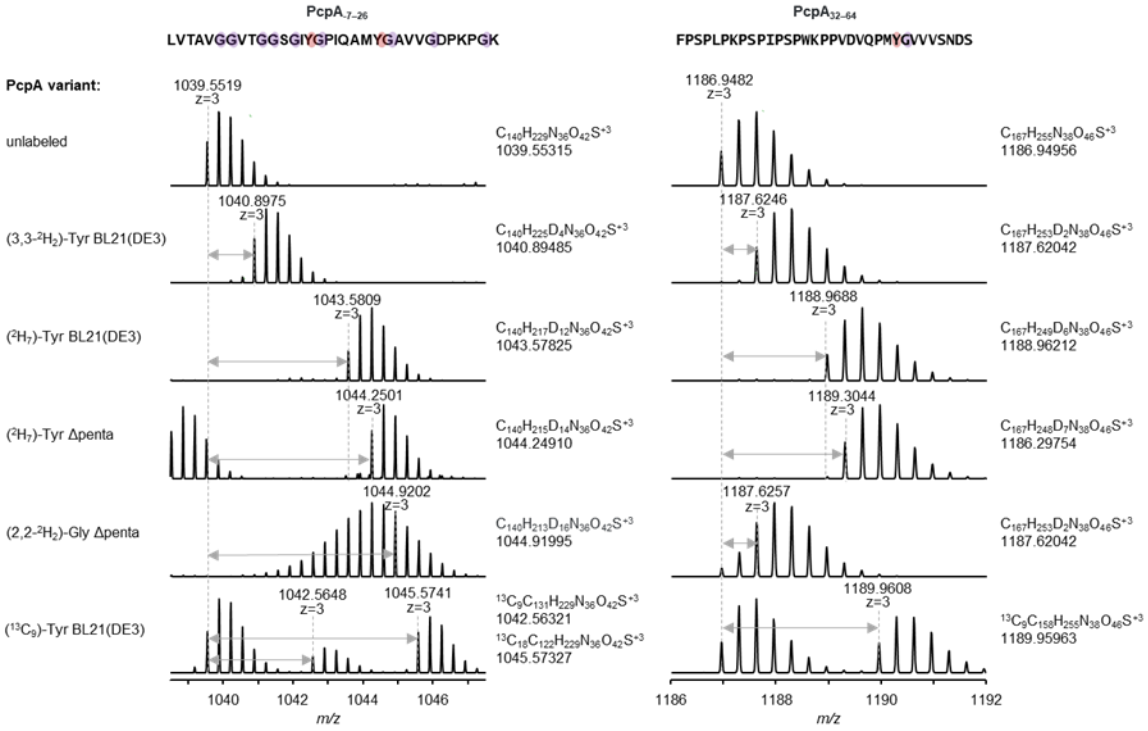


Figure S4.13. Stable isotope-labeled PcpA variants used as substrates for in vitro splicease reactions. LC-HRMS analysis of GluC and trypsin released PcpA$_{-7–26}$ (left) and PcpA$_{32–64}$ (right) core peptides. The expected mass shifts for the peptides with incorporated ^{2}H or ^{13}C atoms are indicated by the vertical dashed lines.

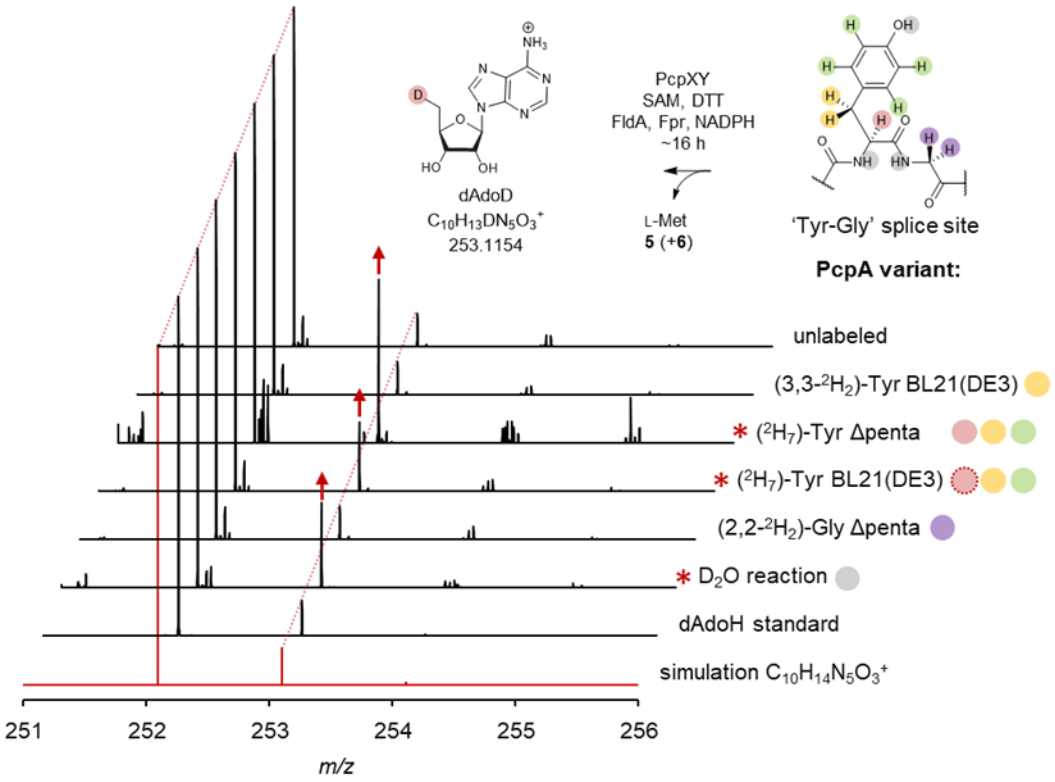


Figure S4.14. In vitro PcpXY splicease reactions (21 h timepoint) with differentially deuterium-labeled PcpA substrates or with unlabeled PcpA in D_2O. a) LC-HRMS detection of the dAdoH/D product. The isotope simulation and a standard of dAdoH are shown for comparison. The dAdoD *m/z* 253.12 was only enriched in ($^2H_7$)-Tyr labeled substrates and the D_2O reaction. The Tyr-Cα deuterium was mostly lost in the ($^2H_7$)-Tyr fed to BL21(DE3) due to reversible activity of transaminases (i.e., IlvE). The E. coli Δpenta transaminase deletion mutant strain was used for retention of the Cα deuteriums in the (2-$^2H_7$)-Tyr and (2,2-$^2H_2$)-Gly fed samples. The higher amounts of dAdoD from the retained Cα deuterium sample strongly suggested abstraction takes place at the Cα of tyrosine. The accumulation of dAdoD in the D_2O reaction could invoke an exchangeable peptide hydrogen (e.g., the phenol oxygen or an amide nitrogen) in the reaction mechanism, but it may also arise from direct quenching of dAdo• with deuterium from uncoupled SAM cleavages. Reconstituted PcpXY was the 6xH-MBP-tagged version. For the D_2O reaction, glycerol was excluded from PcpXY, PcpA, and the buffer components.

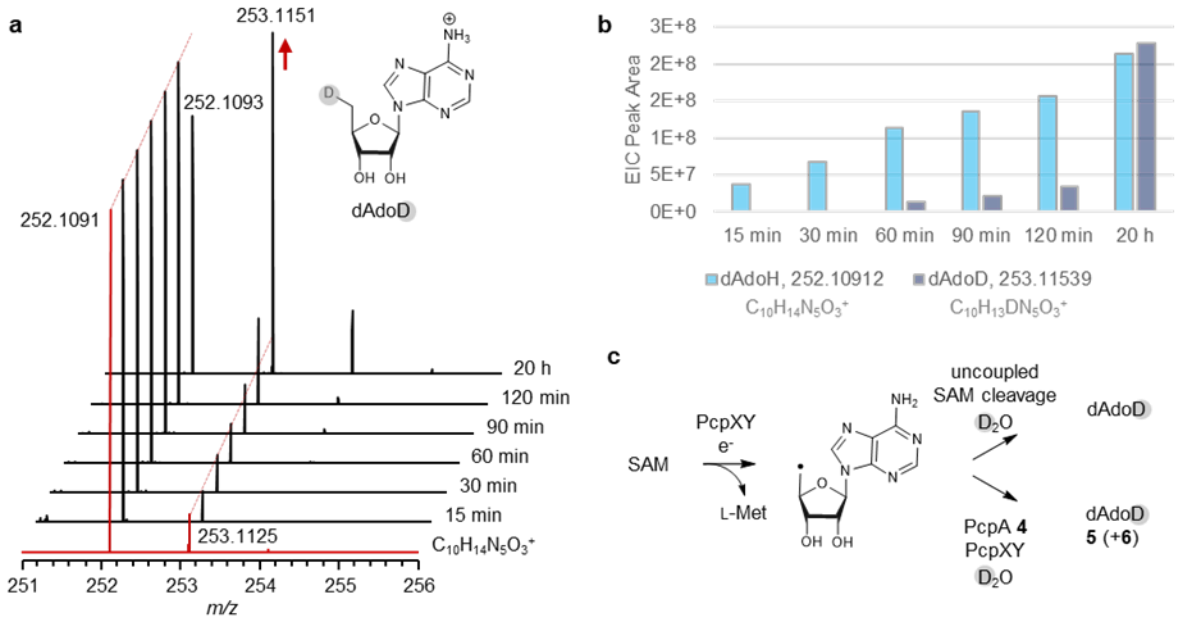


Figure S4.15. In vitro PcpXY splicease reaction time course in D_2O. a) Mass spectra of dAdoH/D product for the reaction timepoints relative to the simulation (red). b) EIC Peak area for the dAdoH and dAdoD products. Note that the $C_{10}H_{13}[^2H]N_5O_3^+$ isotope at *m/z* 253.1154 was not detected above baseline in the 15 or 30 min timepoints and was differentiated from the $C_9[^{13}C]H_{14}N_5O_3^+$ isotope at *m/z* = 253.1125 using 10 ppm error for the EIC mass range. b) The slow incorporation of deuterium does not correlate to accumulation of the spliced product 5, which is already prominent at 15 min. c) dAdoD most likely results from uncoupled cleavage of SAM where the dAdo• is spontaneously quenched by deuterium (top), rather than being a specific product of the splicease reaction (bottom).

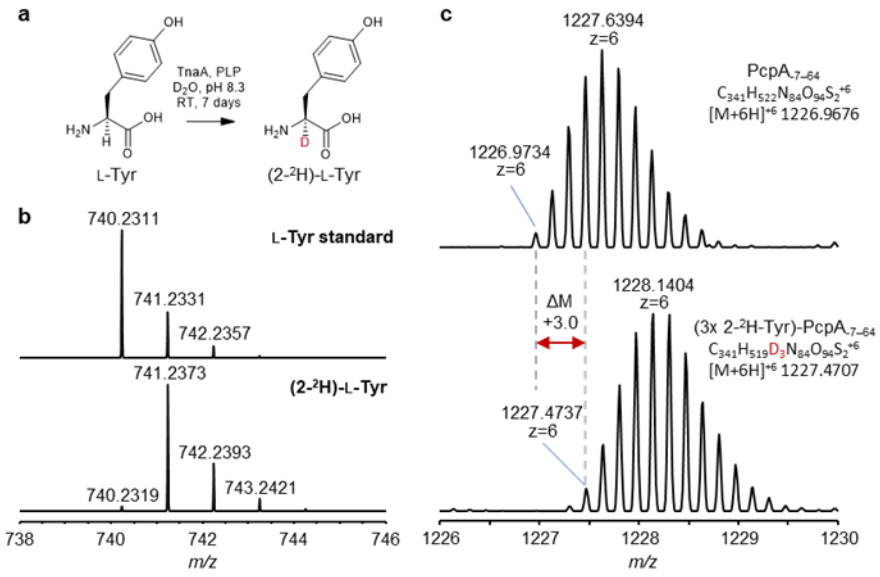


Figure S4.16. Enzymatic production of (2-^{2}H)- L-Tyr and its incorporation into PcpA. a) Production of (2-^{2}H)-L-Tyr by *E. coli* TnaA tryptophanase. b) LC-HRMS analysis of L-FDVA derivatized L-Tyr standard and purified biosynthesized (2-^{2}H)-L-Tyr. c) The (2-^{2}H)-Tyr was fed to E. coli Δpenta harboring pBad-6xH-v-PcpA expressed in LR minimal medium. LC-HRMS analysis of the GluC protease released core fragment of Ni^{2+}-affinity column chromatography purified (2-^{2}H-Tyr)-PcpA (bottom) compared to unlabeled PcpA (top).

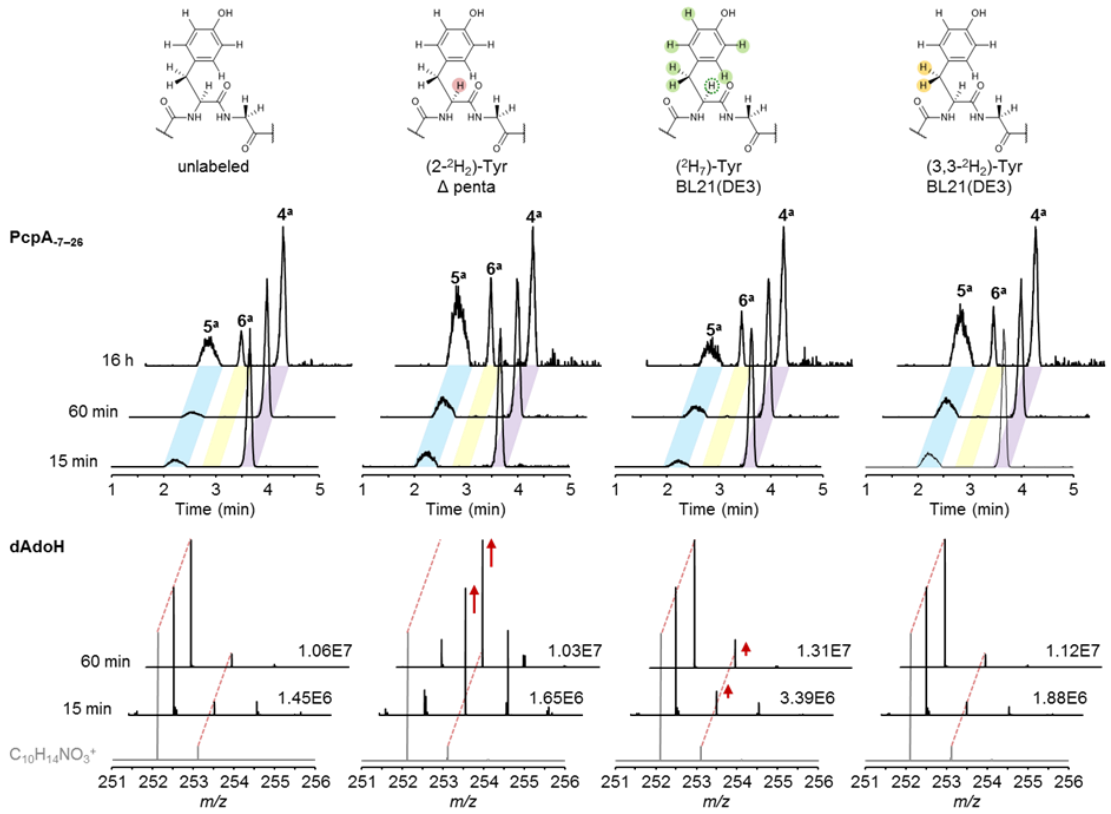


Figure S4.17 . In vitro PcpXY splicease reactions with differentially deuterium labeled PcpA substrates (top). The Tyr-Cα deuterium was mostly lost in the ($^2H_7$)-Tyr fed to BL21(DE3) due to reversible activity of transaminases, as indicated by the dashed green circle around the Cα-H (see also Figure S4.13). The E. coli Δpenta transaminase deletion mutant strain was used for retention of the Cα deuteriums in the (2-$^2H_7$)-Tyr fed sample. The corresponding LC-HRMS EICs for the substrate 4, ketoamide 5/5', and isomeric shunt 6 for the PcpA$_{-7–26}$ fragment released by GluC and trypsin digest (middle, LC Method 2) and the mass spectra for the dAdoH product (bottom) are shown below the relevant PcpA substrate. The simulated mass spectrum of dAdoH is shown for comparison. Enrichment in the dAdoD *m/z* 253.11 mass is indicated with red arrows. The reactions contained 40 µM PcpA, 20 µM reconstituted PcpXY ('6xH-bdSUMO' tagged), 1 mM SAM, and 10 mM DTT in Buffer A with biological reductants: 5 µM ecFldA, 1.25 µM ecFpr, and 1 mM NADPH.

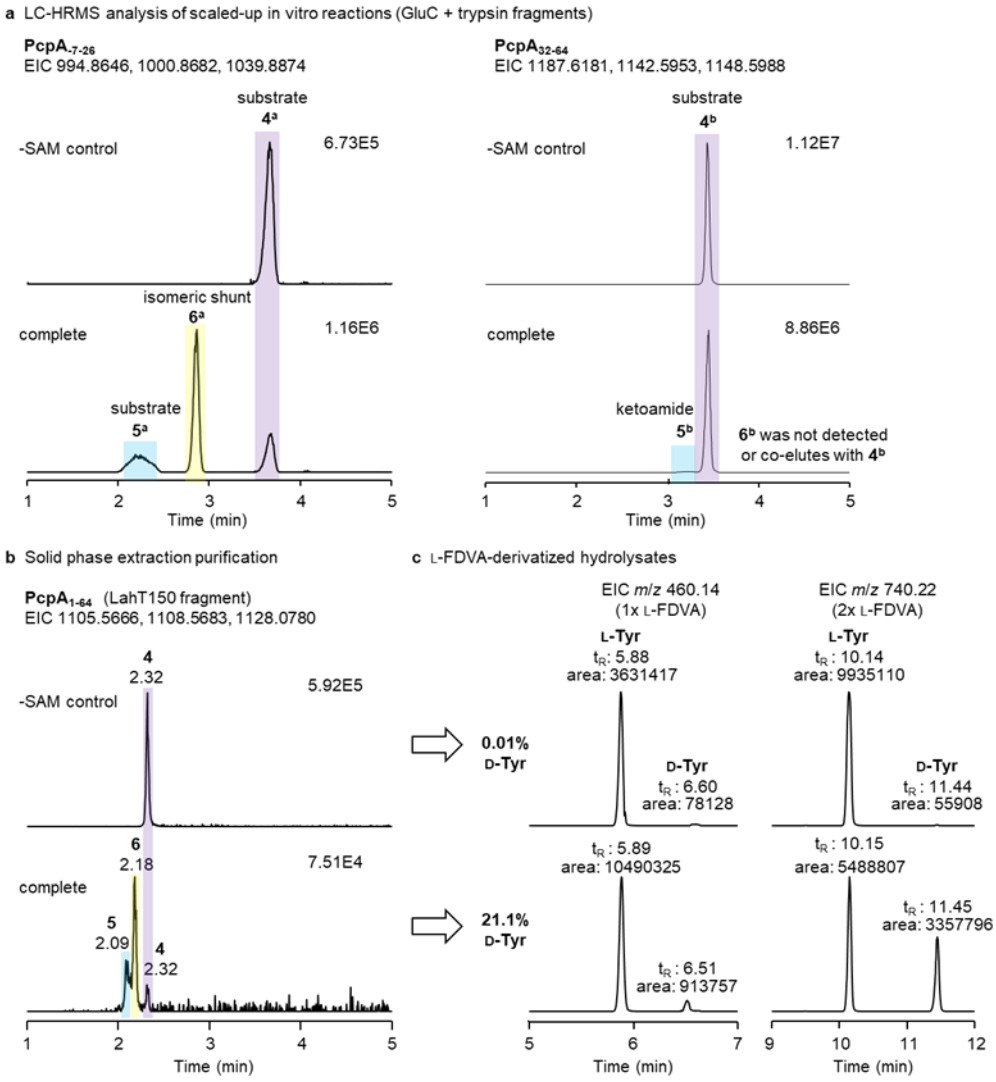


Figure S4.18. Isomeric shunt product 6 contains D-tyrosine. In vitro reactions with and without SAM were used as the test and control sample, respectively. Reaction conditions were: 100 µM PcpA, 50 µM reconstituted PcpXY ('6xH-SUMO' version), and 10 mM DTT with biological reductants (20 µM ecFldA, 5 µM ecFpr, and 2 mM NADPH) and ± 1 mM SAM in Buffer A (1 mL each). The two reactions were incubated at room temperature for 3 days. a) PcpA core peptides were detected by LC-HRMS using LC Method 2 following a diagnostic cleavage with GluC and trypsin to assess the reaction products. b) LC-HRMS analysis of the PcpA core peptides used for advanced Marfey's analysis following cleavage with LahT150 and purification by reverse Ni^{2+}-affinity column chromatography and SPE (LC Method 3). The shown 100% MeOH SPE elution fraction was the most enriched in the isomeric shunt 6. c) This sample was subjected to acid hydrolysis and derivatization with L-FDVA by advanced Marfey's method. Samples were analyzed by LC-HRMS to reveal mono- (left, $[M-H]^-$ = 460.1474) and di- (right, $[M-H]^-$ = 740.2282) derivatized tyrosine monomers. Peak areas for the EICs for these species were calculated in Thermo Xcaliber Qual Browser (v.4.1.31.9) using the ICIS peak detection

algorithm (default settings) to estimate that 21.1% of tyrosine is in the D-configuration relative to only 0.01% in the control. Note that the core peptide contains three tyrosine's (residues 8, 15, and 56); thus, if 6 were 100% pure, we would have expected ~33% D-tyrosine content. Extra L-tyrosine in the test sample is attributed to contaminating peptides in the 100% MeOH SPE elution fraction, including the substrate 4 and ketoamide 5.

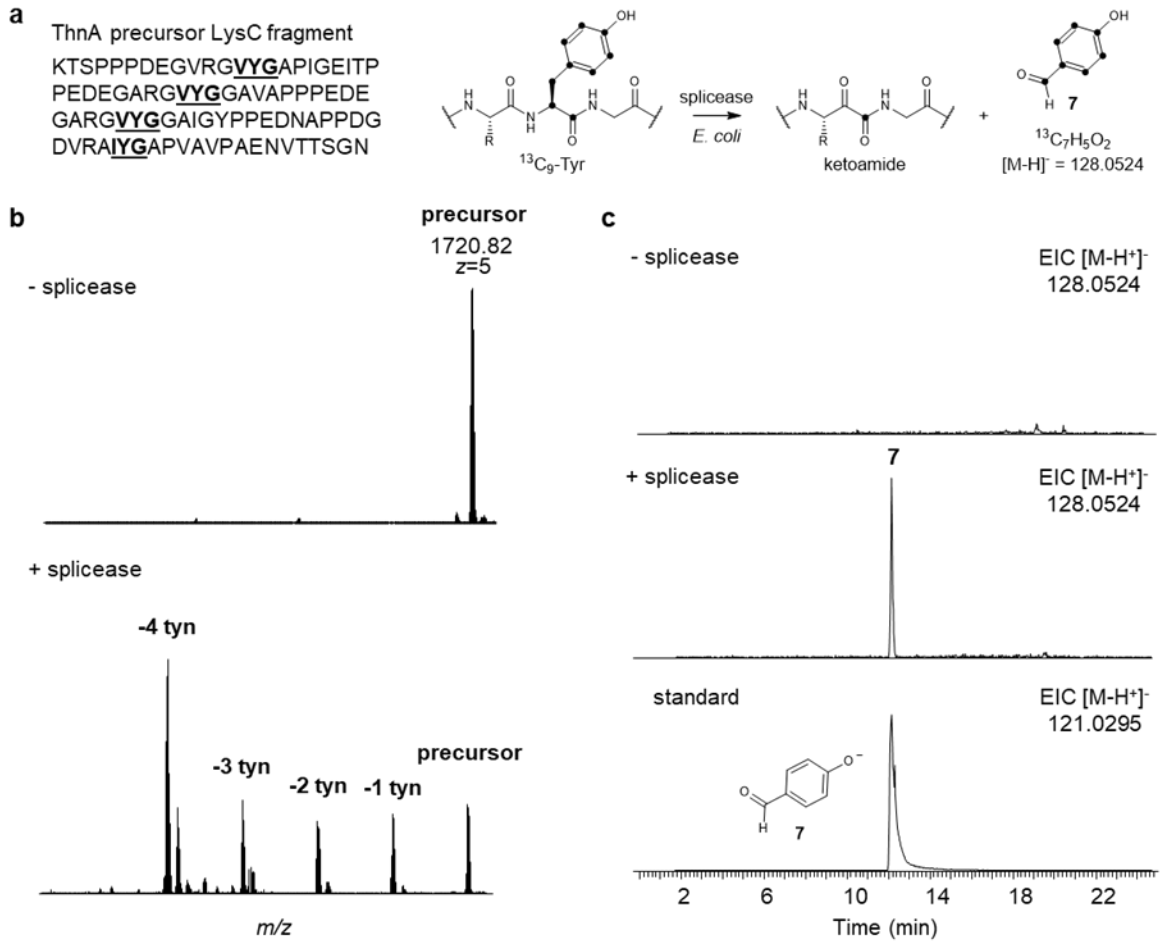


Figure S4.19. 4-Hydroxybenzaldehyde 7 was detected as a co-product of the splicing reaction in extracts of E. coli BL21(DE3) expressing the type III spliceotide system from Thiothrix nivea DSM 5205.10 a) The core peptide of the precursor protein ThnA released by LysC protease digest contains four XYG splice sites. b) (Co-)expression of ThnA precursor +/- ThnX splicease. Up to four ketoamides (indicated by '-1–4 tyn' for loss of tyramine equivalents) were detected in the core peptide fragment by LC-HRMS. c) Extracts of $^{13}C_9$-Tyr fed ThnA produced with ThnX (top) and without ThnX (middle) were analyzed by LC-HRMS in negative ion mode. Extracted ion chromatograms for the $^{13}C_7$-labeled 4-hydroxybenzaldehyde co-product ($[M-H]^-$ = 128.0524) from the expressions elutes identically with the commercial standard 7 ($[M-H]^-$ = 121.0295), strongly suggesting it is the splicease-dependent tyrosine side-chain product released during ketoamide formation.

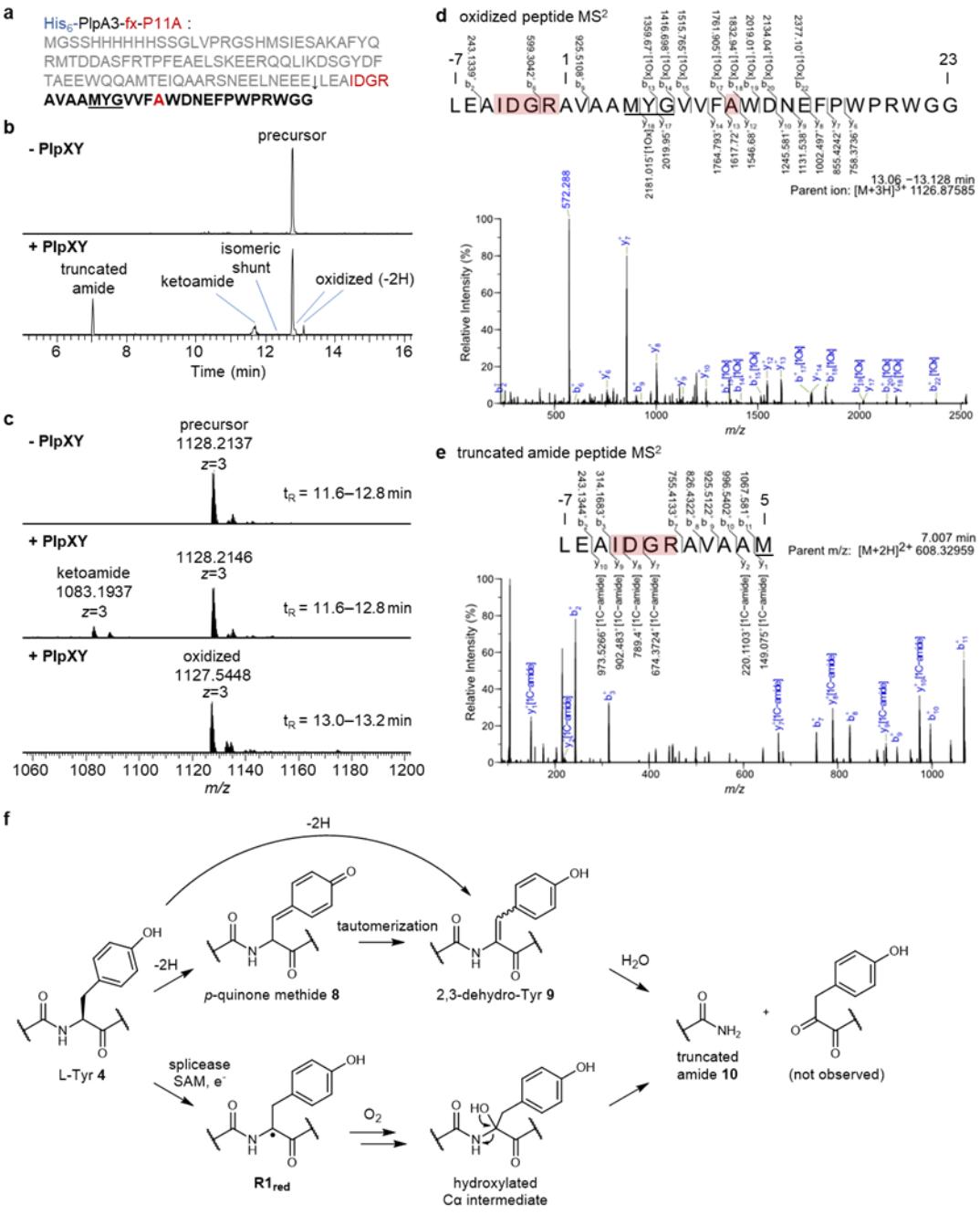


Figure S4.20. Identification of shunt products from the production of PlpA3-P11A mutant with PlpXY in E. coli BL21(DE3). LC-HRMS and MS2 analysis of the Ni^{2+}-affinity column chromatography purified His_6-PlpA3-fx-P11A cleaved with GluC. a) Sequence of the full-length precursor protein. The core sequence is in bold. Red residues are mutations from the wild-type sequence, where 'IDGR' is a Factor Xa cleavage site substituted for residues -4–-1 and P11A is a proline-to-alanine core mutant. The MYG splice site is underlined. b) EICs for the unmodified precursor $[M+3H]^{3+}$ = 1127.5485, ketoamide $[M+3H]^{3+}$ = 1082.5257, oxidized $[M+3H]^{3+}$ =

1126.8755, and truncated amide $[M+2H]^{2+}$ = 608.3293, for the precursor only expression (top) and precursor + plpXY coexpression (bottom). c) Mass spectrum for the precursor peptide (t_R = 12.6–12.8 min, top) from the precursor only expression. Mass spectra for the precursor and ketoamide modified peptides (t_R = 11.6–12.8 min, middle) and the oxidized peptide (t_R = 13.0–13.2 min, bottom) from the precursor + splicease coexpression. d) MS^2 spectrum of the oxidized peptide product (t_R = 13.06–13.13 min). The -2 Da mass shift is localized to Tyr6, as indicated by the '**1$_{ox}$**'-labeled fragment ions. e) MS^2 spectrum of the truncated amide peptide product. The amide is localized to Met5, now at the C-terminus. Glu6 is a missed GluC cleavage site. f) Proposed biosynthetic origin of the truncated amide product 10. Enzymatic oxidation of L-tyrosine substrate 4 to the (E/Z)-2,3-dehydro-Tyr 9 either directly or via a p-quinone methide **8** intermediate (upper route). Alternatively, the initial Cα-radical intermediate of an aborted splicease reaction could undergo spontaneous oxidative degradation (lower route).

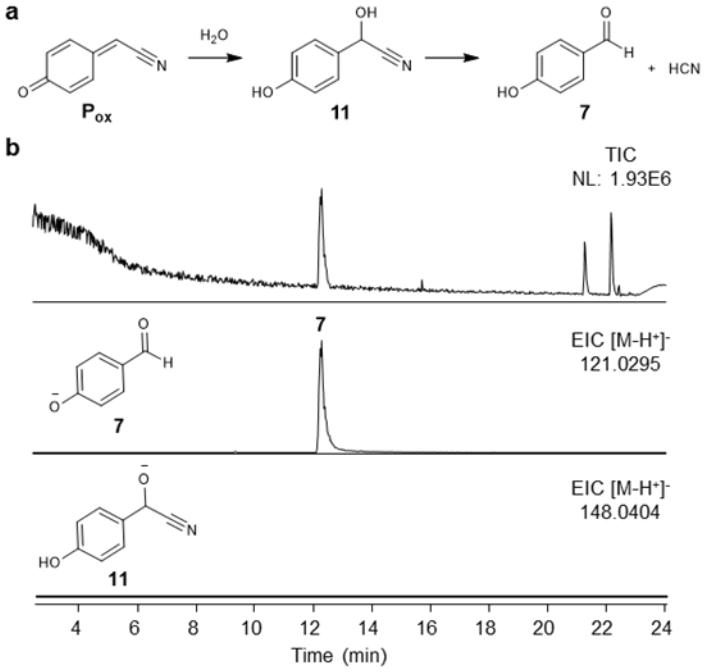


Figure S4.21. Commercial 4-hydroxymandelonitrile **11** rapidly degrades to 4-hydroxybenzaldehyde **7** under our in vitro splicease reaction conditions in support of our mechanistic proposal. a) Spontaneous addition of water to 7-cyano-p-quinone methide **P$_{ox}$** would yield **11** analogous to spontaneous chemistry known from the degradation of cyanogenic glycosides [36]. b) Total ion chromatogram (TIC, top) and EICs for $[M-H]^-$ = 121.0295 (**7**, middle) and $[M-H]^-$ = 148.0404 (**11**, bottom) of **11** dissolved in reaction buffer and quenched with formic acid similar to other small-molecule detection experiments.

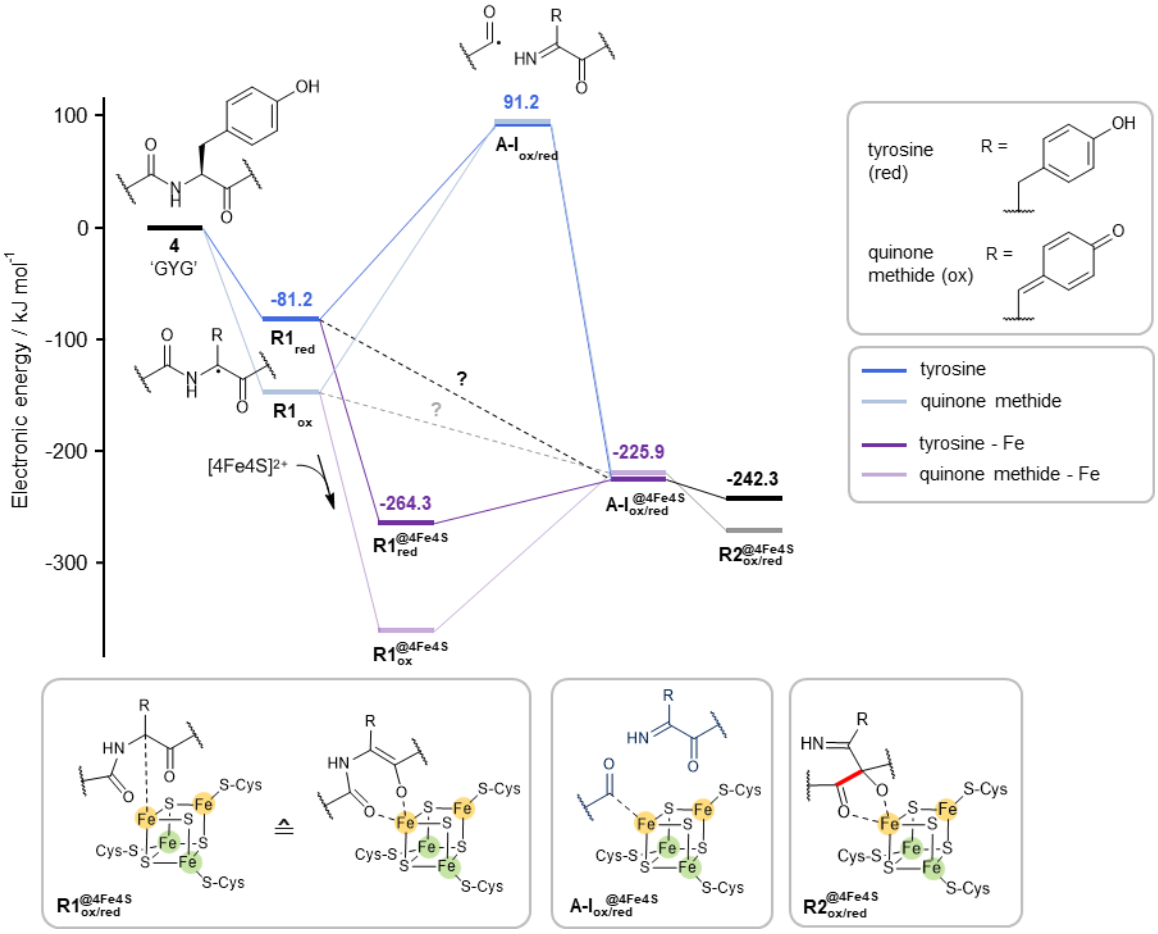


Figure S4.22. Mechanistic proposals for Pathway A of the splicease reaction involving an [4Fe-4S] cubane as catalyst relative to no catalyst. Intermediates with the superscript '@4Fe4S' are coordinated to the cubane. Electronic energies for the reduced tyrosine side chain are given in kJ/mol. We consider conversion of **R1**$_{ox/red}$ to **A-I**$_{ox/red}^{@Fe4S4}$ to be a two-step process proceeding either through **R1**$_{ox/red}^{@Fe4S4}$ (which is alike other resonance forms of **R1** bound to the cubane) or through A-I$_{ox/red}$. An overall concerted mechanism is possible (dashed lines) but unlikely due to the high number of bonds being concurrently formed or broken, and is not considered in this study.

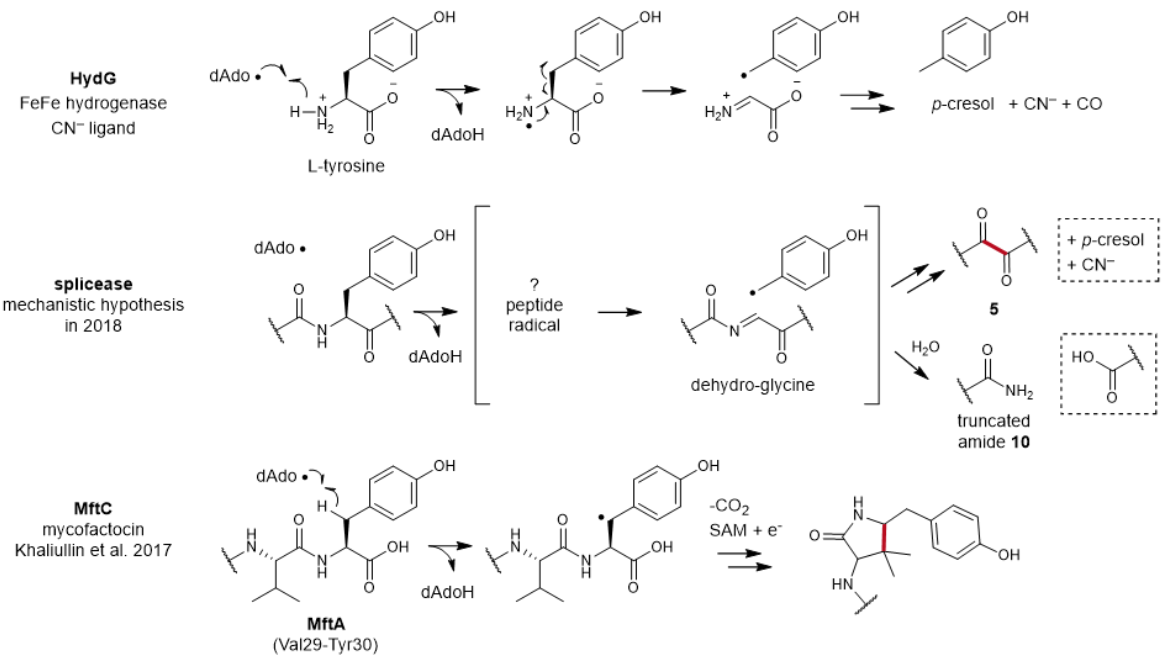


Figure S4.23. rSAM enzymes that act on tyrosine/tyrosyl substrates. Our original mechanistic hypothesis for splicease catalysis (middle) was based on HydG (top) to produce p-cresol and cyanide anion coproducts of the ketoamide 5 [40]. The amide side product was detected by LC-HRMS^2, but p-cresol, cyanide, and the C-terminal peptide fragment were not detected (species in the dashed boxes) in this set of *E. coli* coexpression experiments for the Plp and Pcp systems [8] HydG has a non-SPASM-type auxiliary [4Fe-4S] cluster in addition to its main [4Fe-4S] rSAM cluster and has low protein similarity to spliceases (<15% amino acid identity). MftC (bottom) is the closest characterized rSAM-SPASM enzyme to spliceases and catalyzes oxidative decarboxylation of a C-terminal tyrosine and C–C crosslinking between the Tyr-Cα and neighboring residue Val-Cβ. MftC works in concert with the discrete MftB RRE and uses two equivalents of SAM: one to abstract the Cβ-hydrogen of Tyr30 within the MftA precursor protein to mediate oxidative decarboxylation and one to abstract the Cβ-hydrogen of valine, in a second crosslinking step. MftC from *Mycobacterium ulcerans* Agy99 has 22% identity, 35.5% similarity and 31.2% gaps with PcpX as determined by the EMBOSS Needle pairwise sequence alignment tool [73].

Table S4.1.Type I splicease pathways screened for heterologous production and protein stability. XYG motifs within the core sequences are underlined as potential targets of the splicease reaction.

Gene cluster	Strain	Precursor	Core Sequence	Core Length
plp	*Pleurocapsa* sp. PCC 7319	PlpA2	AVAAMYGVVFPWDNEFPWPRWGG	23
		PlpA3	VDLSIFELLDEEPLFPIRPLYGLPI	25
pcp	*Pleurocapsa* sp. PCC 7327	PlpA	VTGGSGIYGPIQAMYGAVVGDPKPGKDWGWRFPSPLPKPSPIPSPWKPPVDV QPMYGVVVSNDS	64

Table S4.1 Continued.

Gene cluster	Strain	Precursor	Core Sequence	Core Length
nop	*Nostoc* sp. PCC 7120	NopA	TKTIHWIKGIFPGVVALYGVILDPLDPRDYLS	32
npp	*Nostoc punctiforme* PCC 73102	NppA	LTGKPRIQPLYGVVWPPYQLMYGVIRVDDTL	31
pap	*Pseudanabaena* sp. PCC 6802	PapA	YIGKAPIIQPMYGVIWWPWPIRPIRPIDPQPLYGVVIDDMLDK	43

Table S4.2. Sequences of splicease pathway proteins screened for heterologous production in E. coli. The N-terminal affinity and solubility tag fusion sequences are given below.

Protein	Protein ID	Locus Tag	Sequence
PlpA3	WP_019503882	PLEUR7319_RS0103845	MSIESAKAFYQRMTDDASFRTPFEAELSKEERQQLIKDSGYDFTAEEWQQAM TEIQAARSNEELNEEELEAIAGGAVAAMYGVVFPWDNEFPWPRWGG
PlpA2	WP_019503881	PLEUR7319_RS0103840	MSIENAKSFYERVSTDKQFRTQLENTASAEERQKIIQAAGFEFTNQEWEIAKEQ ILATSESNNGELSEAELTAVSGGVDLSIFELLDEEPLFPIRPLYGLPI
PlpX	WP_019503880	PLEUR7319_RS0103835	MTKKYRRVSYAVWEITLKCNLACSHCGSRAGQARTKELSTEEAFNLVRQLAD VGIKEVTLIGGEAFMRSDWLEIAKAVTEAGMICGMTTGGFGVSLETARKMKEA GIKTVSVSIDGGIPETHDRQRGKKGAWHSAFRTMSHLKEVGIYFGCNTQINRL SASEFPIIYERIRDAGARAWQIQLTVPMGNAADNADMLLQPYELLDIYPMLARV AKRAKQEGVRIQAGNNIGYYGPYERLLRGSDEWTFWQGCGAGLNTLGIEADG KIKGCPSLPTAAYTGGNIRDRPLREIVEQTEELKFNLKAGTEQGTDHMWGFCK TCEFAELCRGGCSWTAHVFFDRRGNNPYCHHRALKQAQKDIRERFYLKVKAK GNPFDNGEFVIIEEPFNAPLPENDLLHFNSDHIQWPENWQNSESAYALAK
PlpY	WP_019503879	PLEUR7319_RS41180	MNSNQIPNKVATAAQKSDDSSSVLPRQGWQDKQAFIKALIKAKQSLEIAEISNF LT
PcpA	K9T2X0	Ple7327_1425	MSSNILEKVKEFFVRLVKDDAFQSQLQNNSIDEVRNILQEAGYIFSKEEFETATI ELLDLKERDEFHELTEEELVTAVGGVTGGSGIYGPIQAMYGAVVGDPKPGKDW GWRFPSPLPKPSPIPSPWKPPVDVQPMYGVVVSNDS
PcpX	K9T3W7	Ple7327_1426	MTYRRTSYAVWEITLKCNLACSHCGSRAGHTRAKELSTQEALDLVRQMADVGI IEVTLIGGEAFLRPDWLQIAEAITKAGMLCSMTTGGYGISLETARKMKAAGIASV SVSIDGLEETHDRLRGRKGSWQAAFKTMSHLREVGIFFGCNTQINRLSAPEFP LIYERIRDAGARAWQIQLTVPMGRAADNANILLQPYELLDLYPMIARVARRARQ EGVQIQPGNNIGYYGPYERLLRGRGSDSEWAFWQGCAAGLSTLGIEADGAIK GCPSLPTSAYTGGNIREHSLREIVEESEQLRFNLGAGTSQGTAHLWGFCQTCE FSELCRGGCTWTAHVFFNRRGNNPYCHHRALFQAEQGIRERVVPKVEAQGLP FDNGEFELIEEPIDAPLPENDPLHFTSDLVQWSASWQEESESIGAVVD
PcpY	K9T1S9	Ple7327_1427	MVENIDNEREKSANEIEPESLLLPRQAWQSQIAYLKAILKAKQALDRIEKRYLR
NopA	WP_044521191	All2030	MSIESAKAFYQRITTDPTFRTQIESYSSEERISFLQGTGYNFTEEEWETATAEIL ETSSPDEELNEAELAAIAGGTKTIHWIKGIFPGVVALYGVILDPLDPRDYLS
NopX	WP_010996190	All2029	MSEKHHRTSYAVWEITLKCNLACSHCGSRAGQARHQELSTAEALNLVQQLAE VGIKEVTLIGGEAFLRPDWLVIAKAITDAGMLCGMTTGGYGISLEMAQRMKEAG IAKVSVSTDGMEATHDHLRGRKGSWKSGLRTMSYLKEVGILFGCNTQINRLSA PEFPSIYEHIRDAGARAWQIQLTVPMGNAADNADILLQPSELLDLYPMLARVAQ RANTEGVRVAAGNNIGYYGPYERLLRGQGKEWGFWRGCGAGLSTLGLEADG TIKGCPSLPTTAYAGGNIRERPLREIVEQSEELQFNLYAGTPEGTAYLWGFCKT CKFAELCRGGCTWTAHVFFNRRGNNPYCHHRALELAKRGLRERVYPKVSAP GVPFDNGEFTIIEEPLDAPWIENDPLHFTADSIQWPDSWQSKSELFYSVAR
NopY	WP_010996189	Asl2028	MNHLNEENQDANISSEELLVSQPLLPRFAWEDERAFLREVIKAKQALDIAELTAI IWQKTNH
NppA	B2J0W4	Npun_R3395	MSLEHVKAFYQKLANDEAFSNQIQGVNSKEECSQIVKAAGYDFTLEEYEEYTA QLLESADGEGELKDLSEKELAAVFGGLTGKPRIQPLYGVVWPPYQLMYGVIRV DDTL

Table S4.2 Continued.

Protein	Protein ID	Locus Tag	Sequence
NppX	B2J0W3	Npun_R3393	MTYRRISYAVWEITLKCNLACQHCGSRAGHTRANELSTAEALDLVKQMAEVGI TEVTIIGGEAFLRPDWLEIAQAITKAGMLCGMTTGGYGITLDTARRMKEAGIGVV SVSVDGLEATHDRLRGKQGSWQWAFKTMSNLKEAGIPFGCNTQINRLSAPEF PQIYERIRDAGVFAWQIQLTVPMGNAADNGDILLQPYELLDIYPMIARVAERAKE EGVQIQPGNNIGYYGPYERLLRGGDAWSFWQGCSAGLSALGIEADGAIKGCP SLPTTAYTGGNIRDHSLRTIIEETEELRFNLEADTPKGTSHLWGFCKSCEFAELC RGGCSWTAHVFFDKRGNNPYCHHRALTQEKGGIRERVFLQRRADGNPFDNG EFALIEEPINTAWPENDPLHFTSDRIQWPEGWKEEPLVSSLVSSKSHSDK
NppY	B2J0W2	Npun_R3392	MSSKFIPPEDPNITHIEQSQNEVEPLLTLLPRSAWNSQLNYLRLIFRAKKALDRIE KEAGIFKSYN
PapA	WP_019501034	PSE6802_RS0115865	MSENTFNKLKEFIVRLIKDREFRSALERTERSKRTGFLADRGYAFTTESFETGAI ELMSARQKGEFTDVSEEELAGVFGGYIGKAPIIQPMYGVIWWPWPIRPIRPIDP QPLYGVVIDDMLDK
PapX	WP_019501033	PSE6802_RS0115860	MSYSRKSYAVWEITLNCNLACQHCGSRAGHARNAELTTSEALDLVRQMSDIGI TEVTIIGGEAFMRPDWLEIAQVISQAGMVCSMTTGGFGISLDMARRMKDAGISA VSISVDGLEGTHDRLRGRVGSWASCFRTMGHFREVGLFFGCNTQINRYSAPE LPLVYEKILEAGAKAWQIQLTVPMGNAVDNSAMLLQPYELLDLYPMLAEIAKKA KNDGLSLQPGNNIGYYGPYERLLRGRGDAWGFWQGCAAGLSTLGIEADGAIK GCPSLPTNAYTGGNVRDRTLREIVENSAELRFNIGADTDRLWGFCETCEFAKL CRGGCTWTSHVFFDRRGNNPYCHHRALTQASRGIRERVVLKTKAPGLPFDNG MFEMVAEPTSTELNSDDPLAFSSDRIQWPTNWHQEEVMTNS
PapY	WP_019501032	PSE6802_RS34275	MASFIPLEPAERSTSDLTLLPRDPWPNQLQYLLLVFQAKQALERVEKAFILN

N-terminal tags:	Sequence *(vertical line indicates protease cleavage site)*
'6xH-v' (v = TEVp cleavage site in bold)	MGSSHHHHHHSSG**ENLYFQ|S**H…
'6xH-bdSUMO' (source of *Brachypodium distachyon* SUMO sequence in bold is reference[2])	MGSHHHHHHHSSGLVPRGSASH**INLKVKGQDGNEVFFRIKRSTQLKKLMNA YCDRQSVDMTAIAFLFDGRRLRAEQTPDELEMEDGDEIDAMLHQTGG|**H…
'6xH-MBP-v' (v = TEVp cleavage site; source of MBP-v sequence in bold is plasmid pMalc2T, New England Biolabs)	MGSSHHHHHHSQDP**KIEEGKLVIWINGDKGYNGLAEVGKKFEKDTGIKVTVE HPDKLEEKFPQVAATGDGPDIIFWAHDRFGGYAQSGLLAEITPDKAFQDKLY PFTWDAVRYNGKLIAYPIAVEALSLIYNKDLLPNPPKTWEEIPALDKELKAKG KSALMFNLQEPYFTWPLIAADGGYAFKYENGKYDIKDVGVDNAGAKAGLTFL VDLIKNKHMNADTDYSIAEAAFNKGETAMTINGPWAWSNIDTSKVNYGVTVL PTFKGQPSKPFVGVLSAGINAASPNKELAKEFLENYLLTDEGLEAVNKDKPL GAVALKSYEEELAKDPRIAATMENAQKGEIMPNIPQMSAFWYAVRTAVINAA SGRQTVDEALKDAQTNSSSNNNNNNNNNLGIEGLYFQ|S**H…

Table S4.3. Primers used to amplify splicease pathway genes from cyanobacterial gDNA.

Primer name	**Sequence** 5'→3' (NdeI and XhoI restriction sites in bold; 'GTAA' included as a primer extension for efficient cleavage near DNA ends)
Nif11 precursor protein forward (NdeI):	
plpA3__F	GTAA **CATATG** TCT ATT GAA AGT GCA AAA GCT T
plpA2__F	GTAA **CATATG** TCT ATC GAA AAC GCA AAA TCA T
pcpA_ F	GTAA **CATATG** TCC TCA AAT ATC TTA GAA AAA GTC A
nopA_F	GTAA **CATATG** TCT ATT GAA AGC GCA AAA GC
nppA_ F	GTAA **CATATG** TCT CTA GAA CAC GTC AAA GC
papA_F	GTAA **CATATG** TCA GAA AAT ACG TTC AAC AAG C
Nif11 precursor protein reverse (XhoI):	
plpA3_ R	GTAA **CTCGAG** TTA TCC CCC CCA CCT AGG CC
plpA2_ R	GTAA **CTCGAG** CTA TAT TGG TAA ACC ATA CAG AGG TCT
pcpA_R	GTAA **CTCGAG** TTA TGA ATC GTT TGA GAC AAC TAC CC
nopA_R	GTAA **CTCGAG** CTA TGA AAG ATA ATC GCG TGG ATC
nppA_R	GTAA **CTCGAG** CTA AAG TGT GTC ATC TAC CCG GAT
papA_R	GTAA **CTCGAG** CTA TTT ATC AAG CAT GTC GTC AAT AAC
Splicease forward (NdeI):	
plpX_F	GTAA **CATATG** ACT AAA AAA TAC AGA CGA GTT AGT TA
pcpX_F	GTAA **CATATG** ACT TAT CGC AGA ACC AGT TAT
nopX_F	GTAA **CATATG** TCT GAA AAA CAC CAT CGA ACC
nppX_F	GTAA **CATATG** ACT TAT CGC CGA ATT AGT TAT G
papX_F	GTAA **CATATG** TCT TAT AGT AGA AAA AGC TAT GCG

Table S4.3 Continued.

Primer name	Sequence 5'→3' (NdeI and XhoI restriction sites in bold; 'GTAA' included as a primer extension for efficient cleavage near DNA ends)
Splicease reverse (XhoI):	
plpX_R	GTAA **CTCGAG** TTA CTT TGC TAA AGC GTA AGC AG
pcpX_R	GTAA **CTCGAG** TTA ATC AAC TAC AGC ACC AAT CGA C
nopX_R	GTAA **CTCGAG** TCA TCT TGC TAC AGA ATA AAA AAG TTC
nppX_R	GTAA **CTCGAG** TTA TTT ATC TGA ATG AGA TTT AGA ACT AAC TA
papX_R	GTAA **CTCGAG** TCA GGA ATT AGT CAT TAC TTC TTC TTG
Accessory protein forward (NdeI):	
plpY_F	GTAA **CATATG** AAC TCT AAT CAA ATA CCA AAT AAA GTA G
pcpY_F	GTAA **CATATG** GTC GAA AAT ATA GAC AAC GAG C
nopY_F	GTAA **CATATG** AAT CAT TTA AAC GAA GAA AAT CAG G
nppY_F	GTAA **CATATG** TCA AGT AAA TTT ATC CCT CCA GAA G
papY_F	GTAA **CATATG** GCT TCC TTT ATA CCA CTG GAA C
Accessory protein reverse (XhoI):	
plpY_R	GTAA **CTCGAG** TCA TGT CAG AAA ATT GCT AAT TTC AG
pcpY_R	GTAA **CTCGAG** TTA ACG CAA ATA CCT TTT TTC TAT TCG
nopY_R	GTAA **CTCGAG** TTA ATG ATT TGT TTT TTG CCA AAT AAT AGC
nppY_R	GTAA **CTCGAG** TTA GTT GTA ACT TTT GAA GAT ACC AGC
papY_R	GTAA **CTCGAG** CTA ATT TAG GAT AAA TGC TTT TTC CAC G

Table S4.4. Expression plasmids used in this study. Multigene cassettes were amplified with their native intergenic regions. Forward and reverse primers are provided in Table S3. Plasmids pCDF-6xH-v, pCDF-6xH-MBP-v, and pCDF-6xH-bdSUMO are modified pCDFDuet-1 (Novagen) described in Table S2. Molecular weights were calculated using the Expasy ProtParam web tool.3 Spt, spectinomycin; Amp, ampicillin; Chl, chloramphenicol.

Plasmid name	Antibiotic selection	Expressed protein(s)	Molecular Weight (Da)	Forward/Reverse Primer or Source	Template (gDNA)	Reference
pCDF_6xH-v-plpA3	Spt	6xH-v-PlpA3	13906.27	plpA3_F / plpA3_R	PCC 7319	This study
pCDF_6xH-v-plpA2	Spt	6xH-v-PlpA2	13668.86	plpA2_F / plpA2_R	PCC 7319	This study
pCDF_6xH-v-plpX	Spt	6xH-v-PlpX	49412.97	plpX_F / plpX_R	PCC 7319	This study
pCDF_6xH-v-plpXY	Spt	6xH-v-PlpX + PlpY	49412.97 + 6161.00	plpX_F / plpY_R	PCC 7319	This study
pCDF_6xH-MBP-v-plpY	Spt	6xH-MBP-v-PlpY	50726.117	plpY_F / plpY_R	PCC 7319	This study
pCDF_6xH-v-pcpA	Spt	6xH-v-PcpA	18448.61	pcpA_F / pcpA_R	PCC 7327	This study
pCDF_6xH-v-pcpX	Spt	6xH-v-PcpX	48941.11	pcpX_F / pcpX_R	PCC 7327	This study
pCDF_6xH-v-pcpXY	Spt	6xH-v-PcpX + PcpY	48941.11 + 6411.39	pcpX_F / pcpY_R	PCC 7327	This study
pCDF_6xH-MBP-v-pcpY	Spt	6xH-MBP-v-PcpY	50976.50	pcpY_F / pcpY_R	PCC 7327	This study
pCDF_6xH-bdSUMO-pcpY	Spt	6xH-bdSUMO-PcpY	17608.92	pcpY_F / pcpY_R	PCC 7327	This study
pCDF_6xH-bdSUMO-pcpX	Spt	6xH-bdSUMO-PcpX	57703.11	pcpX_F / pcpX_R	PCC 7327	This study
pCDF_6xH-bdSUMO-pcpXY	Spt	6xH-bdSUMO-PcpX + PcpY	57703.11 + 6411.39	pcpX_F / pcpY_R	PCC 7327	This study
pCDF_6xH-v-nopA	Spt	6xH-v-NopA	14405.79	nopA_F / nopA_R	PCC 7120	This study
pCDF_6xH-v-nopX	Spt	6xH-v-NopX	48870.31	nopX_F / nopX_R	PCC 7120	This study
pCDF_6xH-v-nopXY	Spt	6xH-v-NopX + NopY	48870.31 + 7229.15	nopX_F / nopY_R	PCC 7120	This study
pCDF_6xH-MBP-v-nopX	Spt	6xH-MBP-v-NopY	51794.27	nopY_F / nopY_R	PCC 7120	This study
pCDF_6xH-v-nppA	Spt	6xH-v-NppA	14763.37	nppA_F / nppA_R	PCC 7120	This study
pCDF_6xH-v-nppX	Spt	6xH-v-NppX	49345.53	nppX_F / nppX_R	PCC 73102	This study
pCDF_6xH-v_nppXY	Spt	6xH-v-NppX + NppY	49345.53	nppX_F / nppY_R	PCC 73102	This study
pCDF_6xH-MBP-v-nppY	Spt	6xH-MBP-v-NppY	51794.27	nppY_F / nppY_R	PCC 73102	This study
pCDF_6xH-v-papA	Spt	6xH-v-PapA	16613.81	papA_F / papA_R	PCC 6802	This study
pCDF_6xH-v-papX	Spt	6xH-v-PapX	45367.44	papX_F / papX_R	PCC 6802	This study

Table S4.4 Continued.

Plasmid name	Antibiotic selection	Expressed protein(s)	Molecular Weight (Da)	Forward/Reverse Primer or Source	Template (gDNA)	Reference
pCDF_6xH-v-_papXY	Spt	6xH-v-PapX + PapY	45367.44 + 6013.01	papX_F / papY_R	PCC 6802	This study
pCDF_6xH-MBP-papY	Spt	6xH-MBP-v-PapY	50578.12	papY_F / papY_R	PCC 6802	This study
pBad-6xH-v-PcpA	Amp	6xH-v-PcpA	18448.61	cloned by excising NcoI/XhoI fragment from pCDF_6xH-v-pcpA ligated into pBad/Myc-HisA (Thermo)	This study	pBad-6xH-v-PcpA
JW0671-AM (flavodoxin)	Chl	6xH-ecFldA	21584.92	ASKA clone(-)	NA	JW0671-AM (flavodoxin)
JW3895-AM (flavodoxin reductase)	Chl	6xH-ecFpr	29598.92	ASKA clone(-)	NA	JW3895-AM (flavodoxin reductase)
JW0155-AM (5'-methylthioadenosine nucleosidase)	Chl	6xH-ecMTAN (i.e., pfs)	26688.54	ASKA clone(-)	NA	JW0155-AM (5'-methylthioadenosine nucleosidase)
JW2514-AM (cysteine desulfurase)	Chl	6xH-ecIscS	46937.48	ASKA clone(-)	NA	JW2514-AM (cysteine desulfurase)
JW3686-AM (tryptophanase)	Chl	6xH-ecTnaA	54621.44	ASKA clone(-)	NA	JW3686-AM (tryptophanase)

Table S4.5. Peptides detected by LC-HRMS in positive ion mode. Monoisotopic mass (M) or mass-to-charge (*m/z*) ratios are shown. The extracted ion chromatogram (EIC) list is for the most abundant charge state and isotope.

Peptide	Molecular formula	Exact mass (M)	Charge state (*z*)	Substrate 4 and isomeric shunt 6 (*m/z*)	ketoamide 5 (*m/z*)	α-ketone hydrate 5' (*m/z*)	EIC list (*m/z*)
PcpA$_{7\text{-}64}$ (GluC fragment)	$C_{341}H_{516}N_{84}O_{94}S_2$	7355.7621	+6	1226.9676	1204.4562	1207.4580	1205.1247, 1208.1265, 1227.6361
PcpA$_{7\text{-}26}$ (fragment a)	$C_{140}H_{226}N_{36}O_{42}S$	3115.6376	+3	1039.5532	994.5303	1000.5339	994.8646, 1000.8682, 1039.8874
PcpA$_{32\text{-}64}$ (fragment b)	$C_{167}H_{252}N_{38}O_{46}S$	3557.8269	+3	1186.9496	1141.9268	1147.9303	1187.6181, 1142.5953, 1148.5988
PcpA$_{1\text{-}64}$ (core)	$C_{314}H_{469}N_{77}O_{86}S_2$	6758.4134	+6	1127.4095	1104.8981	1107.8999	1105.5666, 1108.5683, 1128.0780

References

1. Robello, M. et al. The alpha keto amide moiety as a privileged motif in medicinal chemistry: current insights and emerging opportunities. *J. Med. Chem* **2021**, *64*, 3508–3545.

2. Arasappan, A. et al. Discovery of narlaprevir (SCH 900518): a potent, second generation HCV NS3 serine protease inhibitor. *ACS Med. Chem. Lett* **2010**, *1*, 64–69.

3. Zhang, L. et al. α-Ketoamides as broad-spectrum inhibitors of coronavirus and enterovirus replication: structure-based design, synthesis, and activity assessment. *J. Med. Chem*. **2020**, *63*, 4562–4578.

4. Fusetani, N., Sugawara, T., Matsunaga, S. & Hirota, H. Orbiculamide A: a novel cytotoxic cyclic peptide from a marine sponge Theonella sp. *J. Am. Chem. Soc*. **1991**, *113*, 7811–7812.

5. Kimura, M. et al. Calyxamides A and B, cytotoxic cyclic peptides from the marine sponge Discodermia calyx. *J. Nat. Prod*. **2012**, *75*, 290–294.

6. Plaza, A., Viehrig, K., Garcia, R. & Müller, R. Jahnellamides, α-keto-β-methionine-containing peptides from the terrestrial myxobacterium Jahnella sp.: Structure and biosynthesis. *Org. Lett*. **2013**, *15*, 5882–5885.

7. Issac, M. et al. Cyclotheonellazoles A-C, potent protease inhibitors from the marine sponge theonella aff. swinhoei. *J. Nat. Prod*. **2017**, *80*, 1110–1116.

8. Morinaka, B. I. et al. Natural noncanonical protein splicing yields products with diverse β-amino acid residues. *Science* **2018**, *359*, 779–782.

9. Broderick, J. B., Duffus, B. R., Duschene, K. S. & Shepard, E. M. Radical *S*-Adenosylmethionine Enzymes. *Chem. Rev*. **2014**, *114*, 4229–4317.

10. Scott, T. A. et al. Widespread microbial utilization of ribosomal β-amino acid-containing peptides and proteins. *Chem* **2022**, *8*, 2659–2677.

11. Zeng, W., Song, Y., Wang, R., He, R. & Wang, T. Neutrophil elastase: from mechanisms to therapeutic potential. *J. Pharm. Anal*. **2023**, *13*, 355–366.

12. Lakis, E., Magyari, S. & Piel, J. In vivo production of diverse β-amino acid-containing proteins. *Angew. Chem. Int. Ed. Engl*. **2022**, *61*, e202202695.

13. Richter, D., Lakis, E. & Piel, J. Site-specific bioorthogonal protein labelling by tetrazine ligation using endogenous β-amino acid dienophiles. *Nat. Chem*. **2023**, *15*, 1422–1430.

14. Montalbán-López, M. et al. New developments in RiPP discovery, enzymology and engineering. *Nat. Prod. Rep*. **2021**, *38*, 130–239.

15. Hoffman, B. M., Broderick, W. E. & Broderick, J. B. Mechanism of radical Initiation in the radical SAM enzyme superfamily. *Annu. Rev. Biochem*. **2023**, *92*, 333–349.

16. Grell, T. A. J., Goldman, P. J. & Drennan, C. L. SPASM and twitch domains in *S*-adenosylmethionine (SAM) radical enzymes. *J. Biol. Chem*. **2015**, *290*, 3964–3971.

17. Lanz, N. D. & Booker, S. J. Auxiliary iron-sulfur cofactors in radical SAM enzymes. *Biochim. Biophys. Acta* **2015**, *1853* (6), 1316–1334.

18. Haft, D. H., Basu, M. K. & Mitchell, D. A. Expansion of ribosomally produced natural products: a nitrile hydratase- and Nif11-related precursor family. *BMC Biol*. **2010**, *8*, 70.

19. Burkhart, B. J., Hudson, G. A., Dunbar, K. L. & Mitchell, D. A. A prevalent peptide-binding domain guides ribosomal natural product biosynthesis. *Nat. Chem. Biol*. **2015**, *11*, 564–570.

20. Castenholz, R. W. Portrait of a geothermal spring, Hunter's Hot Springs, Oregon. *Life* **2015**, *5*, 332–347.

21. Frey, S. & Görlich, D. A new set of highly efficient, tag-cleaving proteases for purifying recombinant proteins. *J. Chromatogr. A* **2014**, *1337*, 95–105.

22. Ruszczycky, M. W., Zhong, A. & Liu, H. Following the electrons: peculiarities in the catalytic cycles of radical SAM enzymes. *Nat. Prod. Rep*. **2018**, *35*, 615–621.

23. Liu, A. & Gräslund, A. Electron paramagnetic resonance evidence for a novel interconversion of $[3Fe\text{-}4S]^{+}$ and $[4Fe\text{-}4S]^{+}$ clusters with endogenous iron and sulfide in anaerobic ribonucleotide reductase activase in vitro. *J. Biol. Chem*. **2000**, *275*, 12367–12373.

24. Rupp, H., Rao, K. K., Hall, D. O. & Cammack, R. Electron spin relaxation of iron-sulphur proteins studied by microwave power saturation. *Biochim. Biophys. Acta* **1978**, *537*, 255–269.

25. Panufnik, E. & Kañska, M. Enzymatic synthesis of isotopomers of tyramine labeled with deuterium and tritium. *J. Label. Compd. Radiopharm*. **2007**, *50*, 85–89.

26. Kegler, C. et al. Rapid determination of the amino acid configuration of xenotetrapeptide. *ChemBioChem* **2014**, *15*, 826–828.

27. Fujii, K., Ikai, Y., Oka, H., Suzuki, M. & Harada, K. A nonempirical method using LC/MS for determination of the absolute configuration of constituent amino acids in a peptide: combination of Marfey's method with mass spectrometry and its practical application. *Anal. Chem*. **1997**, *69*, 5146–5151.

28. Han, X. X., Rodriguez, R. S., Haynes, C. L., Ozaki, Y. & Zhao, B. Surface-enhanced Raman spectroscopy. *Nat. Rev. Methods Primers* **2022**, *1*, 1–17.

29. Lacroix, C., Saussereau, E., Boulanger, F. & Goullé, J. P. Online liquid chromatography-tandem mass spectrometry cyanide determination in blood. *J. Anal. Toxicol*. **2011**, *35*, 143–147.

30. Storey, J. M. et al. A rapid liquid chromatography determination of free formaldehyde in cod. *Food Addit. Contam. Part A* **2015**, *32*, 657–664.

31. Yea, K. et al. Ultra-sensitive trace analysis of cyanide water pollutant in a PDMS microfluidic channel using surface-enhanced Raman spectroscopy. *Analyst* **2005**, *130*, 1009–1011.

32. Phan, C.-S. et al. Substrate promiscuity of the triceptide maturase XncB leads to incorporation of various amino acids and detection of oxygenated products. *ACS Chem. Biol*. **2024**, *19*, 855–860.

33. Guo, S. et al. Radical SAM-dependent ether crosslink in daropeptide biosynthesis. *Nat. Commun*. **2022**, *13*, 2361.

34. Patchornik, Abraham. & Sokolovsky, Mordechai. Nonenzymatic cleavages of peptide chains at the cysteine and serine residues through their conversion into dehydroalanine. I. Hydrolytic and oxidative cleavage of dehydroalanine residues. *J. Am. Chem. Soc*. **1964**, *86*, 1206–1212.

35. Bateman, R. C., Youngblood, W. W., Busby, W. H. & Kizer, J. S. Nonenzymatic peptide alpha-amidation. Implications for a novel enzyme mechanism. *J. Biol. Chem*. **1985**, *260*, 9088–9091.

36. MacFarlane, I. J., Lees, E. M. & Conn, E. E. The in vitro biosynthesis of dhurrin, the cyanogenic glycoside of Sorghum bicolor. *J. Biol. Chem*. **1975**, *250*, 4708–4713.

37. Gallagher, M. E., Mayhew, S. G., Malthouse, J. P. & Fillat, M. F. Cyanylation of the thiol of the cysteine of flavodoxin from Anabaena PCC 7119. *Biochem. Soc. Trans*. **1996**, *24*, 40S.

38. Chen, D., Scopelliti, R. & Hu, X. Synthesis and reactivity of iron acyl complexes modeling the active site of [Fe]-hydrogenase. *J. Am. Chem. Soc*. **2010**, *132*, 928–929.

39. Noodleman, L. Exchange coupling and resonance delocalization in reduced iron-sulfur $[Fe_4S_4]^+$ and iron-selenium $[Fe_4Se_4]^+$ clusters. 1. Basic theory of spin-state energies and EPR and hyperfine properties. *Inorg. Chem*. **1991**, *30*, 246–256.

40. Britt, R. D., Tao, L., Rao, G., Chen, N. & Wang, L.-P. Proposed mechanism for the biosynthesis of the [FeFe] hydrogenase H-cluster: central roles for the radical SAM enzymes HydG and HydE. *ACS Bio. Med. Chem. Au* **2021**, *2*, 11–21.

41. Vagstad, A. L. et al. Introduction of D-amino acids in minimalistic peptide substrates by an *S*-adenosyl-L-methionine radical epimerase. *Angew. Chem. Int. Ed. Engl*. **2019**, *58*, 2246-2250.

42. Walls, W. G. et al. Direct detection of the α-carbon radical intermediate formed by OspD: mechanistic insights into radical *S*-adenosyl-L-methionine peptide epimerization. *J. Am. Chem. Soc*. **2024**, *146*, 5550–5559.

43. Benjdia, A., Guillot, A., Ruffié, P., Leprince, J. & Berteau, O. Post-translational modification of ribosomally synthesized peptides by a radical SAM epimerase in Bacillus subtilis. *Nat. Chem*. **2017**, *9*, 698–707.

44. Benjdia, A. et al. Thioether bond formation by SPASM domain radical SAM enzymes: Cα H-atom abstraction in subtilosin A biosynthesis. *Chem. Commun*. **2016**, *52*, 6249–6252.

45. Backman, L. R. F., Funk, M. A., Dawson, C. D. & Drennan, Catherine. L. New tricks for the glycyl radical enzyme family. *Crit. Rev. Biochem. Mol. Biol*. **2017**, *52*, 674–695.

46. Goldman, P. J. et al. X-ray structure of an AdoMet radical activase reveals an anaerobic solution for formylglycine posttranslational modification. *Proc. Natl. Acad. Sci. U.S.A*. **2013**, *110*, 8519–8524.

47. Davis, K. M. et al. Structures of the peptide-modifying radical SAM enzyme SuiB elucidate the basis of substrate recognition. *Proc. Natl. Acad. Sci. U.S.A*. **2017**, *114*, 10420–10425.

48. Grove, T. L. et al. Structural insights into thioether bond formation in the biosynthesis of sactipeptides. *J. Am. Chem. Soc*. **2017**, *139*, 11734–11744.

49. Ayikpoe, R. et al. Spectroscopic and electrochemical characterization of the mycofactocin biosynthetic protein, MftC, provides insight into its redox flipping mechanism. *Biochemistry* **2019**, *58*, 940–950.

50. Zhu, W. et al. Structural properties and catalytic implications of the SPASM domain iron-sulfur clusters in *Methylorubrum extorquens* PqqE. *J. Am. Chem. Soc*. **2020**, *142*, 12620–12634.

51. Lien, Y. et al. Structural, biochemical, and bioinformatic basis for identifying radical SAM cyclopropyl synthases. *ACS Chem. Biol*. **2024**, *19*, 370–379.

52. LeMaster, D. M. & Richards, F. M. Preparative-scale isolation of isotopically labeled amino acids. *Anal. Biochem*. **1982**, *122*, 238–247.

53. Laemmli, U. K. Cleavage of structural proteins during the assembly of the head of bacteriophage T4. *Nature* **1970**, *227*, 680–685.

54. Kitagawa, M. et al. Complete set of ORF clones of Escherichia coli ASKA library (a complete set of E. coli K-12 ORF archive): unique resources for biological research. *DNA Res*. **2005**, *12*, 291–299.

55. Desport, J. S., Frache, G. & Patiny, L. MSPolyCalc: A web-based App for polymer mass spectrometry data interpretation. The case study of a pharmaceutical excipient. *Rapid Commun. Mass Spectrom.* **2020**, *34*, e8652.

56. Morinaka, B. I. et al. Radical *S*-adenosyl methionine epimerases: regioselective introduction of diverse D-amino acid patterns into peptide natural products. *Angew. Chem. Int. Ed. Engl.* **2014**, *53*, 8503–8507.

57. Korneli, M. et al. Promiscuous Installation of D-amino acids in gene-encoded peptides. *ACS Synth. Biol*. **2021**, *10*, 236–242.

58. Fish, W. W. Rapid colorimetric micromethod for the quantitation of complexed iron in biological samples. *Methods Enzymol*. **1988**, *158*, 357–364.

59. Beinert, H. Semi-micro methods for analysis of labile sulfide and of labile sulfide plus sulfane sulfur in unusually stable iron-sulfur proteins. *Anal. Biochem*. **1983**, *131*, 373–378.

60. Stoll, S. & Schweiger, A. EasySpin, a comprehensive software package for spectral simulation and analysis in EPR. *J. Magn. Reson*. **2006**, *178*, 42–55.

61. Bobeica, S. C. et al. Insights into AMS/PCAT transporters from biochemical and structural characterization of a double Glycine motif protease. *eLife* **2019**, *8*, e42305.

62. Gasteiger, E. et al. Protein Identification and Analysis Tools on the ExPASy Server. in The Proteomics Protocols Handbook (ed. Walker, J. M.) 571–607 (Humana Press, 2005).

63. TURBOMOLE V7.2 2017, a development of University of Karlsruhe and Forschungszentrum Karlsruhe GmbH, 1989-2007, TURBOMOLE GmbH, since 2007; available from http://www.turbomole.com.

64. Neese, F. The ORCA program system. Wiley *Interdiscip. Rev. Comput. Mol. Sci*. **2012**, *2*, 73–78.

65. Neese, F., Wennmohs, F., Becker, U. & Riplinger, C. The ORCA quantum chemistry program package. *J Chem Phys* **2020**, *152*, 224108.

66. Perdew, J. P., Burke, K. & Ernzerhof, M. Generalized gradient approximation made simple. *Phys. Rev. Lett*. **1996**, *77*, 3865–3868.

67. Perdew, J. P., Burke, K. & Ernzerhof, M. Generalized gradient approximation made simple. *Phys. Rev. Lett*. **1997**, *78*, 1396–1396.

68. Schäfer, A., Huber, C. & Ahlrichs, R. Fully optimized contracted Gaussian basis sets of triple zeta valence quality for atoms Li to Kr. *J. Chem. Phys*. **1994**, *100*, 5829–5835.

69. Grimme, S., Antony, J., Ehrlich, S. & Krieg, H. A consistent and accurate ab initio parametrization of density functional dispersion correction (DFT-D) for the 94 elements H-Pu. *J. Chem. Phys*. **2010**, *132*, 154104.

70. Löwdin, P. On the non-orthogonality problem connected with the use of atomic wave functions in the theory of molecules and crystals. *J. Chem. Phys*. **2004**, *18*, 365–375.

71. Walls, W. G.; Moody, J. D.; McDaniel, E. C.; Villanueva, M.; Shepard, E. M.; Broderick, W. E.; Broderick, J. B., The B_{12}-independent glycerol dehydratase activating enzyme from *Clostridium butyricum* cleaves SAM to produce 5′-deoxyadenosine and not 5′-deoxy-5′-(methylthio)adenosine. *Journal of Inorganic Biochemistry* **2022,** *227*, 111662.

72. Zor, T.; Selinger, Z., Linearization of the Bradford Protein Assay Increases Its Sensitivity: Theoretical and Experimental Studies. *Analytic Biochemistry* **1996,** *236*, 302-308.

73. F. Madeira, M. Pearce, A. R. N. Tivey, P. Basutkar, J. Lee, O. Edbali, N. Madhusoodanan, A. Kolesnikov, R. Lopez, *Nucleic Acids Res*. **2022**, *50*, W276–W279.

CHAPTER FIVE

THE RADICAL SAM ENZYME EpeE EXHIBITS DISTINCT SITE REACTIVITY DURING THE BIOSYNTHESIS OF THE RIPP NATURAL PRODUCT EPIPEPTIDE

Contribution of Authors and Co-Authors

Manuscript in Chapter 5

Author: William G. Walls

Contributions: Conducted most of the experimental work, prepared figures, wrote the manuscript, edited drafts of the manuscript.

Co-Author: Hao Yang

Contributions: Helped with RFQ experiments, edited manuscript.

Co-Author: Madeline B. Ho

Contributions: EPR analysis of RFQ experiments, edited manuscript.

Co-Author: William E. Broderick

Contributions: Provided oversight for the research direction, provided experimental insight, helped edit manuscript.

Co-Author: Joan B. Broderick

Contributions: Provided oversight for the research direction, interpretation of results, wrote sections of the manuscript, helped edited the manuscript, acquired funding for the research.

Co-Author: Brian M. Hoffman

Contributions: Interpretation of results, wrote sections of the manuscript, helped edited the manuscript, acquired funding for the research.

Manuscript Information

William G. Walls, Hao Yang, Madeline B Ho, William E. Broderick, Brian M. Hoffman, Joan B. Broderick

Status of Manuscript:
☒ Prepared for submission to a peer-reviewed journal
☐ Officially submitted to a peer-reviewed journal
☐ Accepted by a peer-reviewed journal
☐ Published in a peer-reviewed journal

Abstract

Radical *S*-adenosyl-L-methionine (SAM) enzymes figure prominently in the formation of ribosomally synthesized and post-translationally modified peptides (RiPPs), where they catalyze peptide modifications including epimerization, thioether crosslink formation, and peptide backbone splicing reactions. Here we use rapid freeze-quench trapping together with electron paramagnetic resonance and electron-nuclear double resonance techniques to probe the mechanistic steps of the two epimerization reactions catalyzed by the radical SAM enzyme EpeE during conversion of the peptide substrate to the epipeptide natural product. Use of the EpeE C223S variant, in which the cysteine residue proposed to be involved in back-side quenching of a peptide Cα radical intermediate, facilitated trapping and characterization of the Cα radical intermediate. We showed that both wild-type and C223S EpeE forms the organometallic intermediate Ω upon reaction with SAM and peptide substrate, and that thermal annealing of Ω results in conversion to an organic radical intermediate. Freeze-quenching at longer times allowed us to directly trap the organic radical intermediate, and isotopic labelling together with use of substrate variants allowed for detailed characterization of the substrate radical intermediates. The results revealed that while LC-MS enzymatic assays point to Ile12 as the initial site of epimerization, freeze-quench EPR reveals that Val4 is the preferred site for initial Cα radical formation. These apparently conflicting results provide new insights into the determinants for substrate binding and epimerization by EpeE.

Introduction

Antimicrobial resistance is a critical public health concern which urgently requires novel therapeutics [1]. Ribosomally synthesized and post-translationally modified peptides (RiPPs) are a structurally diverse class of natural products with a broad range of bioactivities [2, 3]. RiPPs have gained attention in recent years due to their engineerability and potential as a novel source of antibiotics [4-8]. Biosynthesis begins with a precursor peptide that is assembled by the ribosome and is typically composed of an N-terminal leader and a C-terminal core region. One or more maturating enzymes are recruited by the leader region to install post-translational modifications (PTMs) to the core region [9]. The leader is then proteolytically cleaved from the core region to yield the bioactive natural product which may be exported from the cell.

Epipeptides are an emerging class of antimicrobial RiPPs that are restricted to but widespread among the Bacillota phylum [10, 11]. Epipeptides inhibits bacterial growth by dissipating membrane potential via membrane permeabilization, and targets the producing strain or closely related strains [12, 13]. Epipeptides have only one characterized biosynthetic gene cluster from *Bacillus subtilis* strain 168, composed of the precursor peptide EpeX, a radical *S*-adenosyl-L-methionine (SAM) peptide epimerase EpeE, a membrane-associated protease EpeP, and the ABC transporter proteins EpeAB which provide autoimmunity to the producing organism (Fig. 5.1A) [10]. The rSAM epimerase EpeE has been shown to introduce D-Val4 and D-allo-Ile12 on EpeX, which along with proteolytic cleavage and export, are the only modifications to yield the bioactive natural product [12].

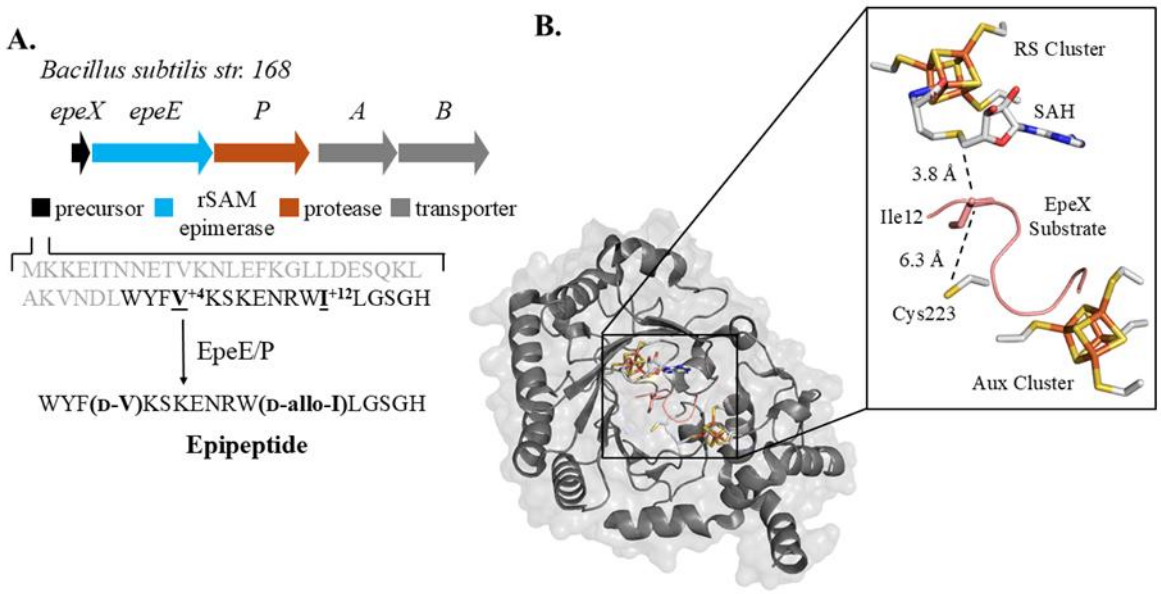
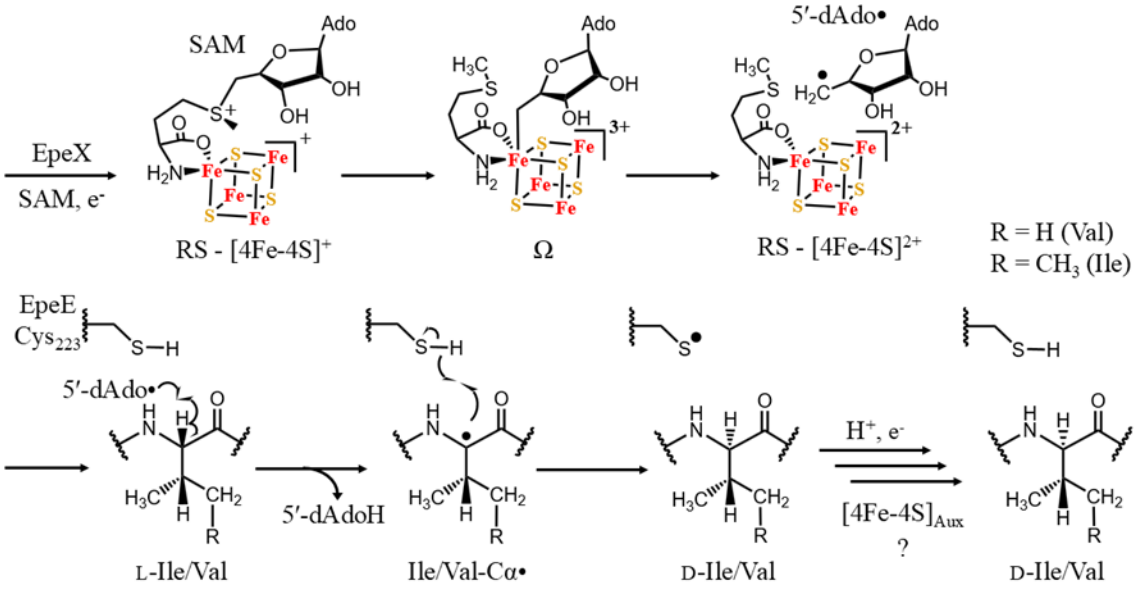


Figure 5.2. Overview of Epipeptide biosynthesis and structure of EpeE peptide epimerase. A. Overview of Epipeptide biosynthetic gene cluster from *B. subtilis* str. 168. B. Crystal structure of EpeE bound by EpeX substrate (PDB ID: 8AI2, see ref. 40). RS cluster and *S*-adenosyl homocysteine (SAH) sit on one face of the EpeX substrate with Cys223 and the Aux cluster on the other face.

EpeE belongs to the radical SAM (rSAM) enzyme superfamily, which are one of the largest in Nature and catalyze a vast array of chemical transformations [14-17]. rSAM enzymes utilize a conserved CX_3CX_2C motif in which the cysteine (Cys) thiolates coordinate three iron ions of a [4Fe-4S] cluster [18, 19]. The unique iron is coordinated by the amino and carboxylate moieties of SAM, positioning the sulfonium sulfur in close proximity to the cluster [20-22]. Electron transfer from the reduced $[4Fe\text{-}4S]^+$ cluster to the sulfonium of SAM leads to homolytic reductive cleavage of the S-C(5′) bond, and formation of the organometallic intermediate **Ω** featuring a direct Fe-C(5′) bond (Scheme 5.1) [23-30]. Homolysis of the Fe-C(5′) bond yields a highly oxidizing 5′-dAdo radical which stereospecifically abstracts an H-atom from the substrate

to form a substrate radical intermediate [31-35]. The particular rSAM enzyme is responsible for the ensuing transformation of the substrate radical into the product.

Scheme 5.1. Proposed mechanism of peptide epimerization by EpeE.



Many rSAM enzymes involved in RiPP biosynthesis contain an additional C-terminal domain known as a SPASM domain that coordinates two auxiliary (Aux) [Fe-S] clusters and are proposed to participate in electron transfer, substrate coordination, and protein stabilization [36-39]. A truncated version of the SPASM domain which coordinates only one [4Fe-4S] cluster is known as a twitch domain [37]. X-ray crystal structures of EpeE showed that the enzyme contains two [4Fe-4S] clusters: one in the rSAM domain and one in the twitch domain (Fig. 5.1B) [40]. However, the twitch domain of EpeE exceeded the typical size to which the authors proposed it be called the T-SPASM domain [40]. Crystal structures of EpeE with a peptide substrate bound showed Ile12 of EpeX positioned for H-atom abstraction, with Cys223 residing on the opposite face on the peptide (Fig. 5.1B) [40]. The observation of Ile12 poised for H-atom

abstraction in crystal structures, and the detection of D-allo-Ile12 prior to D-Val4 in enzyme activity assays led to the proposal that EpeE exhibits a C-to-N directionality [40].

The proposed mechanism for peptide epimerization by EpeE is outlined in Scheme 1 [40, 41]. The mechanism begins with the conserved radical initiation steps, proceeding through formation of Ω and yielding the 5′-dAdo radical. The 5′-dAdo radical stereospecifically abstracts an H-atom from the Cα of Ile12 (or Val4) yielding a central Cα radical intermediate. Cys223 then donates an H-atom to stereospecifically quench the Cα radical, forming a thiyl radical and the D-amino acid. The Aux cluster is proposed to reduce the thiyl radical, with a proton transfer from aspartate 210 [40]. While crystal structures and mutagenesis support this mechanism, direct evidence for the central Cα radical is lacking. The rSAM peptide epimerase OspD, which epimerizes Ile4 and Val13 during the biosynthesis of the RiPP natural product Landornamide, is proposed to proceed through a very similar mechanism [42]. Previous work from our lab trapped and characterized a Cα radical on Ile4 of the substrate OspA by using a Cys334 to Ser mutant of OspD which was impaired in its ability to quench the radical, and provided evidence for the enzymes N-to-C directionality [43]. We hypothesized that a similar approach could be utilized to investigate the proposed mechanism and directionality of peptide epimerization by EpeE.

In this study, we provide new insights into the mechanism of peptide epimerization by EpeE using a combination of site-directed mutagenesis, time-resolved freeze-quench electron paramagnetic resonance (EPR) spectroscopy, and enzyme activity assays. Mutation of Cys223 of EpeE to Ser provides a thermodynamic barrier to H-atom transfer, allowing accumulation of Cα radicals on both Val4 and Ile12. Mutation of Val4 or Ile12 to Trp prevents epimerization by EpeE at that given position, but allows EpeE to continue to act on the remaining position. Freeze

quench reactions of EpeE C223S with the Trp mutated substrates reveals that EpeE preferentially forms Cα radicals on Val4 with minor amounts on Ile12, but each with distinct hyperfine couplings to Cβ-H and the amide proton. Mutation of Ile12 to Val12 on EpeX suggests the distinct hyperfine couplings arise because of their location on the substrate and not the amino acid itself. Time dependent freeze quench reactions and spectral simulations provide evidence that while the Val4 Cα radical accumulates to high concentrations, the Ile12 Cα radical is quenched faster, leading to production of D-allo-Ile12. These results provide unique insights into the radical initiation mechanism exhibited by the rSAM peptide epimerase EpeE during the maturation of the RiPP natural product Epipeptide.

Methods and Materials

Materials

Primers were designed using NEBaseChanger.com. All synthetic DNA was purchased from Integrated DNA Technologies (IDT) with standard desalting. DMSO, Fast digest (FD) NcoI, FD XhoI, and 99.8 % D_2O were obtained from ThermoFisher. Q5 DNA polymerase, dNTPs, and E. coli NEB5α competent cells were obtained from New England Biolabs. *E. coli* BL21(DE3) competent cells were obtained from Novagen. Polymerase chain reaction was performed on an Applied Biosystems MiniAmp thermal cycler. [U-D_{10}]-L-Ile, [3-D_1]-L-Val, and [$^{13}C_{10}$, $^{15}N_5$] – ATP (ammonium salt) were obtained from Cambridge Isotope Laboratories, Inc. Trypsin (Bovine, MS grade) and trifluoroacetic acid (TFA) were obtained from EMD Millipore. Spectinomycin, isopropyl-β-D-thiogalactopyranoside (IPTG), 2-[4-(2-hydroxyethyl)piperazin-1-yl]ethanesulfonic acid (HEPES), and tris(hydroxymethyl)aminomethane (Tris) were obtained from Research Products International. Natural abundance and isotopically labeled SAM was

prepared as previously reported [47]. Extinction coefficients for EpeX substrates were calculated using Protparam (https://web.expasy.org/protparam/).

Cloning

The EpeE gene from *Bacillus subtilis str.* 168 was codon optimized for expression in *E. coli* and synthesized by IDT. The gene was flanked with 20 bp overhangs in order to anneal to NcoI and XhoI digested pCDFDuet-1 vector. The EpeE gene and the NcoI/XhoI digested pCDFDuet-1 vector were incubated with 2x HiFi DNA assembly master mix (New England Biolabs) at 50°C for 30 minutes, then 1 μL used to transform NEB5α cells following the manufacturers protocol.

The EpeX gene from *B. subtilis str.* 168 was codon optimized for expression in *E. coli* and synthesized by IDT containing an N-terminal TEV site and was flanked with 20 bp overhangs that are complementary to a PCR amplified pCDFDuet-1 vector. An in-house pCDFDuet-1 vector containing a 6xHis-MBP tag sequence was PCR amplified with primers MBP-TEV-Amplify Fwd/ Rev to remove the gene in the multiple cloning region. The TEV-EpeX gBlock and the PCR amplified pCDFDuet-1 vector were incubated with 2x HiFi DNA assembly master mix at 50°C for 30 minutes, then used to transform NEB5α cells following the manufacturers protocol. Primers $EpeX_{18\text{-}49}$-Delete-Fwd/ Rev were used to delete residues 1-17 of the EpeX gene, yielding vector pCDF-MBP-$EpeX_{18\text{-}49}$. See Table S5.1 for primer details.

Site-directed Mutagenesis

Q5 DNA Polymerase was used following the manufacturers protocol with 1 ng of template DNA and the addition of 3% (v/v) DMSO. PCR parameters were as follows: 98°C for 30 seconds, followed by 25 cycles of 98°C, 10 seconds, Ta for 25 seconds, and 72°C for 2.5

minutes, after which a final extension at 72°C for 2 minutes was used. All annealing temperatures (T_a) and primer sequences can be found in Table S5.1. Following PCR, 5 µL of the reaction mixture was visualized on a 1% agarose gel with thiazole orange dye. 1 µL of PCR product was then used in a KLD reaction (New England Biolabs) following the manufactures protocol. Following incubation at 25°C for 5 minutes, 5 µL of the KLD reaction was used to transform chemically competent NEB5α cells, plated on LB + 1.5% agar plates supplemented with 50 µg/ mL spectinomycin (Spm), and incubated overnight at 37°C. Single colonies were used to inoculate 5 mL of LB media (10 g/ L tryptone, 10 g/ L NaCl, 5 g/ L yeast extract) supplemented with 50 µg/ mL Spm and grown overnight at 37°C with 250 rpm shaking. Plasmid DNA was purified using GeneJet Plasmid Miniprep Kit (ThermoFisher) following manufactures protocols except that the plasmid DNA was eluted from the column using water instead of elution buffer. DNA sequencing was performed at Functional Biosciences (WI, USA) using standard T7 promoter and T7 terminator primers.

Protein Expression

pCDFDuet-1 plasmids containing either the *epeE* or *epeE* C223S gene were used to transform chemically competent *E. coli* BL21(DE3) cells. A single colony was used to inoculate LB medium supplemented with 50 µg/ mL Spm and was subsequently grown at 37°C with 250 rpm shaking overnight. 2 L of TB medium (12 g/ L tryptone, 24 g/ L yeast extract, 0.4% (v/v) glycerol, 0.017 M KH_2PO_4, 0.072 M K_2HPO_4) was supplemented with 50 µg/ mL Spm and inoculated with the overnight culture (1% v/v). The cultures were grown at 37°C with 220 rpm shaking until an OD_{600nm} = 0.8 was reached. The cultures were then cooled on ice for 15 minutes and supplemented with 250 µM ferric ammonium citrate, 300 µM L-cysteine hydrochloride

monohydrate, and 1 mM IPTG. The cultures grew at 16°C with 180 rpm shaking for 20-24 hours. Cells were pelleted by centrifugation (6754 x g, 15 minutes, 4°C) and flash frozen in liquid nitrogen. Frozen cell paste was stored at -80°C until purification. Expression of EpeE WT or EpeE C223S was visualized on a 12% SDS-PAGE stained with Coomassie Brilliant Blue.

pCDF-MBP-EpeX$_{18\text{-}49}$ (or Trp mutants) plasmids was used to transform chemically competent *E. coli* BL21(DE3) cells. Single colonies were used to inoculate LB medium supplemented with 50 µg/ mL Spm and were grown at 37°C with 250 rpm shaking overnight. 2 L of TB medium was supplemented with 50 µg/ mL Spm and inoculated with overnight culture (1% v/v). The cultures were grown at 37°C with 220 rpm shaking until an OD_{600nm} = 1.2, then supplemented with 1 mM IPTG and grown at 16°C, 180 rpm shaking, overnight for 20-24 hours. Cells were pelleted by centrifugation (6754 x g, 15 minutes, 4°C) and flash frozen in liquid nitrogen. Frozen cell paste was stored at -80°C until purification. Expression of MBP-EpeX$_{18\text{-}49}$ was visualized on a 12% SDS-PAGE gel stained with Coomassie Brilliant Blue.

Expression of Isotopically labeled MBP-EpeX$_{18\text{-}49}$

A single colony *E. coli* BL21(DE3) transformed with plasmid pCDF-MBP-EpeX$_{18\text{-}49}$ was used to inoculate 5 mL of LB medium supplemented with 50 µg/ mL Spm and grown at 37°C with 250 rpm shaking overnight. 0.2 L of LB medium was supplemented with 50 µg/ mL Spm was inoculated with 1% (v/v) of the overnight culture, and grown at 37°C with 250 rpm shaking until OD_{600nm} = 0.8. The culture was then centrifuged at 6754 x g, 4°C for 15 minutes. The cells were washed with 25 mL of 1x buffer salts and centrifuged again (6754 x g, 4°C, 15 minutes). The cell pellet was resuspended in 200 mL LR medium supplemented with amino acid dropout mix (-Ile, -Val), 50 µg/ mL Spm, 1 mM IPTG, 0.2% (w/v) glucose, and 8 mg of [U-D_{10}]-L-Ile,

[3-D_1]-L-Val, or both. Natural abundance L-Ile or L-Val was added to 40 µg/ mL concentration depending on the labeled amino acid added so that all 20 amino acids were present in the media. Cultures were grown at 16°C overnight with 180 rpm shaking. Cells were pelleted by centrifugation (6754 x g, 15 min, 4°C) before being flash frozen in liquid nitrogen and stored at -80°C.

LR medium [48] was prepared from stock solutions of 10x buffer salts (240 g/ L K_2HPO_4, 10 g/ L NaOH), 100x mineral salts (16.5 g $(NH_4)_2SO_4$, 6.16 mg $MgSO_4$ $7H_2O$, 30 mg $FeSO_4$ $7H_2O$, 0.1 mL conc. H_2SO_4, diluted to 100 mL with DI H_2O), and 20% (w/v) D-glucose. The 10x buffer salts were autoclaved to sterilize while the 100x mineral salts and the 20% glucose solution were filter sterilized. 10x amino acid dropout mix (-Ile, -Val) was prepared from all other 18 amino acids at 400 µg/ mL for L-amino acids or 800 µg/ mL for DL-amino acids, dissolved in DI H_2O, and filter sterilized. 100x stock solutions of L-Ile or L-Val at 4 mg/ mL concentration were prepared by dissolving in DI H_2O and filter sterilizing.

Protein Purification

For EpeE WT or C223S variant, frozen cell paste was brought into the anerobic chamber (COY laboratories, Inc.) and resuspended in lysis buffer (50 mM HEPES, pH 8.0, 300 mM KCl, 10% (v/v) glycerol, 5 mM imidazole, 10 mg/ mL Triton X-100, 0.5 mg/ mL lysozyme, 1.15 mg/ mL $MgCl_2$ hexahydrate, 0.01 mg/ mL DNAse, and one Pierce Protease Inhibitor Tablet EDTA-free) at a ratio of 2 mL per gram cell paste. The cells were stirred for one hour before being sonicated on ice for 10 minutes (5 second pulse on, 15 second pulse off, 40% amplitude). The cell lysate was then clarified by centrifugation at 26,790 x g for 1 hour at 4°C. The clarified lysate was then filtered (0.45 µm) and loaded onto a HisTrap 16/10 column (Cytiva) using an

AKTA Start FPLC. The column was washed with buffer A (50 mM HEPES, pH 8.0, 300 mM KCl, 10% (v/v) glycerol) supplemented with 25 mM imidazole. The protein was eluted from the column with buffer A supplemented with 250 mM imidazole. The eluate was desalted using a HiPrep 26/10 column into buffer C (50 mM HEPES, pH 8, 300 mM KCl, 10% glycerol, 3 mM DTT) and concentrated to approximately 25 mg/ mL using a 10 kDa MWCO spin filter (Amicon). The enzyme was aliquoted, flash frozen in liquid nitrogen, and stored at -80°C.

MBP-EpeX$_{18\text{-}49}$ WT and mutants were purified in a similar manner as EpeE except that all steps were aerobic and performed at 4°C. Following elution from the Ni-NTA column, the protein was desalted into buffer A and concentrated with a 10 kDa MWCO spin filter (Amicon) to about 50 mg/ mL. The purified MBP-EpeX$_{18\text{-}49}$ was made anaerobic on a Schlenk line with several vacuum/ nitrogen cycles, then aliquoted, flash frozen in liquid nitrogen, and stored at -80°C. Purified MBP-EpeX$_{18\text{-}49}$ was quantified by its absorbance at 280 nm using a calculated extinction coefficient of 80,330 M^{-1} cm^{-1} (or 85,830 M^{-1} cm^{-1} for the Trp mutants). Absorbances were measured using a Nanodrop Spectrophotometer and blanked with buffer A.

Purification of EpeX$_{18\text{-}49}$

To prepare Epex$_{18\text{-}49}$, MBP-EpeX$_{18\text{-}49}$ was first buffer exchanged into 20 mM Tris, pH 7.5. 65 mg of MBP-EpeX$_{18\text{-}49}$ was then supplemented with 0.65 mg of TEV protease and 1 mM DTT and diluted to 5 mL volume with 20 mM Tris, pH 7.5. Reactions were incubated overnight for 18-20 hours at ambient temperature. The reaction was then centrifuged (26,790 x g, 10 min, 4°C) before being loaded onto two serially connected 5 mL MBPTrap columns (Cytiva), equilibrated in 20 mM Tris, pH 7.5. The flow through was collected and concentrated by rotary evaporation (Bucci) to 0.2 mL. The concentration of EpeX$_{18\text{-}49}$ was determined

spectrophotometrically using a calculated extinction coefficient of 12,490 M^{-1} cm^{-1}. TEV protease was prepared as previously described [42].

Amino Acid Analysis and Protein Quantification

To determine a correction factor for the Bradford assay, an aliquot of purified EpeE was buffer exchanged using a PD-10 column into amino acid analysis buffer (50 mM HEPES, pH 8.0, 100 mM KCl). The buffer exchanged protein was used for a Bradford assay following the method of Zor and Selinger [49] with bovine serum albumin (Thermo Scientific) as a standard. An aliquot of protein was diluted to 1 mg/ mL, in triplicate, and sent to the Molecular Structure Facility at UC Davis, CA, for amino acid analysis. A correction factor of 0.834 ± 0.005 was then multiplied by the concentration calculated by the Bradford assay to achieve a corrected concentration.

Iron Analysis

Iron concentration was determined using an Agilent 240 FS flame atomic absorption spectrometer. A calibration curve was made from 0.4 to 2.0 ppm iron using an iron standard (Ricca, 1000 ppm) diluted in DI water. Protein samples were diluted to 2 μM in buffer C, in quadruplicate, for analysis. Absorbance from buffer was subtracted from each sample. Iron per protein values were obtained by dividing the concentration of iron by the protein concentration in each sample, and represented as the mean ± standard deviation of the quadruplicate samples.

Enzyme Reconstitution

Aliquots of purified EpeE WT or C223S mutant were thawed in the anaerobic chamber. The aliquots were diluted to 0.1 mM with buffer A on ice, supplemented with 5 mM DTT and

stirred for 15 minutes. Stock solutions of ferric ammonium citrate (FAC) and Li_2S were prepared in buffer A to a final concentration of 10 and 50 mM, respectively. FAC was added over the course of 10 minutes to a final concentration of 0.8 mM. After incubating for 5 minutes, Li_2S was added slowly over the course of 10 minutes to a final concentration of 0.8 mM. The reaction stirred on ice for 4 hours before being centrifuged (26,790 x g, 10 minutes, 4°C) and desalted into buffer C using a HiPrep 26/10 column. The reconstituted protein was concentrated to about 25 mg/mL, aliquoted, flash frozen in liquid nitrogen, and stored at -80°C.

D_2O Buffer Preparation and Protein Buffer Exchange

Buffered D_2O was prepared by removing water from 50 mL of buffer A by rotary evaporation for 45 min. The residual glycerol and salt was dissolved with 4 mL of D_2O, and then removed by rotary evaporation, 3 times. After 3 washes, the solution was diluted to the original volume with D_2O and the pH_{app} was measured to be 8.1-8.3. The pH_{app} was not adjusted following the recommendation by Rubinson, K. A., *Analytical Methods* **2017**, *9* (18), 2744-2750. The buffered D_2O was degassed on a Schlenk line using the freeze-pump-thaw method. EpeE WT and C223S variant were exchanged into buffered D_2O using PD MiniTrap columns following the manufacturers protocol and concentrated back to their original volume using 10 kDa MWCO 0.5 mL spin filters. MBP-EpeX_{18-49} substrates were exchanged into buffered D_2O by diluting 2x and reconcentrating to the original volume with 10 kDa MWCO 0.5 mL spin filters, a total of 4 times. The concentration of the D_2O exchanged proteins was remeasured by Bradford (EpeE) or Nanodrop (MBP-EpeX_{18-49}).

UV-Visible Spectrophotometry

UV-visible spectra were recorded using an Agilent Cary 60 UV-visible spectrophotometer scanning from 800-200 nm at 600 nm/ min. Samples were measured in Spectrosil Quartz cuvettes (Starna Cells) with a 10 mm path length.

EPR Sample Preparation

Samples were prepared in an MBraun glovebox maintained at <1 ppm O_2 and 24°C. A solution of EpeE WT or C223S variant and DTT were reduced with sodium dithionite (NaDT) for 5 minutes before being mixed with a solution of MBP-EpeX$_{18-49}$, SAM, and NaDT in an X-band EPR tube (Wilmad Labglass, 4 mm OD). The samples were frozen in liquid nitrogen at the times indicated after mixing. Following mixing, the final concentrations were: 200 μM EpeE (WT or C223S), 200 μM MBP-EpeX$_{18-49}$, 4 mM NaDT, 3 mM DTT and 2 mM SAM in buffer A to a final volume of 250 μL. Radical spin quantitation using a TEMPOL standard was performed as previously described [43].

Rapid Freeze Quench

Rapid freeze-quench (RFQ) experiments were performed following a protocol previously described in order to protect the protein from oxygen despite the RFQ instrument not being housed in an anaerobic chamber [23, 25]. A solution of EpeE WT or C223S variant was reduced with NaDT and DTT for 5-10 min before it was loaded into one loop while MBP-EpeX$_{18-49}$, SAM, and NaDT were loaded into the other loop. Mixing of these solutions yielded a sample with the following concentrations: 200 μM EpeE WT, 300 μM MBP-EpeX$_{18-49}$, 3.5 mM NaDT, 3 mM DTT and 2 mM SAM in buffer A; or 300 μM EpeE C223S, 300 μM MBP-EpeX$_{18-49}$, 5 mM NaDT, 4.5 mM DTT and 3.7 mM SAM in buffer A. The sample loops were connected to a System 100 apparatus from Update Instrument and rapidly mixed. The mixture was quenched by

spraying onto two rotating aluminum-coated copper wheels cooled in liquid nitrogen, at quench times of 20 ms, 500 ms, or 1 s. The frozen powder was collected in a funnel and packed into X-band tubes for EPR analysis.

Continuous Wave X-Band EPR Spectroscopy

Continuous wave X-band EPR spectroscopy was performed using a Bruker EMX EPR spectrometer equipped with a Bruker/ColdEdge (Sumitomo Cyrogenics) 10 K waveguide cryogen free system with an Oxford MercuryITC controller unit and helium Stinger recirculating unit (Sumitomo Cyrogenics, ColdEdge Technologies). Experimental spectra were simulated with Easyspin [50] (5.2.35) within the Matlab R2020b software suite (Mathworks, Inc.).

Enzyme Activity Assays

In the glove box, assays contained 10 µM of EpeE (WT or C223S), 100 µM MBP-EpeX$_{18-49}$, 0.5 mM SAM, 0.5 mM NaDT, 5 mM DTT, in buffer A at a volume of 50 µL. SAM was added last to initiate the reaction and incubated for the indicated amount of time. 20 µL of the reaction (about 0.1 mg of MBP-EpeX$_{18-49}$) was mixed with 1 µg trypsin, 20 mM $CaCl_2$, and diluted with water to 160 µL. The digest was incubated at 37°C for 3 hours before being quenched with 16 µL of 10% trifluoroacetic acid (TFA). Peptides were desalted using 100 µL C18 Zip Tips (Thermo Scientific) and eluted into 25 µL of 60% acetonitrile, 0.1% formic acid, in water. 5 µL was injected for analysis by LC-MS.

Protease Digest of MBP-EpeX$_{18-49}$ and LC-MS Analysis

100 µg of MBP-EpeX$_{18-49}$ was mixed with 1 µg trypsin and 20 mM $CaCl_2$ and brought to 20 µL with water and incubated at 37°C for 3 hours. 2 µL of 10% TFA was added to quench the

digest and diluted to 100 µL with 0.1% TFA in water. The digest was desalted with 100 µL C18 Zip Tips and eluted into 25 µL of 60% acetonitrile and 0.1% formic acid, in water.

An aliquot (5 µL) was injected onto an Agilent UHPLC 1290 Infinity II equipped with a Zorbax RRHD Eclipse Plus C18 column (2.1 x 50 mm, 1.8 µm, 95 Å) coupled to an Agilent 6538 UHD Accurate-mass Q-TOF mass spectrometer. The sample was eluted using the following program: washing with 2% B for 2 min, linear gradient to 50% B from 2 to 12 minutes, 50-98% B from 12-13 min, hold at 98% B from 13.5 to 14.5 min, and equilibration to 2% B from 14.5 to 15 minutes. Solvent A is 0.1% formic acid in water and solvent B is acetonitrile with 0.1% formic acid. The separation was carried out with 0.4 mL/ min flow rate and column temperature of 50°C. Mass spectra was collected with 2 Hz scan rate and a mass range of 103-1700 *m/z*. Expected *m/z* were calculated using the Fiehn laboratory's excel ESI-adduct calculator. B- and y-ions were calculated using the University of Washington's Proteomics Resource peptide fragmentation tool (https://proteomicsresource.washington.edu/cgi-bin/fragment.cgi).

Results

Production and Characterization of EpeE WT and C223S Variant

The codon-optimized EpeE gene from *B. subtilis* str. 168 was cloned into a pCDFDuet-1 vector containing an N-terminal 6xHis-tag for expression in *E. coli*. Primers were designed to mutate Cys223 of EpeE to Ser to yield the C223S variant. EpeE WT and C223S variant were expressed, purified, and reconstituted following standard procedures (Fig. S5.1). The purified and reconstituted WT and C223S variant contained 8.5 ± 0.3 and 8.3 ± 0.1 Fe/ protein, respectively, consistent with incorporation of two [4Fe-4S] clusters. UV-visible spectroscopy of

the reconstituted WT and C223S variant proteins exhibited broad shoulders at 410 nm (Fig. S5.2A). Following reduction with sodium dithionite (NaDT), EPR spectroscopy of both proteins at 30 K exhibited near axial signals that could be well simulated with the *g*-tensor [2.027, 1.935, 1.908] (Fig. S5.2B). These *g*-values are consistent with the $[4Fe\text{-}4S]^{+}$ cluster in the rSAM domain, as the twitch domain cluster has been reported to be not reducible by NaDT and thus EPR silent [40]. Addition of SAM caused a significant change to the EPR spectrum, exhibiting a faster relaxation rate and broadening of the spectra (Fig. S5.2C). Collectively, these results are consistent with EpeE WT and C223S variant containing two [4Fe-4S] clusters per monomer and that mutation of Cys223 to Ser223 does not significantly alter the electronic structure of the [4Fe-4S] cluster in the rSAM domain.

Activity of EpeE towards MBP-EpeX$_{18\text{-}49}$ substrate

The substrate EpeX gene was cloned into a pCDFDuet-1 expression vector encoding an N-terminal MBP tag to enhance solubility and expression in *E. coli*, followed by a TEV protease cleavage site. However, attempts to express and purify this construct were unsuccessful. Primers were designed to remove residues 1-17 of EpeX to afford MBP-EpeX$_{18\text{-}49}$. This truncated construct was previously shown to be a more soluble substrate and was epimerized by EpeE to a greater extent than the full length substrate [12]. To assess the activity of this new construct, 10 μM EpeE and 100 μM MBP-EpeX$_{18\text{-}49}$ were incubated anaerobically in the presence of 0.5 mM SAM, 0.5 mM NaDT, and 5 mM DTT for 18 hours in buffered D_2O. Performing the reaction in D_2O allows incorporation of a solvent deuteron onto the Cα of the amino acid that is epimerized via Cys223, allowing facile detection by liquid chromatography - tandem mass spectrometry (LC-MS/MS) to localize the mass shift to the residue that is epimerized [12, 44].

An aliquot of the reaction mixture was directly digested with trypsin protease to release two core peptides, one containing the Val4 site (VNDLWYFVK) and one containing the Ile12 site (WILGSGH). Analysis by LC-MS/MS revealed that Ile12 was epimerized to a greater extent than Val4, consistent with previous reports (Fig. S5.3 and Tables S5.4-S5.7) [12]. Assays with EpeE C223S variant produced less product overall, but still formed more D-allo-Ile12 than D-Val4 (Fig. S5.3 and Tables S5.8-S5.9). These results confirmed that MBP-EpeX$_{18\text{-}49}$ serves as a viable substrate and are consistent with the proposed role of Cys223 to stereospecifically donate an H-atom to the substrate (Scheme 5.1).

Assays comparing the activity of MBP-EpeX$_{18\text{-}49}$ to TEV-cleaved EpeX$_{18\text{-}49}$ lacking the MBP tag showed similar activity, with more D-allo-Ile12 being produced than D-Val4 in overnight assays, but less overall turnover compared to the MBP-tagged construct (Fig. S5.4 and Table S5.10-S5.11). Because the MBP tag significantly enhanced the solubility and stability of EpeX$_{18\text{-}49}$ it was therefore used for the remainder of the study.

<u>EpeE Forms **Ω** and Anneals to a Substrate Radical</u>

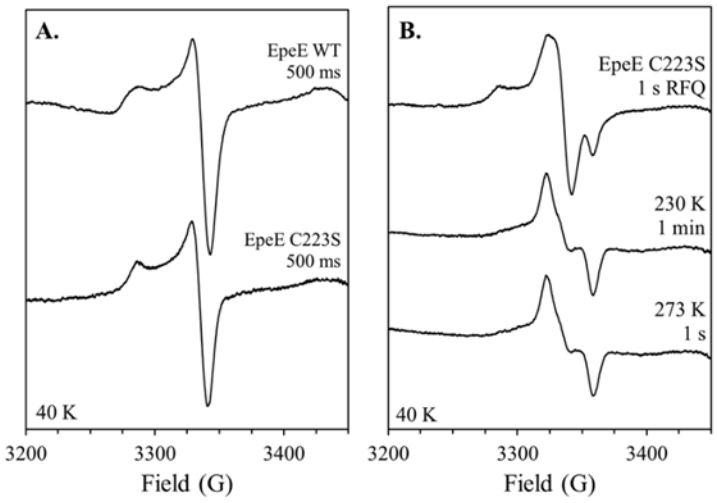


Figure 5.2. EPR spectra of EpeE RFQ. A, EpeE WT or C223S, SAM, and MBP-EpeX$_{18\text{-}49}$ freeze quenched at 500 ms reveals formation of **Ω**. B, RFQ and cryogenic annealing of EpeE C223S, SAM, and MBP-EpeX$_{18\text{-}49}$ at 1 s converts **Ω** into a putative substrate radical intermediate. EPR conditions: microwave frequency, 9.38 GHz; modulation, 10 G; T = 40 K.

Rapid freeze quench (RFQ) EPR experiments were carried out between EpeE WT or C223S variant with SAM and MBP-EpeX$_{18\text{-}49}$ to probe for initial reaction intermediates. Analysis of reactions freeze quenched at 500 ms revealed formation of the organometallic intermediate **Ω** with characteristic *g*-values of $g_{\parallel} = 2.036$, $g_{\perp} = 2.004$ (Fig. 5.2A) [23-25]. The observation of **Ω** further supports that MBP-EpeX$_{18\text{-}49}$ can serve as a suitable substrate for EpeE as it is able to bind and initiate the reductive cleavage of SAM. Furthermore, **Ω** is formed during turnover with both EpeE WT and C223S variant, supporting the hypothesis that the C223S mutation does not alter the initial steps of the proposed catalytic mechanism.

RFQ experiments were carried out over a range of times with EpeE C223S variant, SAM, and MBP-EpeX$_{18\text{-}49}$ (Fig. S5.5). Surprisingly, when the C223S reaction was quenched at 1 s, a new feature appeared that was not present in earlier quench times. We suspected this new species might be a Cα radical on Val4 or Ile12 of MBP-EpeX$_{18\text{-}49}$, as the proposed mechanism involves H-atom abstraction from the Cα by the 5′-dAdo• following formation of the **Ω** intermediate (Scheme 5.1). To probe the conversion of **Ω** to a Cα• intermediate, the 1 s RFQ sample of C223S and MBP-EpeX$_{18\text{-}49}$ was sequentially annealed at higher temperatures while remaining frozen (Fig. 5.2B). Annealing at 230 K for 1 min results in loss of **Ω** and appearance of a symmetric EPR signal centered near $g = 2.0$, consistent with formation of a substrate radical intermediate. Further annealing at 273 K for 1 s did not cause any further changes to the EPR signal, indicating the radical species is stable under these conditions. The conversion of **Ω** to a substrate radical species demonstrates its catalytic competence as an intermediate during EpeE catalysis.

EpeE Preferentially Forms a Cα•
on Val4 of MBP-EpeX$_{18-49}$

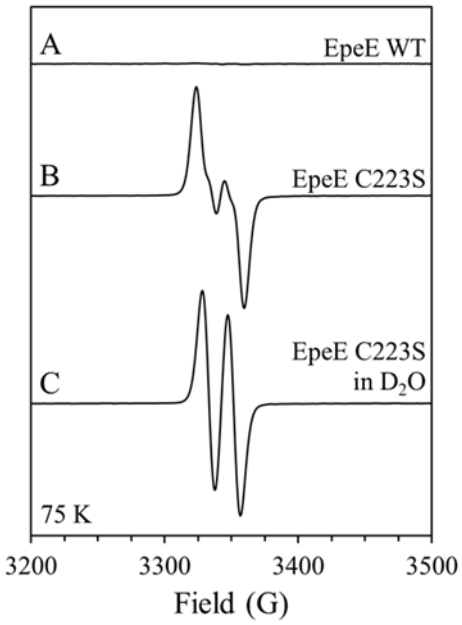


Figure 5.3. EPR spectra of EpeE, SAM, and MBP-EpeX$_{18-49}$ reveals formation of a Cα•. A, EPR spectra of EpeE WT reacted with SAM and MBP-EpeX$_{18-49}$ and freeze quenched at 1 min reveals no EPR signal. B, reaction with EpeE C223S variant forms a symmetric EPR signal. C, reaction with EpeE C223S in buffered D_2O causes collapse of the EPR signal to a doublet, indicating the unpaired electron is coupled to an amide proton. EPR parameters: microwave frequency, 9.38 GHz; modulation, 3 G; microwave power, 0.3 mW; T = 75 K.

To probe whether the substrate radical observed during RFQ could be formed at longer reaction times, EpeE WT or C223S variant were reacted with SAM and MBP-EpeX$_{18-49}$ and freeze quenched at 1 min. Analysis of the freeze quenched reactions by EPR spectroscopy at 75 K revealed no detectable radical formation in the EpeE WT catalyzed reaction (Fig. 5.3A). When the reaction was repeated with EpeE C223S variant and quenched at 1 min, we observed a symmetric EPR signal that resembled the annealed 1 s RFQ sample (Fig. 5.3B). To test whether the observed substrate radical resided on the Cα, the 1 min freeze quench reaction with EpeE C223S was repeated in buffered D_2O (Fig. 5.3C). We observed a collapse of the EPR signal to a

doublet indicating the observed radical resides on Cα and is coupled to the adjacent amide proton.

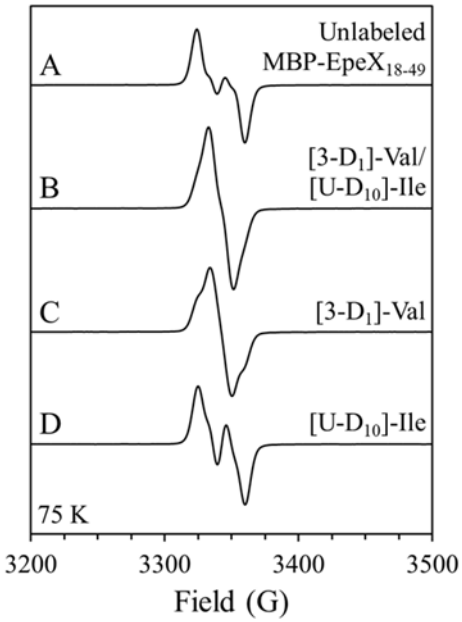


Figure 5.4. EpeX isotopic labeling reveals substrate Cα radical resides primarily on Val4. A, EpeE C223S reacted with SAM and MBP-EpeX$_{18-49}$ and freeze quenched at 1 min. B, reaction performed with MBP-EpeX$_{18-49}$ labeled with [3-D$_1$]-L-Val and [U-D$_{10}$]-L-Ile causes collapse of EPR signal to a singlet. C, reaction with MBP-EpeX$_{18-49}$ labeled with [3-D$_1$]-L-Val causes collapse of EPR signal to a singlet with minor doublet character. D, reaction with MBP-EpeX$_{18-49}$ labeled with [U-D$_{10}$]-L-Ile resembles the unlabeled spectrum A but with minor perturbations. EPR parameters: microwave frequency, 9.38 GHz; modulation, 3 G; microwave power, 0.3 mW; T = 75 K.

The observed Cα radical intermediate formed by EpeE C223S could be installed on Val4, Ile12, or both residues on MBP-EpeX$_{18-49}$. To determine which residue the radical is formed on, MBP-EpeX$_{18-49}$ was expressed in minimal media supplemented with [3-D$_1$]-L-Val, [U-D$_{10}$]-L-Ile, or both. Labeled amino acid incorporation was verified by LC-MS analysis following protein purification and trypsin digestion (Table S5.24-S5.29). The isotopically labeled MBP-EpeX$_{18-49}$ substrates were reacted with EpeE C223S and freeze quenched at 1 min. EPR spectroscopy at 75 K of the reaction containing [3-D$_1$]-L-Val and [U-D$_{10}$]-L-Ile labeled MBP-EpeX$_{18-49}$ revealed a

strong collapse to a singlet, consistent with the radical residing on either Val4 or Ile12 (Fig. 5.4B). When the reaction was carried out with [3-D_1]-L-Val labeled substrate, we observed collapse to a singlet EPR signal, but not completely as the spectrum contained some doublet character (Fig. 5.4C). The reaction with [U-D_{10}]-L-Ile labeled substrate resembled the EPR spectrum with unlabeled substrate, but with minor perturbations to the spectrum (Fig. 5.4D). These results indicate that EpeE C223S primarily forms a Cα radical on Val4 of MBP-Epe$X_{18\text{-}49}$ but with minor amounts on Ile4.

EpeE Forms Cα radicals on Val4 and Ile12
with distinct hyperfine coupling constants

Previous work on the rSAM peptide epimerase OspD demonstrated that mutation of Ile4 or Val13 to Trp on the peptide substrate OspA resulted in no epimerization of these residues [45]. We hypothesized that mutation of Val4 or Ile12 to Trp on MBP-Epe$X_{18\text{-}49}$ would also inhibit epimerization at that site. We mutated Val4 or Ile12 of MBP-Epe$X_{18\text{-}49}$ to Trp, yielding MBP-Epe$X_{18\text{-}49}$ V4W and MBP-Epe$X_{18\text{-}49}$ I12W mutants, respectively. Overnight assays between EpeE (WT or C223S) and MBP-Epe$X_{18\text{-}49}$ V4W or I12W followed by trypsin digestion and LC-MS revealed no epimerization at the Trp site of the V4W or I12W MBP-Epe$X_{18\text{-}49}$ substrates and only epimerization at the remaining site (Figs. S5.6-S5.7 and Table S5.12-S5.19). Using the I12W substrate, EpeE was able to epimerize Val4 to about the same extent as the WT substrate. Using the V4W mutant, however, allowed more D-allo-Ile12 to be produced relative to the WT substrate. The increased epimerization of Ile12 on MBP-Epe$X_{18\text{-}49}$ V4W was particularly pronounced in the EpeE C223S catalyzed reaction, relative to WT MBP-Epe$X_{18\text{-}49}$. These results demonstrate that mutation of Val4 or Ile12 effectively inhibits epimerization at that site while allowing epimerization to occur at the remaining site.

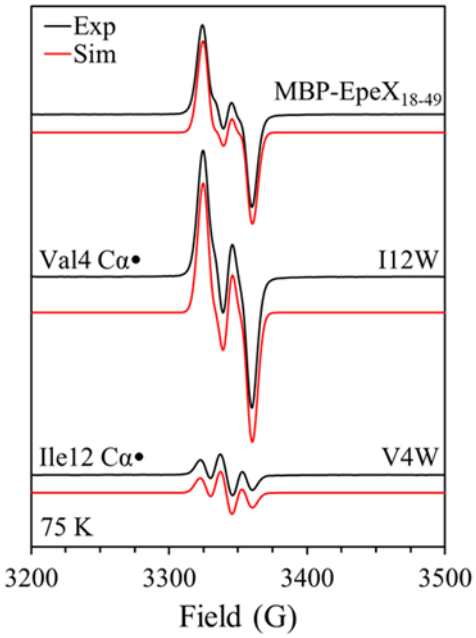


Figure 5.5. EPR spectra of MBP-EpeX$_{18-49}$ Trp mutations shows Val4 Cα• and Ile12 Cα• form with distinct hyperfine coupling interactions. Top, EpeE C223S freeze quenched with SAM and MBP-EpeX$_{18-49}$ at 1 min. Middle, EpeE C223S freeze quenched with SAM and MBP-EpeX$_{18-49}$ I12W at 1 min allows isolation of only Val4 Cα•. Bottom, EpeE C223S freeze quenched with SAM and MBP-EpeX$_{18-49}$ V4W at 1 min allows isolation of only Ile12 Cα•. The WT MBP-EpeX$_{18-49}$ EPR signal was simulated with 90% Val4 Cα• and 10% Ile12 Cα•. Simulation parameters for each radical species are summarized in Table 1. EPR parameters: microwave frequency, 9.38 GHz; modulation, 3 G; microwave power, 0.3 mW; T = 75 K.

Having determined that EpeE will act on both Val4 and Ile12 independently when Trp mutations are present, we next sought to determine if a Cα• could be formed exclusively on Val4 or Ile12. EpeE C223S and MBP-EpeX$_{18-49}$ I12W or V4W was mixed with SAM and freeze quenched at 1 min. Analysis of the reactions by EPR spectroscopy at 75 K revealed that Cα radicals were formed on both substrates but with distinct hyperfine couplings and intensities (Fig. 5.5).

Isotopic labeling and spectral simulations were used to gain further insights into the two different substrate radicals formed and are summarized in Table 5.1. The Val4 Cα• (using MBP-

EpeX$_{18-49}$ I12W) was simulated with two isotropic hyperfine coupling constants of 53 and 24 MHz, which were assigned to Cβ-H and N-H protons, respectively. Hyperfine coupling constants were verified by labeling MBP-EpeX$_{18-49}$ I12W with [3-D$_1$]-L-Val, performing the reaction in buffered D_2O, or both (Fig. S5.8 and Table S5.32). The Ile12 Cα• (using MBP-EpeX$_{18-49}$ V4W) was simulated with two isotropic hyperfine coupling constants of 42 and 37 MHz which were assigned to the Cβ-H and N-H protons, respectively. Couplings were verified by labeling with [U-D$_{10}$]-L-Ile, performing the reaction in buffered D_2O, or both (Fig. S5.9 and Table S5.30-S5.31). The differences in hyperfine coupling constants for the Val4 and Ile12 Cα radicals likely reflects different conformations in the active site, as β-coupling to unpaired electrons in carbon 2pπ orbitals are known to be dihedral angle dependent [46]. Determining the simulation parameters for the Val4 and the Ile12 Cα radical allowed us to accurately simulate the EPR spectrum from the WT substrate as being composed of 90% Val4 Cα radical and 10% Ile12 Cα radical (Fig. 5.5, top).

Table 5.1. Simulation parameters of Val4 and Ile12 Cα radicals.

Radical	Mutation	g_{iso}	a_{iso} (C_β-^{1}H) (MHz)	a_{iso} (N-^{1}H) (MHz)
Val4 Cα•	I12W	2.0036	53	24
Ile12 Cα•	V4W	2.0036	42	37

Spin quantitation of the EPR signals in Fig. 5.5 revealed 56 μM spin was formed on Val4 when using MBP-EpeX$_{18-49}$ I12W while only 9 μM spin was formed on Ile12 when using MBP-EpeX$_{18-49}$ V4W (Table S5.2). Interestingly, almost twice as much Cα radical was formed on Ile12 when using the V4W substrate mutant when compared to the WT substrate. This indicates that preventing binding to the preferred Val4 site allowed more enzyme to bind and install a Cα

radical at Ile12. Conversely, preventing radical formation at Ile12 only modestly increased the amount of Cα radical installed at Val4 and did not result in more D-Val4 formation. Our data clearly demonstrate that EpeE installs Cα radicals on both Val4 and Ile12 but with different hyperfine couplings which enabled deconvolution the WT substrate EPR spectrum. Spin quantitation's confirmed that EpeE preferentially installs a Cα radical on Val4.

Substrate Position Determines Radical Conformation

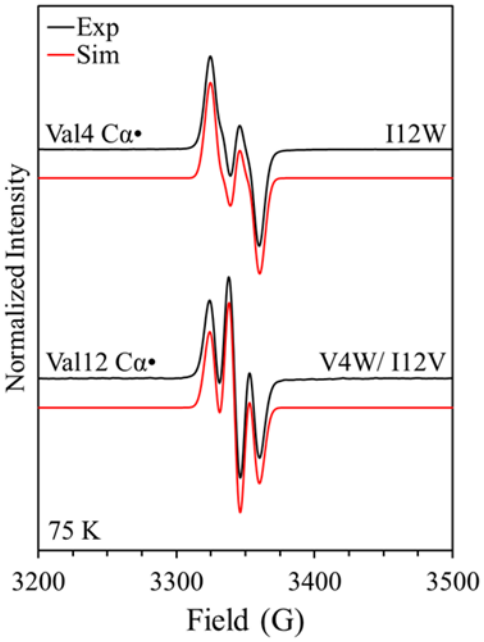


Figure 5.6. EpeE forms Val Cα radicals on MBP-EpeX$_{18\text{-}49}$ at position 4 and 12 with distinct hyperfine coupling constants. EpeE C223S freeze quenched with SAM and MBP-EpeX$_{18\text{-}49}$ I12W (top) or MBP-EpeX$_{18\text{-}49}$ V4W/ I12V (bottom) at 1 min. The Val12 Cα• was simulated with the same parameters as the Ile12 Cα• except that the Cβ-^{1}H coupling was reduced to 37 MHz. EPR parameters: microwave frequency, 9.38 GHz; modulation, 3 G; microwave power, 0.3 mW; T = 75 K.

Previous bioinformatic analyses of the substrate EpeX have shown that many homologs encode a Val at position 12 [10]. We hypothesized that mutating Ile12 to Val12 would allow us to directly compare Val Cα radicals that differed only by location on the substrate. We therefore

produced a V4W/ I12V double mutant of the substrate MBP-EpeX$_{18-49}$, to prevent radical formation at the preferred Val4 position and allow us to solely detect Cα radical formation at position 12. Assays with EpeE WT or C223S and MBP-EpeX$_{18-49}$ V4W/ I12W confirmed that no epimerization occurred at Trp4, while Val12 was epimerized to a greater extent than the native Ile12 (Fig. S5.10 and Table S5.20-S5.23). EpeE C223S was then reacted with MBP-EpeX$_{18-49}$ V4W/ I12V and freeze quenched at 1 min (Fig. 5.6). EPR spectroscopy revealed a substrate radical that was almost identical to the Ile12 Cα radical, and could be simulated with two identical isotropic hyperfine coupling constants of 37 MHz (Fig. 5.5, bottom). This result suggests that substrate binding interactions in the active site orient the amino acid at position 12 (Ile or Val) to form a specific conformation, which gives rise to very similar hyperfine coupling constants for both Ile12 or Val12 Cα radicals. Comparison between the Val4 Cα radical (from reaction with MBP-EpeX$_{18-49}$ I12W) and the Val12 Cα radical reveal clear differences in hyperfine coupling despite both being Val Cα radicals. This comparison highlights how position 4 and position 12 on the substrate must be held in distinct conformations in the active site of EpeE to cause hyperfine couplings to the Cα radicals.

<u>Ile12 Cα• is Quenched Faster than Val4 Cα•</u>

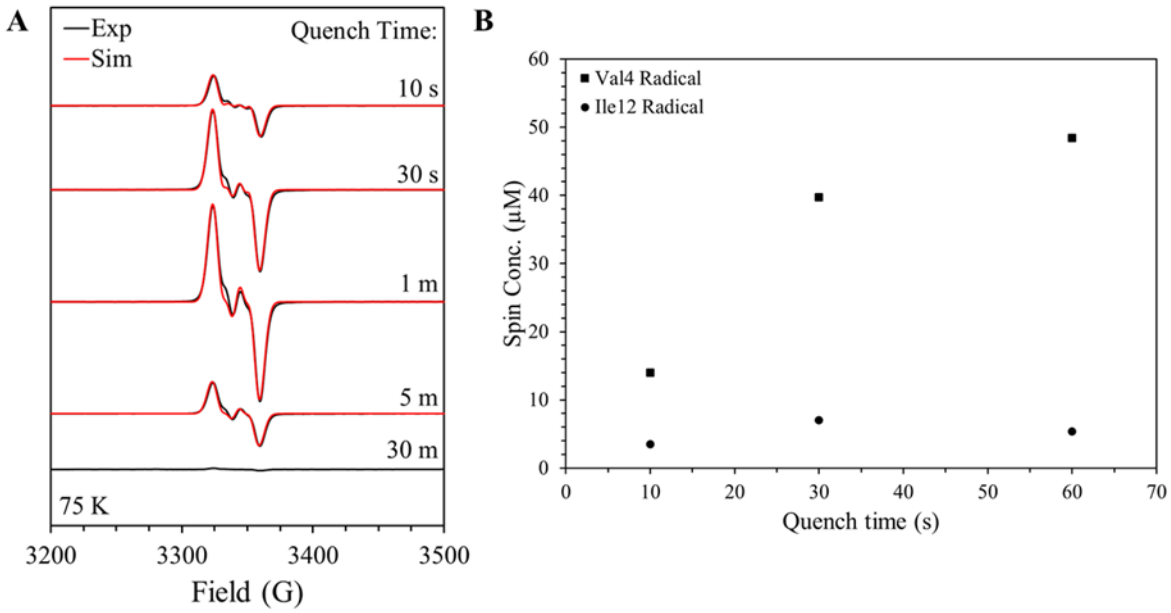


Figure 5.7. Ile12 Cα• decays faster than Val4 Cα•. A. EPR spectra of the EpeE C223S, MBP-EpeX$_{18-49}$, SAM reaction quenched at various times from 10 s to 30 min. B. Spin quantitation of Val4 Cα• and Ile12 Cα• from A plotted vs. quench time.

To probe Cα radical formation and decay, EpeE C223S, MBP-EpeX$_{18-49}$, and SAM were reacted and quenched over a range of times from 10 s to 30 min (Fig. 5.7A). Maximum radical formation was observed at 1 min but decayed at longer times and disappeared by 30 min. Conversely, quench times up to 1 min revealed an EPR signal that resembled the 1 min EPR signal but with changes in the central hyperfine coupling region. These changes could be well simulated as changes in the relative weights of the Val4 Cα• and Ile12 Cα• (Table S5.3). Spin quantitation of Val4 Cα• and Ile12 Cα• and plotting as a function of time revealed formation of both radicals from 10 s to 30 s, but decay of the Ile12 Cα• and growth of the Val4 Cα• from 30 s to 1 min (Fig. 5.7B). To determine if the loss of Ile12 Cα• after 1 min was due to quenching, and thus D-allo-Ile12 formation, we reacted EpeE C223S, MBP-EpeX$_{18-49}$, and SAM under the same conditions as the EPR samples, but instead of freeze quenching the sample, the reaction was

digested with trypsin protease and analyzed by LC-MS. After reacting for 1 min, we observed formation of a small amount of D-allo-Ile12 and no D-Val4 (Fig. S5.11). At 30 min, both D-Val4 and D-allo-Ile12 were detected. These results demonstrate that while less Ile12 Cα• is formed, it is quenched faster than the Val4 Cα•, and thus epimerized Ile12 is observed before epimerized Val4.

Discussion

Radical SAM peptide epimerases have attracted attention for installation of D-amino acids into peptides to endow them with antimicrobial properties. Epipeptides are potent antibacterial RiPP natural products which feature only two d-amino acids installed by the radical SAM enzyme EpeE. While epipeptides have only one characterized member to date, they are widespread among the Bacillota phylum which encompasses many opportunistic human pathogens. The catalytic mechanism of the maturase EpeE contained multiple intermediates which lacked evidence. We therefore wanted to investigate the hypothesized catalytic mechanism.

Here, we used a combination of time-resolved EPR freeze-quench, enzyme activity assays, and site-directed mutagenesis to provide key insights into the mechanism and directionality of EpeE. We showed that the EpeE WT and C223S variant were capable of forming the organometallic intermediate **Ω**, which is a ubiquitous intermediate among the superfamily. Remarkably, annealing of the EpeE C223S 1 s RFQ sample led to conversion of **Ω** into the substrate Cα•, providing evidence as a catalytically competent intermediate. A recent computation description of omega along with the experimental insights presented here help support the observation that omega is a ubiquitous intermediate among the superfamily.

Using substrate Trp mutants, we were able to show that EpeE C223S forms a Cα• on both Val4 and Ile12 but with different hyperfine couplings and intensities. We hypothesize that the difference in Cα• intensity observed for position 4 and position 12 is due to differential affinity of EpeE for those sites. The difference in hyperfine coupling likely reflects differences in radical conformation at position 4 compared to position 12. Of particular significance is the observation of coupling to the amide proton, which indicates a deviation from a planar conformation about the Cα position. In the radical SAM enzyme pyruvate formate-lyase activating enzyme (PFL-AE), reaction with a 7-mer peptide substrate mimic containing the Gly734 formed a Gly734 Cα• that was distorted from planarity, resulting in a higher energy conformation. These results are in contrast with glycyl radicals that are formed on glycyl radical enzymes which are fully planar and maximize delocalization and thus stability. Recently, the GRE superfamily has been expanded to include alanyl, serinyl, and threonyl radicals, which also exhibited minimal coupling to the amide proton, and thus a planar conformation. The higher energy conformation of the Cα• formed on Val4 and Ile12 of MBP-EpeX$_{18\text{-}49}$ may be related to the differences in reactivity observed at each site.

The initial observation of a Cα• on Val4 was surprising given that activity assays and crystal structures of EpeE with substrate bound indicated that Ile12 was the preferred site of epimerization, and thus the enzyme would exhibit a C-to-N directionality. Our time-resolved EPR freeze quench experiments clearly show accumulation of the Val4 Cα• to high levels with quenching to form D-Val4 occurring at times past 1 min. In contrast, the Ile12 Cα• only accumulates to modest levels and is already converted to D-allo-Ile12 product by 1 min. This may be due to more efficient quenching of the Ile12 Cα• by Cys223 (or Ser223) than the Val4

Cα•. These observations seem to go against a true directionality exhibited by EpeE, where one site would need to be acted on before the progression onto the next site, similar to what was observed with the radical SAM peptide epimerase OspD.

Crystal structures of EpeE with a peptide substrate bound indicated the Cys223 thiol was over 6 Å from the Ile12 Cα. While this distance is too large for H-atom transfer, the Cys223 resides on a flexible loop that could move closer during catalysis. The auxiliary [4Fe-4S] cluster may also play a role in the reduction of the putative thiyl radical following quenching of the substrate Cα•. During the course of our studies, we attempted to mutate residues that coordinate the Aux cluster, however, all mutations resulted in insoluble protein. Thus, the role of the Aux cluster during catalysis, if any, remains obscure.

The results presented here illustrate the invaluable role of EPR spectroscopy when investigating the mechanism and directionality of radical SAM enzymes involved in RiPP biosynthesis, which provides a unique perspective to complement the typical MS-based approach. Understanding the mechanism of amino acid epimerization by EpeE paves the way for future bioengineering efforts to utilize epipeptides as minimalistic peptide antibiotics to help address antibacterial resistance.

Supplemental Material

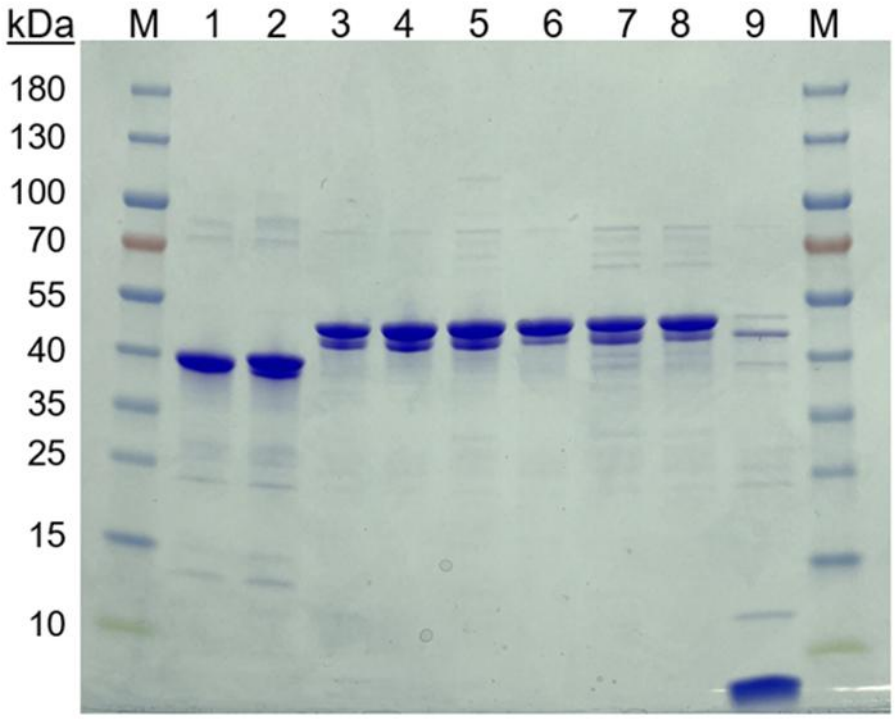


Figure S5.1. 4-20% SDS-PAGE analysis of purified proteins used in this study. M = molecular weight marker, 1 = EpeE WT, 2 = EpeE C223S, 3 = MBP-EpeX$_{18\text{-}49}$, 4 = MBP-EpeX$_{18\text{-}49}$ I12W, 5 = MBP-EpeX$_{18\text{-}49}$ I12W [3-D$_1$]-Val, 6 = MBP-EpeX$_{18\text{-}49}$ V4W, 7 = MBP-EpeX$_{18\text{-}49}$ V4W [U-D$_{10}$]-Ile, 8 = MBP-EpeX$_{18\text{-}49}$ V4W/ I12V, 9 = EpeX$_{18\text{-}49}$. Approximately 2 µg of each protein was loaded onto the gel. Stained with Coomassie Brilliant Blue.

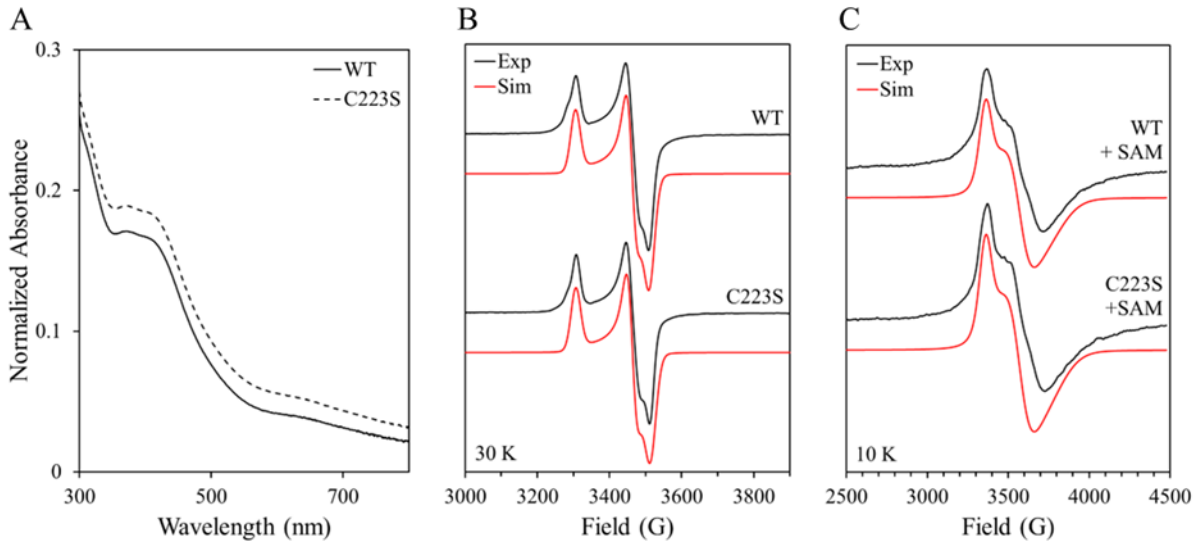


Figure S5.2. Spectroscopic characterization of EpeE WT and C223S variant. A. UV-visible spectra of reconstituted EpeE WT and C223S. B. EPR spectra of NaDT reduced EpeE WT and C223S measured at 30 K. Spectra were simulated with the g-tensor [2.027, 1.935, 1.908], g-strain [0.016, 0.014, 0.016], and linewidth [1.2, 0.2]. C**.** EPR spectra of NaDT reduced EpeE WT and C223S incubated with SAM, and measured at 10 K. Spectra were simulated with the g-tensor [1.989 1.870 1.790], g-strain [0.02, 0.06, 0.12], and linewidth [4, 3]. EPR conditions: microwave frequency, 9.38 GHz; microwave power, 1 mW; modulation, 10 G.

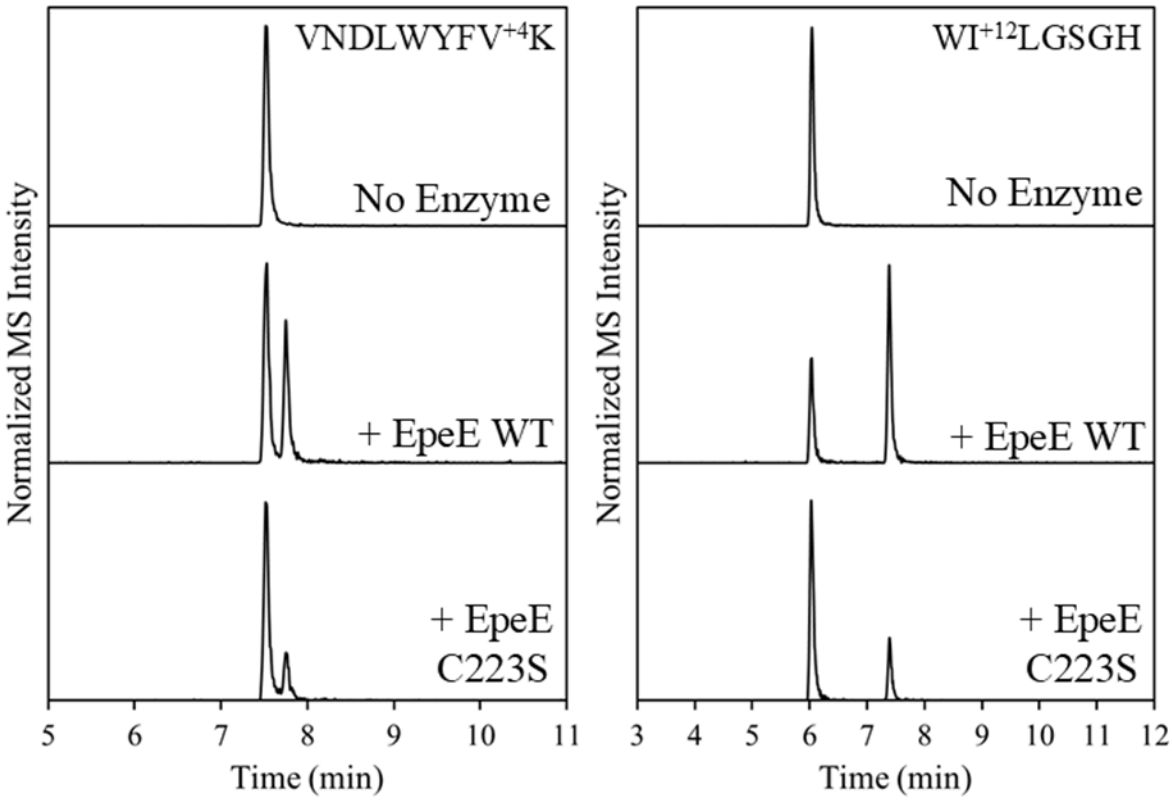


Figure S5.3. EICs of 18-hour assays of EpeE, SAM, and MBP-EpeX$_{18-49}$ in buffered D_2O. Unmodified peptide VNDLWYFVK from no enzyme controls elutes at 7.5 min and was extracted at 592.3109 *m/z*. Unmodified peptide WILGSGH from no enzyme controls elutes at 6 min and was extracted at 385.2032 *m/z*. Epimerized peptide VNDLWYF(D-V)K elutes at 7.7 min and was extracted between 592.3 – 594.3 *m/z*. Epimerized peptide W(D-I)LGSGH elutes at 7.3 min and was extracted between 385.2 – 386.7 *m/z*.

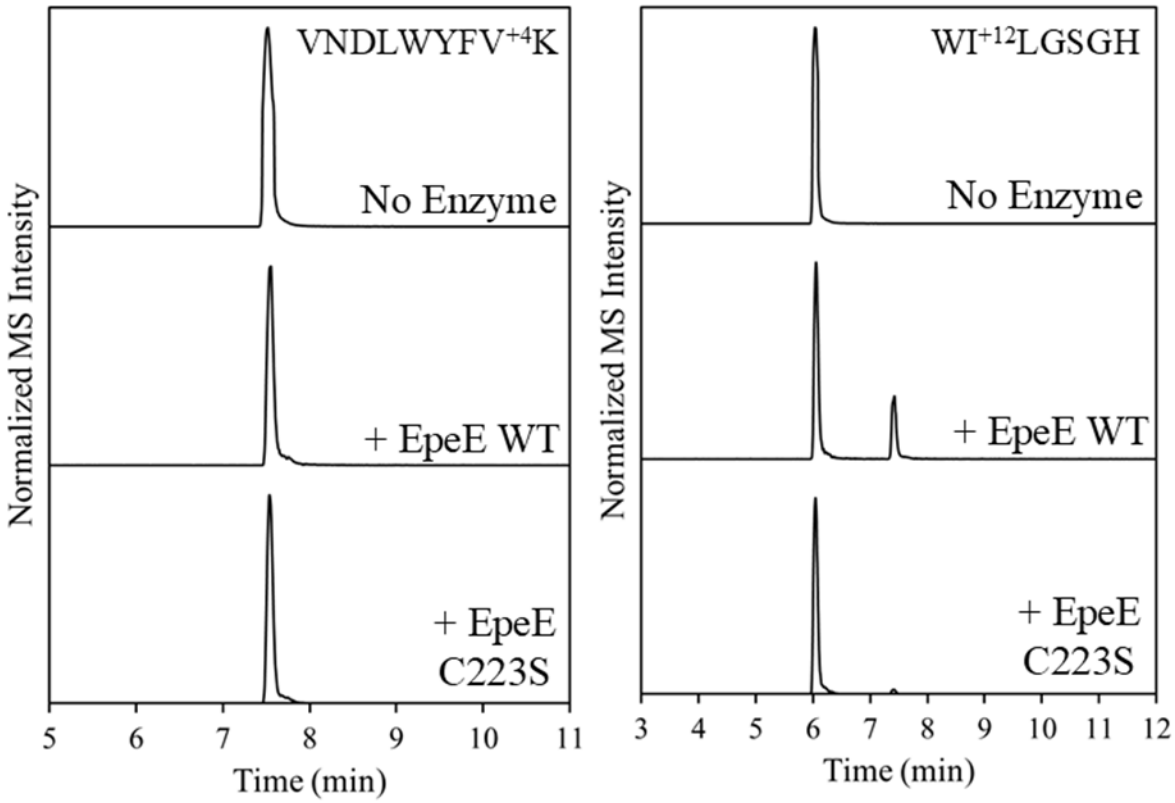


Figure S5.4. EICs of 18-hour assays between EpeE and $EpeX_{18-49}$ in buffered D_2O. Unmodified peptide VNDLWYFVK elutes at 7.5 min and was extracted at 592.3109 *m/z*. Unmodified peptide WILGSGH elutes at 6 min and was extracted at 385.2032 *m/z*. Epimerized peptide VNDLWYF(D-V)K elutes at 7.7 min and was extracted between 592.3 – 594.3 *m/z*. Epimerized peptide W(D-I)LGSGH elutes at 7.3 min and was extracted between 385.2 – 386.7 *m/z*.

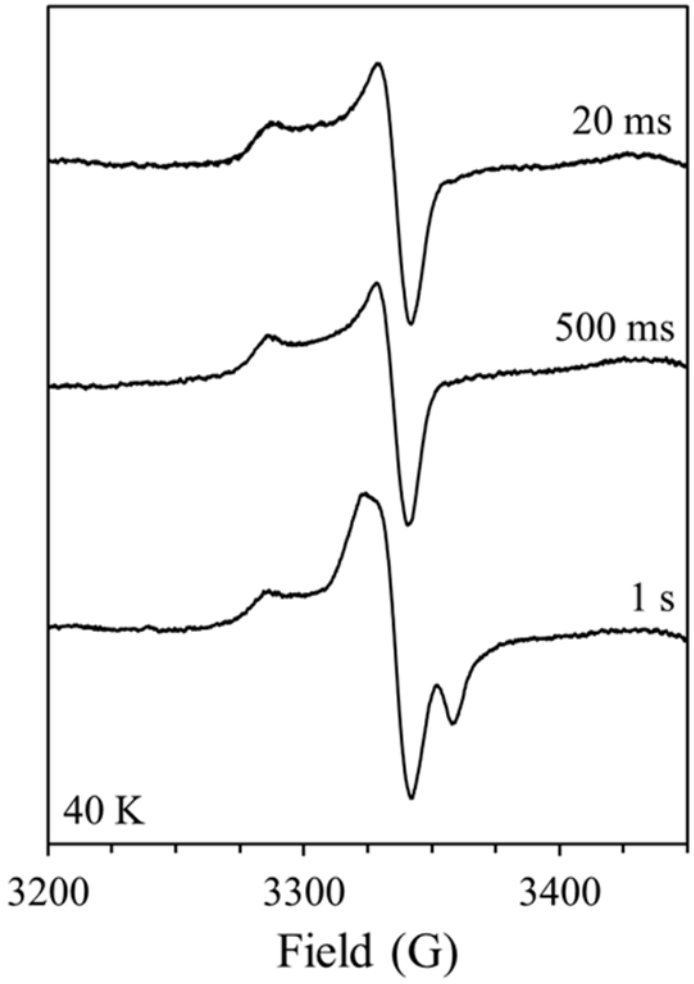


Figure S5.5. RFQ EPR spectra of EpeE C223S, SAM, and MBP-EpeX$_{18-49}$ at 20 ms, 500 ms, and 1 s. The **Ω** intermediate is observed at all quench times and as early as 20 ms. As a second species is observed when the reaction is quenched at 1 s.

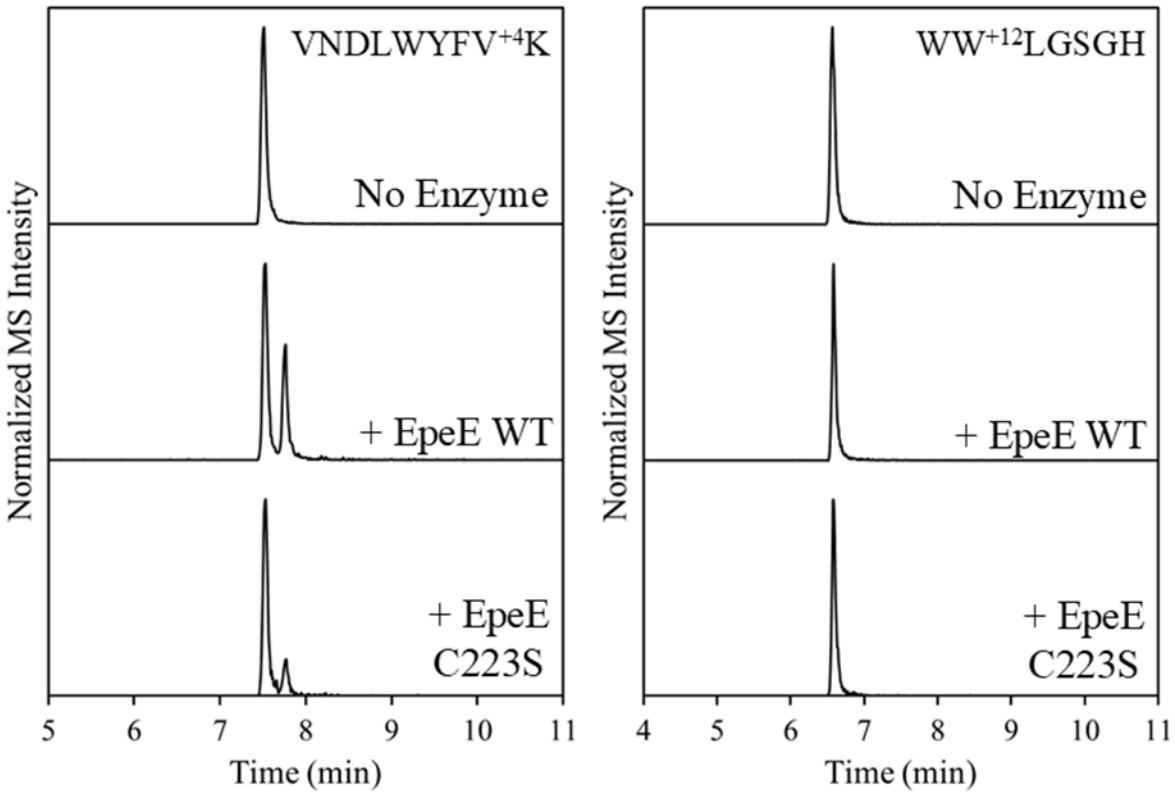


Figure S5.6. EICs of 18-hour assays of EpeE and MBP-EpeX$_{18\text{-}49}$ I12W in buffered D_2O. Unmodified peptide VNDLWYFVK elutes at 7.5 min and was extracted at 592.3109 *m/z*. Unmodified peptide WWLGSGH elutes at 6.8 min and was extracted at 421.7008 *m/z*. Epimerized peptide VNDLWYF(D-V)K elutes at 7.7 min and was extracted between 592.3 – 594.3 *m/z*.

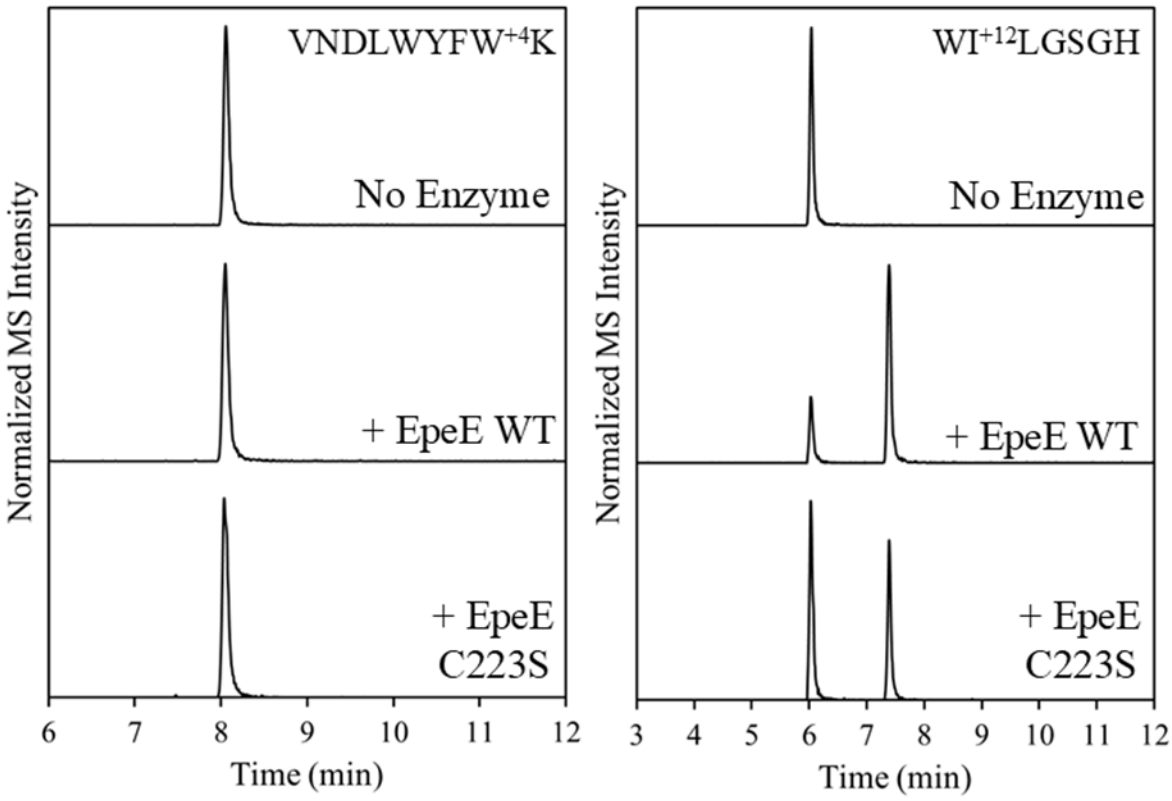


Figure S5.7. EICs of 18-hour assays of EpeE and MBP-EpeX$_{18\text{-}49}$ V4W in buffered D_2O. Unmodified peptide VNDLWYFWK elutes at 8.05 min and was extracted at 635.8164 *m/z*. Unmodified peptide WILGSGH elutes at 6 min and was extracted at 385.2032 *m/z*. Epimerized peptide W(D-I)LGSGH elutes at 7.3 min and was extracted between 385.2 – 386.7 *m/z*.

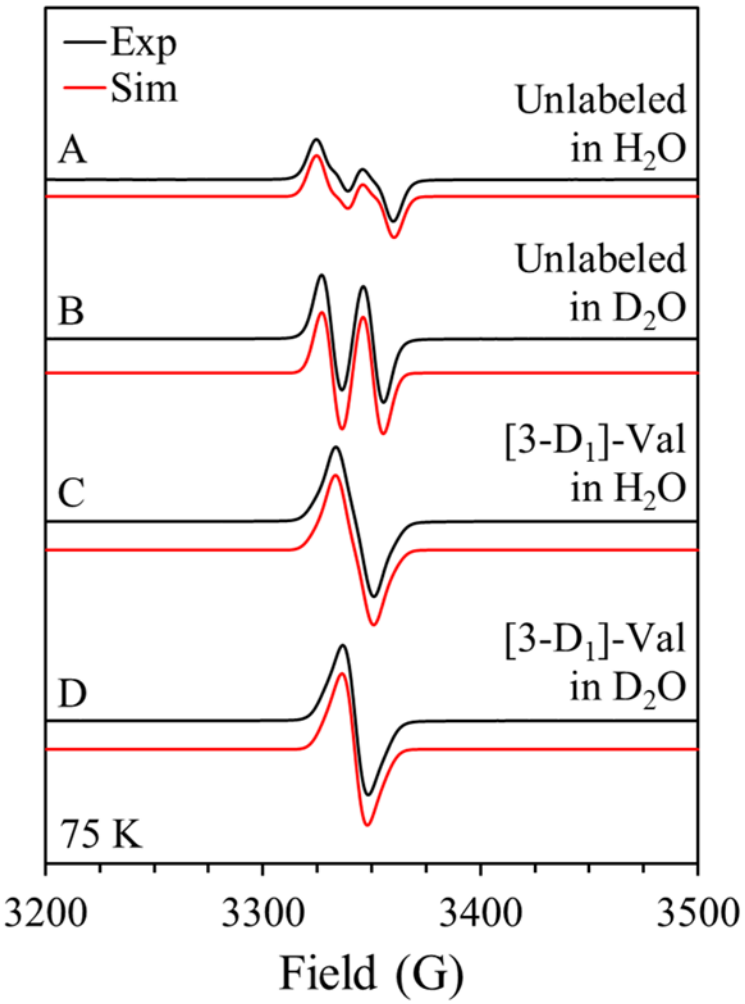


Figure S5.8. Isotopic labeling of MBP-EpeX$_{18\text{-}49}$ I12W to determine hyperfine coupling constants. A, reduced EpeE C223S, SAM, and MBP-EpeX$_{18\text{-}49}$ I12W freeze quenched at 1 min. B, reaction in buffered D_2O. C, reaction with [3-D_1]-L-Val labeled MBP-EpeX$_{18\text{-}49}$ I12W. D, reaction with [3-D_1]-L-Val labeled MBP-EpeX$_{18\text{-}49}$ I12W in buffered D_2O. Simulation parameters can be found in Table 1. Deuterium exchanged hyperfine couplings were achieved by simulating with ^2H and dividing the coupling constant by 6.514. EPR parameters: microwave frequency, 9.38 GHz; modulation, 3 G; microwave power, 0.3 mW; T = 75 K.

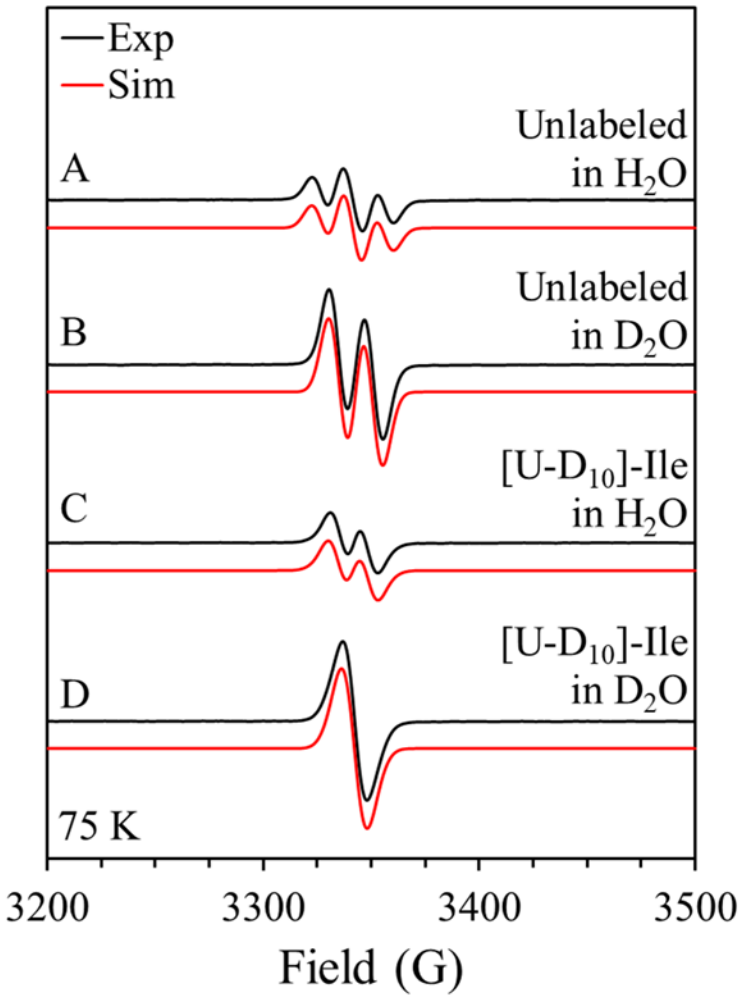


Figure S5.9. Isotopic labeling of MBP-EpeX$_{18\text{-}49}$ V4W to determine hyperfine coupling constants. A, reduced EpeE C223S, SAM, and MBP-EpeX$_{18\text{-}49}$ V4W freeze quenched at 1 min. B, reaction in buffered D_2O. C, reaction with [U-D_{10}]-L-Ile labeled MBP-EpeX$_{18\text{-}49}$ V4W. D, reaction with [U-D_{10}]-L-Ile labeled MBP-EpeX$_{18\text{-}49}$ V4W in buffered D_2O. Simulation parameters can be found in Table 1. Deuterium exchanged hyperfine couplings were achieved by simulating with ^2H and dividing the coupling constant by 6.514. EPR parameters: microwave frequency, 9.38 GHz; modulation, 3 G; microwave power, 0.3 mW; T = 75 K.

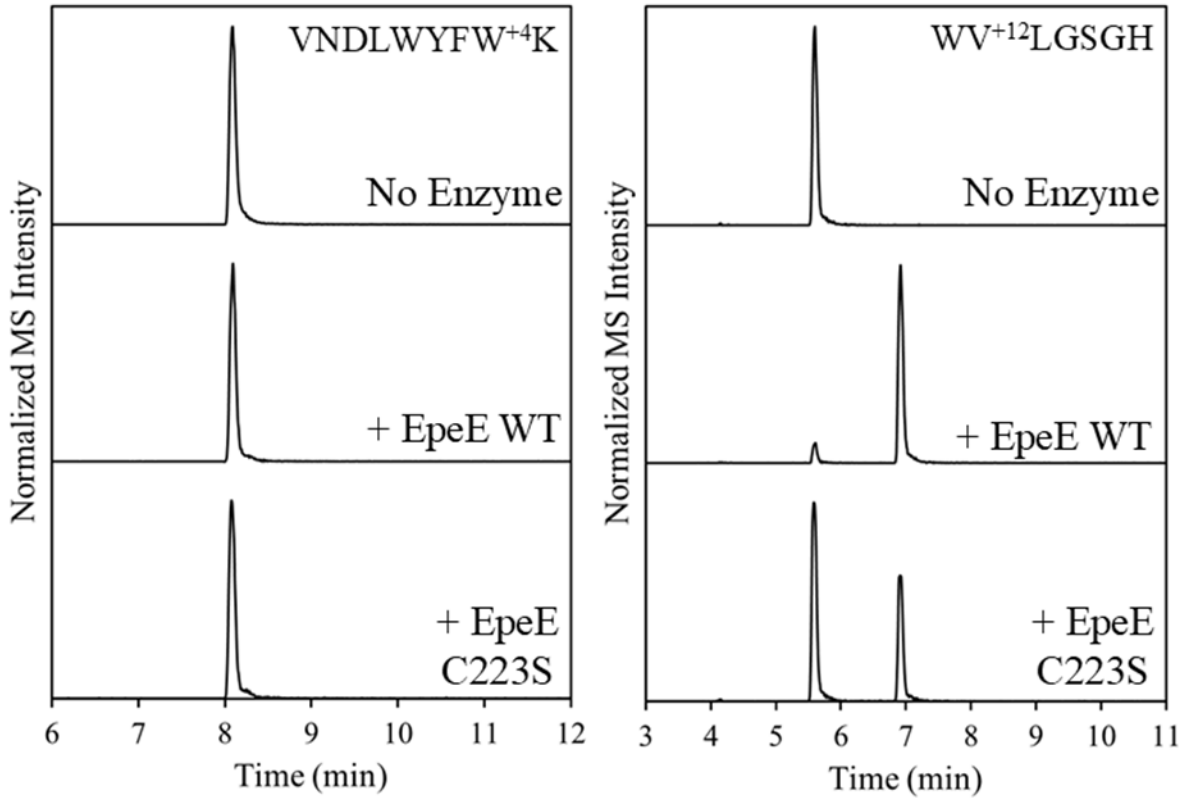


Figure S5.10. EICs of 18-hour assays of EpeE and MBP-EpeX$_{18\text{-}49}$ V4W/ I12V in buffered D_2O. Unmodified peptide VNDLWYFWK elutes at 8.05 min and was extracted at 635.8164 *m/z*. Unmodified peptide WVLGSGH elutes at 5.6 min and was extracted at 378.1954 *m/z*. Epimerized peptide W(D-V)LGSGH elutes at 6.9 min and was extracted between 378.1 – 379.7 *m/z*.

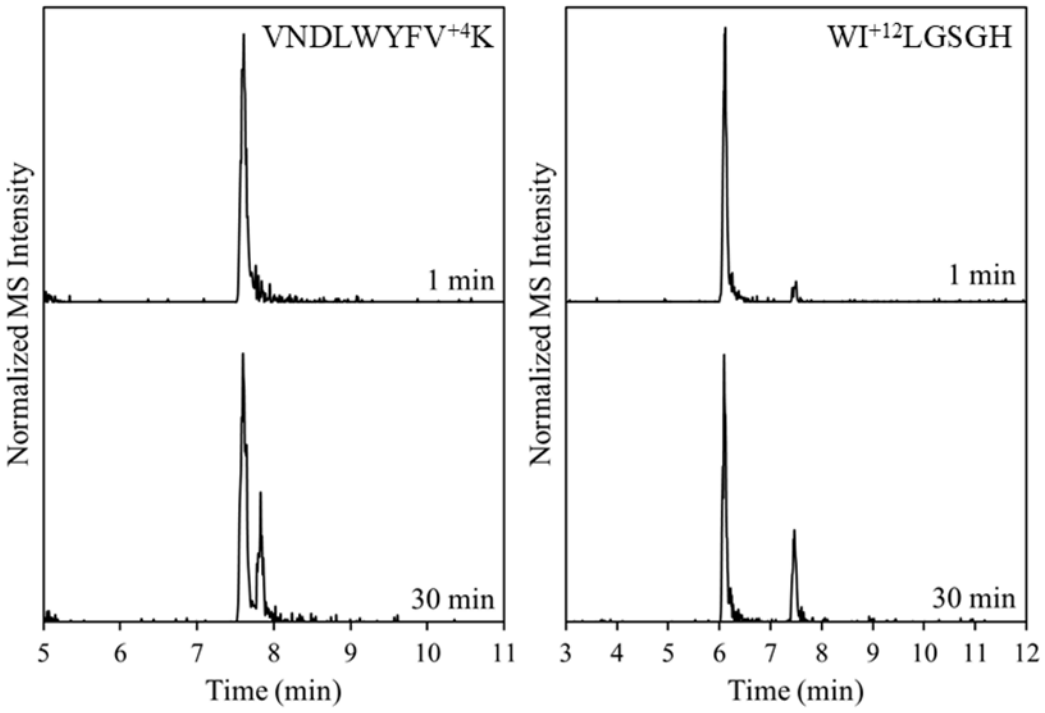


Figure S5.11. EICs of peptide VNDLWYFVK and peptide WILGSGH following reaction of EpeE C223S, MBP-EpeX$_{18-49}$, and SAM for 1 min or 30 min and trypsin digestion. The reaction contained the same concentrations used to prepare EPR samples (see Methods), but instead of freeze quenching at the indicated time, the sample was digested with trypsin protease and analyzed by LC-MS.

Table S5.1. Primers used in this study were designed using NEBasechanger.com. Sequences in lowercase are the introduced mutations.

Primer	Sequence (5′→ 3′)	Ta (°C)
EpeE C223S Fwd	TTACCCATGCagcAGTCCAGCCA	62
EpeE C223S Rev	ATCTCACCATCGTGATGATAC	-
MBP-TEV-Amplify Fwd	CTCGAGTCTGGTAAAGAAAC	60.6
MBP-TEV-Amplify Rev	GATCCCGAGGTTGTTGTTATTG	-
EpeX$_{18-49}$-Delete-Fwd	GGATTATTAGATGAAAGTCAGAAG	56
EpeX$_{18-49}$-Delete-Rev	CTGGAAGTACAGATTCTC	-

Table S5.1 Continued.

Primer	Sequence (5′→ 3′)	Ta (°C)
EpeX V4W Fwd	TTGGTATTTTtggAAAAGTAAGGAGAATC	57
EpeX V4W Rev	AGGTCATTTACCTTAGC	-
EpeX I12W Fwd	GAATCGTTGGtggCTGGGAAGCG	57
EpeX I12W Rev	TCCTTACTTTTCACAAAATAC	-
EpeX_I12V_Fwd	GAATCGTTGGgtgCTGGGAAGCG	63
EpeX_I12V_Rev	TCCTTACTTTTCACAAAATACCAAAG	-

Table S5.2. Spin quantitation's of EPR signals for Figure 5.5. See Methods for spin quantitation details.

MBP-EpeX$_{18\text{-}49}$ Mutant	Val4 Cα• (μM)	Ile12 Cα• (μM)
WT	48.4	5.4
I12W	56.0	-
V4W	-	9.0

Table S5.3. Spin quantitation's and simulation weights of Val4 Cα• and Ile12 Cα• used for Fig. 5.7.

Quench Time	Val4 Cα• Conc. (μM)	Val4 Cα• %weight	Ile12 Cα• Conc. (μM)	Ile12 Cα• %weight
10 s	14	80	3.5	20
30 s	40	85	7.0	15
1 min	48	90	5.4	10
5 min	17	90	1.9	10

Table S5.4. MS/MS fragment ions of peptide VNDLWYFVK from trypsin digestion of no enzyme control reaction with MBP-EpeX$_{18\text{-}49}$ (Fig. S5.3, top).

Ion	Calc. *m/z*	Obs. *m/z*	Δppm	Sequence
b_1^{1+}	100.0756	Not Obs.	-	V
b_2^{1+}	214.1186	214.1197	5.1	VN
b_3^{1+}	329.1455	329.1465	3.0	VND
b_4^{1+}	442.2296	442.2319	5.2	VNDL
b_5^{1+}	628.3089	628.3139	8.0	VNDLW
b_6^{1+}	791.3722	791.3758	4.5	VNDLWY
b_7^{1+}	938.4406	Not Obs.	-	VNDLWYF
b_8^{1+}	1037.5090	Not Obs.	-	VNDLWYFV
b_9^{1+}	-	-	-	VNDLWYFVK
y_1^{1+}	147.1128	147.1128	0.0	K
y_2^{1+}	246.1812	246.1820	3.2	VK
y_3^{1+}	393.2496	393.2514	4.6	FVK
y_4^{1+}	556.3129	556.3162	5.9	YFVK
y_5^{1+}	742.3922	742.3953	4.2	WYFVK
y_6^{1+}	855.4763	855.4783	2.3	LWYFVK
y_7^{1+}	970.5032	970.5085	5.5	DLWYFVK
y_8^{1+}	1084.5462	1084.5503	3.8	NDLWYFVK
y_9^{1+}	-	-	-	VNDLWYFVK

Table S5.5. MS/MS fragment ions of peptide WILGSGH from trypsin digestion of no enzyme control reaction with MBP-EpeX$_{18\text{-}49}$ (Fig. S5.3, top).

Ion	Calc. *m/z*	Obs. *m/z*	Δppm	Sequence
b_1^{1+}	187.0865	187.0846	-10.1	W
b_2^{1+}	300.1706	300.1714	2.7	WI
b_3^{1+}	413.2547	413.2523	-5.8	WIL
b_4^{1+}	470.2761	Not Obs.	-	WILG
b_5^{1+}	557.3082	Not Obs.	-	WILGS
b_6^{1+}	614.3296	Not Obs.	-	WILGSG
b_7^{1+}	-	-	-	WILGSGH
y_1^{1+}	156.0767	156.0769	1.3	H
y_2^{1+}	213.0982	213.1003	9.8	GH
y_3^{1+}	300.1302	300.1309	2.3	SGH
y_4^{1+}	357.1517	357.1535	5.0	GSGH
y_5^{1+}	470.2357	470.2380	4.9	LGSGH
y_6^{1+}	583.3198	583.3205	1.2	ILGSGH
y_7^{1+}	-	-	-	WILGSGH

Table S5.6. MS/MS fragment ions of peptide VNDLWYF(D-V)K from trypsin digestion following reaction of EpeE WT and MBP-EpeX$_{18\text{-}49}$ (Fig. S5.3, middle).

Ion	Calc. *m/z*	Obs. *m/z*	Δppm	Sequence
b_1^{1+}	100.0756	Not Obs.	-	V
b_2^{1+}	214.1186	214.1181	-2.3	VN
b_3^{1+}	329.1455	329.1481	7.9	VND
b_4^{1+}	442.2296	442.2319	5.2	VNDL
b_5^{1+}	628.3089	628.3079	-1.6	VNDLW
b_6^{1+}	791.3722	Not Obs.	-	VNDLWY
b_7^{1+}	938.4406	Not Obs.	-	VNDLWYF
b_8^{1+} +1	1038.5152	1038.5209	5.5	VNDLWYFV
b_9^{1+} +1	-	-	-	VNDLWYFVK
y_1^{1+}	147.1128	147.1140	8.2	K
y_2^{1+} +1	247.1874	247.1886	4.9	VK
y_3^{1+} +1	394.2558	394.2597	9.9	FVK
y_4^{1+} +1	557.3191	557.3198	1.3	YFVK
y_5^{1+} +1	743.3984	743.4001	2.3	WYFVK
y_6^{1+} +1	856.4825	856.4844	2.2	LWYFVK
y_7^{1+} +1	971.5094	971.5135	4.2	DLWYFVK
y_8^{1+} +1	1085.5524	1085.5529	0.5	NDLWYFVK
y_9^{1+} +1	-	-	-	VNDLWYFVK

Table S5.7. MS/MS fragment ions of peptide W(D-I)LGSGH from trypsin digestion following reaction of EpeE WT and MBP-EpeX$_{18\text{-}49}$ (Fig. S5.3, middle).

Ion	Calc. *m/z*	Obs. *m/z*	Δppm	Sequence
b_1^{1+}	187.0865	187.0891	-	W
b_2^{1+} +1	301.1768	301.1788	6.6	WI
b_3^{1+} +1	414.2609	414.2626	4.1	WIL
b_4^{1+} +1	471.2823	Not Obs.	-	WILG
b_5^{1+} +1	558.3144	Not Obs.	-	WILGS
b_6^{1+} +1	615.3358	Not Obs.	-	WILGSG
b_7^{1+} +1	-	-	-	WILGSGH
y_1^{1+}	156.0767	156.0778	7.0	H
y_2^{1+}	213.0982	213.0998	7.5	GH
y_3^{1+}	300.1302	300.1337	11.7	SGH
y_4^{1+}	357.1517	357.1529	3.4	GSGH
y_5^{1+}	470.2357	470.2388	6.6	LGSGH
y_6^{1+} +1	584.3260	584.3277	2.9	ILGSGH
y_7^{1+} +1	-	-	-	WILGSGH

Table S5.8. MS/MS fragment ions of peptide VNDLWYF(D-V)K from trypsin digestion following reaction of EpeE C223S and MBP-EpeX$_{18-49}$ (Fig. S5.3, bottom).

Ion	Calc. *m/z*	Obs. *m/z*	Δppm	Sequence
b_1^{1+}	100.0756	Not Obs.	-	V
b_2^{1+}	214.1186	214.1179	-3.3	VN
b_3^{1+}	329.1455	329.1507	15.8	VND
b_4^{1+}	442.2296	Not Obs.	-	VNDL
b_5^{1+}	628.3089	628.3176	13.8	VNDLW
b_6^{1+}	791.3722	Not Obs.	-	VNDLWY
b_7^{1+}	938.4406	Not Obs.	-	VNDLWYF
b_8^{1+} +1	1038.5152	Not Obs.	-	VNDLWYFV
b_9^{1+} +1	-	-	-	VNDLWYFVK
y_1^{1+}	147.1128	147.1132	2.7	K
y_2^{1+} +1	247.1874	Not Obs.	-	VK
y_3^{1+} +1	394.2558	394.2515	-10.9	FVK
y_4^{1+} +1	557.3191	557.3167	-4.3	YFVK
y_5^{1+} +1	743.3984	743.3978	-0.8	WYFVK
y_6^{1+} +1	856.4825	856.4789	-4.2	LWYFVK
y_7^{1+} +1	971.5094	971.5123	3.0	DLWYFVK
y_8^{1+} +1	1085.5524	1085.5537	1.2	NDLWYFVK
y_9^{1+} +1	-	-	-	VNDLWYFVK

Table S5.9. MS/MS fragment ions of peptide W(D-I)LGSGH from trypsin digestion following reaction of EpeE C223S and MBP-EpeX$_{18-49}$ (Fig. S5.3, bottom).

Ion	Calc. *m/z*	Obs. *m/z*	Δppm	Sequence
b_1^{1+}	187.0865	187.0882	9.1	W
b_2^{1+}	300.1706	300.1753	15.7	WI
b_3^{1+}	413.2547	413.2578	7.5	WIL
b_4^{1+}	470.2761	Not Obs.	-	WILG
b_5^{1+}	557.3082	Not Obs.	-	WILGS
b_6^{1+}	614.3296	Not Obs.	-	WILGSG
b_7^{1+}	-	-	-	WILGSGH
y_1^{1+}	156.0767	156.0790	14.7	H
y_2^{1+}	213.0982	213.0987	2.3	GH
y_3^{1+}	300.1302	300.1285	-5.7	SGH
y_4^{1+}	357.1517	357.1564	13.2	GSGH
y_5^{1+}	470.2357	470.2389	6.8	LGSGH
y_6^{1+}	583.3198	583.3258	10.3	ILGSGH
y_7^{1+}	-	-	-	WILGSGH

Table S5.10. MS/MS fragment ions of peptide VNDLWYFVK from $EpeX_{18-49}$ following trypsin digestion (Fig. S5.4, left panel).

Ion	Calc. *m/z*	Obs. *m/z*	Δppm	Sequence
b_1^{1+}	100.0756	Not Obs.	-	V
b_2^{1+}	214.1186	214.1191	2.3	VN
b_3^{1+}	329.1455	329.1468	3.9	VND
b_4^{1+}	442.2296	442.2305	2.0	VNDL
b_5^{1+}	628.3089	628.3110	3.3	VNDLW
b_6^{1+}	791.3722	791.3726	0.5	VNDLWY
b_7^{1+}	938.4406	938.4418	1.3	VNDLWYF
b_8^{1+}	1037.5090	1037.5082	-0.8	VNDLWYFV
b_9^{1+}	-	-	-	VNDLWYFVK
y_1^{1+}	147.1128	147.1130	1.4	K
y_2^{1+}	246.1812	246.1815	1.2	VK
y_3^{1+}	393.2496	393.2508	3.0	FVK
y_4^{1+}	556.3129	556.3144	2.7	YFVK
y_5^{1+}	742.3922	742.3939	2.3	WYFVK
y_6^{1+}	855.4763	855.4774	1.3	LWYFVK
y_7^{1+}	970.5032	970.5052	2.0	DLWYFVK
y_8^{1+}	1084.5462	1084.5473	1.0	NDLWYFVK
y_9^{1+}	-	-	-	VNDLWYFVK

Table S5.11. MS/MS fragment ions of peptide WILGSGH from $EpeX_{18-49}$ following trypsin digestion (Fig. S5.4, top).

Ion	Calc. *m/z*	Obs. *m/z*	Δppm	Sequence
b_1^{1+}	187.0865	187.0865	0.0	W
b_2^{1+}	300.1706	300.1713	2.3	WI
b_3^{1+}	413.2547	413.2556	2.2	WIL
b_4^{1+}	470.2761	Not Obs.	-	WILG
b_5^{1+}	557.3082	Not Obs.	-	WILGS
b_6^{1+}	614.3296	Not Obs.	-	WILGSG
b_7^{1+}	-	-	-	WILGSGH
y_1^{1+}	156.0767	156.0769	1.3	H
y_2^{1+}	213.0982	213.0983	0.5	GH
y_3^{1+}	300.1302	300.1308	2.0	SGH
y_4^{1+}	357.1517	357.1528	3.1	GSGH
y_5^{1+}	470.2357	470.2368	2.3	LGSGH
y_6^{1+}	583.3198	583.3208	1.7	ILGSGH
y_7^{1+}	-		-	WILGSGH

Table S5.12. MS/MS fragment ions of peptide VNDLWYFVK from trypsin digestion of no enzyme control reaction with MBP-EpeX$_{18\text{-}49}$ I12W (Fig. S5.6, top).

Ion	Calc. *m/z*	Obs. *m/z*	Δppm	Sequence
b_1^{1+}	100.0756	Not Obs.	-	V
b_2^{1+}	214.1186	214.1188	0.9	VN
b_3^{1+}	329.1455	329.1467	3.6	VND
b_4^{1+}	442.2296	442.2310	3.2	VNDL
b_5^{1+}	628.3089	628.3130	6.5	VNDLW
b_6^{1+}	791.3722	791.3731	1.1	VNDLWY
b_7^{1+}	938.4406	938.4472	7.0	VNDLWYF
b_8^{1+}	1037.5090	1037.5133	4.1	VNDLWYFV
b_9^{1+}	-	-	-	VNDLWYFVK
y_1^{1+}	147.1128	147.1131	2.0	K
y_2^{1+}	246.1812	246.1821	3.7	VK
y_3^{1+}	393.2496	393.2514	4.6	FVK
y_4^{1+}	556.3129	556.3143	2.5	YFVK
y_5^{1+}	742.3922	742.3948	3.5	WYFVK
y_6^{1+}	855.4763	855.4765	0.2	LWYFVK
y_7^{1+}	970.5032	970.5057	2.6	DLWYFVK
y_8^{1+}	1084.5462	1084.5496	3.1	NDLWYFVK
y_9^{1+}	-	-	-	VNDLWYFVK

Table S5.13. MS/MS fragment ions of peptide WWLGSGH from trypsin digestion of no enzyme control reaction with MBP-EpeX$_{18\text{-}49}$ I12W (Fig. S5.6, right panel).

Ion	Calc. m/z	Obs. m/z	Δppm	Sequence
b_1^{1+}	187.0865	187.0873	4.3	W
b_2^{1+}	373.1659	373.1656	-0.8	WW
b_3^{1+}	486.2499	486.2507	1.6	WWL
b_4^{1+}	543.2714	Not Obs.	-	WWLG
b_5^{1+}	630.3034	Not Obs.	-	WWLGS
b_6^{1+}	687.3249	Not Obs.	-	WWLGSG
b_7^{1+}	-	-	-	WWLGSGH
y_1^{1+}	156.0767	156.0770	1.9	H
y_2^{1+}	213.0982	213.0985	1.4	GH
y_3^{1+}	300.1302	300.1315	4.3	SGH
y_4^{1+}	357.1517	357.1522	1.4	GSGH
y_5^{1+}	470.2357	470.2363	1.3	LGSGH
y_6^{1+}	656.3150	656.3174	3.7	WLGSGH
y_7^{1+}	-	-	-	WWLGSGH

Table S5.14. MS/MS fragment ions of peptide VNDLWYF(D-V)K from trypsin digestion following reaction of EpeE WT and MBP-EpeX$_{18\text{-}49}$ I12W (Fig. S5.6, middle).

Ion	Calc. *m/z*	Obs. *m/z*	Δppm	Sequence
b_1^{1+}	100.0756	Not Obs.	-	V
b_2^{1+}	214.1186	214.1203	7.9	VN
b_3^{1+}	329.1455	329.1444	-3.3	VND
b_4^{1+}	442.2296	442.2352	12.7	VNDL
b_5^{1+}	628.3089	628.3082	-1.1	VNDLW
b_6^{1+}	791.3722	791.3783	7.7	VNDLWY
b_7^{1+}	938.4406	938.4497	9.7	VNDLWYF
b_8^{1+} +1	1038.5152	1038.5187	3.4	VNDLWYFV
b_9^{1+} +1	-	-	-	VNDLWYFVK
y_1^{1+}	147.1128	147.1128	0.0	K
y_2^{1+} +1	247.1874	247.1920	18.6	VK
y_3^{1+} +1	394.2558	394.2578	5.1	FVK
y_4^{1+} +1	557.3191	557.3266	13.5	YFVK
y_5^{1+} +1	743.3984	743.4029	6.1	WYFVK
y_6^{1+} +1	856.4825	856.4930	12.3	LWYFVK
y_7^{1+} +1	971.5094	971.5139	4.6	DLWYFVK
y_8^{1+} +1	1085.5524	1085.5570	4.2	NDLWYFVK
y_9^{1+} +1	-	-	-	VNDLWYFVK

Table S5.15. MS/MS fragment ions of peptide VNDLWYF(D-V)K from trypsin digestion following reaction of EpeE C223S and MBP-EpeX$_{18\text{-}49}$ I12W (Fig. S5.6, bottom).

Ion	Calc. *m/z*	Obs. *m/z*	Δppm	Sequence
b_1^{1+}	100.0756	Not Obs.	-	V
b_2^{1+}	214.1186	Not Obs.	-	VN
b_3^{1+}	329.1455	329.1450	-1.5	VND
b_4^{1+}	442.2296	442.2280	-3.6	VNDL
b_5^{1+}	628.3089	Not Obs.	-	VNDLW
b_6^{1+}	791.3722	Not Obs.	-	VNDLWY
b_7^{1+}	938.4406	Not Obs.	-	VNDLWYF
b_8^{1+} +1	1038.5152	Not Obs.	-	VNDLWYFV
b_9^{1+} +1	-	-	-	VNDLWYFVK
y_1^{1+}	147.1128	147.1106	-15.0	K
y_2^{1+} +1	247.1874	247.1899	10.1	VK
y_3^{1+} +1	394.2558	394.2567	2.3	FVK
y_4^{1+} +1	557.3191	557.3263	12.9	YFVK
y_5^{1+} +1	743.3984	743.4046	8.3	WYFVK
y_6^{1+} +1	856.4825	856.4797	-3.3	LWYFVK
y_7^{1+} +1	971.5094	971.5168	7.6	DLWYFVK

Table S5.15 Continued.

Ion	Calc. *m/z*	Obs. *m/z*	Δppm	Sequence
y_8^{1+} +1	1085.5524	1085.5478	-4.2	NDLWYFVK
y_9^{1+} +1	-	-	-	VNDLWYFVK

Table S5.16. MS/MS fragment ions of peptide VNDLWYFWK from trypsin digestion following no enzyme control reaction with MBP-EpeX$_{18\text{-}49}$ V4W (Fig. S5.7, left panel).

Ion	Calc. *m/z*	Obs. *m/z*	Δppm	Sequence
b_1^{1+}	100.0756	Not Obs.	-	V
b_2^{1+}	214.1186	214.1187	0.5	VN
b_3^{1+}	329.1455	329.1469	4.3	VND
b_4^{1+}	442.2296	442.2311	3.4	VNDL
b_5^{1+}	628.3089	628.3117	4.5	VNDLW
b_6^{1+}	791.3722	791.3738	2.0	VNDLWY
b_7^{1+}	938.4406	938.4425	2.0	VNDLWYF
b_8^{1+}	1124.5199	1124.5280	7.2	VNDLWYFV
b_9^{1+}	-	-	-	VNDLWYFWK
y_1^{1+}	147.1128	147.1134	4.1	K
y_2^{1+}	333.1921	333.1933	3.6	WK
y_3^{1+}	480.2605	480.2626	4.4	FWK
y_4^{1+}	643.3238	643.3252	2.2	YFWK
y_5^{1+}	829.4031	829.4046	1.8	WYFWK
y_6^{1+}	942.4872	942.4921	5.2	LWYFWK
y_7^{1+}	1057.5141	1057.5160	1.8	DLWYFWK
y_8^{1+}	1171.5571	1171.5594	2.0	NDLWYFWK
y_9^{1+}	-	-	-	VNDLWYFWK

Table S5.17. MS/MS fragment ions of peptide WILGSGH from trypsin digestion following no enzyme control reaction with MBP-EpeX$_{18\text{-}49}$ V4W (Figure S5.7, top).

Ion	Calc. *m/z*	Obs. *m/z*	Δppm	Sequence
b_1^{1+}	187.0865	187.0875	5.3	W
b_2^{1+}	300.1706	300.1717	3.7	WI
b_3^{1+}	413.2547	413.2562	3.6	WIL
b_4^{1+}	470.2761	Not Obs.	-	WILG
b_5^{1+}	557.3082	Not Obs.	-	WILGS
b_6^{1+}	614.3296	Not Obs.	-	WILGSG
b_7^{1+}	-	-	-	WILGSGH
y_1^{1+}	156.0767	156.0774	4.5	H
y_2^{1+}	213.0982	213.0981	-0.5	GH
y_3^{1+}	300.1302	300.1319	5.7	SGH

Table S5.17 Continued.

Ion	Calc. *m/z*	Obs. *m/z*	Δppm	Sequence
y_4^{1+}	357.1517	357.1527	2.8	GSGH
y_5^{1+}	470.2357	470.2370	2.8	LGSGH
y_6^{1+}	583.3198	583.3219	3.6	ILGSGH
y_7^{1+}	-	-	-	WILGSGH

Table S5.18. MS/MS fragment ions of peptide W(D-I)LGSGH from trypsin digestion following reaction of EpeE WT and MBP-EpeX$_{18\text{-}49}$ V4W (Figure S5.7, middle).

Ion	Calc. *m/z*	Obs. *m/z*	Δppm	Sequence
b_1^{1+}	187.0865	187.0864	-0.5	W
b_2^{1+} +1	301.1768	301.1773	1.7	WI
b_3^{1+} +1	414.2609	414.2626	4.1	WIL
b_4^{1+} +1	471.2823	Not Obs.	-	WILG
b_5^{1+} +1	558.3144	Not Obs.	-	WILGS
b_6^{1+} +1	615.3358	Not Obs.	-	WILGSG
b_7^{1+} +1	-	-	-	WILGSGH
y_1^{1+}	156.0767	156.0766	-0.6	H
y_2^{1+}	213.0982	213.0981	-0.5	GH
y_3^{1+}	300.1302	300.1301	-0.3	SGH
y_4^{1+}	357.1517	357.1523	1.7	GSGH
y_5^{1+}	470.2357	470.2367	2.1	LGSGH
y_6^{1+} +1	584.3260	584.3260	0.0	ILGSGH
y_7^{1+} +1	-	-	-	WILGSGH

Table S5.19. MS/MS fragment ions of peptide W(D-I)LGSGH from trypsin digestion following reaction of EpeE C223S and MBP-EpeX$_{18\text{-}49}$ V4W (Figure S5.7, bottom).

Ion	Calc. *m/z*	Obs. *m/z*	Δppm	Sequence
b_1^{1+}	187.0865	187.0842	-12.3	W
b_2^{1+}	300.1706	300.1719	4.3	WI
b_3^{1+}	413.2547	413.2571	5.8	WIL
b_4^{1+}	470.2761	Not Obs.	-	WILG
b_5^{1+}	557.3082	Not Obs.	-	WILGS
b_6^{1+}	614.3296	Not Obs.	-	WILGSG
b_7^{1+}	-	-	-	WILGSGH
y_1^{1+}	156.0767	156.0765	-1.3	H
y_2^{1+}	213.0982	213.0980	-0.9	GH
y_3^{1+}	300.1302	300.1296	-2.0	SGH
y_4^{1+}	357.1517	357.1531	3.9	GSGH
y_5^{1+}	470.2357	470.2371	3.0	LGSGH

Table S5.19 Continued.

Ion	Calc. *m/z*	Obs. *m/z*	Δppm	Sequence
y_6^{1+}	583.3198	583.3230	5.5	ILGSGH
y_7^{1+}	-	-	-	WILGSGH

Table S5.20. MS/MS fragment ions of peptide VNDLWYFWK from trypsin digestion following no enzyme control reaction with MBP-EpeX$_{18\text{-}49}$ V4W/ I12V (Figure S5.10, left panel).

Ion	Calc. *m/z*	Obs. *m/z*	Δppm	Sequence
b_1^{1+}	100.0756	Not Obs.	-	V
b_2^{1+}	214.1186	214.1188	0.9	VN
b_3^{1+}	329.1455	329.1460	1.5	VND
b_4^{1+}	442.2296	442.2294	-0.5	VNDL
b_5^{1+}	628.3089	628.3080	-1.4	VNDLW
b_6^{1+}	791.3722	791.3698	-3.0	VNDLWY
b_7^{1+}	938.4406	938.4355	-5.4	VNDLWYF
b_8^{1+}	1124.5199	1124.5172	-2.4	VNDLWYFW
b_9^{1+}	-	-	-	VNDLWYFWK
y_1^{1+}	147.1128	147.1130	1.4	K
y_2^{1+}	333.1921	333.1923	0.6	WK
y_3^{1+}	480.2605	480.2607	0.4	FWK
y_4^{1+}	643.3238	643.3242	0.6	YFWK
y_5^{1+}	829.4031	829.4045	1.7	WYFWK
y_6^{1+}	942.4872	942.4854	-1.9	LWYFWK
y_7^{1+}	1057.5141	1057.5126	-1.4	DLWYFWK
y_8^{1+}	1171.5571	1171.5543	-2.4	NDLWYFWK
y_9^{1+}	-	-	-	VNDLWYFWK

Table S5.21. MS/MS fragment ions of peptide WVLGSGH from trypsin digestion following no enzyme control reaction with MBP-EpeX$_{18\text{-}49}$ V4W/ I12V (Figure S5.10, top).

Ion	Calc. *m/z*	Obs. *m/z*	Δppm	Sequence
b_1^{1+}	187.0865	187.0854	-5.9	W
b_2^{1+}	286.1550	286.1545	-1.7	WV
b_3^{1+}	399.2390	399.2407	4.3	WVL
b_4^{1+}	456.2605	456.2619	3.1	WVLG
b_5^{1+}	543.2925	Not Obs.	-	WVLGS
b_6^{1+}	600.3140	Not Obs.	-	WVLGSG
b_7^{1+}	-	-	-	WVLGSGH
y_1^{1+}	156.0767	156.0762	-3.2	H
y_2^{1+}	213.0982	213.0976	-2.8	GH
y_3^{1+}	300.1302	300.1305	1.0	SGH

Table S5.21 Continued.

Ion	Calc. *m/z*	Obs. *m/z*	Δppm	Sequence
y_4^{1+}	357.1517	357.1521	1.1	GSGH
y_5^{1+}	470.2357	470.2352	-1.1	LGSGH
y_6^{1+}	569.3041	569.3011	-5.3	VLGSGH
y_7^{1+}	-	-	-	WVLGSGH

Table S5.22. MS/MS fragment ions of peptide W(D-V)LGSGH from trypsin digestion following reaction of EpeE WT and MBP-EpeX$_{18\text{-}49}$ V4W/ I12V (Figure S5.10, middle).

Ion	Calc. *m/z*	Obs. *m/z*	Δppm	Sequence
b_1^{1+}	187.0865	187.0858	-3.7	W
b_2^{1+} +1	287.1612	287.1609	-1.0	WV
b_3^{1+} +1	400.2452	400.2458	1.5	WVL
b_4^{1+} +1	457.2667	Not Obs.	-	WVLG
b_5^{1+} +1	544.2987	Not Obs.	-	WVLGS
b_6^{1+} +1	601.3202	Not Obs.	-	WVLGSG
b_7^{1+}	-	-	-	WVLGSGH
y_1^{1+}	156.0767	156.0767	0.0	H
y_2^{1+}	213.0982	213.0984	0.9	GH
y_3^{1+}	300.1302	300.1310	2.7	SGH
y_4^{1+}	357.1517	357.1514	-0.8	GSGH
y_5^{1+}	470.2357	470.2361	0.9	LGSGH
y_6^{1+} +1	570.3103	570.3117	2.5	VLGSGH
y_7^{1+} +1	-	-	-	WVLGSGH

Table S5.23. MS/MS fragment ions of peptide W(D-V)LGSGH from trypsin digestion following reaction of EpeE C223S and MBP-EpeX$_{18\text{-}49}$ V4W/ I12V (Figure S5.10, bottom).

Ion	Calc. *m/z*	Obs. *m/z*	Δppm	Sequence
b_1^{1+}	187.0865	187.0867	1.1	W
b_2^{1+}	286.1550	286.1541	-3.1	WV
b_3^{1+}	399.2390	Not Obs.	-	WVL
b_4^{1+}	456.2605	Not Obs.	-	WVLG
b_5^{1+}	543.2925	Not Obs.	-	WVLGS
b_6^{1+}	600.3140	Not Obs.	-	WVLGSG
b_7^{1+}	-	-	-	WVLGSGH
y_1^{1+}	156.0767	156.0756	-7.0	H
y_2^{1+}	213.0982	213.0968	-6.6	GH
y_3^{1+}	300.1302	300.1306	1.3	SGH
y_4^{1+}	357.1517	357.1519	0.6	GSGH
y_5^{1+}	470.2357	470.2360	0.6	LGSGH

Table S5.23 Continued.

Ion	Calc. *m/z*	Obs. *m/z*	Δppm	Sequence
y_6^{1+}	569.3041	569.3027	-2.5	VLGSGH
y_7^{1+}	-	-	-	WVLGSGH

Table S5.24. MS/MS fragment ions of peptide VNDLWYFVK from trypsin digested MBP-EpeX$_{18\text{-}49}$ labeled with [3-D$_1$]-L-Val.

Ion	Calc. *m/z*	Obs. *m/z*	Δppm	Sequence
b_1^{1+} +1	101.0817	Not Obs.	-	V
b_2^{1+} +1	215.1247	215.1242	-2.3	VN
b_3^{1+} +1	330.1516	330.1515	-0.3	VND
b_4^{1+} +1	443.2357	443.2341	-3.6	VNDL
b_5^{1+} +1	629.3150	629.3130	-3.1	VNDLW
b_6^{1+} +1	792.3783	Not Obs.	-	VNDLWY
b_7^{1+} +1	939.4467	939.4426	-4.3	VNDLWYF
b_8^{1+} +2	1039.5212	1039.5176	-3.4	VNDLWYFV
b_9^{1+} +2	-	-	-	VNDLWYFVK
y_1^{1+}	147.1128	147.1127	-0.6	K
y_2^{1+} +1	247.1873	247.1870	-1.2	VK
y_3^{1+} +1	394.2557	394.2547	-2.5	FVK
y_4^{1+} +1	557.3190	557.3167	-4.1	YFVK
y_5^{1+} +1	743.3983	743.3952	-4.1	WYFVK
y_6^{1+} +1	856.4824	856.4782	-4.9	LWYFVK
y_7^{1+} +1	971.5093	971.5063	-3.0	DLWYFVK
y_8^{1+} +1	1085.5523	1085.5467	-5.1	NDLWYFVK
y_9^{1+} +2	-	-	-	VNDLWYFVK

Table S5.25. MS/MS fragment ions of peptide WILGSGH from trypsin digested MBP-EpeX$_{18\text{-}49}$ labeled with [3-D$_1$]-L-Val.

Ion	Calc. *m/z*	Obs. *m/z*	Δppm	Sequence
b_1^{1+}	187.0865	187.0861	-2.1	W
b_2^{1+}	300.1706	300.1704	-0.6	WI
b_3^{1+}	413.2547	413.2548	0.2	WIL
b_4^{1+}	470.2761	Not Obs.	-	WILG
b_5^{1+}	557.3082	Not Obs.	-	WILGS
b_6^{1+}	614.3296	Not Obs.	-	WILGSG
b_7^{1+}	-	-	-	WILGSGH
y_1^{1+}	156.0767	156.0769	1.3	H
y_2^{1+}	213.0982	213.0979	-1.4	GH
y_3^{1+}	300.1302	300.1305	1.0	SGH

Table S5.25 Continued.

Ion	Calc. *m/z*	Obs. *m/z*	Δppm	Sequence
y_4^{1+}	357.1517	357.1512	-1.4	GSGH
y_5^{1+}	470.2357	470.2355	-0.4	LGSGH
y_6^{1+}	583.3198	583.3199	0.1	ILGSGH
y_7^{1+}	-		-	WILGSGH

Table S5.26. MS/MS fragment ions of peptide VNDLWYFVK from trypsin digested MBP-EpeX$_{18\text{-}49}$ labeled with [U-D$_{10}$]-L-Ile.

Ion	Calc. *m/z*	Obs. *m/z*	Δppm	Sequence
b_1^{1+}	100.0756	Not Obs.	-	V
b_2^{1+}	214.1186	214.1180	-2.8	VN
b_3^{1+}	329.1455	329.1451	-1.2	VND
b_4^{1+}	442.2296	442.2296	0.0	VNDL
b_5^{1+}	628.3089	628.3067	-3.5	VNDLW
b_6^{1+}	791.3722	791.3695	-3.4	VNDLWY
b_7^{1+}	938.4406	938.4432	2.7	VNDLWYF
b_8^{1+}	1037.5090	1037.5031	-5.6	VNDLWYFV
b_9^{1+}	-	-	-	VNDLWYFVK
y_1^{1+}	147.1128	147.1127	-0.6	K
y_2^{1+}	246.1812	246.1805	-2.8	VK
y_3^{1+}	393.2496	393.2486	-2.5	FVK
y_4^{1+}	556.3129	556.3108	-3.7	YFVK
y_5^{1+}	742.3922	742.3907	-2.0	WYFVK
y_6^{1+}	855.4763	855.4742	-2.4	LWYFVK
y_7^{1+}	970.5032	970.5000	-3.3	DLWYFVK
y_8^{1+}	1084.5462	1084.5429	-3.0	NDLWYFVK
y_9^{1+}	-	-	-	VNDLWYFVK

Table S5.27. MS/MS fragment ions of peptide WILGSGH from trypsin digested MBP-EpeX$_{18\text{-}49}$ labeled with [U-D$_{10}$]-L-Ile.

Ion	Calc. *m/z*	Obs. *m/z*	Δppm	Sequence
b_1^{1+}	187.0865	187.0858	-3.7	W
b_2^{1+} +9	309.2255	309.2262	2.2	WI
b_3^{1+} +9	422.3096	422.3060	-8.5	WIL
b_4^{1+} +9	479.3310	Not Obs.	-	WILG
b_5^{1+} +9	566.3631	Not Obs.	-	WILGS
b_6^{1+} +9	623.3845	Not Obs.	-	WILGSG
b_7^{1+} +9	-	-	-	WILGSGH
y_1^{1+}	156.0767	156.0764	-1.9	H

Table S5.27 Continued.

Ion	Calc. *m/z*	Obs. *m/z*	Δppm	Sequence
y_2^{1+}	213.0982	213.0974	-3.7	GH
y_3^{1+}	300.1302	300.1284	-6.0	SGH
y_4^{1+}	357.1517	357.1505	-3.3	GSGH
y_5^{1+}	470.2357	470.2346	-2.3	LGSGH
y_6^{1+} +9	592.3747	592.3746	-0.1	ILGSGH
y_7^{1+} +9	-		-	WILGSGH

Table S5.28. MS/MS fragment ions of peptide VNDLWYFVK from trypsin digested MBP-EpeX$_{18\text{-}49}$ labeled with both [U-D$_{10}$]-L-Ile and [3-D$_1$]-L-Val.

Ion	Calc. *m/z*	Obs. *m/z*	Δppm	Sequence
b_1^{1+} +1	101.0817	Not Obs.	-	V
b_2^{1+} +1	215.1247	215.1241	-2.8	VN
b_3^{1+} +1	330.1516	330.1508	-2.4	VND
b_4^{1+} +1	443.2357	443.2341	-3.6	VNDL
b_5^{1+} +1	629.3150	629.3109	-6.5	VNDLW
b_6^{1+} +1	792.3783	792.3721	-7.8	VNDLWY
b_7^{1+} +1	939.4467	939.4402	-6.9	VNDLWYF
b_8^{1+} +2	1039.5212	1039.5163	-4.7	VNDLWYFV
b_9^{1+} +2	-	-	-	VNDLWYFVK
y_1^{1+}	147.1128	147.1124	-2.7	K
y_2^{1+} +1	247.1873	247.1866	-2.8	VK
y_3^{1+} +1	394.2557	394.2543	-3.5	FVK
y_4^{1+} +1	557.3190	557.3177	-2.3	YFVK
y_5^{1+} +1	743.3983	743.3958	-3.3	WYFVK
y_6^{1+} +1	856.4824	856.4800	-2.8	LWYFVK
y_7^{1+} +1	971.5093	971.5049	-4.5	DLWYFVK
y_8^{1+} +1	1085.5523	1085.5455	-6.2	NDLWYFVK
y_9^{1+} +2	-	-	-	VNDLWYFVK

Table S5.29. MS/MS fragment ions of peptide WILGSGH from trypsin digested MBP-EpeX$_{18\text{-}49}$ labeled with both [U-D$_{10}$]-L-Ile and [3-D$_1$]-L-Val.

Ion	Calc. *m/z*	Obs. *m/z*	Δppm	Sequence
b_1^{1+}	187.0865	187.0856	-4.8	W
b_2^{1+} +9	309.2255	309.2269	4.5	WI
b_3^{1+} +9	422.3096	422.3101	1.1	WIL
b_4^{1+} +9	479.3310	Not Obs.	-	WILG
b_5^{1+} +9	566.3631	Not Obs.	-	WILGS
b_6^{1+} +9	623.3845	Not Obs.	-	WILGSG

Table S5.29 Continued.

Ion	Calc. *m/z*	Obs. *m/z*	Δppm	Sequence
b_7^{1+} +9	-	-	-	WILGSGH
y_1^{1+}	156.0767	156.0766	-0.6	H
y_2^{1+}	213.0982	213.0971	-5.1	GH
y_3^{1+}	300.1302	300.1290	-4.0	SGH
y_4^{1+}	357.1517	357.1512	-1.4	GSGH
y_5^{1+}	470.2357	470.2347	-2.1	LGSGH
y_6^{1+} +9	592.3747	592.3733	-2.3	ILGSGH
y_7^{1+} +9	-		-	WILGSGH

Table S5.30. MS/MS fragment ions of peptide VNDLWYFVK from trypsin digested MBP-EpeX$_{18\text{-}49}$ V4W labeled with [U-D$_{10}$]-L-Ile.

Ion	Calc. *m/z*	Obs. *m/z*	Δppm	Sequence
b_1^{1+}	100.0756	Not Obs.	-	V
b_2^{1+}	214.1186	214.1182	-1.9	VN
b_3^{1+}	329.1455	329.1458	0.9	VND
b_4^{1+}	442.2296	442.2300	0.9	VNDL
b_5^{1+}	628.3089	628.3098	1.4	VNDLW
b_6^{1+}	791.3722	791.3742	2.5	VNDLWY
b_7^{1+}	938.4406	938.4349	-6.1	VNDLWYF
b_8^{1+}	1124.5199	1124.5143	-5.0	VNDLWYFW
b_9^{1+}	-	-	-	VNDLWYFWK
y_1^{1+}	147.1128	147.1128	0.0	K
y_2^{1+}	333.1921	333.1919	-0.6	WK
y_3^{1+}	480.2605	480.2604	-0.2	FWK
y_4^{1+}	643.3238	643.3241	0.5	YFWK
y_5^{1+}	829.4031	829.4023	-1.0	WYFWK
y_6^{1+}	942.4872	942.4883	1.2	LWYFWK
y_7^{1+}	1057.5141	1057.5116	-2.4	DLWYFWK
y_8^{1+}	1171.5571	1171.5549	-1.9	NDLWYFWK
y_9^{1+}	-	-	-	VNDLWYFWK

Table S5.31. MS/MS fragment ions of peptide WILGSGH from trypsin digested MBP-EpeX$_{18\text{-}49}$ V4W labeled with [U-D$_{10}$]-L-Ile.

Ion	Calc. *m/z*	Obs. *m/z*	Δppm	Sequence
b_1^{1+}	187.0865	187.0861	-2.1	W
b_2^{1+} +9	309.2255	309.2268	4.2	WI
b_3^{1+} +9	422.3096	422.3108	2.8	WIL
b_4^{1+} +9	479.3310	Not Obs.	-	WILG

Table S5.31 Continued.

Ion	Calc. *m/z*	Obs. *m/z*	Δppm	Sequence
b_5^{1+} +9	566.3631	Not Obs.	-	WILGS
b_6^{1+} +9	623.3845	Not Obs.	-	WILGSG
b_7^{1+} +9	-	-	-	WILGSGH
y_1^{1+}	156.0767	156.0771	2.6	H
y_2^{1+}	213.0982	213.0982	0.0	GH
y_3^{1+}	300.1302	300.1294	-2.7	SGH
y_4^{1+}	357.1517	357.1518	0.3	GSGH
y_5^{1+}	470.2357	470.2364	1.5	LGSGH
y_6^{1+} +9	592.3747	592.3775	4.7	ILGSGH
y_7^{1+} +9	-		-	WILGSGH

Table S5.32. MS/MS fragment ions of peptide VNDLWYFVK from trypsin digested MBP-Epe$X_{18\text{-}49}$ I12W labeled with [3-D_1]-L-Val.

Ion	Calc. *m/z*	Obs. *m/z*	Δppm	Sequence
b_1^{1+} +1	101.0817	Not Obs.	-	V
b_2^{1+} +1	215.1247	215.1258	5.1	VN
b_3^{1+} +1	330.1516	330.1535	5.7	VND
b_4^{1+} +1	443.2357	443.2371	3.1	VNDL
b_5^{1+} +1	629.3150	629.3149	-0.1	VNDLW
b_6^{1+} +1	792.3783	792.3776	-0.9	VNDLWY
b_7^{1+} +1	939.4467	939.4545	8.3	VNDLWYF
b_8^{1+} +2	1039.5212	1039.5123	-8.5	VNDLWYFV
b_9^{1+} +2	-	-	-	VNDLWYFVK
y_1^{1+}	147.1128	147.1123	-3.4	K
y_2^{1+} +1	247.1873	247.1873	0.0	VK
y_3^{1+} +1	394.2557	394.2580	5.8	FVK
y_4^{1+} +1	557.3190	557.3199	1.6	YFVK
y_5^{1+} +1	743.3983	743.4021	5.1	WYFVK
y_6^{1+} +1	856.4824	856.4831	0.8	LWYFVK
y_7^{1+} +1	971.5093	971.5115	2.3	DLWYFVK
y_8^{1+} +1	1085.5523	1085.5547	2.2	NDLWYFVK
y_9^{1+} +2	-	-	-	VNDLWYFVK

References

1. Okeke, I. N.; de Kraker, M. E. A.; Van Boeckel, T. P.; Kumar, C. K.; Schmitt, H.; Gales, A. C.; Bertagnolio, S.; Sharland, M.; Laxminarayan, R., The scope of the antimicrobial resistance challenge. *The Lancet* **2024**, *403* (10442), 2426-2438.

2. Montalban-Lopez, M.; Scott, T. A.; Ramesh, S.; Rahman, I. R.; van Heel, A. J.; Viel, J. H.; Bandarian, V.; Dittmann, E.; Genilloud, O.; Goto, Y.; Grande Burgos, M. J.; Hill, C.; Kim, S.; Koehnke, J.; Latham, J. A.; Link, A. J.; Martinez, B.; Nair, S. K.; Nicolet, Y.; Rebuffat, S.; Sahl, H. G.; Sareen, D.; Schmidt, E. W.; Schmitt, L.; Severinov, K.; Sussmuth, R. D.; Truman, A. W.; Wang, H.; Weng, J. K.; van Wezel, G. P.; Zhang, Q.; Zhong, J.; Piel, J.; Mitchell, D. A.; Kuipers, O. P.; van der Donk, W. A., New developments in RiPP discovery, enzymology and engineering. *Nat Prod Rep* **2021**, *38* (1), 130-239.

3. Arnison, P. G.; Bibb, M. J.; Bierbaum, G.; Bowers, A. A.; Bugni, T. S.; Bulaj, G.; Camarero, J. A.; Campopiano, D. J.; Challis, G. L.; Clardy, J.; Cotter, P. D.; Craik, D. J.; Dawson, M.; Dittmann, E.; Donadio, S.; Dorrestein, P. C.; Entian, K. D.; Fischbach, M. A.; Garavelli, J. S.; Goransson, U.; Gruber, C. W.; Haft, D. H.; Hemscheidt, T. K.; Hertweck, C.; Hill, C.; Horswill, A. R.; Jaspars, M.; Kelly, W. L.; Klinman, J. P.; Kuipers, O. P.; Link, A. J.; Liu, W.; Marahiel, M. A.; Mitchell, D. A.; Moll, G. N.; Moore, B. S.; Muller, R.; Nair, S. K.; Nes, I. F.; Norris, G. E.; Olivera, B. M.; Onaka, H.; Patchett, M. L.; Piel, J.; Reaney, M. J.; Rebuffat, S.; Ross, R. P.; Sahl, H. G.; Schmidt, E. W.; Selsted, M. E.; Severinov, K.; Shen, B.; Sivonen, K.; Smith, L.; Stein, T.; Sussmuth, R. D.; Tagg, J. R.; Tang, G. L.; Truman, A. W.; Vederas, J. C.; Walsh, C. T.; Walton, J. D.; Wenzel, S. C.; Willey, J. M.; van der Donk, W. A., Ribosomally synthesized and post-translationally modified peptide natural products: overview and recommendations for a universal nomenclature. *Nat Prod Rep* **2013**, *30* (1), 108-60.

4. Pfeiffer, I. P.; Schroder, M. P.; Mordhorst, S., Opportunities and challenges of RiPP-based therapeutics. *Nat Prod Rep* **2024**, *41*, 990-1019.

5. Vagstad, A. L., Engineering ribosomally synthesized and posttranslationally modified peptides as new antibiotics. *Curr Opin Biotechnol* **2023**, *80*, 102891.

6. Do, T.; Link, A. J., Protein Engineering in Ribosomally Synthesized and Post-translationally Modified Peptides (RiPPs). *Biochemistry* **2023**, *62* (2), 201-209.

7. Ayikpoe, R. S.; Shi, C.; Battiste, A. J.; Eslami, S. M.; Ramesh, S.; Simon, M. A.; Bothwell, I. R.; Lee, H.; Rice, A. J.; Ren, H.; Tian, Q.; Harris, L. A.; Sarksian, R.; Zhu, L.; Frerk, A. M.; Precord, T. W.; van der Donk, W. A.; Mitchell, D. A.; Zhao, H., A scalable platform to discover antimicrobials of ribosomal origin. *Nat Commun* **2022**, *13* (1), 6135.

8. Ruijne, F.; Kuipers, O. P., Combinatorial biosynthesis for the generation of new-to-nature peptide antimicrobials. *Biochem Soc Trans* **2021**, *49* (1), 203-215.

9. Oman, T. J.; donk, W. a. v. d., Follow the leader: the use of leader peptides to guide natural product biosynthesis. *Nature Chemical Biology* **2010**, *6*, 9-18.

10. Popp, P. F.; Friebel, L.; Benjdia, A.; Guillot, A.; Berteau, O.; Mascher, T., The Epipeptide Biosynthesis Locus epeXEPAB Is Widely Distributed in Firmicutes and Triggers Intrinsic Cell Envelope Stress. *Microb Physiol* **2021**, *31* (3), 306-318.

11. Butcher, B. G.; Lin, Y. P.; Helmann, J. D., The yydFGHIJ operon of Bacillus subtilis encodes a peptide that induces the LiaRS two-component system. *J Bacteriol* **2007**, *189* (23), 8616-25.

12. Benjdia, A.; Guillot, A.; Ruffie, P.; Leprince, J.; Berteau, O., Post-translational modification of ribosomally synthesized peptides by a radical SAM epimerase in Bacillus subtilis. *Nat Chem* **2017**, *9* (7), 698-707.

13. Popp, P. F.; Benjdia, A.; Strahl, H.; Berteau, O.; Mascher, T., The Epipeptide YydF Intrinsically Triggers the Cell Envelope Stress Response of Bacillus subtilis and Causes Severe Membrane Perturbations. *Front Microbiol* **2020**, *11*.

14. Broderick, J. B.; Duffus, B. R.; Duschene, K. S.; Shepard, E. M., Radical S-adenosylmethionine enzymes. *Chem Rev* **2014**, *114* (8), 4229-317.

15. Nicolet, Y., Structure–function relationships of radical SAM enzymes. *Nature Catalysis* **2020**, *3* (4), 337-350.

16. Sofia, H. J.; Chen, G.; Hetzler, B. G.; Reyes-Spindola, J. F.; Miller, N. E., Radical SAM, a novel protein superfamily linking unresolved steps in familiar biosynthetic pathways with radical mechanisms: functional characterization using new analysis and information visualization methods. *Nucleic Acids Research* **2001**, *29* (5), 1097–1106.

17. Oberg, N.; Precord, T. W.; Mitchell, D. A.; Gerlt, J. A., RadicalSAM.org: A Resource to Interpret Sequence-Function Space and Discover New Radical SAM Enzyme Chemistry. *ACS Bio & Med Chem Au* **2022**, *2* (1), 22-35.

18. Krebs, C.; Henshaw, T. F.; Cheek, J.; Huynh, B. H.; Broderick, J. B., Conversion of 3Fe-4S to 4Fe-4S Clusters in Native Pyruvate Formate-Lyase Activating Enzyme: Mo¨ssbauer Characterization and Implications for Mechanism. *J. Am. Chem. Soc*. **2000**, *122* (50), 12497-12506.

19. Cheek, J.; Broderick, J. B., Adenosylmethionine-dependent iron-sulfur enzymes: versatile clusters in a radical new role. *Journal of Biological Inorganic Chemistry* **2001**, *6* (3), 209-226.

20. Walsby, C. J.; Ortillo, D.; Broderick, W. E.; Broderick, J. B.; Hoffman, B. M., An Anchoring Role for FeS Clusters: Chelation of the Amino Acid Moiety of *S*-Adenosylmethionine to the Unique Iron Site of the [4Fe-4S] Cluster of Pyruvate Formate-Lyase Activating Enzyme. *J Am Chem Soc* **2002**, *124*, 11270-11271.

21. Walsby, C. J.; Hong, W.; Broderick, W. E.; Cheek, J.; Ortillo, D.; Broderick, J. B.; Hoffman, B. M., Electron-Nuclear Double Resonance Spectroscopic Evidence That *S*-Adenosylmethionine Binds in Contact with the Catalytically Active $[4Fe\text{-}4S]^{+}$ Cluster of Pyruvate Formate-Lyase Activating Enzyme. *J Am Chem Soc* **2002**, *124*, 3143-3151.

22. Krebs, C.; Broderick, W. E.; Henshaw, T. F.; Broderick, J. B.; Huynh, B. H., Coordination of Adenosylmethionine to a Unique Iron Site of the [4Fe-4S] of Pyruvate Formate-Lyase Activating Enzyme: A Mossbauer Spectroscopic Study. *Journal of the American Chemical Society* **2002**, *124*, 912-913.

23. Horitani, M.; Shisler, K.; Broderick, W. E.; Hutcheson, R. U.; Duschene, K. S.; Marts, A. R.; Hoffman, B. M.; Broderick, J. B., Radical SAM catalysis via an organometallic intermediate with an Fe–[5′-C]-deoxyadenosyl bond. *Science* **2016**, *352* (6287), 822-824.

24. Pagnier, A.; Yang, H.; Jodts, R.; James, C.; Shepard, E. M.; Impano, S.; Broderick, W.; Hoffman, B. M.; Broderick, J. B., The Radical SAM enzyme Spore Photoproduct Lyase: Properties of the Omega Organometallic Intermediate and Identification of Stable Protein Radicals Formed During Substrate-Free Turnover. *J Am Chem Soc* **2020**, *142* (43), 18652–18660.

25. Byer, A. S.; Yang, H.; McDaniel, E. C.; Kathiresan, V.; Impano, S.; Pagnier, A.; Watts, H.; Denler, C.; Vagstad, A. L.; Piel, J.; Duschene, K. S.; Shepard, E. M.; Shields, T. P.; Scott, L. G.; Lilla, E. A.; Yokoyama, K.; Broderick, W. E.; Hoffman, B. M.; Broderick, J. B., Paradigm Shift for Radical *S*-Adenosyl-L-methionine Reactions: The Organometallic Intermediate Omega Is Central to Catalysis. *J Am Chem Soc* **2018**, *140* (28), 8634-8638.

26. Jodts, R. J.; Wittkop, M.; Ho, M. B.; Broderick, W. E.; Broderick, J. B.; Hoffman, B. M.; Mosquera, M. A., Computational Description of Alkylated Iron-Sulfur Organometallic Clusters. *J Am Chem Soc* **2023**, *145* (25), 13879-13887.

27. Henshaw, T. F.; Cheek, J.; Broderick, J. B., The $[4Fe\text{-}4S]^{1+}$ Cluster of Pyruvate Formate-Lyase Activating Enzyme Generates the Glycyl Radical on Pyruvate Formate-Lyase: EPR-Detected Single Turnover. *J Am Chem Soc* **2000**, *122*, 8331-8332.

28. Hoffman, B. M.; Broderick, W. E.; Broderick, J. B., Mechanism of Radical Initiation in the Radical SAM Enzyme Superfamily. *Annu Rev Biochem* **2023**, *92*, 333-349.

29. Broderick, J. B.; Broderick, W. E.; Hoffman, B. M., Radical SAM enzymes: Nature's choice for radical reactions. *FEBS Lett* **2023,** *597*, 92-101.

30. Broderick, W. E.; Hoffman, B. M.; Broderick, J. B., Mechanism of Radical Initiation in the Radical *S*-Adenosyl-L-methionine Superfamily. *Acc Chem Res* **2018**, *51* (11), 2611-2619.

31. Yang, H.; Ho, M. B.; Lundahl, M. N.; Mosquera, M. A.; Broderick, W. E.; Broderick, J. B.; Hoffman, B. M., ENDOR Spectroscopy Reveals the "Free" 5'-Deoxyadenosyl Radical in a Radical SAM Enzyme Active Site Actually is Chaperoned by Close Interaction with the Methionine-Bound [4Fe-4S](2+) Cluster. *J Am Chem Soc* **2024,** *146* (6), 3710-3720.

32. Lundahl, M. N.; Yang, H.; Broderick, W. E.; Hoffman, B. M.; Broderick, J. B., Pyruvate formate-lyase activating enzyme: The catalytically active 5'-deoxyadenosyl radical caught in the act of H-atom abstraction. *Proc Natl Acad Sci U S A* **2023**, *120* (47), e2314696120.

33. Lundahl, M. N.; Sarksian, R.; Yang, H.; Jodts, R. J.; Pagnier, A.; Smith, D. F.; Mosquera, M. A.; van der Donk, W. A.; Hoffman, B. M.; Broderick, W. E.; Broderick, J. B., Mechanism of Radical *S*-Adenosyl-L-methionine Adenosylation: Radical Intermediates and the Catalytic Competence of the 5'-Deoxyadenosyl Radical. *J Am Chem Soc* **2022**, *144* (11), 5087-5098.

34. Yang, H.; McDaniel, E. C.; Impano, S.; Byer, A. S.; Jodts, R. J.; Yokoyama, K.; Broderick, W. E.; Broderick, J. B.; Hoffman, B. M., The Elusive 5'-Deoxyadenosyl Radical: Captured and Characterized by Electron Paramagnetic Resonance and Electron Nuclear Double Resonance Spectroscopies. *J Am Chem Soc* **2019**, *141* (30), 12139-12146.

35. Horitani, M.; Byer, A. S.; Shisler, K. A.; Chandra, T.; Broderick, J. B.; Hoffman, B. M., Why Nature Uses Radical SAM Enzymes so Widely: Electron Nuclear Double Resonance Studies of Lysine 2,3-Aminomutase Show the 5'-dAdo "Free Radical" Is Never Free. *J Am Chem Soc* **2015**, *137* (22), 7111-21.

36. Zhu, W.; Walker, L. M.; Tao, L.; Iavarone, A. T.; Wei, X.; Britt, R. D.; Elliott, S. J.; Klinman, J. P., Structural Properties and Catalytic Implications of the SPASM Domain Iron-Sulfur Clusters in *Methylorubrum extorquens* PqqE. *J Am Chem Soc* **2020**, *142* (29), 12620-12634.

37. Grell, T. A.; Goldman, P. J.; Drennan, C. L., SPASM and twitch domains in *S*-adenosylmethionine (SAM) radical enzymes. *J Biol Chem* **2015**, *290* (7), 3964-71.

38. Rush, K. W.; Eastman, K. A. S.; Kincannon, W. M.; Blackburn, N. J.; Bandarian, V., Peptide Selenocysteine Substitutions Reveal Direct Substrate-Enzyme Interactions at Auxiliary Clusters in Radical *S*-Adenosyl-L-methionine Maturases. *J Am Chem Soc* **2023**, *145* (18), 10167–10177.

39. Eastman, K. A. S.; Jochimsen, A.; Bandarian, V., Intermolecular electron transfer in radical SAM enzymes as a new paradigm for reductive activation. *J Biol Chem* **2023**, 105058.

40. Kubiak, X.; Polsinelli, I.; Chavas, L. M. G.; Fyfe, C. D.; Guillot, A.; Fradale, L.; Brewee, C.; Grimaldi, S.; Gerbaud, G.; Thureau, A.; Legrand, P.; Berteau, O.; Benjdia, A., Structural and mechanistic basis for RiPP epimerization by a radical SAM enzyme. *Nat Chem Biol* **2023**, *20*, 382-391.

41. Benjdia, A.; Berteau, O., Radical SAM Enzymes and Ribosomally-Synthesized and Post-translationally Modified Peptides: A Growing Importance in the Microbiomes. *Front Chem* **2021**, *9*, 678068.

42. Vagstad, A. L.; Kuranaga, T.; Puntener, S.; Pattabiraman, V. R.; Bode, J. W.; Piel, J., Introduction of D-Amino Acids in Minimalistic Peptide Substrates by an *S*-Adenosyl-L-Methionine Radical Epimerase. *Angew Chem Int Ed Engl* **2019**, *58* (8), 2246-2250.

43. Walls, W. G.; Vagstad, A. L.; Delridge, T.; Piel, J.; Broderick, W. E.; Broderick, J. B., Direct Detection of the α-Carbon Radical Intermediate Formed by OspD: Mechanistic Insights into Radical *S*-Adenosyl-L-methionine Peptide Epimerization. *J Am Chem Soc* **2024**, *146* (8), 5550-5559.

44. Morinaka, B. I.; Verest, M.; Freeman, M. F.; Gugger, M.; Piel, J., An Orthogonal D_2O-Based Induction System that Provides Insights into D-Amino Acid Pattern Formation by Radical *S*-Adenosylmethionine Peptide Epimerases. *Angew Chem Int Ed Engl* **2017**, *56* (3), 762-766.

45. Korneli, M.; Fuchs, S. W.; Felder, K.; Ernst, C.; Zinsli, L. V.; Piel, J., Promiscuous Installation of D-Amino Acids in Gene-Encoded Peptides. *ACS Synth Biol* **2021**, *10* (2), 236-242.

46. Heller, C.; McConnell, H. M., Radiation Damage in Organic Crystals. II. Electron Spin Resonance of (CO2H)CH2CH(CO2H) in β-Succinic Acid. *The Journal of Chemical Physics* **1960**, *32* (5), 1535-1539.

47. Byer, A. S.; McDaniel, E. C.; Impano, S.; Broderick, W. E.; Broderick, J. B., Mechanistic Studies of Radical SAM Enzymes: Pyruvate Formate-Lyase Activating Enzyme and Lysine 2,3-Aminomutase Case Studies. *Methods in Enzymology* **2018**, *606*, 269-318.

48. LeMaster, D. M.; Richards, F. M., Preparative-Scale Isolation of Isotopically Labeled Amino Acids. *Anal Biochem* **1982**, *122*, 238-247.

49. Zor, T.; Selinger, Z., Linearization of the Bradford Protein Assay Increases Its Sensitivity: Theoretical and Experimental Studies. *Analytic Biochemistry* **1996**, *236*, 302-308.

50. Stoll, S.; Schweiger, A., EasySpin, a comprehensive software package for spectral simulation and analysis in EPR. *J. Magn. Res*. **2006**, *178* (1), 42-55.

CONCLUSION

Radical SAM enzymes form one of the largest superfamilies in Nature and are found in all kingdoms of life [1]. They are united by the use of a [4Fe-4S] cluster and SAM to generate a 5′-dAdo radical that regio- and stereoselectively abstracts a hydrogen atom from the substrate to initiate a myriad of chemical transformations [2-5]. Since the initial identification of the superfamily in 2001, which consisted of about 600 proteins, it has since grown to over 700,000 members due to advances in bioinformatics [6, 7]. The rate at which protein sequences are predicted outpaces the rate at which they are characterized, and only a fraction of characterized members have experimental evidence supporting their proposed catalytic mechanisms. Thus, this work has focused on trapping and characterizing radical intermediates formed by radical SAM enzymes to test proposed mechanisms, specifically those that catalyze post-translational modifications (PTMs) on glycyl radical enzymes (GREs) and ribosomally synthesized and post-translationally modified peptide (RiPP) natural products.

GRE Activation

Chapter Two focuses on elucidating the reductive cleavage product produced by GD-AE during glycyl radical installation on the GRE, GD [8]. A previous study reported that GD-AE cleaved the unconventional S-$C_{\gamma,\,Met}$ bond of SAM to yield 5′-deoxy-5′-methylthioadenosine (MTA) as the reductive cleavage product during GD activation [9]. To test this proposed result, we first expressed, purified, and reconstituted GD-AE and GD from *Clostridium butyricum*. GD-AE was shown to contain approx. 12 iron and acid-labile sulfide per monomer, consistent with

three [4Fe-4S] clusters. Electron paramagnetic resonance (EPR) spectroscopic characterization supported the assignment.

Assays to activate GD with GD-AE in the presence of SAM and sodium dithionite (NaDT) led to the production of 5′-dAdo, the expected SAM reductive cleavage product. Control reactions lacking any one of the reaction components resulted in small amounts of MTA but no production of 5′-dAdo. Time-dependent assays revealed formation of 5′-dAdo increasing with time when all reaction components were present, while MTA formation rates were the same independent of reaction components. These results were consistent with MTA being produced as a degradation product of SAM, and not a product of enzymatic activation of GD by GD-AE. Incubating GD and GD-AE in the presence of SAM and NaDT, then freezing and analyzing by EPR spectroscopy resulted in the observation of a glycyl radical on GD. Subsequent thawing of the sample and analysis by HPLC again led to the observation of 5′-dAdo and MTA, but 5′-dAdo was not present in a control reaction lacking GD-AE, while MTA was. Altogether, these results clearly demonstrate that GD-AE from *Clostridium butyricum* cleaves the S-C(5′) bond of SAM to produce 5′-dAdo, but not MTA, during the activation of GD.

RiPP Maturation

Chapter Four focuses on mechanistic studies of radical SAM enzymes (spliceases) involved in the maturation of the RiPP natural product spliceotides which feature α-keto-β^3 amides (ketoamides) [10]. Spliceotides are potent protease inhibitors and are widespread among the bacterial kingdom with some members possibly in archaea [11]. Spliceases act on a substrate XYG motif to catalyze excision of a “tyramine equivalent” with splicing of the peptide fragments to yield the ketoamide moiety [12]. The fate of the “tyramine equivalent” and the

reaction mechanism of the splicease enzyme are largely unknown and are the focus of this chapter.

The splicease PcpX from the cyanobacterial species *Pleurocapsa sp*. PCC 7327 was heterologously expressed, purified, and reconstituted. The reconstituted enzyme contained approx. 12 iron and acid-labile sulfide, consistent with three [4Fe-4S] cluster: one in the radical SAM domain, and two auxiliary [4Fe-4S] clusters in the predicted SPASM domain. EPR and UV-visible spectroscopic characterization of the enzyme were consistent with the assignment of [4Fe-4S] clusters. Major perturbations to the EPR spectrum were observed in the presence of SAM, consistent with binding to the radical SAM [4Fe-4S] cluster.

Isotopic labeling of the substrate protein, PcpA, revealed that the Cα of tyrosine in the XYG motif was the site of the initial H-atom abstraction of the 5′-dAdo radical. This was supported by deuterium transfer from the Tyr Cα position to 5′-dAdo during the reaction, and the observation of D-Tyr production resulting from non-specific quenching of a putative Tyr Cα radical. Accumulation of the D-Tyr intermediate was particularly pronounced at later timepoints, suggesting that production along the reaction coordinate to the on-path ketoamide product was inhibited, while abstraction of the Cα-H by the 5′-dAdo radical could still occur. Analysis of reaction products from other splicease homologs (referred to as types [11]) identified the production of para-hydroxybenzaldehyde that retained the ^{13}C-ring label derived from labeled tyrosine (in the XYG motif). This observation suggested that the released “tyramine equivalent” did not remain intact but instead fragments to form para-hydroxybenzaldehyde, presumably acquiring the aldehyde oxygen atom from water. The backbone carbon and nitrogen are currently hypothesized to leave as cyanide, however, all attempts to detect formation of cyanide have

failed [10]. Perhaps the released cyanide binds to one of the [4Fe-4S] clusters and inhibits formation of more ketoamide product and this may be why D-Tyr accumulates at later reaction time points.

The experimental results discussed above have led to two primary mechanistic proposals, both beginning with the formation of a Tyr Cα radical following H-atom abstraction by the 5′-dAdo radical. Pathway 1 involves formation of an acyl radical that undergoes a 1,3 migration to attack to the backbone carbonyl. Pathway 2 instead rearranges to form a cyclic azetine species that is proposed to coordinate the open coordination site on the AuxI [4Fe-4S] cluster. Both pathways then propose elimination of the "tyramine equivalent" with hydrolysis to yield 4-hydroxymandelonitrile which spontaneously eliminates cyanide to form para-hydroxybenzaldehyde. Energetic calculations of species along both pathways indicate the 1,3 acyl radical migration (pathway 1) is much higher in energy than formation of a cyclic intermediate (pathway 2). Thus, pathway 2 is the currently favored mechanistic proposal for ketoamide formation. While there is still much work to be done to understand this complex transformation, this study provides key insights that lay a foundation for future work.

Chapter Three focuses on the mechanistic investigations of the radical SAM peptide epimerase OspD, involved in the maturation of the proteusin RiPP natural product Landornamide A [13, 14]. OspD is responsible for epimerizing Ile4 and Val13 on the substrate OspA. The proposed mechanism begins with reductive cleavage of SAM to form Ω, which releases the 5′-dAdo radical to abstract an H-atom from the α-carbon (Cα) of Ile4 or Val13 to form a Cα radical intermediate. The Cα radical is then stereospecifically quenched on the opposite face of the peptide by a conserved Cys residue to yield the D-amino acid and a thiyl radical. The thiyl radical

is thought to be reductively quenched by proton coupled electron transfer via redox-active amino acids14. Work from our lab had previously trapped Ω at 500 ms following mixing of OspD, OspA, SAM, and NaDT [15]. This indicated that the putative Cα radical would likely be formed at times longer than 500 ms.

To trap and characterize the Cα radical, we constructed a mutant of OspD in which the quenching Cys334 was mutated to serine (Ser) which would provide a thermodynamic barrier to H-atom transfer because of the strong O-H bond. When this mutant was reacted with OspA, freeze quenched after 15 s, and analyzed by EPR spectroscopy, we observed a narrow doublet with a T_{opt} near 77 K, indicating a C-centered radical. This was consistent with a Cα radical on Ile4 or Val13, which would be coupled to Hβ and possibly the amide proton. The substrate OspA was expressed in minimal media to label Ile4 with [U-D_{10}]-L-Ile, and Val13 with [3-D_1]-L-Val, which would collapse any hyperfine coupling to the Cα radical. This experiment revealed that OspD C334S exclusively formed a Cα radical on Ile4 that best simulated with 61 MHz coupling to Hβ and 11 MHz coupling to the amide proton. The observation of a Cα radical only on Ile4 suggests an N-to-C directionality of the enzyme, consistent with previous activity assays where production of D-allo-Ile4 was observed prior to D-Val13 [16]. We were also able to trap the Cα radical during turnover with OspD WT by performing the reaction in buffered D_2O, and quenching at 13 s. The signal was weak, but could be simulated with parameters for the Ile4 Cα radical, indicating that the same mechanism for amino acid epimerization was operative in the WT and C334S OspD enzymes. In summary, these results provide the first experimental evidence of a peptidyl Cα radical formed by a radical SAM epimerase, allowing key insights into enzyme mechanism and directionality.

Chapter Five focuses on probing the mechanism of the radical SAM peptide epimerase EpeE during the biosynthesis of the RiPP natural product epipeptide. EpeE epimerizes Val4 and Ile12 on the substrate EpeX. These two epimerizations, along with proteolysis of the leader region, are the only PTMs to yield mature epipeptide. The proposed mechanism for amino acid epimerization by EpeE beings with reductive cleavage of SAM to form **Ω**, which releases the 5′-dAdo radical to abstract an H-atom from the Cα of Val4 or Ile12 to form a Cα radical intermediate. The Cα radical is then stereospecifically quenched on the opposite face of the peptide by Cys223 to yield the D-amino acid and a thiyl radical. The thiyl radical is thought to be reduced by the Aux [4Fe-4S] cluster with proton transfer from Asp210 [17]. We sought to test this proposed mechanism using a combination of time-resolved freeze quench EPR spectroscopy, enzyme activity assays, and site-directed mutagenesis.

A mutant of EpeE in which Cys223 was mutated to Ser223 was first prepared. Rapid freeze quench (RFQ) experiments were carried out between EpeE (WT or C223S), MBP-EpeX$_{18-49}$, SAM, and NaDT and quenched at 500 ms. **Ω** was observed for both EpeE WT and C223S catalyzed reactions. RFQ experiments with the C223S variant that were quenched at 1 s revealed formation of a second paramagnetic intermediate in addition to **Ω**. Thermal annealing allowed conversion of **Ω** into a putative substrate radical intermediate, further demonstrating its catalytic competence as an intermediate. Direct conversion of **Ω** into a substrate radical intermediate has only been observed following annealing of reactions with PFL-AE with the native substrate PFL or a peptide substrate mimic with a dehydroalanine residue in place of the target Gly residue [18, 19].

To better study the substrate radical formed by EpeE C223S on MBP-EpeX$_{18-49}$, reactions were quenched at 1 min. Analysis by EPR spectroscopy revealed a hyperfine coupled signal that collapsed to a characteristic doublet when the reaction was carried out in D_2O, suggesting a Cα radical was formed with strong coupling to the amide proton. EpeE C223S was then reacted with MBP-EpeX$_{18-49}$ that was isotopically labeled with [U-D_{10}]-L-Ile, [3-D_1]-L-Val, or both. Reactions with doubly labeled substrate caused collapse to a singlet, consistent with a radical being formed on Val4 or Ile12. Reactions with Val4 labeled substrate caused collapse to a singlet as well, but still contained some doublet character. Finally, reaction with labeled Ile12 caused minor perturbations to the EPR spectrum. Collectively, these results indicate that EpeE installs a Cα radical on both Val4 and Ile12 but with most of the spin on Val4. This result was very surprising, given than activity assays with EpeE show formation of D-allo-Ile12 precedes formation of D-Val4 [20].

Mutation of Val4 or Ile12 to tryptophan (Trp) effectively inhibited epimerization at that site while allowing the other epimerization site to still be acted on by EpeE, consistent with experiments between OspD and OspA [21]. Reaction of MBP-EpeX$_{18-49}$ I12W or V4W with EpeE C223S and analysis by EPR spectroscopy revealed Cα radicals were formed on both substrates but with distinct hyperfine coupling parameters and intensities. The Cα radical on Val4 was best simulated with 53 MHz coupling to Hβ and 24 MHz coupling to the amide proton, with a spin quantitation of 56 μM. Conversely, the Cα radical on Ile12 was best simulated with 42 MHz coupling to Hβ and 37 MHz coupling to the amide proton, with a spin quantitation of only 9 μM. Using the simulation parameters derived for each species, we were able to simulate the

EPR spectrum from reaction with WT MBP-EpeX$_{18-49}$ as being composed of 90% Val4 Cα radical and 10% Ile12 Cα radical.

Both Cα radicals exhibit significant hyperfine coupling to the amide proton indicating a deviation from planarity as β-hyperfine coupling is known to be dependent on the dihedral angle between the 2pπ orbital with the unpaired electron and the β-proton [22]. The hyperfine couplings to the amide protons for both Val4 and Ile12 Cα radicals are similar to those observed during the reaction of PFL-AE with peptide substrate mimics bearing the natural Gly residue or a dehydroalanine peptide. With the natural Gly residue, PFL-AE installs a Gly Cα radical with isotropic N-H coupling of 18 MHz [23], while reaction with the dehydroalanine containing peptide leads to adenosylation and formation of tertiary Cα radical with N-H coupling of 30 MHz [19]. This is contrast to natural glycyl radicals formed on GREs which are fully planarized and have minimal coupling to the amide proton, which maximizes delocalization and increases the stability of the radical [24, 25]. Therefore, the deviation from planarity observed for the Val4 and Ile12 Cα radicals on MBP-EpeX$_{18-49}$ indicates a decrease in stability and may relate to their reactivity. We also hypothesize that the difference in spin quantitation at each site is due to differential binding affinities of EpeE for those sites. A direct measurement of dissociation constants with truncated peptide substrates may be an approach to test this hypothesis.

Some homologs of EpeX encode Val in place of Ile at position 12 [26]. We therefore constructed a double mutant of MBP-EpeX$_{18-49}$ with both V4W and I12V mutations to remove contributions from the Val4 Cα radical. Reaction of this double substrate mutant with EpeE C223S revealed a Val12 Cα radical with simulation parameters and intensity almost identical to Ile12, but with a decreased coupling to Hβ from 42 to 37 MHz, suggesting a slight twisting of

the Val12 side chain. This allowed us to directly compare two Val Cα radicals that only differed by position on the core region of EpeX: one at position 4 and one at position 12. This clearly demonstrated that the conformation of the Cα radical in the enzyme active site was largely influenced by the core peptide region surrounding the epimerization site. Future work should focus on mutations to amino acids surrounding the epimerization site (position 4 or 12) and assess the effect on activity and Cα radical formation.

Time dependent freeze quench experiments were carried out by reacting EpeE C223S and MBP-EpeX$_{18\text{-}49}$ over a range of times from 10 s to 30 min. Maximum radical formation was observed at 1 min and had disappeared by 30 min. Spectral simulation revealed that the 1 min and 5 min quench times were composed of 90% Val4 Cα radical and 10% Ile12 Cα radical. Conversely, the 10 s quench time was best simulated with 80% Val4 Cα radical and 20% Ile12 Cα radical. The 30 s quench time was best simulated with 85% Val4 Cα radical and 15% Ile12 Cα radical. Spin quantitation using the simulation weights for both species indicated that the Ile12 Cα radical was formed maximally at 30 s and began to decrease by 1 min. Trypsin digestion and LC-MS analysis of the 1 min reaction revealed a small formation of D-allo-Ile12 but no detectable D-Val4 formation. These results indicate that the Val4 Cα radical builds to high concentrations and is quenched at later time points, while the Ile12 Cα radical only builds to modest levels and is quenched more readily to give D-allo-Ile12. These results provide some answers to the apparent discrepancy between the activity assay experiments with EpeE which show a preference for D-allo-Ile12 formation, with the EPR freeze quench results which reveal a clear preference for Cα radical installation on Val4. These results may have broader significance for other radical SAM enzymes involved in RiPP maturation where activity assays with LC-MS

detection are the standard method, and highlight the importance of utilizing EPR spectroscopy when studying mechanism.

The results presented in Chapters Three and Five highlight clear differences and similarities between proteusin epimerases (OspD) and epipeptide epimerases (EpeE). The proposed mechanism for both types of enzymes involves formation of **Ω**, abstraction of Hα to form a Cα radical intermediate, and stereospecific H-atom transfer from a conserved Cys residue to yield the D-amino acid. The mechanisms diverge in their proposals for thiyl radical quenching, yet both are based on proton-coupled electron transfer that's facilitated by redox-active amino acids (proteusins) or Aux [4Fe-4S] clusters (epipeptides). Here, we have provided spectroscopic evidence for the formation of **Ω**, and the formation of a Cα radical intermediate with both types of epimerases. Trapping the Cα radical with both epimerases was made possible by identification and mutation of the quenching Cys to Ser. While both OspD and EpeE epimerize Val and Ile residues, the Cα radicals formed display clear differences. The Ile4 Cα radical formed on OspA exhibited stronger coupling to Hβ and weaker coupling to N-H than the Ile12 Cα radical on EpeX, indicating the radicals are held in different conformations in their respective enzyme active sites. Why these differences exist and if they relate to reactivity awaits further characterization. Future work should focus on the formation and quenching of the putative thiyl radical (in both enzymes) following formation of the Cα radical.

In summary, this work has provided key insights into the mechanism of radical SAM enzymes involved in the post-translational modification of GREs and RiPP natural products. The identification of 5′-dAdo production instead of MTA by GD-AE has provided a correction to the literature. Spectroscopic characterization of the splicease enzyme PcpX has helped form a

mechanistic proposal for ketoamide formation that will aid future investigations. Finally, studies on peptide epimerization by OspD and EpeE has provided key insights into mechanism and directionality that will aid future efforts to further understand these enzymes, and bioengineering efforts to produce novel antiviral and antibacterial therapeutics.

References

1. Broderick, J. B.; Duffus, B. R.; Duschene, K. S.; Shepard, E. M., Radical *S*-adenosylmethionine enzymes. *Chem Rev* **2014**, *114* (8), 4229-317.

2. Hoffman, B. M.; Broderick, W. E.; Broderick, J. B., Mechanism of Radical Initiation in the Radical SAM Enzyme Superfamily. *Annu Rev Biochem* **2023**, *92*, 333-349.

3. Broderick, J. B.; Broderick, W. E.; Hoffman, B. M., Radical SAM enzymes: Nature's choice for radical reactions. *FEBS Lett* **2023**, *597*, 92-101.

4. Broderick, W. E.; Broderick, J. B., Radical SAM enzymes: surprises along the path to understanding mechanism. *J. Biol. Inorg. Chem*. **2019**, *24* (6), 769-776.

5. Broderick, W. E.; Hoffman, B. M.; Broderick, J. B., Mechanism of Radical Initiation in the Radical *S*-Adenosyl-L-methionine Superfamily. *Acc Chem Res* **2018**, *51* (11), 2611-2619.

6. Sofia, H. J.; Chen, G.; Hetzler, B. G.; Reyes-Spindola, J. F.; Miller, N. E., Radical SAM, a novel protein superfamily linking unresolved steps in familiar biosynthetic pathways with radical mechanisms: functional characterization using new analysis and information visualization methods. *Nucleic Acids Research* **2001**, *29* (5), 1097–1106.

7. Blum, M.; Andreeva, A.; Florentino, Laise C.; Chuguransky, Sara R.; Grego, T.; Hobbs, E.; Pinto, Beatriz L.; Orr, A.; Paysan-Lafosse, T.; Ponamareva, I.; Salazar, Gustavo A.; Bordin, N.; Bork, P.; Bridge, A.; Colwell, L.; Gough, J.; Haft, Daniel H.; Letunic, I.; Llinares-López, F.; Marchler-Bauer, A.; Meng-Papaxanthos, L.; Mi, H.; Natale, Darren A.; Orengo, Christine A.; Pandurangan, Arun P.; Piovesan, D.; Rivoire, C.; Sigrist, Christian J. A.; Thanki, N.; Thibaud-Nissen, F.; Thomas, Paul D.; Tosatto, Silvio C. E.; Wu, Cathy H.; Bateman, A., InterPro: the protein sequence classification resource in 2025. *Nucleic Acids Research* **2024**, *53* (D1), D444-D456.

8. Walls, W. G.; Moody, J. D.; McDaniel, E. C.; Villanueva, M.; Shepard, E. M.; Broderick, W. E.; Broderick, J. B., The B_{12}-independent glycerol dehydratase activating enzyme from *Clostridium butyricum* cleaves SAM to produce 5′-deoxyadenosine and not

5′-deoxy-5′-(methylthio)adenosine. *Journal of Inorganic Biochemistry* **2022**, *227*, 111662.

9. Demick, J. M.; Lanzilotta, W. N., Radical SAM activation of the B_{12}-independent glycerol dehydratase results in formation of 5'-deoxy-5'-(methylthio)adenosine and not 5'-deoxyadenosine. *Biochemistry* **2011**, *50* (4), 440-2.

10. Vagstad, A. L.; Lakis, E.; Csizi, K. S.; Walls, W.; Richter, D.; Soo Lee, K.; Stocker, R.; Gugger, M.; Broderick, W. E.; Broderick, J. B.; Reiher, M.; Piel, J., Mechanistic Insights Into Post-Translational α-Keto-β-Amino Acid Formation by a Radical *S*-Adenosyl Methionine Peptide Splicease. *Angew Chem Int Ed Engl* **2025**, e202418054.

11. Scott, T. A.; Verest, M.; Farnung, J.; Forneris, C. C.; Robinson, S. L.; Ji, X.; Hubrich, F.; Chepkirui, C.; Richter, D. U.; Huber, S.; Rust, P.; Streiff, A. B.; Zhang, Q.; Bode, J. W.; Piel, J., Widespread microbial utilization of ribosomal β-amino acid-containing peptides and proteins. *Chem* **2022**, *8* (10), 2659-2677.

12. Morinaka, B. I.; Lakis, E.; Verest, M.; Helf, M. J.; Scalvenzi, T.; Vagstad, A. L.; Sims, J.; Sunagawa, S.; Gugger, M.; Piel, J., Natural noncanonical protein splicing yields products with diverse β-amino acid residues. *Science* **2018**, *359*, 779-782.

13. Bosch, N. M.; Borsa, M.; Greczmiel, U.; Morinaka, B. I.; Gugger, M.; Oxenius, A.; Vagstad, A. L.; Piel, J., Landornamides: Antiviral Ornithine-Containing Ribosomal Peptides Discovered through Genome Mining. *Angew Chem Int Ed Engl* **2020**, *59* (29), 11763-11768.

14. Walls, W. G.; Vagstad, A. L.; Delridge, T.; Piel, J.; Broderick, W. E.; Broderick, J. B., Direct Detection of the α-Carbon Radical Intermediate Formed by OspD: Mechanistic Insights into Radical *S*-Adenosyl-L-methionine Peptide Epimerization. *J Am Chem Soc* **2024**, *146* (8), 5550-5559.

15. Byer, A. S.; Yang, H.; McDaniel, E. C.; Kathiresan, V.; Impano, S.; Pagnier, A.; Watts, H.; Denler, C.; Vagstad, A. L.; Piel, J.; Duschene, K. S.; Shepard, E. M.; Shields, T. P.; Scott, L. G.; Lilla, E. A.; Yokoyama, K.; Broderick, W. E.; Hoffman, B. M.; Broderick, J. B., Paradigm Shift for Radical *S*-Adenosyl-L-methionine Reactions: The Organometallic Intermediate **Ω** Is Central to Catalysis. *J Am Chem Soc* **2018**, *140* (28), 8634-8638.

16. Vagstad, A. L.; Kuranaga, T.; Puntener, S.; Pattabiraman, V. R.; Bode, J. W.; Piel, J., Introduction of d-Amino Acids in Minimalistic Peptide Substrates by an *S*-Adenosyl-L-Methionine Radical Epimerase. *Angew Chem Int Ed Engl* **2019**, *58* (8), 2246-2250.

17. Kubiak, X.; Polsinelli, I.; Chavas, L. M. G.; Fyfe, C. D.; Guillot, A.; Fradale, L.; Brewee, C.; Grimaldi, S.; Gerbaud, G.; Thureau, A.; Legrand, P.; Berteau, O.; Benjdia, A., Structural and mechanistic basis for RiPP epimerization by a radical SAM enzyme. *Nat Chem Biol* **2023**, *20*, 382-391.

18. Horitani, M.; Shisler, K.; Broderick, W. E.; Hutcheson, R. U.; Duschene, K. S.; Marts, A. R.; Hoffman, B. M.; Broderick, J. B., Radical SAM catalysis via an organometallic intermediate with an Fe–[5′-C]-deoxyadenosyl bond. *Science* **2016**, *352* (6287), 822-824.

19. Lundahl, M. N.; Sarksian, R.; Yang, H.; Jodts, R. J.; Pagnier, A.; Smith, D. F.; Mosquera, M. A.; van der Donk, W. A.; Hoffman, B. M.; Broderick, W. E.; Broderick, J. B., Mechanism of Radical *S*-Adenosyl-L-methionine Adenosylation: Radical Intermediates and the Catalytic Competence of the 5'-Deoxyadenosyl Radical. *J Am Chem Soc* **2022**, *144* (11), 5087-5098.

20. Benjdia, A.; Guillot, A.; Ruffie, P.; Leprince, J.; Berteau, O., Post-translational modification of ribosomally synthesized peptides by a radical SAM epimerase in *Bacillus subtilis*. *Nat Chem* **2017**, *9* (7), 698-707.

21. Korneli, M.; Fuchs, S. W.; Felder, K.; Ernst, C.; Zinsli, L. V.; Piel, J., Promiscuous Installation of D-Amino Acids in Gene-Encoded Peptides. *ACS Synth Biol* **2021**, *10* (2), 236-242.

22. Heller, C.; McConnell, H. M., Radiation Damage in Organic Crystals. II. Electron Spin Resonance of (CO2H)CH2CH(CO2H) in β-Succinic Acid. *The Journal of Chemical Physics* **1960**, *32* (5), 1535-1539.

23. Lundahl, M. N.; Yang, H.; Broderick, W. E.; Hoffman, B. M.; Broderick, J. B., Pyruvate formate-lyase activating enzyme: The catalytically active 5'-deoxyadenosyl radical caught in the act of H-atom abstraction. *Proc Natl Acad Sci U S A* **2023**, *120* (47), e2314696120.

24. Duboc-Toia, C.; Hassan, A. K.; Mulliez, E.; Choudens, S. O.-d.; Fontecave, M.; Leutwein, C.; Heider, J., Very High-Field EPR Study of Glycyl Radical Enzymes. *J Am Chem Soc* **2003**, *125*, 38-39.

25. Hioe, J.; Savasci, G.; Brand, H.; Zipse, H., The stability of Cα peptide radicals: why glycyl radical enzymes? *Chemistry* **2011**, *17* (13), 3781-9.

26. Popp, P. F.; Friebel, L.; Benjdia, A.; Guillot, A.; Berteau, O.; Mascher, T., The Epipeptide Biosynthesis Locus epeXEPAB Is Widely Distributed in Firmicutes and Triggers Intrinsic Cell Envelope Stress. *Microb Physiol* **2021**, *31* (3), 306-318.

CUMULATIVE REFERENCES CITED

Andorfer, M. C.; Backman, L. R. F.; Li, P. L.; Ulrich, E. C.; Drennan, C. L., Rescuing activity of oxygen-damaged pyruvate formate-lyase by a spare part protein. *J Biol Chem* **2021**, *297* (6), 101423.

Arasappan, A. et al. Discovery of narlaprevir (SCH 900518): a potent, second generation HCV NS3 serine protease inhibitor. *ACS Med. Chem. Lett* **2010**, *1*, 64–69.

Arcinas, A. J.; Maiocco, S. J.; Elliott, S. J.; Silakov, A.; Booker, S. J., Ferredoxins as interchangeable redox components in support of MiaB, a radical *S*-adenosylmethionine methylthiotransferase. *Protein Sci* **2019**, *28* (1), 267-282.

Arnison, P. G.; Bibb, M. J.; Bierbaum, G.; Bowers, A. A.; Bugni, T. S.; Bulaj, G.; Camarero, J. A.; Campopiano, D. J.; Challis, G. L.; Clardy, J.; Cotter, P. D.; Craik, D. J.; Dawson, M.; Dittmann, E.; Donadio, S.; Dorrestein, P. C.; Entian, K. D.; Fischbach, M. A.; Garavelli, J. S.; Goransson, U.; Gruber, C. W.; Haft, D. H.; Hemscheidt, T. K.; Hertweck, C.; Hill, C.; Horswill, A. R.; Jaspars, M.; Kelly, W. L.; Klinman, J. P.; Kuipers, O. P.; Link, A. J.; Liu, W.; Marahiel, M. A.; Mitchell, D. A.; Moll, G. N.; Moore, B. S.; Muller, R.; Nair, S. K.; Nes, I. F.; Norris, G. E.; Olivera, B. M.; Onaka, H.; Patchett, M. L.; Piel, J.; Reaney, M. J.; Rebuffat, S.; Ross, R. P.; Sahl, H. G.; Schmidt, E. W.; Selsted, M. E.; Severinov, K.; Shen, B.; Sivonen, K.; Smith, L.; Stein, T.; Sussmuth, R. D.; Tagg, J. R.; Tang, G. L.; Truman, A. W.; Vederas, J. C.; Walsh, C. T.; Walton, J. D.; Wenzel, S. C.; Willey, J. M.; van der Donk, W. A., Ribosomally synthesized and post-translationally modified peptide natural products: overview and recommendations for a universal nomenclature. *Nat Prod Rep* **2013**, *30* (1), 108-60.

Ayikpoe, R. S.; Shi, C.; Battiste, A. J.; Eslami, S. M.; Ramesh, S.; Simon, M. A.; Bothwell, I. R.; Lee, H.; Rice, A. J.; Ren, H.; Tian, Q.; Harris, L. A.; Sarksian, R.; Zhu, L.; Frerk, A. M.; Precord, T. W.; van der Donk, W. A.; Mitchell, D. A.; Zhao, H., A scalable platform to discover antimicrobials of ribosomal origin. *Nat Commun* **2022**, *13* (1), 6135.

Ayikpoe, R. S.; Zhu, L.; Chen, J. Y.; Ting, C. P.; van der Donk, W. A., Macrocyclization and Backbone Rearrangement During RiPP Biosynthesis by a SAM-Dependent Domain-of-Unknown-Function 692. *ACS Cent Sci* **2023**, *9* (5), 1008-1018.

Ayikpoe, R. S.; van der Donk, W. A., Chapter Eighteen - Peptide backbone modifications in lanthipeptides. In *Methods in Enzymology*, Petersson, E. J., Ed. Academic Press: **2021**; Vol. *656*, pp 573-621.

Ayikpoe, R.; Ngendahimana, T.; Langton, M.; Bonitatibus, S.; Walker, L. M.; Eaton, S. S.; Eaton, G. R.; Pandelia, M. E.; Elliott, S. J.; Latham, J. A., Spectroscopic and Electrochemical Characterization of the Mycofactocin Biosynthetic Protein, MftC, Provides Insight into Its Redox Flipping Mechanism. *Biochemistry* **2019**, *58* (7), 940-950.

Ayikpoe, R.; Salazar, J.; Majestic, B.; Latham, J. A., Mycofactocin Biosynthesis Proceeds through 3-Amino-5-[(p-hydroxyphenyl)methyl]-4,4-dimethyl-2-pyrrolidinone (AHDP); Direct Observation of MftE Specificity toward MftA. *Biochemistry* **2018**, *57* (37), 5379-5383.

Backman, L. R. F.; Funk, M. A.; Dawson, C. D.; Drennan, C. L., New tricks for the glycyl radical enzyme family. *Crit Rev Biochem Mol Biol* **2017**, *52* (6), 674-695.

Balo, A. R.; Caruso, A.; Tao, L.; Tantillo, D. J.; Seyedsayamdost, M. R.; Britt, R. D., Trapping a cross-linked lysine–tryptophan radical in the catalytic cycle of the radical SAM enzyme SuiB. *Proc. Natl. Acad. Sci. U.S.A.* **2021**, *118* (21), e2101571118.

Balty, C.; Guillot, A.; Fradale, L.; Brewee, C.; Lefranc, B.; Herrero, C.; Sandström, C.; Leprince, J.; Berteau, O., Biosynthesis of the sactipeptide Ruminococcin C by the human microbiome: Mechanistic insights into thioether bond formation by radical SAM enzymes. *J. Biol. Chem*. **2020**, *295* (49), 16665-16677.

Barr, I.; Latham, J. A.; Iavarone, A. T.; Chantarojsiri, T.; Hwang, J. D.; Klinman, J. P., Demonstration that the radical S-adenosylmethionine (SAM) enzyme PqqE Catalyzes de Novo carbon-carbon cross-linking within a peptide substrate PqqA in the presence of the peptide chaperone PqqD. *J. Biol. Chem*. **2016**, *291* (17), 8877-8884.

Barr, I.; Stich, T. A.; Gizzi, A. S.; Grove, T. L.; Bonanno, J. B.; Latham, J. A.; Chung, T.; Wilmot, C. M.; Britt, R. D.; Almo, S. C.; Klinman, J. P., X-ray and EPR Characterization of the Auxiliary Fe-S Clusters in the Radical SAM Enzyme PqqE. *Biochemistry* **2018**, *57* (8), 1306-1315.

Bateman, R. C., Youngblood, W. W., Busby, W. H. & Kizer, J. S. Nonenzymatic peptide alpha-amidation. Implications for a novel enzyme mechanism. *J. Biol. Chem*. **1985**, *260*, 9088–9091.

Beinert, H. Semi-micro methods for analysis of labile sulfide and of labile sulfide plus sulfane sulfur in unusually stable iron-sulfur proteins. *Anal. Biochem*. **1983**, *131*, 373–378.

Benjdia, A., Guillot, A., Ruffié, P., Leprince, J. & Berteau, O. Post-translational modification of ribosomally synthesized peptides by a radical SAM epimerase in Bacillus subtilis. *Nat. Chem*. **2017**, *9*, 698–707.

Benjdia, A.; Balty, C.; Berteau, O., Radical SAM Enzymes in the Biosynthesis of Ribosomally Synthesized and Post-translationally Modified Peptides (RiPPs). *Front Chem* **2017**, *5*, 87.

Benjdia, A.; Guillot, A.; Lefranc, B.; Vaudry, H.; Leprince, J.; Berteau, O., Thioether bond formation by SPASM domain radical SAM enzymes: Cα H-atom abstraction in subtilosin A biosynthesis. *Chem. Commun*. **2016**, *52*, 6249-6252.

Benjdia, A.; Guillot, A.; Ruffie, P.; Leprince, J.; Berteau, O., Post-translational modification of ribosomally synthesized peptides by a radical SAM epimerase in Bacillus subtilis. *Nat Chem* **2017**, *9* (7), 698-707.

Benjdia, A.; Berteau, O., Radical SAM Enzymes and Ribosomally-Synthesized and Post-translationally Modified Peptides: A Growing Importance in the Microbiomes. *Front Chem* **2021**, *9*, 678068.

Besandre, R. A.; Chen, Z.; Davis, I.; Zhang, J.; Ruszczycky, M. W.; Liu, A.; Liu, H.-w., HygY is a twitch radical SAM epimerase with latent dehydrogenase activity revealed upon mutation of a single cysteine residue. *J. Am. Chem. Soc*. **2021**, *143* (37), 15152-15158.

Bianchi, V.; Eliasson, R.; Fontecave, M.; Mulliez, E.; Hoover, D. M.; Matthews, R. G.; Reichard, P., Flavodoxin Is Required for the Activation of the Anaerobic Ribonucleotide Reductase. *Biochemical and Biophysical Research Communications* **1993**, *197* (2), 792-797.

Blum, M.; Andreeva, A.; Florentino, Laise C.; Chuguransky, Sara R.; Grego, T.; Hobbs, E.; Pinto, Beatriz L.; Orr, A.; Paysan-Lafosse, T.; Ponamareva, I.; Salazar, Gustavo A.; Bordin, N.; Bork, P.; Bridge, A.; Colwell, L.; Gough, J.; Haft, Daniel H.; Letunic, I.; Llinares-López, F.; Marchler-Bauer, A.; Meng-Papaxanthos, L.; Mi, H.; Natale, Darren A.; Orengo, Christine A.; Pandurangan, Arun P.; Piovesan, D.; Rivoire, C.; Sigrist, Christian J. A.; Thanki, N.; Thibaud-Nissen, F.; Thomas, Paul D.; Tosatto, Silvio C. E.; Wu, Cathy H.; Bateman, A., InterPro: the protein sequence classification resource in 2025. *Nucleic Acids Research* **2024**, *53* (D1), D444-D456.

Bobeica, S. C. et al. Insights into AMS/PCAT transporters from biochemical and structural characterization of a double Glycine motif protease. *eLife* **2019**, *8*, e42305.

Bode, H. B.; Reimer, D.; Fuchs, S. W.; Kirchner, F.; Dauth, C.; Kegler, C.; Lorenzen, W.; Brachmann, A. O.; Grün, P., Determination of the absolute configuration of peptide natural products by using stable isotope labeling and mass spectrometry. *Chem. Eur. J.* **2012**, *18*, 2342-2348.

Bösch, N. M.; Borsa, M.; Greczmiel, U.; Morinaka, B. I.; Gugger, M.; Oxenius, A.; Vagstad, A. L.; Piel, J., Landornamides: Antiviral Ornithine-Containing Ribosomal Peptides Discovered through Genome Mining. *Angew Chem Int Ed Engl* **2020**, *59* (29), 11763-11768.

Bowman, S. E. J.; Backman, L. R. F.; Bjork, R. E.; Andorfer, M. C.; Yori, S.; Caruso, A.; Stultz, C. M.; Drennan, C. L., Solution structure and biochemical characterization of a spare part protein that restores activity to an oxygen-damaged glycyl radical enzyme. *J Biol Inorg Chem* **2019**, *24* (6), 817-829.

Bradford, M. M., A rapid and sensitive method for the quantitation of microgram quantities of protein utilizing the principle of protein-dye binding. *Anal. Biochem*. **1976**, *72*, 248-254.

Bridwell-Rabb, J.; Grell, T. A. J.; Drennan, C. L., A rich man, poor man story of *S*-adenosylmethionine and cobalamin revisited. *Annu. Rev. Biochem*. **2018**, *87*, 555-584.

Britt, R. D., Tao, L., Rao, G., Chen, N. & Wang, L.-P. Proposed mechanism for the biosynthesis of the [FeFe] hydrogenase H-cluster: central roles for the radical SAM enzymes HydG and HydE. *ACS Bio. Med. Chem. Au* **2021**, *2*, 11–21.

Broderick, J. B.; Broderick, W. E.; Hoffman, B. M., Radical SAM enzymes: Nature's choice for radical reactions. *FEBS Lett* **2023,** *597*, 92-101.

Broderick, J. B.; Duffus, B. R.; Duschene, K. S.; Shepard, E. M., Radical *S*-Adenosylmethionine Enzymes. *Chem. Rev*. **2014**, *114*, 4229-4317.

Broderick, J. B.; Henshaw, T. F.; Cheek, J.; Wojtuszewski, K.; Smith, S. R.; Trojan, M. R.; McGhan, R. M.; Kopf, A.; Kibbey, M.; Broderick, W. E., Pyruvate formate-lyase activating enzyme: strictly anaerobic isolation yields active enzyme containing a [3Fe-4S]$^{+}$ cluster. *Biochem. Biophys. Res. Comm*. **2000**, *269*, 451-456.

Broderick, W. E.; Hoffman, B. M.; Broderick, J. B., Mechanism of Radical Initiation in the Radical *S*-Adenosyl-L-methionine Superfamily. *Acc. Chem. Res*. **2018**, *51* (11), 2611-2619.

Broderick, W. E.; Broderick, J. B., Radical SAM enzymes: surprises along the path to understanding mechanism. *J. Biol. Inorg. Chem*. **2019**, *24* (6), 769-776.

Brown, A. C.; Suess, D. L. M., Reversible Formation of Alkyl Radicals at [Fe_4S_4] Clusters and Its Implications for Selectivity in Radical SAM Enzymes. *J Am Chem Soc* **2020**, *142* (33), 14240-14248.

Bruender, N. A.; Wilcoxen, J.; Britt, R. D.; Bandarian, V., Biochemical and Spectroscopic Characterization of a Radical *S*-Adenosyl-L-methionine Enzyme Involved in the Formation of a Peptide Thioether Cross-Link. *Biochemistry* **2016**, *55* (14), 2122-34.

Bruender, N. A.; Young, A. P.; Bandarian, V., Chemical and Biological Reduction of the Radical SAM Enzyme 7-Carboxy-7-deazaguanine Synthase. *Biochemistry* **2015**, *54* (18), 2903-10.

Bruender, N. A.; Bandarian, V., SkfB abstracts a hydrogen atom from Cα on SkfA to initiate thioether cross-link formation. *Biochemistry* **2016**, *55* (30), 4131-4134.

Burkhart, B. J., Hudson, G. A., Dunbar, K. L. & Mitchell, D. A. A prevalent peptide-binding domain guides ribosomal natural product biosynthesis. *Nat. Chem. Biol*. **2015**, *11*, 564–570.

Bushin, L. B.; Clark, K. A.; Pelczer, I.; Seyedsayamdost, M. R., Charting an Unexplored Streptococcal Biosynthetic Landscape Reveals a Unique Peptide Cyclization Motif. *J Am Chem Soc* **2018**, *140* (50), 17674-17684.

Bushin, L. B.; Covington, B. C.; Rued, B. E.; Federle, M. J.; Seyedsayamdost, M. R., Discovery and biosynthesis of streptosactin, a sactipeptide with an alternative topology encoded by commensal bacteria in the human microbiome. *J. Am. Chem. Soc*. **2020**, *142* (38), 16265-16275.

Butcher, B. G.; Lin, Y. P.; Helmann, J. D., The yydFGHIJ operon of Bacillus subtilis encodes a peptide that induces the LiaRS two-component system. *J Bacteriol* **2007**, *189* (23), 8616-25.

Byer, A. S.; McDaniel, E. C.; impano, S.; Broderick, W. E.; Broderick, J. B., Mechanistic Studies of Radical SAM Enzymes: Pyruvate Formate-Lyase Activating Enzyme and Lysine 2,3-Aminomutase Case Studies. *Methods Enzymol*. **2018**, *606*, 269-318.

Byer, A. S.; Yang, H.; McDaniel, E. C.; Kathiresan, V.; impano, S.; Pagnier, A.; Watts, H.; Denler, C.; Vagstad, A. L.; Piel, J.; Duschene, K. S.; Shepard, E. M.; Shields, T. P.; Scott, L. G.; Lilla, E. A.; Yokoyama, K.; Broderick, W. E.; Hoffman, B. M.; Broderick, J. B., Paradigm shift for radical *S*-adenosyl-L-methionine reactions: The organometallic intermediate Ω is central to catalysis. *J. Am. Chem. Soc*. **2018**, *140* (28), 8634-8638.

Castenholz, R. W. Portrait of a geothermal spring, Hunter's Hot Springs, Oregon. *Life* **2015**, *5*, 332–347.

Chandra, T.; Silver, S. C.; Zilinskas, E.; Shepard, E. M.; Broderick, W. E.; Broderick, J. B., Spore Photoproduct Lyase Catalyzes Specific Repair of the 5R but Not the 5S Spore Photoproduct *J. Am. Chem. Soc*. **2009**, *131* (7), 2420-2421.

Cheek, J.; Broderick, J. B., Adenosylmethionine-dependent iron-sulfur enzymes: versatile clusters in a radical new role. *Journal of Biological Inorganic Chemistry* **2001**, *6* (3), 209-226.

Chen, D., Scopelliti, R. & Hu, X. Synthesis and reactivity of iron acyl complexes modeling the active site of [Fe]-hydrogenase. *J. Am. Chem. Soc*. **2010**, *132*, 928–929.

Clark, K. A.; Seyedsayamdost, M. R., Bioinformatic Atlas of Radical SAM Enzyme-Modified RiPP Natural Products Reveals an Isoleucine-Tryptophan Crosslink. *J Am Chem Soc* **2022,** *144* (39), 17876–17888.

Cogan, D. P.; Bhushan, A.; Reyes, R.; Zhu, L.; Piel, J.; Nair, S. K., Structure and mechanism for iterative amid N-methylation in the biosynthesis of channel-forming peptide cytotoxins. *Proc. Natl. Acad. Sci. U. S. A*. **2022**, *119* (13), e2116578119.

Cooper, S.; Khatib, F.; Treuille, A.; Barbero, J.; Lee, J.; Beenen, M.; Leaver-Fay, A.; Baker, D.; Popovic, Z.; Players, F., Predicting protein structures with a multiplayer online game. *Nature* **2010**, *466*, 756-760.

Crain, A. V.; Broderick, J. B., Flavodoxin cofactor binding induces structural changes that are required for protein-protein interactions with NADP(+) oxidoreductase and pyruvate formate-lyase activating enzyme. *Biochim Biophys Acta* **2013**, *1834* (12), 2512-9.

Dauter, Z.; Wilson, K. S.; Sieker, L. C.; Meyer, J.; Moulis, J.-M., Atomic resolution (0.94Å) structure of *Clostridium acidurici* ferredoxin. Detailed geometry of [4Fe-4S] clusters in a protein. *Biochemistry* **1997**, *36* (51), 16065-16073.

Davis, K. M.; Schramma, K. R.; Hansen, W. A.; Bacik, J. P.; Khare, S. D.; Seyedsayamdost, M. R.; Ando, N. Structures of the peptide-modifying radical SAM enzyme SuiB elucidate the basis of substrate recognition. *Proc. Natl. Acad. Sci. USA* **2017**, *114* (39), 10420-10425.

Demick, J. M.; Lanzilotta, W. N., Radical SAM activation of the B_{12}-independent glycerol dehydratase results in formation of 5'-deoxy-5'-(methylthio)adenosine and not 5'-deoxyadenosine. *Biochemistry* **2011**, *50*, 440-442.

Desport, J. S., Frache, G. & Patiny, L. MSPolyCalc: A web-based App for polymer mass spectrometry data interpretation. The case study of a pharmaceutical excipient. *Rapid Commun. Mass Spectrom.* **2020**, *34*, e8652.

Do, T.; Link, A. J., Protein Engineering in Ribosomally Synthesized and Post-translationally Modified Peptides (RiPPs). *Biochemistry* **2023**, *62* (2), 201-209.

Dong, M.; Horitani, M.; Dzikovski, B.; Freed, J. H.; Ealick, S. E.; Hoffman, B. M.; Lin, H., Substrate-dependent cleavage site selection by unconventional radical *S*-adenosylmethionine enzymes in diphthamide biosynthesis. *J. Am. Chem. Soc*. **2017**, *139*, 5680-5683.

Dong, M.; Horitani, M.; Dzikovski, B.; Pandelia, M.-E.; Krebs, C.; Freed, J. H.; Hoffman, B. M.; Lin, H., Organometallic complex formed by an unconventional radical *S*-adenosylmethionine enzyme. *J. Am. Chem. Soc*. **2016**, *138*, 9755-9758.

Dong, M.; Kathiresan, V.; Fenwick, M. K.; Torelli, A. T.; Zhang, Y.; Caranto, J.; Dzikovski, B.; Sharma, A.; Lancaster, K. M.; Freed, J. H.; Ealick, S. E.; Hoffman, B. M.; Lin, H., Organometallic and radical intermediates reveal mechanism of diphthamide biosynthesis. *Science* **2018**, *359* (6381), 1247-1250.

Dong, M.; Su, X.; Dzikovski, B.; Dando, E. E.; Zhu, X.; Du, J.; Freed, J. H.; Lin, H., Dph3 is an electron donor for Dph1-Dph2 in the first step of eukaryotic diphthamide biosynthesis. *J. Am. Chem. Soc*. **2014**, *136* (5), 1754-1757.

Duboc-Toia, C.; Hassan, A. K.; Mulliez, E.; Choudens, S. O.-d.; Fontecave, M.; Leutwein, C.; Heider, J., Very High-Field EPR Study of Glycyl Radical Enzymes. *J Am Chem Soc* **2003**, *125*, 38-39.

Eastman, K. A. S.; Jochimsen, A.; Bandarian, V., Intermolecular electron transfer in radical SAM enzymes as a new paradigm for reductive activation. *J Biol Chem* **2023**, *299* (9), 105058.

Emsley, P.; Lohkamp, B.; Scott, W. G.; Cowtan, K., Features and development of Coot. *Acta Cryst D* **2010**, *66*, 486-501.

F. Madeira, M. Pearce, A. R. N. Tivey, P. Basutkar, J. Lee, O. Edbali, N. Madhusoodanan, A. Kolesnikov, R. Lopez, *Nucleic Acids Res*. **2022**, *50*, W276–W279.

Fan, P.-H.; Geng, Y.; Romo, A. J.; Zhong, A.; Zhang, J.; Yeh, Y.-C.; Lee, Y.-H.; Liu, H.-w., Two radical SAM enzymes are necessary and sufficient for the in vitro production of the oxetane nucleoside antiviral agent albucidin. *Angew. Chem. Int. Ed*. **2022**, *61* (42), e202210362.

Feng, Z.; Ogasawara, Y.; Dairi, T., Identification of the peptide epimerase MslH responsible for D-amino acid introduction at the C-terminus of ribosomal peptides. *Chem Sci* **2020**, *12* (7), 2567-2574.

Feng, Z.; Xu, B., Inspiration from the mirror: D-amino acid containing peptides in biomedical approaches. *BioMol. Concepts* **2016**, *7* (3), 179-187.

Fish, W. W. Rapid colorimetric micromethod for the quantitation of complexed iron in biological samples. *Methods Enzymol*. **1988**, *158*, 357–364.

Fleishman, S. J.; Leaver-Fay, A.; Corn, J. E.; Strauch, E.-M.; Khare, S. D.; Koga, N.; Ashworth, J.; Murphy, P.; Richter, F.; Lemmon, G.; Meiler, J.; Baker, D., RosettaScripts: A scripting language interface to the Rosetta macromolecular modeling suite. *PLoS ONE* **2011**, *6* (6), e20161.

Freeman, M. F.; Gurgui, C.; Helf, M. J.; Morinaka, B. I.; Uria, A. R.; Oldham, N. J.; Sahl, H.-G.; Matsunaga, S.; Piel, J., Metagenome Mining Reveals Polytheonamides as Posttranslationally Modified Ribosomal Peptides. *Science* **2012**, *338* (6105), 387-390.

Freeman, M. F.; Helf, M. J.; Bhushan, A.; Morinaka, B. I.; Piel, J., Seven enzymes create extraordinary molecular complexity in an uncultivated bacterium. *Nat Chem* **2017**, *9* (4), 387-395.

Frey, M.; Rothe, M.; Wagner, A. F. V.; Knappe, J., Adenosylmethionine-dependent synthesis of the glycyl radical in pyruvate formate-lyase by abstraction of the glycine C-2 pro-*S* hydrogen atom. *J. Biol. Chem*. **1994**, *269* (17), 12432-12437.

Frey, P. A.; Hegeman, A. D.; Ruzicka, F. J., The radical SAM superfamily. *Crit. Rev. Biochem. Mol. Biol.* **2008**, *43* (1), 63-88.

Frey, S. & Görlich, D. A new set of highly efficient, tag-cleaving proteases for purifying recombinant proteins. *J. Chromatogr. A* **2014**, *1337*, 95–105.

Fu, B.; Yang, H.; Kountz, D. J.; Lundahl, M. N.; Beller, H. R.; Broderick, W. E.; Broderick, J. B.; Hoffman, B. H.; Balskus, E. P., Discovery of a New Class of Aminoacyl Radical Enzymes Expands Nature's Known Radical Chemistry. *J Am Chem Soc* **2024,** *146* (43), 29645–29655.

Fu, Y.; Jaarsma, A. H.; Kuipers, O. P., Antiviral activities and applications of ribosomally synthesized and post-translationally modified peptides (RiPPs). *Cell Mol Life Sci* **2021**, *78* (8), 3921-3940.

Fujii, K., Ikai, Y., Oka, H., Suzuki, M. & Harada, K. A nonempirical method using LC/MS for determination of the absolute configuration of constituent amino acids in a peptide: combination of Marfey's method with mass spectrometry and its practical application. *Anal. Chem*. **1997**, *69*, 5146–5151.

Fusetani, N., Sugawara, T., Matsunaga, S. & Hirota, H. Orbiculamide A: a novel cytotoxic cyclic peptide from a marine sponge Theonella sp. *J. Am. Chem. Soc*. **1991**, *113*, 7811–7812.

Gallagher, M. E., Mayhew, S. G., Malthouse, J. P. & Fillat, M. F. Cyanylation of the thiol of the cysteine of flavodoxin from Anabaena PCC 7119. *Biochem. Soc. Trans*. **1996**, *24*, 40S.

Gasteiger, E. et al. Protein Identification and Analysis Tools on the ExPASy Server. in The Proteomics Protocols Handbook (ed. Walker, J. M.) 571–607 (Humana Press, 2005).

Goldman, P. J. et al. X-ray structure of an AdoMet radical activase reveals an anaerobic solution for formylglycine posttranslational modification. *Proc. Natl. Acad. Sci. U.S.A*. **2013**, *110*, 8519–8524.

Goldman, P. J.; Grove, T. L.; Sites, L. A.; McLaughlin, M. I.; Booker, S. J.; Drennan, C. L., X-ray structure of an AdoMet radical activase reveals an anaerobic solution for formylglycine posttranslational modification. *Proc Natl Acad Sci U S A* **2013**, *110* (21), 8519-24.

Grell, T. A. J., Goldman, P. J. & Drennan, C. L. SPASM and twitch domains in *S*-adenosylmethionine (SAM) radical enzymes. *J. Biol. Chem*. **2015**, *290*, 3964–3971.

Grell, T. A. J.; Kincannon, W. M.; Bruender, N. A.; Blaesi, E. J.; Krebs, C.; Bandarian, V.; Drennan, C. L., Structural and spectroscopic analyses of the sporulation killing factor biosynthetic enzyme SkfB, a bacterial AdoMet radical sactisynthase. *J Biol Chem* **2018**, *293* (45), 17349-17361.

Grimme, S., Antony, J., Ehrlich, S. & Krieg, H. A consistent and accurate ab initio parametrization of density functional dispersion correction (DFT-D) for the 94 elements H-Pu. *J. Chem. Phys*. **2010**, *132*, 154104.

Grove, T. L. et al. Structural insights into thioether bond formation in the biosynthesis of sactipeptides. *J. Am. Chem. Soc*. **2017**, *139*, 11734–11744.

Guo, S. et al. Radical SAM-dependent ether crosslink in daropeptide biosynthesis. *Nat. Commun*. **2022**, *13*, 2361.

Haft, D. H., Basu, M. K. & Mitchell, D. A. Expansion of ribosomally produced natural products: a nitrile hydratase- and Nif11-related precursor family. *BMC Biol*. **2010**, *8*, 70.

Hamada, T.; Matsunaga, S.; Yano, G.; Fusetani, N., Polytheonamides A and B, Highly Cytotoxic, Linear Polypeptides with Unprecedented Structural Features, from the Marine Sponge, Theonella swinhoei. *J. Am. Chem. Soc*. **2005**, *127* (1), 110-118.

Han, X. X., Rodriguez, R. S., Haynes, C. L., Ozaki, Y. & Zhao, B. Surface-enhanced Raman spectroscopy. *Nat. Rev. Methods Primers* **2022**, *1*, 1–17.

Harder, J.; Eliasson, R.; Pontis, E.; Ballinger, M. D.; Reichard, P., Activation of the Anaerobic Ribonucleotide Reductase from Escherichia coli by *S*-Adenosylmethionine. *J. Biol. Chem*. **1992**, *267*, 25548-25552.

Heller, C.; McConnell, H. M., Radiation Damage in Organic Crystals. II. Electron Spin Resonance of (CO2H)CH2CH(CO2H) in β-Succinic Acid. *The Journal of Chemical Physics* **1960**, *32* (5), 1535-1539.

Henshaw, T. F.; Cheek, J.; Broderick, J. B., The $[4Fe\text{-}4S]^{+}$ cluster of pyruvate formate-lyase activating enzyme generates the glycyl radical on pyruvate formate-lyase: EPR-detected single turnover. *J. Am. Chem. Soc*. **2000**, *122*, 8331-8332.

Hioe, J.; Savasci, G.; Brand, H.; Zipse, H., The stability of Cα peptide radicals: why glycyl radical enzymes? *Chemistry* **2011**, *17* (13), 3781-9.

Hoffman, B. M., Broderick, W. E. & Broderick, J. B. Mechanism of radical Initiation in the radical SAM enzyme superfamily. *Annu. Rev. Biochem*. **2023**, *92*, 333–349.

Holliday, G. L.; Akiva, E.; Meng, E. C.; Brown, S. D.; Calhoun, S.; Pieper, U.; Sali, A.; Booker, S. J.; Babbitt, P. C., Atlas of the radical SAM superfamily: Divergent evolution of function using a “Plug and Play” domain. *Methods Enzymol*. **2018**, *606*, 1-71.

Hoover, D., M.; Lubkowski, J., DNAWorks: an automated method for designing oligonucleotides for PCR-based gene synthesis. *Nucl. Acids Res.* **2002**, *30* (10), e43.

Horitani, M.; Byer, A. S.; Shisler, K. A.; Chandra, T.; Broderick, J. B.; Hoffman, B. M., Why Nature Uses Radical SAM Enzymes so Widely: Electron Nuclear Double Resonance Studies of Lysine 2,3-Aminomutase Show the 5'-dAdo• "Free Radical" is Never Free. *J. Am. Chem. Soc*. **2015**, *137*, 7111-7121.

Horitani, M.; Shisler, K. A.; Broderick, W. E.; Hutcheson, R. U.; Duschene, K. S.; Marts, A. R.; Hoffman, B. M.; Broderick, J. B., Radical SAM catalysis via an organometallic intermediate with an Fe-[5'-C]-deoxyadenosyl bond. *Science* **2016**, *352* (6287), 822-825.

Huang, P.-S.; Ban, Y.-E. A.; Richter, F.; Andre, I.; Vernon, R.; Schief, W. R.; Baker, D., RosettaRemodel: A generalized framework for flexible backbone protein design. *PLoS ONE* **2011**, *6* (8), e24109.

Hubrich, F.; Lotti, A.; Scott, T. A.; Piel, J., Uncovering Novel Peptide Chemistry from Bacterial Natural Products. *Chimia* (Aarau) **2021**, *75* (6), 543-547.

Hudson, G. A.; Mitchell, D. A., RiPP antibiotics: biosynthesis and engineering potential. *Curr. Op. Microbiol*. **2018**, *45*, 61-69.

Impano, S.; Yang, H.; Jodts, R. J.; Pagnier, A.; Swimley, R.; McDaniel, E. C.; Shepard, E. M.; Broderick, W. E.; Broderick, J. B.; Hoffman, B. M., Active-Site Controlled, Jahn-Teller Enabled Regioselectivity in Reductive S-C Bond Cleavage of *S*-Adenosylmethionine (SAM) in Radical-SAM Enzymes. *J. Am .Chem. Soc*. **2021**, *143* (1), 335-348.

Impano, S.; Yang, H.; Shepard, E. M.; Swimley, R.; Pagnier, A.; Broderick, W. E.; Hoffman, B. M.; Broderick, J. B., *S*-Adenosyl-L-ethionine is a catalytically competent analog of *S*-adenosyl-L-methionine (SAM) in the radical SAM enzyme HydG. *Angew. Chem. Int. Ed.* **2021**, *60*, 4666-4672.

Issac, M. et al. Cyclotheonellazoles A-C, potent protease inhibitors from the marine sponge theonella aff. swinhoei. *J. Nat. Prod*. **2017**, *80*, 1110–1116.

Jodts, R. J.; Wittkop, M.; Ho, M. B.; Broderick, W. E.; Broderick, J. B.; Hoffman, B. M.; Mosquera, M. A., Computational description of alkylated iron-sulfur organometallic clusters. *J. Am. Chem. Soc*. **2023**, *145* (25), 13879-13887.

Johnson, B. A.; Clark, K. A.; Bushin, L. B.; Spolar, C. N.; Seyedsayamdost, M. R., Expanding the Landscape of Noncanonical Amino Acids in RiPP Biosynthesis. *J Am Chem Soc* **2024,** *146* (6), 3805-3815.

Kamisetty, H.; Ovchinnikov, S.; Baker, D., Assessing the utility of coevolution-based residue-residue contact predictions in a sequence- and structure-rich era. *Proc. Natl. Acad. Sci. U. S. A.* **2013**, *110* (39), 15674-15679.

Kearse, M.; Moir, R.; Wilson, A.; Stones-Havas, S.; Cheung, M.; Sturrock, S.; Buxton, S.; Cooper, A.; Markowitz, S.; Duran, C.; Thierer, T.; Ashton, B.; Meintjes, P.; Drummond, A., Geneious Basic: An integrated and extendable desktop software platform for the organization and analysis of sequence data. *Bioinformatics* **2012**, *28* (12), 1647-1649.

Kegler, C. et al. Rapid determination of the amino acid configuration of xenotetrapeptide. *ChemBioChem* **2014**, *15*, 826–828.

Kegler, C.; Nollman, F. I.; Ahrendt, T.; Fleischhacker, F.; Bode, E.; Bode, H. B., Rapid determination of the amino acid configuration of xenotetrapeptide. *Chem. Bio. Chem*. **2014**, *15*, 826-828.

Khaliullin, B.; Ayikpoe, R.; Tuttle, M.; Latham, J. A., Mechanistic elucidation of the mycofactocin-biosynthetic radical *S*-adenosylmethionine protein, MftC. *J Biol Chem* **2017**, *292* (31), 13022-13033.

Kimura, M. et al. Calyxamides A and B, cytotoxic cyclic peptides from the marine sponge Discodermia calyx. *J. Nat. Prod*. **2012**, *75*, 290–294.

King, D. S.; Reichard, P., Mass Spectrometric Determination of the Radical Scission Site in the Anaerobic Ribonucleotide Reductase of Escherichia Coli. *Biochemical and Biophysical Research Communications* **1995**, *206*, 731-735.

Kitagawa, M. et al. Complete set of ORF clones of Escherichia coli ASKA library (a complete set of E. coli K-12 ORF archive): unique resources for biological research. *DNA Res*. **2005**, *12*, 291–299.

Kooser, R. G.; Kirchmann, E.; Matkov, T., Measurements of Spin Electron Paramagnetic Concentration in Resonance Spectroscopy. *Concepts in Magnetic Resonance* **1992**, *4*, 145-152.

Korneli, M.; Fuchs, S. W.; Felder, K.; Ernst, C.; Zinsli, L. V.; Piel, J., Promiscuous Installation of D-Amino Acids in Gene-Encoded Peptides. *ACS Synth Biol* **2021**, *10* (2), 236-242.

Krebs, C.; Broderick, W. E.; Henshaw, T. F.; Broderick, J. B.; Huynh, B. H., Coordination of adenosylmethionine to a unique iron site of the [4Fe-4S] of pyruvate formate-lyase activating enzyme: A Mössbauer spectroscopic study. *J. Am. Chem. Soc*. **2002**, *124* (6), 912-913.

Krebs, C.; Henshaw, T. F.; Cheek, J.; Huynh, B. H.; Broderick, J. B., Conversion of 3Fe-4S to 4Fe-4S Clusters in Native Pyruvate Formate-Lyase Activating Enzyme: Mössbauer Characterization and Implications for Mechanism. *J. Am. Chem. Soc*. **2000**, *122* (50), 12497-12506.

Kubiak, X.; Polsinelli, I.; Chavas, L. M. G.; Fyfe, C. D.; Guillot, A.; Fradale, L.; Brewee, C.; Grimaldi, S.; Gerbaud, G.; Thureau, A.; Legrand, P.; Berteau, O.; Benjdia, A., Structural and mechanistic basis for RiPP epimerization by a radical SAM enzyme. *Nat Chem Biol* **2023**, *20*, 382-391.

Kudo, F.; Hoshi, S.; Kawashima, T.; Kamachi, T.; Eguchi, T., Characterization of a radical *S*-adenosyl-L-methionine epimerase, NeoN, in the last step of neomycin B biosynthesis. *J. Am. Chem. Soc*. **2014**, *136* (39), 13909-13915.

Lachowicz, J.; Lee, J.; Sagatova, A.; Jew, K.; Grove, T. L., The new epoch of structural insights into radical SAM enzymology. *Current Opinion in Structural Biology* **2023**, *83*, 102720.

Lacroix, C., Saussereau, E., Boulanger, F. & Goullé, J. P. Online liquid chromatography-tandem mass spectrometry cyanide determination in blood. *J. Anal. Toxicol*. **2011**, *35*, 143–147.

Laemmli, U. K. Cleavage of structural proteins during the assembly of the head of bacteriophage T4. *Nature* **1970**, *227*, 680–685.

Lakis, E., Magyari, S. & Piel, J. In vivo production of diverse β-amino acid-containing proteins. *Angew. Chem. Int. Ed. Engl*. **2022**, *61*, e202202695.

Landgraf, B. J.; Arcinas, A. J.; Lee, K.-H.; Booker, S. J., Identification of an intermediate methyl carrier in the radical *S*-adenosylmethionine methylthiotransferases RimO and MiaB. *J. Am. Chem. Soc*. **2013**, *135*, 15404-15416.

Landgraf, B. J.; McCarthy, E. L.; Booker, S. J., Radical *S*-adenosylmethionine enzymes in human health and disease. *Annu. Rev. Biochem*. **2016**, *85*, 485-514.

Landgraf, B. J.; Booker, S. J., Stereochemical course of the reaction catalyzed by RimO, a radical SAM methylthiotransferase. *J. Am. Chem. Soc*. **2016**, *138* (9), 2889-2892.

Lanz, N. D. & Booker, S. J. Auxiliary iron-sulfur cofactors in radical SAM enzymes. *Biochim. Biophys. Acta* **2015**, *1853* (6), 1316–1334.

Latham, J. A.; Barr, I.; Klinman, J. P., At the confluence of ribosomally synthesized peptide modification and radical *S*-adenosylmethionine (SAM) enzymology. *J Biol Chem* **2017**, *292* (40), 16397-16405.

Leaver-Fay, A.; Tyka, M.; Lewis, S. M.; Lange, O. F.; Thompson, J.; Jacak, R.; Kaufman, K.; Renfrew, P. D.; Smith, C. A.; Sheffler, W.; Davis, I. W.; Cooper, S.; Treuille, A.; Mandell, D. J.; Richter, F.; Ban, Y.-E. A.; Fleishman, S. J.; Corn, J. E.; Kim, D. E.; Lyskov, S.; Berrondo, M.; Mentzer, S.; Popovic, Z.; Havranek, J. J.; Karanicolas, J.; Das, R.; Meiler, J.; Kortemme, T.; Gray, J. J.; Kuhlman, B.; Baker, D.; Bradley, P., Rosetta3: An object-oriented software suite for the simulation and design of macromolecules. *Methods Enzymol*. **2011**, *487*, 545-547.

Lees, N. S.; Ha¨nzelmann, P.; Hernandez, H. L.; Subramanian, S.; Schindelin, H.; Johnson, M. K.; Hoffman, B. M., ENDOR Spectroscopy Shows That Guanine N1 Binds to [4Fe-4S] Cluster II of the *S*-Adenosylmethionine-Dependent Enzyme MoaA: Mechanistic Implications. *J Am Chem Soc* **2009**, *131* (26), 9184–9185.

LeMaster, D. M. & Richards, F. M. Preparative-scale isolation of isotopically labeled amino acids. *Anal. Biochem*. **1982**, *122*, 238–247.

Lien, Y. et al. Structural, biochemical, and bioinformatic basis for identifying radical SAMcyclopropyl synthases. *ACS Chem. Biol*. **2024**, *19*, 370–379.

Lilla, E. A.; Yokoyama, K., Carbon extension in peptidylnucleoside biosynthesis by radical SAM enzymes. *Nat. Chem. Biol*. **2016**, *12*, 905-907.

Liu, A. & Gräslund, A. Electron paramagnetic resonance evidence for a novel interconversion of $[3Fe\text{-}4S]^{+}$ and $[4Fe\text{-}4S]^{+}$ clusters with endogenous iron and sulfide in anaerobic ribonucleotide reductase activase in vitro. *J. Biol. Chem*. **2000**, *275*, 12367–12373.

Löwdin, P. On the non-orthogonality problem connected with the use of atomic wave functions in the theory of molecules and crystals. *J. Chem. Phys*. **2004**, *18*, 365–375.

Lu, J.; Xu, H.; Xia, J.; Ma, J.; Xu, J.; Li, Y.; Feng, J., D- and Unnatural Amino Acid Substituted Antimicrobial Peptides With Improved Proteolytic Resistance and Their Proteolytic Degradation Characteristics. *Front Microbiol* **2020**, *11*, 563030.

Lundahl, M. N.; Sarksian, R.; Yang, H.; Jodts, R. J.; Pagnier, A.; Smith, D. F.; Mosquera, M. A.; van der Donk, W. A.; Hoffman, B. M.; Broderick, W. E.; Broderick, J. B., Mechanism of Radical *S*-Adenosyl-L-methionine Adenosylation: Radical Intermediates and the Catalytic Competence of the 5'-Deoxyadenosyl Radical. *J Am Chem Soc* **2022**, *144* (11), 5087-5098.

Lundahl, M. N.; Yang, H.; Broderick, W. E.; Hoffman, B. M.; Broderick, J. B., Pyruvate formate-lyase activating enzyme: The catalytically active 5'-deoxyadenosyl radical caught in the act of H-atom abstraction. *Proc Natl Acad Sci U S A* **2023**, *120* (47), e2314696120.

MacFarlane, I. J., Lees, E. M. & Conn, E. E. The in vitro biosynthesis of dhurrin, the cyanogenic glycoside of Sorghum bicolor. *J. Biol. Chem*. **1975**, *250*, 4708–4713.

Mahanta, N.; Hudson, G. A.; Mitchell, D. A., Radical *S*-Adenosylmethionine Enzymes Involved in RiPP Biosynthesis. *Biochemistry* **2017**, *56* (40), 5229-5244.

Maiocco, S. J.; Grove, T. L.; Booker, S. J.; Elliott, S. J., Electrochemical Resolution of the [4Fe-4S] Centers of the AdoMet Radical Enzyme BtrN: Evidence of Proton Coupling and an Unusual, Low-Potential Auxiliary Cluster. *J Am Chem Soc* **2015**, *137* (27), 8664-7.

Maiocco, S. J.; Walker, L. M.; Elliott, S. J., Determining Redox Potentials of the Iron-Sulfur Clusters of the AdoMet Radical Enzyme Superfamily. *Methods Enzymol* **2018**, *606*, 319-339.

Mayhew, S. G., The Redox Potential of Dithionite and SO; from Equilibrium Reactions with Flavodoxins, Methyl Viologen and Hydrogen plus Hydrogenase. *Eur. J. Biochem* **1978**, *85*, 535-547.

Montalban-Lopez, M.; Scott, T. A.; Ramesh, S.; Rahman, I. R.; van Heel, A. J.; Viel, J. H.; Bandarian, V.; Dittmann, E.; Genilloud, O.; Goto, Y.; Grande Burgos, M. J.; Hill, C.;

Kim, S.; Koehnke, J.; Latham, J. A.; Link, A. J.; Martinez, B.; Nair, S. K.; Nicolet, Y.; Rebuffat, S.; Sahl, H. G.; Sareen, D.; Schmidt, E. W.; Schmitt, L.; Severinov, K.; Sussmuth, R. D.; Truman, A. W.; Wang, H.; Weng, J. K.; van Wezel, G. P.; Zhang, Q.; Zhong, J.; Piel, J.; Mitchell, D. A.; Kuipers, O. P.; van der Donk, W. A., New developments in RiPP discovery, enzymology and engineering. *Nat Prod Rep* **2021**, *38* (1), 130-239.

Moody, J. D.; Hill, S.; Lundahl, M. N.; Saxton, A. J.; Galambas, A.; Broderick, W. E.; Lawrence, C. M.; Broderick, J. B., Computational engineering of previously crystallized pyruvate formate-lyase activating enzyme reveals insights into SAM binding and reductive cleavage. *J Biol Chem* **2023**, *299* (6), 104791.

Mordhorst, S.; Badmann, T.; Bosch, N. M.; Morinaka, B. I.; Rauch, H.; Piel, J.; Groll, M.; Vagstad, A. L., Structural and Biochemical Insights into Post-Translational Arginine-to-Ornithine Peptide Modifications by an Atypical Arginase. *ACS Chem Biol* **2023,** *18* (3), 528-536.

Mordhorst, S.; Morinaka, B. I.; Vagstad, A. L.; Piel, J., Posttranslationally Acting Arginases Provide a Ribosomal Route to Non-proteinogenic Ornithine Residues in Diverse Peptide Sequences. *Angew Chem Int Ed Engl* **2020**, *59* (48), 21442-21447.

Morinaka, B. I.; Lakis, E.; Verest, M.; Helf, M. J.; Scalvenzi, T.; Vagstad, A. L.; Sims, J.; Sunagawa, S.; Gugger, M.; Piel, J., Natural noncanonical protein splicing yields products with diverse β-amino acid residues. *Science* **2018**, *359*, 779-782.

Morinaka, B. I.; Vagstad, A. L.; Helf, M. J.; Gugger, M.; Kegler, C.; Freeman, M. F.; Bode, H. B.; Piel, J., Radical *S*-adenosyl methionine epimerases: regioselective introduction of diverse D-amino acid patterns into peptide natural products. *Angew Chem Int Ed Engl* **2014**, *53* (32), 8503-7.

Morinaka, B. I.; Vagstad, A. L.; Piel, J., Radical S-Adenosylmethionine Peptide Epimerases: Detection of Activity and Characterization of D-Amino Acid Products. *Methods Enzymol* **2018**, *604*, 237-257.

Morinaka, B. I.; Verest, M.; Freeman, M. F.; Gugger, M.; Piel, J., An orthogonal D_2O-based induction system that provides insights into D-amino acid pattern formation by radical *S*-adenosylmethionine peptide epimerases. *Angew. Chem*. **2017**, *129*, 780-784.

Nakashima, Y.; Kawakami, A.; Ogasawara, Y.; Maeki, M.; Tokeshi, M.; Dairi, T.; Morita, H., Structure of lasso peptide epimerase MslH reveals metal-dependent acid/base catalytic mechanism. *Nat Commun* **2023**, *14* (1), 4752.

Neese, F. The ORCA program system. Wiley *Interdiscip. Rev. Comput. Mol. Sci*. **2012**, *2*, 73–78.

Neese, F., Wennmohs, F., Becker, U. & Riplinger, C. The ORCA quantum chemistry program package. *J Chem Phys* **2020**, *152*, 224108.

Németh, B.; Land, H.; Magnuson, A.; Hofer, A.; Berggren, G., The maturase HydF enables [FeFe] hydrogenase assembly via transient, cofactor-dependent interactions. *J. Biol. Chem*. **2020**, *295* (33), 11891-11901.

Nguyen, D. T.; Mitchell, D. A.; van der Donk, W. A., Genome Mining for New Enzyme Chemistry. *ACS Catal* **2024**, *14* (7), 4536-4553.

Nguyen, D. T.; Zhu, L.; Gray, D. L.; Woods, T. J.; Padhi, C.; Flatt, K. M.; Mitchell, D. A.; van der Donk, W. A., Biosynthesis of Macrocyclic Peptides with C-Terminal β-Amino-α-keto Acid Groups by Three Different Metalloenzymes. *ACS Central Science* **2024,** *10* (5), 1022–1032.

Nicolet, Y., Structure-function relationships of radical of radical SAM enzymes. *Nat. Catal.* **2020**, *3*, 337-2020.

Nicolet, Y.; Drennan, C. L., AdoMet radical proteins--from structure to evolution--alignment of divergent protein sequences reveals strong secondary structure element conservation. *Nucleic Acids Res*. **2004**, *32* (13), 4015-4025.

Noodleman, L. Exchange coupling and resonance delocalization in reduced iron-sulfur $[Fe_4S_4]^+$ and iron-selenium $[Fe_4Se_4]^+$ clusters. 1. Basic theory of spin-state energies and EPR and hyperfine properties. *Inorg. Chem*. **1991**, *30*, 246–256.

Oberg, N.; Precord, T. W.; Mitchell, D. A.; Gerlt, J. A., RadicalSAM.org: A Resource to Interpret Sequence-Function Space and Discover New Radical SAM Enzyme Chemistry. *ACS Bio & Med Chem Au* **2022,** *2* (1), 22-35.

O'Brien, J. R.; Raynaud, C.; Croux, C.; Girbal, L.; Soucaille, P.; Lanzilotta, W. N., Insight into the mechanism of the B_{12}-independent glycerol dehydratase from *Clostridium butyricum*: Preliminary biochemical and structural characterization. *Biochemistry* **2004**, *43* (16), 4635-4645.

Ogasawara, Y.; Dairi, T., Peptide epimerization machineries found in microorganisms. *Front. Microbiol*. **2018**, *9*, 156.

Okeke, I. N.; de Kraker, M. E. A.; Van Boeckel, T. P.; Kumar, C. K.; Schmitt, H.; Gales, A. C.; Bertagnolio, S.; Sharland, M.; Laxminarayan, R., The scope of the antimicrobial resistance challenge. *The Lancet* **2024**, *403* (10442), 2426-2438.

Oman, t. J.; donk, W. a. v. d., Follow the leader: the use of leader peptides to guide natural product biosynthesis. *Nature Chemical Biology* **2010**, *6*, 9-18.

Pagnier, A.; Yang, H.; Jodts, R.; James, C.; Shepard, E. M.; Impano, S.; Broderick, W.; Hoffman, B. M.; Broderick, J. B., The Radical SAM enzyme Spore Photoproduct Lyase: Properties of the Omega Organometallic Intermediate and Identification of Stable Protein

Radicals Formed During Substrate-Free Turnover. *J Am Chem Soc* **2020,** *142* (43), 18652–18660.

Panavas, T.; Sanders, C.; Butt, T. R., SUMO fusion technology for enhanced protein production in prokaryotic expression systems. *Methods Mol. Biol*. **2009**, *497*, 303-317.

Panufnik, E. & Kañska, M. Enzymatic synthesis of isotopomers of tyramine labeled with deuterium and tritium. *J. Label. Compd. Radiopharm*. **2007**, *50*, 85–89.

Parent, A.; Benjdia, A.; Guillot, A.; Kubiak, X.; Balty, C.; Lefranc, B.; Leprince, J.; Berteau, O., Mechanistic investigations of PoyD, a radical *S*-adenosyl-L-methionine enzyme catalyzing iterative and directional epimerizations in polytheonamide A biosynthesis. *J. Am .Chem. Soc*. **2018**, *140*, 2469-2477.

Patchornik, Abraham. & Sokolovsky, Mordechai. Nonenzymatic cleavages of peptide chains at the cysteine and serine residues through their conversion into dehydroalanine. I. Hydrolytic and oxidative cleavage of dehydroalanine residues. *J. Am. Chem. Soc*. **1964**, *86*, 1206–1212.

Pei, Z.-F.; Zhu, L.; Nair, S. K., Core-dependent post-translational modifications guide the biosynthesis of a new class of hypermodified peptides. *Nat. Commun*. **2023**, *14*, 7734.

Peng, Y.; Veneziano, S. E.; Gillispie, G. D.; Broderick, J. B., Pyruvate formate-lyase, evidence for an open conformation favored in the presence of its activating enzyme. *J Biol Chem* **2010**, *285* (35), 27224-27231.

Perdew, J. P., Burke, K. & Ernzerhof, M. Generalized gradient approximation made simple. *Phys. Rev. Lett*. **1996**, *77*, 3865–3868.

Perdew, J. P., Burke, K. & Ernzerhof, M. Generalized gradient approximation made simple. *Phys. Rev. Lett*. **1997**, *78*, 1396–1396.

Pfeiffer, I. P.; Schroder, M. P.; Mordhorst, S., Opportunities and challenges of RiPP-based therapeutics. *Nat Prod Rep* **2024,** *41*, 990-1019.

Phan, C.-S. et al. Substrate promiscuity of the triceptide maturase XncB leads to incorporation of various amino acids and detection of oxygenated products. *ACS Chem. Biol*. **2024**, *19*, 855–860.

Plaza, A., Viehrig, K., Garcia, R. & Müller, R. Jahnellamides, α-keto-β-methionine-containing peptides from the terrestrial myxobacterium Jahnella sp.: Structure and biosynthesis. *Org. Lett*. **2013**, *15*, 5882–5885.

Popp, P. F.; Benjdia, A.; Strahl, H.; Berteau, O.; Mascher, T., The Epipeptide YydF Intrinsically Triggers the Cell Envelope Stress Response of Bacillus subtilis and Causes Severe Membrane Perturbations. *Front Microbiol* **2020**, *11*.

Popp, P. F.; Friebel, L.; Benjdia, A.; Guillot, A.; Berteau, O.; Mascher, T., The Epipeptide Biosynthesis Locus epeXEPAB Is Widely Distributed in Firmicutes and Triggers Intrinsic Cell Envelope Stress. *Microb Physiol* **2021**, *31* (3), 306-318.

Raynaud, C.; Sarcabal, P.; Meynial-Salles, I.; Croux, C.; Soucaille, P., Molecular characterization of the 1,3-propanediol (1,3-PD) operon of Clostridium butyricum. *Proc. Natl. Acad. Sci. U.S.A.* **2003**, *100* (9), 5010-5015.

Richter, D., Lakis, E. & Piel, J. Site-specific bioorthogonal protein labelling by tetrazine ligation using endogenous β-amino acid dienophiles. *Nat. Chem*. **2023**, *15*, 1422–1430.

Robello, M. et al. The alpha keto amide moiety as a privileged motif in medicinal chemistry: current insights and emerging opportunities. *J. Med. Chem* **2021**, *64*, 3508–3545.

Rödel, W.; Plaga, W.; Frank, R.; Knappe, J., Primary structures of Escherichia coli pyruvate formate-lyase and pyruvate formate-lyase-activating enzyme deduced from the DNA nucleotide sequences. *Eur. J. Biochem*. **1988**, *177*, 153-158.

Rubinson, K. A., Practical corrections for p(H,D) measurements in mixed H_2O/D_2O biological buffers. *Analytical Methods* **2017**, *9* (18), 2744-2750.

Ruijne, F.; Kuipers, O. P., Combinatorial biosynthesis for the generation of new-to-nature peptide antimicrobials. *Biochem Soc Trans* **2021**, *49* (1), 203-215.

Rupp, H., Rao, K. K., Hall, D. O. & Cammack, R. Electron spin relaxation of iron-sulphur proteins studied by microwave power saturation. *Biochim. Biophys. Acta* **1978**, *537*, 255–269.

Rush, K. W.; Eastman, K. A. S.; Kincannon, W. M.; Blackburn, N. J.; Bandarian, V., Peptide Selenocysteine Substitutions Reveal Direct Substrate-Enzyme Interactions at Auxiliary Clusters in Radical *S*-Adenosyl-L-methionine Maturases. *J Am Chem Soc* **2023,** *145* (18), 10167–10177.

Ruszczycky, M. W., Zhong, A. & Liu, H. Following the electrons: peculiarities in the catalytic cycles of radical SAM enzymes. *Nat. Prod. Rep*. **2018**, *35*, 615–621.

Sato, S.; Kudo, F.; Rohmer, M.; Eguchi, T., Biochemical and mutational analysis of radical *S*-adenosyl-L-methionine adenosylhopane synthase HpnH *Zymomonas mobilis* reveals that conserved residue cysteine-106 reduces a radical intermediate and determines the stereochemistry. *J. Am. Chem. Soc*. **2021**, *60* (38), 2865-2874.

Sayler, R. I.; Stich, T. A.; Joshi, S.; Cooper, N.; Shaw, J. T.; Begley, T. P.; Tantillo, D. J.; Britt, R. D., Trapping and electron paramagnetic resonance characterization of the 5'-dAdo• radical in a radical *S*-adenosylmethionine enzyme reaction with a non-native substrate. *ACS Cent. Sci*. **2019**, *5* (11), 1777-1785.

Schäfer, A., Huber, C. & Ahlrichs, R. Fully optimized contracted Gaussian basis sets of triple zeta valence quality for atoms Li to Kr. *J. Chem. Phys*. **1994**, *100*, 5829–5835.

Scott, T. A.; Verest, M.; Farnung, J.; Forneris, C. C.; Robinson, S. L.; Ji, X.; Hubrich, F.; Chepkirui, C.; Richter, D. U.; Huber, S.; Rust, P.; Streiff, A. B.; Zhang, Q.; Bode, J. W.; Piel, J., Widespread microbial utilization of ribosomal β-amino acid-containing peptides and proteins. *Chem* **2022**, *8* (10), 2659-2677.

Selmer, T.; Pierik, A. J.; Heider, J., New glycyl radical enzymes catalysing key metabolic steps in anaerobic bacteria. *Biol. Chem*. **2005**, *386*, 981-988.

Selvaraj, B.; Pierik, A. J.; Bill, E.; Martins, B. M., 4-Hydroxyphenylacetate decarboxylase activating enzyme catalyses a classical *S*-adenosylmethionine reductive cleavage reaction. *J. Biol. Inorg. Chem*. **2013**, *18*, 633-643.

Shisler, K. A.; Hutcheson, R. U.; Horitani, M.; Duschene, K. S.; Crain, A. V.; Byer, A. S.; Shepard, E. M.; Rasmussen, A.; Yang, J.; Broderick, W. E.; Vey, J. L.; Drennan, C. L.; Hoffman, B. M.; Broderick, J. B., Monovalent cation activation of the radical SAM enzyme pyruvate formate-lyase activating enzyme. *J. Am. Chem. Soc*. **2017**, *139* (34), 11803-11813.

Shisler, K. A.; Broderick, J. B., Glycyl Radical Activating Enzymes: Structure, Mechanism, and Substrate Interactions. *Archives of biochemistry and biophysics* **2014**, *546*, 64-71.

Sikandar, A.; Franz, L.; Adam, S.; Santos-Aberturas, J.; Horbal, L.; Luzhetskyy, A.; Truman, A. W.; Kalinina, O. V.; Koehnke, J., The bottromycin epimerase BotH defines a group of atypical α/β-hydrolase-fold enzymes. *Nat Chem Biol* **2020**, *16* (9), 1013-1018.

Silver, S. C.; Chandra, T.; Zilinskas, E.; Ghose, S.; Broderick, W. E.; Broderick, J. B., Complete Stereospecific Repair of a Synthetic Dinucleotide Spore Photoproduct by Spore Photoproduct Lyase. *J. Biol. Inorg. Chem*. **2010**, *15* (6), 943-955.

Sofia, H. J.; Chen, G.; Hetzler, B. G.; Reyes-Spindola, J. F.; Miller, N. E., Radical SAM, a novel protein superfamily linking unresolved steps in familiar biosynthetic pathways with radical mechanisms: functional characterization using new analysis and information visualization methods. *Nucleic Acids Res*. **2001**, *29* (5), 1097-1106.

Stoll, S.; Schweiger, A., EasySpin, a comprehensive software package for spectral simulation and analysis in EPR. *J. Magn. Res*. **2006**, *178* (1), 42-55.

Storey, J. M. et al. A rapid liquid chromatography determination of free formaldehyde in cod. *Food Addit. Contam. Part A* **2015**, *32*, 657–664.

Sugiyama, R.; Suarez, A. F. L.; Morishita, Y.; Nguyen, T. Q. N.; Tooh, Y. W.; Roslan, M. N. H. B.; Lo Choy, J.; Su, Q.; Goh, W. Y.; Gunawan, G. A.; Wong, F. T.; Morinaka, B. I., The Biosynthetic Landscape of Triceptides Reveals Radical SAM Enzymes That Catalyze

Cyclophane Formation on Tyr- and His-Containing Motifs. *Journal of the American Chemical Society* **2022,** *144* (26), 11580–11593.

Tao, L.; Zhu, W.; Klinman, J. P.; Britt, R. D., Electron Paramagnetic Resonance Spectroscopic Identification of the Fe-S Clusters in the SPASM Domain-Containing Radical SAM Enzyme PqqE. *Biochemistry* **2019**, *58* (51), 5173-5187.

TURBOMOLE V7.2 2017, a development of University of Karlsruhe and Forschungszentrum Karlsruhe GmbH, 1989-2007, TURBOMOLE GmbH, since 2007; available from http://www.turbomole.com.

Vagstad, A. L., Engineering ribosomally synthesized and posttranslationally modified peptides as new antibiotics. *Curr Opin Biotechnol* **2023**, *80*, 102891.

Vagstad, A. L.; Kuranaga, T.; Puntener, S.; Pattabiraman, V. R.; Bode, J. W.; Piel, J., Introduction of D-Amino Acids in Minimalistic Peptide Substrates by an *S*-Adenosyl-L-Methionine Radical Epimerase. *Angew Chem Int Ed Engl* **2019**, *58* (8), 2246-2250.

Vagstad, A. L.; Lakis, E.; Csizi, K. S.; Walls, W.; Richter, D.; Soo Lee, K.; Stocker, R.; Gugger, M.; Broderick, W. E.; Broderick, J. B.; Reiher, M.; Piel, J., Mechanistic Insights Into Post-Translational α-Keto-β-Amino Acid Formation by a Radical *S*-Adenosyl Methionine Peptide Splicease. *Angew Chem Int Ed Engl* **2025**, *64*, e202418054.

Varadi, M.; Anyango, S.; Deshpande, M.; Nair, S.; Natassia, C.; Yordanova, G.; Yuan, D.; Stroe, O.; Wood, G.; Laydon, A.; Žídek, A.; Green, T.; Tunyasuvunakool, K.; Petersen, S.; Jumper, J.; Clancy, E.; Green, R.; Vora, A.; Lutfi, M.; Figurnov, M.; Cowie, A.; Hobbs, N.; Kohli, P.; Kleywegt, G.; Birney, E.; Hassabis, D.; Velankar, S., AlphaFold Protein Structure Database: massively expanding the structural coverage of protein-sequence space with high-accuracy models. *Nucl. Acids Res*. **2022**, *50* (D1), D439-D444.

Vey, J. L.; Yang, J.; Li, M.; Broderick, W. E.; Broderick, J. B.; Drennan, C. L., Structural basis for glycyl radical formation by pyruvate formate-lyase activating enzyme. *Proc. Natl. Acad. Sci. U.S.A*. **2008**, *105* (42), 16137-16141.

Wagner, A. F.; Schultz, S.; Bomke, J.; Pils, T.; Lehmann, W. D.; Knappe, J., YfiD of Escherichia coli and Y06I of bacteriophage T4 as autonomous glycyl radical cofactors reconstituting the catalytic center of oxygen-fragmented pyruvate formate-lyase. *Biochem Biophys Res Commun* **2001**, *285* (2), 456-62.

Walker, L. M.; Kincannon, W. M.; Bandarian, V.; Elliott, S. J., Deconvoluting the Reduction Potentials for the Three [4Fe-4S] Clusters in an AdoMet Radical SCIFF Maturase. *Biochemistry* **2018**, *57* (42), 6050-6053.

Walls, W. G.; Moody, J. D.; McDaniel, E. C.; Villanueva, M.; Shepard, E. M.; Broderick, W. E.; Broderick, J. B., The B_{12}-independent glycerol dehydratase activating enzyme from

Clostridium butyricum cleaves SAM to produce 5′-deoxyadenosine and not 5′-deoxy-5′-(methylthio)adenosine. *Journal of Inorganic Biochemistry* **2022,** *227*, 111662.

Walls, W. G.; Vagstad, A. L.; Delridge, T.; Piel, J.; Broderick, W. E.; Broderick, J. B., Direct Detection of the α-Carbon Radical Intermediate Formed by OspD: Mechanistic Insights into Radical *S*-Adenosyl-L-methionine Peptide Epimerization. *J Am Chem Soc* **2024**, *146* (8), 5550-5559.

Walsby, C. J.; Hong, W.; Broderick, W. E.; Cheek, J.; Ortillo, D.; Broderick, J. B.; Hoffman, B. M., Electron-nuclear double resonance spectroscopic evidence that *S*-adenosylmethionine binds in contact with the catalytically active $[4Fe\text{-}4S]^{+}$ cluster of pyruvate formate-lyase activating enzyme. *J. Am. Chem. Soc*. **2002**, *124* (12), 3143-3151.

Walsby, C. J.; Ortillo, D.; Broderick, W. E.; Broderick, J. B.; Hoffman, B. M., An anchoring role for FeS Clusters: Chelation of the amino acid moiety of *S*-adenosylmethionine to the unique iron site of the [4Fe-4S] cluster of pyruvate formate-lyase activating enzyme. *J. Am. Chem. Soc*. **2002**, *124* (38), 11270-11271.

Walsby, C. J.; Ortillo, D.; Yang, J.; Nnyepi, M. R.; Broderick, W. E.; Hoffman, B. M.; Broderick, J. B., Spectroscopic Approaches to Elucidating Novel Iron−Sulfur Chemistry in the “Radical-SAM” Protein Superfamily. *Inorganic Chemistry* **2005**, *44*, 727-741.

Wang, Y.; Hu, X.; Morales-Rivera, C. A.; Li, G.-X.; Huang, X.; He, G.; Liu, P.; Chen, G., Epimerization of tertiary carbon centers via reversible radical cleavage of unactivated $C(sp^3)$–H bonds. *J. Am. Chem. Soc*. **2018**, *140*, 9678-9684.

Wecksler, S. R.; Stoll, S.; Tran, H.; Magnusson, O. T.; Wu, S. P.; King, D.; Britt, R. D.; Klinman, J. P., Pyrroloquinoline quinone biogenesis: demonstration that PqqE from Klebsiella pneumoniae is a radical *S*-adenosyl-L-methionine enzyme. *Biochemistry* **2009**, *48* (42), 10151-61.

Wu, C.; van der Donk, W. A., Engineering of new-to-nature ribosomally synthesized and post-translationally modified peptide natural products. *Curr. Op. Biotech*. **2021**, *69*, 221-231.

Xiong, J.; Luo, S.; Qin, C. X.; Cui, J. J.; Ma, Y. X.; Guo, M. X.; Zhang, S. S.; Li, Y.; Gao, K.; Dong, S. H., Biochemical Reconstitution Reveals the Biosynthetic Timing and Substrate Specificity for Thioamitides. *Org Lett* **2022**, *24* (7), 1518-1523.

Yang, H.; Ho, M. B.; Lundahl, M. N.; Mosquera, M. A.; Broderick, W. E.; Broderick, J. B.; Hoffman, B. M., ENDOR Spectroscopy Reveals the "Free" 5'-Deoxyadenosyl Radical in a Radical SAM Enzyme Active Site Actually is Chaperoned by Close Interaction with the Methionine-Bound $[4Fe\text{-}4S]^{2+}$ Cluster. *J Am Chem Soc* **2024,** *146* (6), 3710-3720.

Yang, H.; Impano, S.; Shepard, E. M.; James, C. D.; Broderick, W. E.; Broderick, J. B.; Hoffman, B. M., Photoinduced electron transfer in a radical SAM enzyme generates an *S*-adenosylmethionine derived methyl radical. *J. Am. Chem. Soc*. **2019**, *141* (40), 16117-16124.

Yang, H.; McDaniel, E. C.; Impano, S.; Byer, A. S.; Jodts, R. J.; Yokoyama, K.; Broderick, W. E.; Broderick, J. B.; Hoffman, B. M., The elusive 5′-deoxyadenosyl radical: Captured and Characterized by Electron Paramagnetic Resonance and Electron Nuclear Double Resonance Spectroscopies. *J. Am. Chem. Soc*. **2019**, *141* (30), 12139-12146.

Ye, M.; Brown, A. C.; Suess, D. L. M., Reversible Alkyl-Group Migration between Iron and Sulfur in [Fe_4S_4] Clusters. *J Am Chem Soc* **2022**, *144* (29), 13184-13195.

Yea, K. et al. Ultra-sensitive trace analysis of cyanide water pollutant in a PDMS microfluidic channel using surface-enhanced Raman spectroscopy. *Analyst* **2005**, *130*, 1009–1011.

Yokoyama, K.; Lilla, E. A., C-C bond forming radical SAM enzymes involved in the construction of carbon skeletons of cofactors and natural products. *Nat. Prod. Rep*. **2018**, *35*, 660-694.

Zeng, W., Song, Y., Wang, R., He, R. & Wang, T. Neutrophil elastase: from mechanisms to therapeutic potential. *J. Pharm. Anal*. **2023**, *13*, 355–366.

Zhang, L. et al. α-Ketoamides as broad-spectrum inhibitors of coronavirus and enterovirus replication: structure-based design, synthesis, and activity assessment. *J. Med. Chem*. **2020**, *63*, 4562–4578.

Zhang, Y.; Zhu, X.; Torelli, A. T.; Lee, M.; Dzikovski, B.; Koralewski, R. M.; Wang, E.; Freed, J.; Krebs, C.; Ealick, S. E.; Lin, H., Diphthamide biosynthesis requires an organic radical generated by an iron-sulphur enzyme. *Nature* **2010**, *465*, 891-896.

Zheng, L.; Cash, V. L.; Flint, D. H.; Dean, D. R., Assembly of Iron-Sulfur Clusters. Identification of an iscSUA-hscBA-fds gene cluster from *Azotobacter vinelandii*. *J. Biol. Chem.* **1998**, *273* (21), 13264-13272.

Zhu, W. et al. Structural properties and catalytic implications of the SPASM domain iron-sulfur clusters in *Methylorubrum extorquens* PqqE. *J. Am. Chem. Soc*. **2020**, *142*, 12620–12634.

Zor, T.; Selinger, Z., Linearization of the Bradford Protein Assay Increases Its Sensitivity: Theoretical and Experimental Studies. *Analytic Biochemistry* **1996**, *236*, 302-308.